# New developments for a multidimensional maximum likelihood approach to analyzing VERITAS data

by

**Alisha Jeanette Barr Chromey**

A dissertation submitted to the graduate faculty

in partial fulfillment of the requirements for the degree of

DOCTOR OF PHILOSOPHY

Major: Astrophysics

Program of Study Committee:
Amanda J. Weinstein, Major Professor
Frank Krennrich
Charles Kerton
Soeren Prell
Robyn Lutz

The student author, whose presentation of the scholarship herein was approved by the program of study committee, is solely responsible for the content of this dissertation. The Graduate College will ensure this dissertation is globally accessible and will not permit alterations after a degree is conferred.

Iowa State University

Ames, Iowa

2022

## DEDICATION

To my beloved Dad, Paul Chromey

*Requiescat in pace*

# TABLE OF CONTENTS

## LIST OF TABLES

# LIST OF FIGURES

# NOMENCLATURE

## Abbreviations

**4D-MLM** 4-Dimension maximum likelihood method

**EA** effective area

**FoV** field of view

**IACT** imaging atmospheric Cherenkov telescope

**IRF** instrument response function

**LT** lookup table

**MAGIC** Major Atmospheric Gamma Imaging Cherenkov

**MSL** mean scaled length

**MSW** mean scaled width

**NSB** night sky background

**PWNe** pulsar wind nebulae

**PSF** point spread function

**RRM** reflected region method

**RBM** ring background method

**SNR** supernovae remnant

**VEGAS** VERITAS Gamma-ray Analysis Suite

**VERITAS** Very Energetic Radiation Imaging Telescope Array System

**VHE** very high energy

# ACKNOWLEDGMENTS

One parcel of advice I received when I was undergraduate preparing to begin graduate studies came from an old friend, who achieved his physics PhD. He told me that dedication is much more essential to a complete thesis than smarts.

He is right of course. What I found is that dedication is not something I can pull out of myself all on my own, anymore than I can extract myself out of a bog by pulling on my own hair. Of all the people in my life who encouraged me the most that person was my Dad, from the moment he showed his young daughter comet Hale-Bopp through his spotting scope set up in what was then our backyard. Even when I doubted myself he never doubted me.

My Dad passed away from from COVID-19 on December 19th 2020.

While I was at my lowest ebb of misery in the weeks and months afterwards, during which I needed to continue on with finishing my thesis, several people kept me afloat. They helped support me emotionally and gave me the help I needed to finish my thesis research. Countless friends and family of myself and my father reached out to me to give support and share our grief. I am sorry that I cannot name all of you. All of you have my deepest gratitude. Multiple times Caleb and Sara Lampen shared their experiences, which helped me keep perspective. Amanda Herzberg, thank you for being the best friend I could ask for in so many ways, including help with some figures in Chapter 2 and Chapter 3.

I would like to thank my committee members, Dr. Charles Kerton, Dr. Frank Krennrich, Dr. Soeren Prell, and Dr. Robyn Lutz for all their patience, feedback, and contributions to my work. Several members of the VERITAS collaboration, in particular Lucy Fortson and Jodi Christiansen, shared their experiences and efforts to help me do better. My high school teachers Dr. Daniel Erickson and Dr. Valerie Navarro have been founts of wisdom in my life even after all these years and helped me remember how far I have come. My advisor, Dr. Amanda Weinstein, what can I say? I could not ask for a better advisor. She has been an indispensable rock in the storms of my life this past year.

Thanks be to God!

## ABSTRACT

Gamma-ray observations from a few hundred MeV up to tens of TeV are a valuable tool for studying particle acceleration and diffusion within our galaxy. Constructing a coherent physical picture of particle accelerators such as supernova remnants, pulsar wind nebulae, and star-forming regions requires the ability to detect extended regions of gamma-ray emission, the ability to analyze small-scale spatial variation within these regions, and the ability to synthesize data from multiple observatories across multiple wavebands. Imaging atmospheric Cherenkov telescopes (IACTs) provide fine angular resolution ($< 0.1$ degree) for gamma rays above 100 GeV. However, their limited fields of view typically make detection of extended sources challenging. Maximum likelihood methods are well-suited to simultaneous analysis of multiple fields with overlapping sources and combining data from multiple gamma-ray observatories. Such methods also offer an alternative approach to estimating the IACT cosmic ray background and consequently an enhanced sensitivity to sources as large as the telescope field of view. I report here on the current status and performance of a maximum likelihood technique for the IACT, VERITAS.

This likelihood method employs source models and a background model, fitted to VERITAS data. A gamma/hadron discrimination parameter, *mean scaled width*, is included in the likelihood making the method four-dimensional. A series of validation studies and crosschecks settled on a preferred function for the point spread function and criteria for controlling systematic and statistical errors in background models. A fully developed 4D-maximum likelihood method was performed on multiple test sources, using the open analysis framework Gammapy. The 4D-MLM results are comparable with those from classical analyses. The discrepancies are greatest at low energies, and further discussion outlines probable causes and future solutions. The 4D-MLM was applied to VERITAS observations on a moderately extended gamma-ray source ($r \sim 0.6°$),

Gamma-Cygni. The observed morphology from the 4D-MLM analysis is consistent with previous IACT studies.

# CHAPTER 1. SCIENTIFIC MOTIVATION

## 1.1 Introduction to Cosmic Ray Origins

In the year 1912, Victor Hess flew himself with a charged electroscope in an air balloon high in the earth's atmosphere. The goal was to measure radiation rates according to atmospheric height. Contrary to expectations, he found strong evidence that radiation no longer decreased, but steadily increased above 2000 meters altitude. The correlation between increasing signal with greater height meant that this radiation must have a cosmic origin. This experiment marked the discovery of cosmic rays and the genesis of high energy astrophysics.

While this was a significant discovery, Hess could not make any other conclusions about the cosmic ray radiation apart from its isotropic nature and cosmic origin. It would not be until the arrival of space science in the 1960s that instruments were placed above the earth's atmosphere to detect the particles themselves. In the intermediate time between the discovery of cosmic rays and the era of satellites, scientists could hypothesize and prove that cosmic rays produced particle shower cascades in the Earth's atmosphere. A crucial discovery with consequences for both cosmic ray physics and gamma-ray astronomy was the 1952 discovery of optical Cherenkov radiation produced by cosmic-ray induced air showers. Observations of atmospheric Cherenkov radiation looking for point sources began almost immediately and once satellites were available particle detectors were developed and launched as well. None have found definitive point sources; the cosmic ray radiation field remains isotropic. The reason for this is well understood ever since the discovery of galactic and inter-galactic magnetic fields. Cosmic rays are charged, moving particles, and therefore passage through galactic scale magnetic fields deviates their trajectories to the point where it is impossible to directly trace their astrophysical production point.

What is generally understood is that the overwhelming number of cosmic rays are protons, followed in lesser fractions by electrons and heavier nuclei. The spectral energy of these particles has also been measured with good precision and ranges up to $10^{20}$ electron volts, requiring acceleration as an essential component of cosmic ray production. While cosmic rays below 1 GeV originate from inside the heliosphere, the origins of cosmic rays at higher energies remain unclear. Where these very high and ultra high energy particles originate is the question underlying the subject of several studies, including this thesis. To answer the question of cosmic ray origins, astronomers observe astrophysical phenomena with acceleration mechanisms (Longair, 2011; Hess, 2018).

## 1.2 Galactic Cosmic Ray Sources

The following subsections focus on three galactic astrophysical objects with known particle acceleration and cosmic ray production, although the type of particle and production mechanism in some scenarios are poorly understood.

### 1.2.1 Pulsar Wind Nebulae

Pulsar wind nebulae (PWNe) or plerions (Gaensler, 2006) are associated with the aftermath of supernovae and created by interactions of relativistic charged particles, ejected into surrounding material by a rapidly spinning, young pulsar. Although not characteristic of most PWNe, the Crab nebula is the poster child of this class of objects. Much of the attention paid to the Crab is due to its confident association with a supernova event observed in 1054 CE, making dating possible. Thirty seven known PWNe have been discovered with energies up to 1 TeV, making them a prominent class of very high energy galactic sources [1].

Gradual spin down of a pulsar's rapid rotation (33 ms for the Crab pulsar) drives the entire process. The lost rotational energy translates into ejection of electrons and positrons from the surface of the pulsar and along intense magnetic fields, into the surroundings. This wind of particles, traveling outward relativistically, interacts with surrounding material, the interstellar medium and gases that were previously the progenitor star's outer layers. The constant stream of

[1]Numbers accessed September 2020, from http://tevcat.uchicago.edu

particles buffering against the denser material form forward and reverse shocks in these layers. As a result, leptons are accelerated, creating a halo of energized particles.

In different environments and with greater pulsar age, PWNe form unique features such a bow shocks and energized particle halos offset from the pulsar. Bright PWNe typically have the smallest source size discussed in this work, on average a few to tens of parsecs in diameter. However, with age, PWNe evolve into more extended sources. A class of evolved PWNe has recently been classified as TeV halos, with emission powered by the Geminga pulsar being the first one of its kind defined with this name (Di Mauro et al., 2019).

The main differences between conventional PWNe and TeV halos are age, size, and nature of confinement. A TeV halo is powered by cosmic rays diffusing from the host PWNe, which then interact non-thermally with background photons and produce TeV radiation. As leptons diffuse from the host PWNe the surrounding region is still dominated by pulsar activity over conventional diffusion. Therefore, TeV halos form much later after the initial SNRs than the PWNe, only after there is a significant population of electrons and positrons that have diffused from the PWNe. An average TeV halo size is on the order of 10 parsecs, significantly larger than PWNe. Typical PWNe size is on the order of 1 parsec. Many details of TeV halos remain unknown and current and future observations across the GeV and TeV spectrum will elucidate the open questions (Sudoh et al., 2019).

A PWNe brightness at high energy largely comes from synchrotron radiation. Relativistic leptons peal off the pulsar surface and, while they traverse through some of the most intense magnetic fields known in the galaxy, the electrons radiate at energies reaching up to X-ray levels. This synchrotron emission can act as an interactive radiation field for the accelerated electrons themselves. In this scenario, X-ray synchrotron is re-emitted at gamma-ray energies reaching TeV levels, in a process called synchrotron self Compton emission. The cosmic microwave background (CMB) and background infrared fields are also radiation fields active in inverse Compton (IC) emission in PWNe. Both of these particle interactions are further described in Chapter 2.

Several PWNe have been observed at TeV energies in the electromagnetic spectrum, radiation that is well explained by IC. With both the known production mechanism and the observed radiation spectrum, properties of PWNe, such as the particle content, injection rate of particles, and magnetic field strength, can be determined. However, since the particle content is well understood to be electrons, PWNe do not account for the majority of cosmic rays. The contribution of PWNe to observed flux levels of electrons and positrons at and above TeV energies remains a question for debate.

### 1.2.2 Supernova Remnants

Despite including the word *supernova* in the name, supernova remnants (SNR) are not the core-collapse or thermonuclear events themselves. Rather, they are emitted radiation from the shock waves, traveling initially thousands of kilometers per second, after thousands of years of evolution. However, the energy source does derive from a portion of $\sim 10^{51}$ ergs of kinetic energy (Reynolds, 2008).

The initial ejecta travels into the surrounding medium with speeds of order $10^4$ km s$^{-1}$ for Type 1a SNR and 5000 km s$^{-1}$ for core-collapse. Interior to the blast wave, ejecta expand almost freely and thus cool adiabatically. After only a few days the shock is slowed down enough by the surrounding medium to produce an inward facing reverse shock that decelerates and gradually reheats the ejecta interior to the blast wave. The surrounding ambient medium is also heated. The bulk movement is still outward and the reverse-plus-forward shock structure persists until an amount of mass comparable to the ejected mass is swept up. This phase is named the pre-Sedov phase and lasts from hundreds to thousands of years.

In the Sedov phase the entire ejected mass has been shocked and the system can be described as an adiabatic point explosion in a uniform region of negligible pressure. This second phase lasts up to tens of thousands of years and ends when the shock is slow enough that significant radiative cooling takes place and the adiabatic approximation breaks down.

The timescales for each phase are rough estimates; the apparent age of an SNR depends on multiple factors. Large scale inhomogeneities, formed by past stellar activity or supernova jets, often exist within circumstellar medium surrounding expanding supernova shocks. Large differences in surrounding material density will cause the SNR shock waves to become asymmetric over time. In a direction where the shock wave encounters higher density material more and more gas is swept up and heated sooner and the shock wave will decelerate at a faster rate. Therefore, it is possible that one region of the expanding SNR will exist at one evolutionary phase while the other region of the SNR will be in a different phase. Furthermore, one rim of the SNR could radiate with a type of emission that is nonexistent along the other rim. The roughly spherical shape observed in most young SNR indicates that circumstellar and interstellar inhomogeneities do not dominate evolution in the initial stages.

The two primary questions to address for cosmic ray production in supernova remnants are what are the particle seed populations and what are the acceleration mechanisms. The most important phases for particle acceleration are pre-Sedov and the transition to the Sedov phase. The particle populations either come from the surrounding medium, interstellar or circumstellar, or the supernova ejecta. Particle acceleration occurs across the boundaries of shock waves. The physical processes of acceleration in SNR shocks are described in more detail in Chapter 2.

Many of the details to go with this general model of SNR evolution remain unknown. These details would resolve the question of how and where cosmic rays are accelerated in SNR shock waves and the maximum generated energy. Signatures of lepton acceleration to ultrarelativistic speeds, namely X-ray continuum emission, are observed in several SNR. Protons and ions must experience acceleration in SNR shocks to very high energies. In the past decade, *Fermi*-LAT observations of some SNR at MeV energies have spectral features that match models of hadronic acceleration, strongly supporting SNR as major contributors to cosmic ray acceleration up at least $10^9$ GeV (Lingenfelter, 2017).

### 1.2.3 Superbubbles and Star Forming Regions

Cosmic ray ions heavier than helium are synthesized in evolved, massive stars; their acceleration to higher energies occurs later. Therefore, confinement must keep heavy ions in local abundance in regions where there is both synthesis and an accelerator. Confinement of accelerating particles must also last long enough to attain observed energies before diffusing out into the greater interstellar medium.

Massive star forming regions host both heavy ion synthesis and supernova shockwaves (Lingenfelter, 2017; Ackermann and et al., 2011). Such environments also host clusters of massive stars, called OB associations. Both strong stellar winds and supernova shockwaves carve out large low density cavities and when the two work together the resulting cavities, over a hundred light years across, are called superbubbles. Turbulent environments from stellar winds and overlapping shocks from multiple supernovae accelerate cosmic rays and confine them in supperbubbles.

The presence of local abundances of freshly accelerated cosmic rays in superbubbles is confirmed by detection of interaction products. Massive star forming regions produce intense infrared radiation fields for IC emission at gamma energy levels. The local over-density of high energy ions is also ideal for gamma-ray emission resulting from cosmic ray ion interactions. Very high energy diffuse emission has been observed at TeV energies from the Galactic Center, indicating the presence of sources of cosmic ray acceleration and high cosmic ray density at VHE. The Cygnus Cocoon is another superbubble, created by multiple OB associations and past supernovae, and radiating bright diffuse gamma-ray emission generated by freshly accelerated cosmic rays, as shown in Figure 1.1.

### 1.2.4 Gamma-Cygni

Gamma Cygni (SNR G78.2+2.1)[2] is a shell-like supernova remnant $\sim 1^\circ$ in diameter (Higgs et al., 1977), first detected in radio at 1210 MHz (Piddington and Minnett, 1952). It is located at a distance between 1.7 to 2.6 kpc, with an age range of 6800-10000 years, within the Sedov phase

[2] A bright star, overlapping the remnant extension, is also named Gamma Cygni

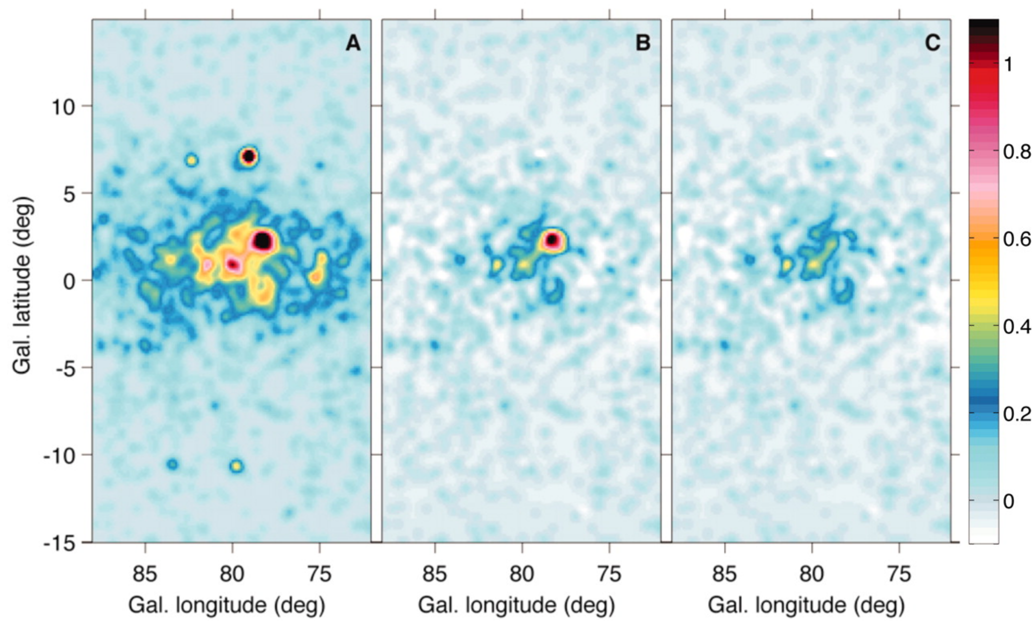


Figure 1.1: Photon counts maps of Cygnus region from 10-100GeV, smoothed with a $\sigma$=0.25° Gaussian kernel, for total emission (left), post-subtraction of all known emission but $\gamma$ Cygni (center), and post-removal of known sources (right) Ackermann and et al. (2011).

(Leahy et al., 2013). A pulsar, PSR J2021+4026, observed in gamma-rays and X-rays, is associated, though not conclusively, with the remnant (Hui et al., 2015). Both are located near a strong, extended source of star formation, Cygnus X, 78° in longitude from galactic center and distance $1.40^{+0.08}_{-0.08}$ kpc. This is one of the most complex regions of star formation in the galactic plane due to the immense amount of activity in a localized region (Rygl et al., 2012).

Gamma-Cygni's bright radio emission indicates the presence of enhanced magnetic fields and accelerated electrons. In radio, at 1420 MHz and 408 MHz, the remnant shows spatial variations, with the greatest brightness along the south-east rim and weaker, but still enhanced, extended emission along the north-west rim. Multiple plausible scenarios can explain these features. The relatively low density region surrounding the remnant is likely caused by the progenitor's high intensity solar wind (Ladouceur and Pineault, 2008).

Gamma-Cygni also emits both thermal and non-thermal x-ray emission (Uchiyama et al., 2002). The thermal radiation, bright along the SNR limb, is plasma emission from the immediate postshock region of the SNR blast wave, radiating with a temperature that gives an age estimate of $\sim 6600$ years. The hard X-ray emission originates from multiple clumps localized along the northern part of the remnant.

Multiple instruments have discovered very high energy (VHE) emission associated with Gamma-Cygni, proving that it is a cosmic ray accelerator. First, VERITAS detected emission between 320 GeV and 10 TeV, coincident with the north-west rim of the radio remnant (Aliu and et al., 2013). *Fermi*-LAT studies at GeV energies have reported gamma-rays across the entire radio extension, with a hotspot also in the north-west (Fraija and Araya, 2016). The location of this hotspot is consistent with the region of highest VHE emission seen by ground based astrophysical gamma-ray detectors, a source named VER J2019+407. Gamma-Cygni is likely an originating point of freshly accelerated cosmic rays observed in a region called the Cygnus Cocoon, a region adjacent to and overlapping Gamma-Cygni. Other likely sources of cosmic rays and their containment in this region include the stellar cluster Cyg OB2, located within a few degrees of Gamma-Cygni (Ackermann and et al., 2011).

The multiwavelength results of Gamma-Cygni reveal a complex region of electromagnetic radiation and cosmic ray production, even at the highest energies. Latest results strongly suggest that the non-thermal emission occurs in two different regions of the remnant, by different processes (Piano et al., 2019). However, this interpretation is not conclusive, and other studies have struggled to reach conclusions about which populations of cosmic rays are accelerated and where in Gamma-Cygni. The nonthermal X-ray emission points to a population of accelerated electrons in Gamma-Cygni (Uchiyama et al., 2002). Studies performed on observations covering energies in the GeV-TeV range report gamma-ray emission across the entire remnant, with brighter emission along the northern rim (Fraija and Araya, 2016). Studies performed on observations with energies above 100 GeV find gamma-ray emission overwhelmingly along the northern rim, indicating that this region may encompass SNR shocks expanding into an over-dense cloud and therefore this segment of the SNR may be at a different stage of evolution compared to the rest of the remnant (Acciari and MAGIC Collaboration, 2020)(Aliu and et al.,

Figure 1.2: The Cygnus region in radio (74 and 21 cm) and infrared (60 and 25 micron). The bright circular cloud in the upper right is SNR G78.2+2.1 (Gamma-Cygni) (Rector et al., 2007). Image Credit: Jayanne English (U. of Manitoba) and Russ Taylor (U. of Calgary) of the Canadian Galactic Plane Survey

2013). As of the writing of this work neither a process driven by electrons or a process driven by protons has been ruled out to explain the origin of gamma-ray emission in Gamma-Cygni. What makes determining the production process in Gamma-Cygni especially difficult is that several factors that determine energy distribution; acceleration efficiency, diffusion coefficient, material density, and magnetic turbulence are difficult to measure and largely unknown for the region local to Gamma-Cygni. Further details from these and other studies, including the results and conclusions of this thesis, are in Chapter 8.

## 1.3 Astrophysical Gamma Ray Detectors

Over the past decades several satellites and high altitude balloon detectors have directly measured cosmic ray abundances and energies, with all elements present. Cosmic rays from

1GeV-$10^9$ GeV are thought to be of Galactic origin and the highest energy cosmic rays are probably of extragalactic origin.

However, the astrophysical production sites of very high energy charged particles are not well known because galactic magnetic fields divert the trajectories of charged particles. The direction of charge-neutral radiation is not affected, therefore one way to determine the production sites is to observe sources of neutral radiation created in the same production chain as the charged particles. Another way is to observe neutral products of cosmic rays interacting with the local production environment. Photons, both abundant and neutral, are an ideal radiation to observe for this purpose. For highest energy cosmic rays the associated photons are gamma rays.

Gamma-ray astronomy (100 keV - 100 TeV) covers a wide range of astrophysical phenomena and detection methods. At these energies photons do not pass unaffected through the Earth's atmosphere, therefore satellites are essential. However, above 10s of GeV, maximum feasible payload mass and size of satellites do not allow for sensitive detection from space. At this energy transition, gamma-ray astronomy returns to Earth. Two different types of Earth-based detectors collect the secondary products of gamma-rays interacting with the Earth's atmosphere to reconstruct astrophysical energies and position.

The following sections detail current day astrophysical gamma-ray telescopes. The earliest precursors to present day detectors are briefly described. More focus is given on Imaging Atmospheric Cherekov Telescopes (IACTs), since this type of detector is used for data collection in this thesis.

### 1.3.1 Early Gamma Ray Satellites

The satellite Explorer 11, launched in 1961, carried a scintillation counter and Cherenkov counter, the first cosmic gamma-ray detector into space. Explorer 11 detected 1012 accepted gamma-ray events (Kraushaar et al., 1965). The Vela satellites, the first of which were launched in 1963, unintentionally became the first astrophysical gamma-ray detectors. Built to monitor terrestrial nuclear detonations, the Vela satellites also detected flashes of gamma radiation and discovered what are now called gamma-ray bursts. The first satellite built for gamma-ray astronomy was SAS-2, launched in 1972, which operated in the low energy gamma-ray range of 20 to 300 MeV. COS-B, launched in 1975, operated in the gamma-ray regime of 30 MeV to 5 GeV.

The number of gamma-ray sources detected from space exploded in 1991 with the operation of Compton Gamma Ray Observatory (CGRO), which operated for nine years with four instruments spanning from 20 keV to 30 GeV across the electromagnetic spectrum. The discoveries by CGRO, SAS-2, and COS-B motivated next generation satellites, as well as spurring on further development into ground based instruments aimed toward operating at higher energies, even as the ground based technology struggled to detect more than a handful of sources leading up to the last decade of the twentieth century.

### 1.3.2 Fermi Large Area Telescope

The successor to previous satellite telescopes, NASA's built and operated *Fermi*, was launched in June 2008 with two detectors, Gamma-ray Burst Monitor (GBM) and Large Area Telescope (LAT) (Abdollahi and et al., 2020). To date, both instruments have been continually surveying the sky. The LAT is the higher energy detector of the two, a gamma-ray to electron-positron particle converter with a 1 $m^2$ collection area. With over twelve years of operation, eight years of data cataloged, and the latest background models and instrument response functions, *Fermi*-LAT has detected 5064 sources above $4\sigma$ significance, in the energy range from 0.05 GeV - 1 TeV, plus a number of one-time gamma-ray transients. Seventy-five of these sources are spatially extended.

The bulk of the LAT instrument are an anticoincidence shield, alternating layers of silicon and tungsten for tracking, and CsI calorimeters. The 36 silicon stripes are layered with 12 thin layers of tungsten at the front end of the detector and four thicker layers of tungsten on the back end. The conversion of the gamma-ray to an electron-positron pair usually takes place in the tungsten. The silicon layers track the particle shower's trajectory. The CsI calorimeter modules measure the energy deposited due to the electromagnetic particle shower and discriminate background by imaging the shower development profile. An anticoincidence detector (ACD), enclosing the entire tracking array, provides charged-particle background rejection. The ACD is segmented to reduce false rejection due to backsplash. The parts were constructed so the ratio of the LAT's height/width is 0.4, allowing a large field-of-view (FoV) (2.4 steradians, $\sim$ 20% sky). The LAT performs almost uniform coverage of the sky about once every 3 hours (Atwood and et al., 2009).

Design of the LAT is a balance between resolution at different energies. Peak sensitivity is just above 1 GeV. With lower energies, there is more scattering and bremsstrahlung radiation, reducing position resolution. Secondary particles creating false signals, often referred to as backsplash, are more prevalent at higher energies. While the photons to background ratio continues to increase for higher energies, the photon rate decreases with higher energies; only 566 photons exceeded 1 TeV energy after 8 years of data (Abdollahi and et al., 2020). *Fermi*-LAT has a counterpart of similar design and operating energy, Italian Space Agency's AGILE-GRID.

### 1.3.3 High Altitude Water Cherenkov Detectors

At high altitude (>2000 meters), particles in very high energy (VHE) atmospheric shower cascades reach the ground before losing significant energy. With this physics in mind, an instrument built at high altitude can detect Cherenkov light produced by relativistic particles traversing a liquid component of the detector. A series of photomultiplier tubes, attached to large water tanks, will detect Cherenkov light flashes as the high energy particle component of air showers traverse through the bodies of water. Subsequent data analyses reconstruct the initial astrophysical energy. This concept lead to the previous Milagro detector and the current day High Altitude Water Cherenkov (HAWC) detector.

Milagro operated in northern New Mexico at an altitude of 2630 meters above sea level from years 2000 to 2008 (Abdo and et al., 2012). The HAWC observatory began sky monitoring in 2015 at the base of Sierra Negra in Mexico, altitude 4100 meters (Abeysekara and The HAWC Collaboration, 2017). The instrument consists of 300 water tanks, each filled with $\sim$ 200,000 liters of purified water and during operation is sensitive to gamma-rays from hundreds of GeV to hundreds of TeV. With continuous operation possible both night and day and large field of view

(HAWC: FoV $> 1.5$ sr and $> 90\%$ duty cycle), water Cherenkov telescopes are well-suited to collect large amounts of data. The high duty cycle is critically important for the viability of water Cherenkov detectors due to the low flux rate of photons and 10s and 100s of TeV. A significant limitation of HAWC is that multiple systematic issues affect spectral fits, resulting in typical errors on point sources of $\pm 50\%$ for overall flux and $\pm 0.2$ for spectral index (Abeysekara and The HAWC Collaboration, 2017). The most recent catalog reports position and spectral parameters from 65 sources with significance $\geq 5\sigma$ (Albert, 2020). Other water Cherenkov detectors currently in operation that are not elaborated on in this thesis are Tibet-AS$\gamma$, LHAASO, and ARGO-YBJ.

### 1.3.4 Imaging Atmospheric Cherenkov Telescopes (IACTs)

At first appearances, TeV gamma-ray astronomy burst onto the scenes in 1989. In reality, the discoveries made in the last decade of the twentieth century were the culmination of decades of trial and error, and instrument development (Fegan, 2019).

The concept for ground based detection was realized for the first time in 1952 with the discovery that relativistic air showers emit UV-optical Cherenkov light. This flash of Cherenkov light, lasting $\sim$5ns, could be focused by a mirror onto a device with fast readout, which ended up being photomultiplier tubes (PMTs). Above 10 GeV and from high altitude, the mirror-PMT combination can detect the maximum Cherenkov light brightness of gamma-ray induced air-showers. However, gamma-rays make up $< 1\%$ of air showers; most are produced by charged cosmic rays (predominately protons). This overwhelming background, combined with other dark-time optical light sources, starlight, light pollution, etc., requires multiple very high levels of background rejection.

It was not until simulations could point to differences in gamma-ray showers versus hadronic showers that astronomers could define parameters that discriminate between different air showers. Imaging the projected shape of the shower in the telescope's observing plane was understood to be as essential as flux sensitivity. Relying on simulations, Michael Hillas defined a set of "gamma-ray rich domains" for shower image parameters (Hillas, 1985). Shower image measurements not falling within this domain would be removed in data reduction.

From the late 1970s through the 1980s, single mirror dish IACT experiments put their photomultiplier cameras through several iterations of arrangement and number of PMTs in the camera. By the time the Whipple 10-meter IACT was able to extract a gamma-ray signal, it had a camera of 37 PMTs. In 1989, the Whipple Collaboration published their first confirmed detection of an astrophysical gamma-ray source, the Crab PWN, reporting a $9\sigma$ detection above 0.7 TeV (Weekes and et al., 1989).

Through the 1990s the Whipple telescope and HEGRA array detected the Crab nebula and active galactic nuclei (AGN) Markarian 421 and Markarian 501. However, they could not detect much more than a hand-full of the brightest gamma-ray sources. Creating an IACT array with next generation technology and multiple telescopes was the next step to improving sensitivity and background discrimination. Three major IACT arrays were built in the early 2000s and are currently operated by research collaborations: **H.E.S.S.**, **MAGIC**, and **VERITAS**. A single Cherenkov telescope, **F**irst G-**A**PD **C**herenkov **T**elescope (**FACT**), is located at La Palma, Canary Islands, Spain, operating primarily to monitor bright AGN since 2011 (Anderhub and et al., 2010). All operate from GeV to TeV energies and are roughly similar in design and operation. Lower energy (10s of GeV) and higher energy (10s of TeV) instrument thresholds differ slightly due to instrument and array design.

The greatest disadvantage of IACTs is their narrow time window for data collection, compared to the previously mentioned detectors. They can only detect UV-optical Cherenkov light flashes in dark sky conditions while the moon is sufficiently dim. They do have better angular and energy resolution compared to water Cherenkov detectors. There are currently 227 astrophysical TeV sources detected by ground based instruments (water Cherenkov or IACT)[3], a testament to decades of invention and scientific ingenuity by multiple generations of astronomers.

[3]Numbers accessed October 2020, from http://tevcat.uchicago.edu

The next generation of IACTs, **C**herenkov **T**elescope **A**rray (CTA), is currently under development. Sites for both the northern and southern observatories are under construction and multiple prototype telescopes are undergoing testing, including a **p**rototype **S**chwarzschild-**C**ouder **T**elescope (pSCT) located adjacent to VERITAS. Details of IACT detection methods, specifically for VERITAS, are described in Chapter 3.

## 1.4 Thesis Overview

This thesis develops, validates, and employs a new analysis technique, which is designed to increase the sensitivity of IACT observations to extended sources, several of which are SNRs. The aim is to determine the populations of galactic cosmic rays originating from SNR. Analyses performed with standard methods on one SNR, Gamma-Cygni, present the deepest observations of VERITAS data on this source to date. In addition, a novel technique is employed on a subset of the total Gamma-Cygni dataset. This latter analysis discerns between different models of source emission from Gamma-Cygni, and therefore makes claims about source morphology.

For context concerning the underlying physics, Chapter 2 is entirely devoted to astrophysical particle acceleration in shocks, charged particle propagation, and cosmic ray interactions that produce gamma rays. VERITAS is the telescope used for data collection in this thesis. The telescope array, hardware, and current standard analysis methods are described in Chapter 3.

The bulk of the new work in this thesis covers the development and validation of new components in the 4D Maximum Likelihood Method (4D-MLM), a new data analysis method currently under development. Gamma-Cygni is a moderately extended source and a different approach from the standard methods is needed to determine morphology from data collected by IACTs, especially in complex regions with multiple gamma-ray sources. An analysis employing likelihood estimations, as applied in the 4D-MLM, utilizes background models derived from VERITAS data fields without known IACT gamma-ray emission. In the previous performance of the method, derivation of background IRFs from real data introduced the problem of statistically limited models into the likelihood calculation. This issue was partially addressed by reducing the number of bins on the background parameter down to two bins, which are now referred to a event classes. The implementation of event classes is laid out in Chapter 4. Since the implementation of event classes necessitates the creation of new IRFs validation of the VERITAS point spread function (PSF) was repeated. The process, results, and conclusions are presented in Chapter 5. Chapter 6 describes and validates a modification to the standard likelihood equations with Barlow Beeston terms for addressing statistical fluctuations, especially in the modeling of background rates.

Chapter 7 presents validation studies performed with the fully constructed 4D-MLM. The studies were performed on a point source, the Crab, and a blank field, Ursa Minor. Chapter 8 begins with a brief literature review study on Gamma-Cygni, with an emphasis on publications from IACTs. The rest of this chapter presents new analyses on Gamma-Cygni data, observed by VERITAS. Final conclusions and future work that will improve the 4D-MLM are presented in Chapter 9.

The appendices summarize work undertaken to validate the quality of a new set of simulations and determine the most appropriate function to model the VERITAS PSF in all observing conditions. The development of the PSF includes documented changes to the PSF model equations in the open analysis framework for gamma-ray astronomy, Gammapy.

# CHAPTER 2. ASTROPHYSICAL COSMIC AND GAMMA RAYS

In recent years, especially since the first direct detection of gravitational waves, *multimessenger astronomy* has become a popular term, used to refer to astrophysical observations combined across both electromagnetic and various non-electromagnetic extrasolar signals. However, this practice was in play decades before the term became commonplace. For a century, observations of astrophysical particles have informed our understanding of astrophysical objects and interstellar and intergalactic space.

This chapter gives a detailed, though not exhaustive, overview of production mechanisms and propagation of both astrophysical cosmic rays and gamma rays. The first half of this chapter outlines current models of production and acceleration of astrophysical charged particles, with emphasis on very high energies (VHE, E>100 GeV). Major gaps in these models are pointed out, as well as how those gaps can be filled through current and future observations. The second half of this chapter discusses production of electromagnetic radiation through cosmic ray interactions and how one can deduce properties of cosmic rays from detection of gamma-ray emission.

## 2.1 Cosmic Ray Production

Since the earliest decades of the twentieth century, particle physicists and astronomers have asked the question: What are the astrophysical power centers accelerating cosmic rays to very high energies? Even from the earliest years after the discovery of cosmic rays, supernovae were a proposed answer, based solely on the massive energy output of the initial core-collapse or runaway thermonuclear reaction. A century later, some questions about cosmic ray origins have been answered and supernovae are indeed responsible for at least a subset of VHE cosmic rays.

However, several gaps remain in our understanding. The percentage of accelerated particle populations across energies attributed to specific classes of galactic sources remains unknown.

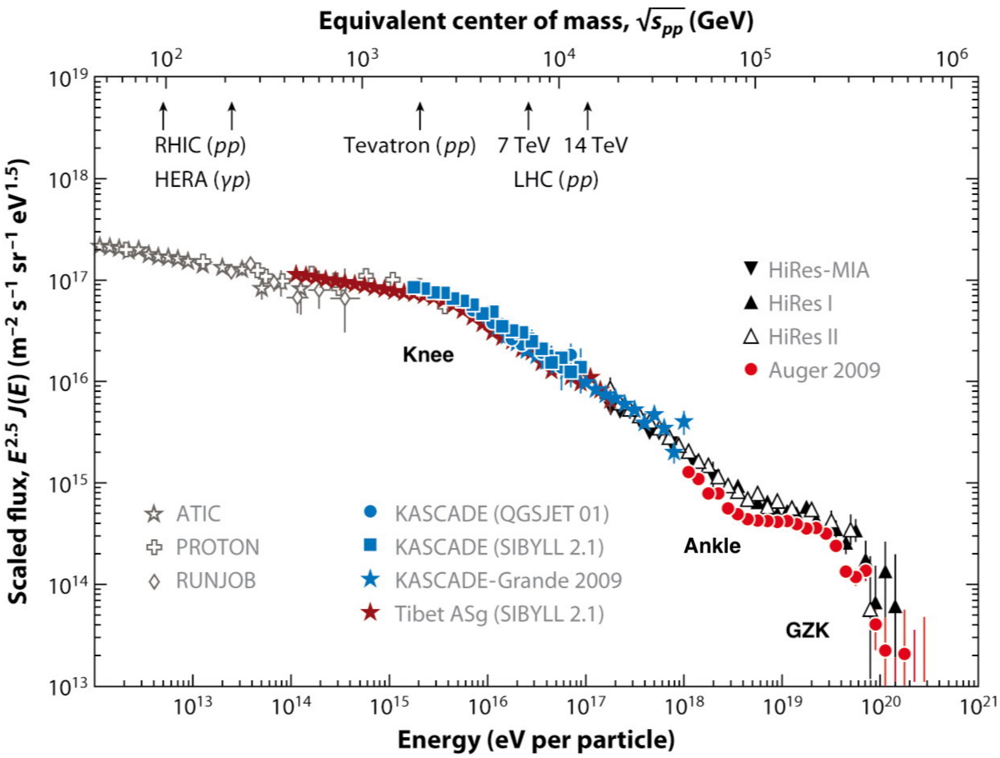


Figure 2.1: All-particle cosmic ray spectrum measured at Earth above 1 TeV, by the ATIC, PROTON, and RUNJOB, as well as air shower experiments Tibet AS-gamma, KASCADE, Akeno, HiRes, and Auger. The top horizontal axis is equivalent center-of-mass energy for protons (Engel et al. (2011)).

Recent observations suggest that local interactive environments play an important part in determining the subsequent particle species produced in the shock environment.

This section introduces the cosmic ray spectrum, followed by an in depth coverage of particle-acceleration mechanisms, especially in supernovae shock waves. This section also covers how cosmic rays propagate out of their local environments and subsequent interactions in interstellar space.

### 2.1.1 Cosmic Ray Spectrum

The energy distribution of cosmic rays has been measured for several decades. Modern day instruments, such as particle spectrometers aboard satellites (e.g. AMS-02 and PAMELA) and air shower arrays (e.g. HiRes and Pierre Auger), measure the cosmic-ray spectrum (Figure 2.1) with precision across several decades of energy and detect heavy ions up to uranium. Cosmic rays with energies less than a few GeV originate from the sun and the fluxes at these energies vary with solar wind intensity. Cosmic rays at greater energies have a steady flux and extrasolar origins (Gaisser et al., 2016).

Changes in the shape of the energy spectrum above a few GeV hint at possible origins. From 10 GeV to about 1 PeV ($10^{15}$), the proton spectrum is a powerlaw with a differential spectral index of -2.7. From about 10 PeV to 1 EeV the index is about -3.1. The break in the power law at E $\sim 3 \times 10^{15}$ eV is referred to as the **knee**. Above 1 EeV ($10^{18}$), the spectrum hardens once again, corresponding to a feature called the **ankle**, before a steep cutoff around $10^{20}$ eV (Engel et al., 2011). There are slight differences between the proton and heavier nuclei spectrum, and additional subtler features in spectra of heavy nuclei. The reason why features such as the knee are so intriguing is because they hint at possible change in the particle production mechanism responsible for cosmic rays; the knee could be the superposition of multiple spectral cutoffs (Blasi, 2013).

A few features of the cosmic ray spectrum are straightforward to connect to astrophysical phenomena. Above $10^{18}$ eV, cosmic rays traversing Milky Way magnetic fields (local strength $\approx 6\mu G$ (Beck and Wielebinski, 2013)) have gyroradii greater than the radius of our galaxy. Therefore, cosmic rays at and above this energy cannot remained confined within the extents of typical galaxies, strongly suggesting that in this energy range the origin is extragalactic. The spectral cutoff around $10^{20}$ eV is explained by the increased probability of interaction of cosmic rays with cosmic-microwave background photons and subsequent pion production at ultra high energies, known as the Greisen-Zatsepin-Kuzmin (**GZK**) limit. Across astrophysical distances, this physical limit makes the universe opaque to protons and nuclei with energies approaching $10^{20}$ eV (Zatsepin and Kuzmin, 1966)(Greisen, 1966). However, which types of astrophysical sources produce cosmic rays with energies between the **knee** and **ankle** remains unclear. Moreover, the energy at which the transition from galactic to extragalactic sources of cosmic rays occurs is also unknown.

### 2.1.2 Cosmic Ray Acceleration

In order to accelerate astrophysical particles to higher energies there are multiple requirements that need to be satisfied. The necessary constraints are continuous emitting sources with power equivalent to that observed in cosmic rays, an astrophysical mechanism to transfer the injected energy to the cosmic rays, and means of confinement long enough for acceleration to observed energies.

The power required to maintain the observed proton and nuclei cosmic ray energy and flux from a uniform distribution of sources in the Milky Way disk is about

$$L_{CR} = \frac{V_D \rho_e}{\tau_R} \sim 7 \times 10^{40} \frac{\text{erg}}{\text{sec}} \tag{2.1}$$

where the local energy density of cosmic rays, $\rho_e \approx 0.5$ eV cm$^{-3}$, $V_D$ is the volume of the galactic disk, $\pi R^2 D = \pi(15,000\text{kpc})^2(200\text{pc})$, and $\tau_R$ is escape time derived from primary to secondary nuclei ratios (Gaisser et al., 2016). Understandably, supernova were the first suggested sources of cosmic rays (Baade and Zwicky, 1934). For example, the luminosity of type II supernovae occurring every 30 years and with ejecta traveling with velocity, $u \sim 5 \times 10^8$ cm s$^{-1}$ is

$$L_{SN} \sim 3 \times 10^{42} \frac{\text{erg}}{\text{sec}}. \tag{2.2}$$

With efficiency of at least a few percent supernova blast waves alone provide enough energy to energize all galactic cosmic rays. Magnetic fields can confine charged particles, as long as the gyroradius of the charged particle remains smaller than the size of the accelerating region.

Another initial question posed in cosmic ray physics was whether major astrophysical acceleration occurred on large or small scales. In 1949, Enrico Fermi proposed that cosmic ray acceleration occurs on large scales. A charged particle gains multiple minuscule boosts of energy over the entire galactic transit time through collisions against moving clouds of plasma and magnetic field irregularities (Fermi, 1949). This mechanism is called **Fermi acceleration**.

Collision off galactic disk plasma clouds and magnetic fields, as Enrico Fermi hypothesized, cannot be the sole cosmic ray accelerator for reasons to be explained further in this section, hence it is referred to as **second-order Fermi acceleration**. A greater boost in energy comes from particle encounters with shock fronts, such as those produced in supernova, referred to as **first-order Fermi acceleration** or **diffusive shock acceleration**.

What follows is a review of how the mechanism of second-order and particularly first-order Fermi acceleration operates for charged particles encountering a planar supernova shock or a plasma cloud and a derivation of the energy gain in these scenarios. The derivation is taken from (Gaisser et al., 2016). A portion of the shock's macroscopic kinetic energy, $\Delta E$, transfers to each individual particle in each collision. If $\Delta E = \epsilon E$ per encounter, after $n$ encounters

$$E_n = E_0(1+\epsilon)^n \tag{2.3}$$

where $E_0$ is the energy of the particle at injection. The number of encounters needed to reach final energy, $E$, is

$$\mathrm{n} = \frac{\ln(\frac{\mathrm{E}}{\mathrm{E_0}})}{\ln(1+\epsilon)}. \tag{2.4}$$

In order to derive the energy obtained by the entire particle population over multiple collisions the probability of escape from the accelerating region needs to be taken into account. For probability of escape per encounter, $P_{esc}$, the probability of remaining in the acceleration region after $n$ encounters is $(1-P_{esc})^n$. The proportion of particles accelerated to energies greater than $E$ and after a number of encounters $m \geq n$ is

$$N(\geq E) \propto \sum_{m=n}^{\infty}(1-Pesc)^n = \frac{(1-P_{esc})^n}{P_{esc}}. \tag{2.5}$$

Substituting Equation 2.4 into Equation 2.5 gives

$$N(\geq E) \propto \frac{1}{P_{esc}}(\frac{E}{E_0})^{-\gamma} \tag{2.6}$$

where

$$\gamma = \frac{ln(\frac{1}{1-P_{esc}})}{ln(1+\epsilon)} \approx \frac{P_{esc}}{\epsilon}. \tag{2.7}$$

Since Equation 2.6 takes the form $N(E) = \text{constant} \times E^{-\gamma}$ Fermi acceleration results in a power law energy spectrum, exactly what is needed to explain the cosmic ray spectrum.

To quantify $\Delta E$ depends on the physics of charged particles scattering in magnetic fields generated in moving clouds of plasma or scattering in a planar shock wave. The first case considers a gas cloud moving with velocity $\vec{V}$ in the rest frame. The second case is that of a shock wave large enough that it can be modeled as planar, moving with velocity $-\vec{u_1}$. The surrounding material, shocked by the planar wave, moves away from the shock with velocity $\vec{u_2}$ relative to the shock front, where $|u_2| < |u_1|$. In the lab frame, the gas behind the shock moves with velocity $\vec{V} = -\vec{u_1} + \vec{u_2}$. A visual representation is provided in Figure 2.2.

To find the average fractional energy gained per encounter, $\epsilon = \frac{\Delta E}{E_0}$, for relativistic energies the reference frame needs to be considered and a Lorentz transformation performed. First, some notation to clarify:

- **Primed ($'$):** Quantities in the rest frame of the moving cloud or shock.
- **Unprimed :** Quantities in the lab frame.
- **Subscript 0:** Quantities before interaction with gas or shock.
- **Subscript 1:** Quantities after interaction with gas or shock.

The Lorentz transformation of the energy-momentum vector from the lab frame to the rest frame of the moving gas or shock wave, where the scenario is sufficiently relativistic such that $E \approx pc$, is

$$\begin{bmatrix} \frac{E_0'}{c} & p_x' & 0 & 0 \end{bmatrix} = \begin{bmatrix} \Gamma & -\Gamma\beta & 0 & 0 \\ -\Gamma\beta & \Gamma & 0 & 0 \\ 0 & 0 & 1 & 0 \\ 0 & 0 & 0 & 1 \end{bmatrix} \begin{bmatrix} \frac{E_0}{c} \\ p_x \\ 0 \\ 0 \end{bmatrix}$$

where after the transformation

$$\frac{E_0'}{c} = \Gamma \frac{E_0}{c} - \Gamma\beta p_x = \Gamma \frac{E_0}{c} - \Gamma\beta p cos(\theta_0). \tag{2.8}$$

In the rest frame of the moving gas or shock wave, the energy of a single relativistic particle is

$$E_0' = \Gamma E_0(1 - \beta cos(\theta_0)) \tag{2.9}$$

where $\Gamma$ is the Lorentz factor of the cloud or gas and $\beta$ is the velocity of the cloud or gas in units of speed of light. After the collision and after transforming back to the lab frame the energy of the particle is

$$E_1 = \Gamma E_1'(1 - \beta cos(\theta_1')). \tag{2.10}$$

The scatterings are due to magnetic fields, therefore the collisions can be considered elastic and the energies in the moving frame, before and after the interactions are equal, $E_0' = E_1'$. Substituting Equation 2.9 into Equation 2.10 gives the change in energy based on the initial energy and angles,

$$\frac{\Delta E}{E_0} = \frac{1 - \beta cos(\theta_0) + \beta cos(\theta_1') - \beta^2 cos(\theta_0) cos(\theta_1')}{1 - \beta^2} - 1. \tag{2.11}$$

When taking the average of both the incoming and outgoing angles to obtain the average fractional energy gained per encounter, the averaging is done differently for the two cases, a planar shock wave and plasma clouds.

**For plasma clouds,** $\frac{dn}{dcos(\theta_1^{'})}$ = constant, $-1 \leq cos(\theta_1^{'}) \leq 1$,

therefore $< cos(\theta_1^{'}) >= 0$ and

$$\frac{< \Delta E >_1}{E_0} = \frac{1 - \beta cos(\theta_0)}{1 - \beta^2} - 1. \tag{2.12}$$

**For a planar shock,** $\frac{dn}{dcos(\theta_1^{'})} = 2cos(\theta_1^{'}), 0 \leq cos(\theta_1^{'}) \leq 1$,

therefore $< cos(\theta_1^{'}) >= 2/3$ and

$$\frac{< \Delta E >_1}{E_0} = \frac{1 - \beta cos(\theta_0) + \frac{2}{3}\beta - \frac{2}{3}\beta^2 cos(\theta_0)}{1 - \beta^2} - 1. \tag{2.13}$$

Taking the average of the incoming angle is also different for a planar shock versus a cloud. **For plasma clouds**, the probability of collision is proportional to the relative velocity between the cloud and particle, therefore

$$\frac{dn}{dcos(\theta_0)} = \frac{c - V cos(\theta_0)}{2c}, -1 \leq cos(\theta_0) \leq 1, \tag{2.14}$$

where $< cos(\theta_0) >= -\frac{V}{3c}$. **For the planar shock**, the average of $cos(\theta_0)$ is the projection of isotropic flux onto a plane with $-1 \leq cos(\theta_0) \leq 0$ and $< cos(\theta_0) >= -\frac{2}{3}$. Therefore the average fractional energy gain per encounter, $\epsilon = \frac{\Delta E}{E_0}$, is

$$\textbf{for plasma clouds: } \epsilon = \frac{1 + \frac{1}{3}\beta^2}{1 - \beta^2} - 1 \approx \frac{4}{3}\beta^2 \tag{2.15}$$

$$\textbf{and for a planar shock: } \epsilon = \frac{1 + \frac{4}{3}\beta + \frac{4}{9}\beta^2}{1 - \beta^2} - 1 \approx \frac{4}{3}\beta. \tag{2.16}$$

Both scenarios provide the means to accelerate particles to higher energy. However, the second order effect in shock velocity $\beta$, a value always less than one, means that the energy gain from scattering in a plasma cloud is less than that for interaction in a planar shock. The particles always have a net gain of energy, but for scatterings in a plasma cloud the particle can lose energy

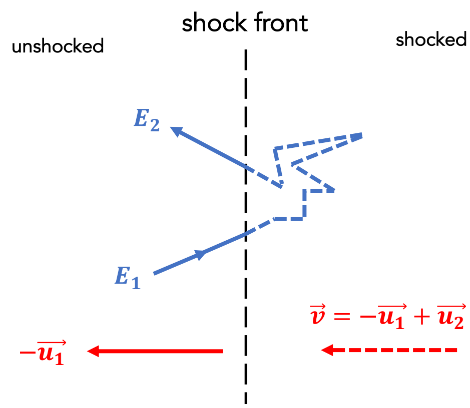


Figure 2.2: A visual representation of particle acceleration across a planar shock front in the lab frame, also known as first-order fermi acceleration.

depending on the angle. Conversely, for an infinite plane shockwave, the geometry is such that an encounter always results in energy gain.

The maximum energy obtained by a cosmic ray is constrained by environmental confinement and SNR evolution. The first condition to consider is that the acceleration time be less than the age of the SNR.

The estimated maximum energy, presented by (Gaisser et al., 2016) and derived from estimates of the minimum diffusion coefficient by (Lagage and Cesarsky, 1983), is

$$E_{max} \leq \frac{3}{20}\frac{u_1}{c} ZeB(u_1 T_A) \tag{2.17}$$

where $T_A$ is the acceleration time scale. For a supernova remnant an initial input for the acceleration time is the Sedov-Taylor (ST) phase, where most of the initial energy of expansion has dissipated, $T_A = T_{ST} \approx 1000$ years. For an estimated interstellar magnetic field strength of $\approx 3\mu G$ and the acceleration process occurring over the ST phase the maximum energy is

$$E_{max} \leq Z \times 3 \times 10^4 GeV. \tag{2.18}$$

For shocks undergoing expansion, equation can be rewritten as

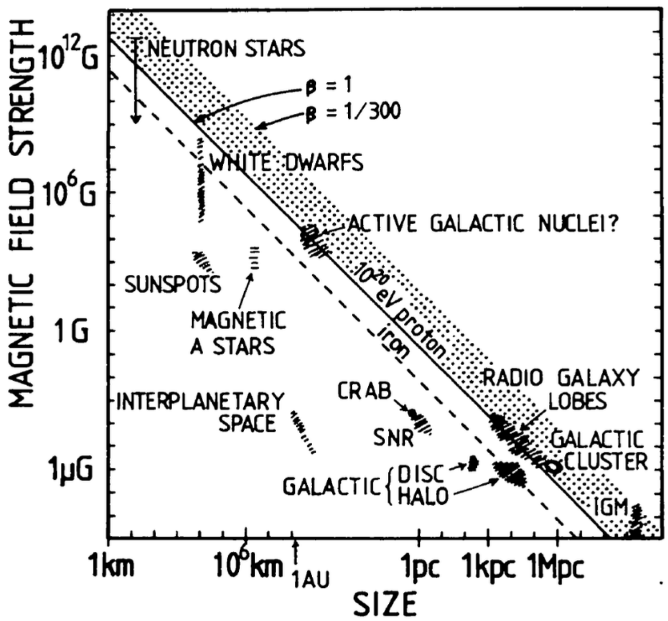


Figure 2.3: The Hillas plot of potential sites of cosmic acceleration, according to magnetic field strength and object size. Astrophysical accelerators below the solid line cannot accelerate protons to $10^{20}$ eV, given the simple assumptions of Equation 2.20 (Hillas, 1984).

$$E_{max} = \text{const} \times \beta ZeBR, \tag{2.19}$$

where $u_1 \times T_A$, the radius of the expanding shock before deceleration begins. This radial distance acts as a limit on the gyroradius of the astrophysical accelerator, $r_L < R$, and a limit on the maximum possible accelerated energy, $E < ZeBR$. Therefore, the size of candidates for astrophysical acceleration of cosmic rays is one indicator of which are most likely responsible for cosmic ray production for certain energies (Hillas, 1984). Figure 2.3 show the Hillas plot of potential cosmic ray accelerators.

As of this writing, there is yet to be definitive evidence for acceleration of hadrons in SNR up to PeV energies(Vink, 2020). Such sources are referred to as Pevatrons. Both Figure 2.3 and Equation 2.19 suggest that SNRs do not quite reach the capability to accelerate protons to the cosmic ray spectrum knee, $\sim 3 \times 10^6$ GeV.

However, even after ST ends, supernova shockwaves continue to expand. Also, magnetic fields in the shock fronts are amplified by nonlinear effects, creating a much greater local magnetic field strength than the average interstellar value.

## 2.2 Cosmic Ray Diffusion

The process of accelerated astrophysical particles escaping from the accelerator environment is another aspect of VHE cosmic ray production that remains poorly understood. Conservation of particles in a stationary medium can be expressed as

$$\frac{\partial N_i(E,\vec{r})}{\partial t} = \boldsymbol{\nabla} \cdot [D(r) \boldsymbol{\nabla} \cdot N] \tag{2.20}$$

where $N$ is the density of particles of type $i$ at point $\vec{r}$ and $D$ is the diffusion coefficient. Equation 2.20's terms need expanding and additional terms are needed to account for losses in order to model complex systems, such as supernova environments and the interstellar medium. A general equation for cosmic ray propagation can be written as

$$\begin{aligned}\frac{\partial N_i(E,\vec{r})}{\partial t} &= \boldsymbol{\nabla} \cdot [D_i \boldsymbol{\nabla} \cdot N_i] - \vec{V} \cdot \boldsymbol{\nabla} \cdot N_i - \frac{\partial}{\partial E}(b_i N_i) \\ &+ \frac{1}{2}\frac{\partial^2}{\partial E^2}(d_i N_i) + Q_i(E,\vec{r},t) - p_i N_i \\ &+ \sum_k \int P_k^i(E^{'},E) N_k(E^{'},\vec{r},t) dE\end{aligned} \tag{2.21}$$

where

$Q_i(E,\vec{r},t)$ is the intensity of cosmic ray sources of particle type $i$,

$\boldsymbol{\nabla} \cdot [D_i \boldsymbol{\nabla} \cdot N_i]$ describes spatial diffusion of particles with diffusion coefficient $D_i = D(E,\vec{r},t)$,

$\vec{V}$ is the convection velocity,

$\frac{\partial}{\partial E}(b_i N_i)$ allows for minor, continuous change of particle energy resulting from acceleration and particle-particle interactions,

$\frac{1}{2}\frac{\partial^2}{\partial E^2}(d_i N_i)$ allows for fluctuations in the continuous variation in energy,

$p_i N_i$ represents catastrophic energy loss via processes such as spallation and decay, and $\sum_k \int P_k^i(E^{'}, E)N_k(E^{'}, \vec{r}, t)dE$ describes the influx of particles as a result of collisions, where $P_k^i(E^{'}, E)$ is the probability of a particle of type $i$ and unit energy $E$ in a collision resulting from a collision involving a particle of type $k$ and energy $E^{'}$.

The diffusion coefficient depends on energy and location in the galaxy, since magnetic fields are different at the production site versus averaged over the galaxy. The coefficient also depends on the type of cosmic ray since the charged particle's motion depends on its radius of curvature which in turn depends on the total charge (Ginzburg and Syrovatskii, 1964; Gaisser et al., 2016).

After departing the local production environment, cosmic rays spend an additional duration of time confined to their host galaxies due to coupling between charged particles and galactic magnetic fields. As cosmic rays propagate through diffusion they move according to magnetic field configurations, which are permeated with distortions caused by energetic events. Certain elements are more abundant in cosmic rays than they are in solar system material, such as lithium, boron, and beryllium. This observation gives evidence that cosmic rays experience spallation and also change trajectory due to particle collisions in the interstellar medium. The secondary particles produced in these collisions also have very high energies.

From the ratios of primary to secondary nuclei, one can deduce the average hydrogen matter traversed by GeV cosmic rays between injection and observation, 5-10 g cm$^{-2}$. Since the density of the Milky Way is only about one proton per cm$^3$, the total distance traveled through the galaxy for a cosmic ray with mean traversed matter of 5 g cm$^{-2}$ is

$$l = \frac{X}{m_p \rho_N} = \frac{5g/cm^2}{m_p \cdot 1/cm^3} = 3 \cdot 10^{24}\,\text{cm} \approx 1,000,000\,\text{parsecs}. \tag{2.22}$$

This implies that cosmic ray confinement time in the galaxy is on the order of millions of years.

Energy is significant for determining interactions of cosmic rays while traversing interstellar space. The ratio of secondary particles to parent nuclei decreases as energy increases, indicating that the lower the cosmic ray energy, the greater the period of confinement (Gaisser et al., 2016).

## 2.3 Gamma-Ray Production Mechanisms

Astrophysical gamma rays originate as products of interactions of particle populations accelerated to high energies. The processes in astrophysical environments which produce gamma radiation are **bremsstrahlung** radiation, **inverse compton scattering**, **synchrotron** radiation, and **neutral pion decay**. Typically, these four mechanisms are classified depending on the primary interacting particle, leptonic (bremsstrahlung, inverse compton, and synchrotron) or hadronic (pion decay). For the sources studied in this work and energies observable by IACTs, bremsstrahlung and synchrotron radiation are a significantly lesser contribution to observations than that emitted by the other mechanisms. However, synchrotron radiation plays a role in the particle population responsible for inverse compton and bremsstrahlung is a vital interaction in the development of particle air showers. This section details the components and sequence of events in these four interactions (Longair, 2011)[1].

### 2.3.1 Bremsstrahlung Radiation

Bremsstrahlung, from the German word for 'braking radiation', is emission resulting from the interaction of a charged particle (primarily an electron) with an electromagnetic field. As an unbound electron passes near a ion and through the Coulomb field, the electron decelerates and subsequently radiates. Because an electron cannot radiate with energy more than its total kinetic energy, at nonrelativistic speeds the energy loss rate of electrons emitting bremsstrahlung is $-\frac{dE_e}{dt} \propto Z^2 N E_e^{1/2}$. The proportionality of loss rate to the number of protons in the nucleus, $Z$, and ion density, $N$, shows that we expect high bremsstrahlung intensities in dense, metal-rich environs near an astrophysical particle accelerator. For the relativistic regime, starting at about electron energy of 1 MeV, the energy loss rate changes to $-\frac{dE_e}{dt} \propto E_e$, resulting in exponential energy loss at highest kinetic energies. For this reason, bremsstrahlung radiation falls short of emission up to 100 GeV, the low energy range of IACTs. Bremsstrahlung is a major component in atmospheric air shower evolution and energy loss, as described in Section 3.1.1

[1]Unless otherwise specified this is the only reference for the content in this section.

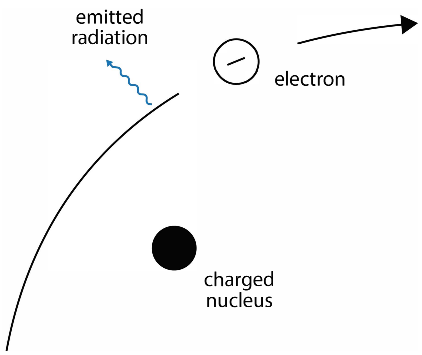


(a) Bremsstrahlung

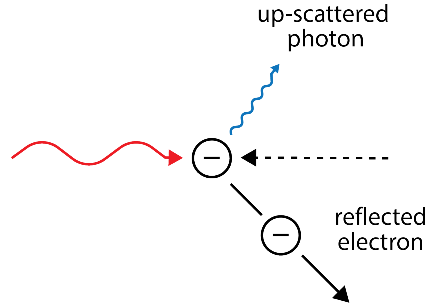


(b) Inverse Compton scattering

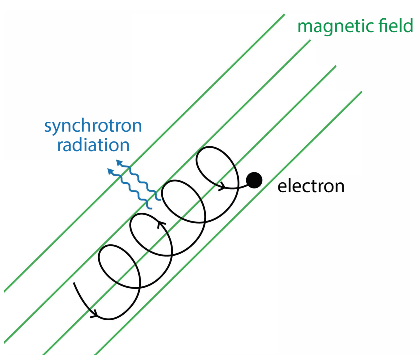


(c) Synchrotron radiation

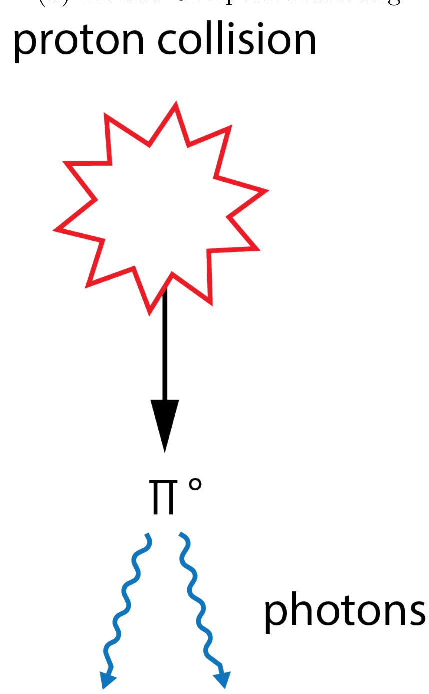


(d) Proton-proton collision, followed by decay of neutral pions

Figure 2.4: Four different particle interactions producing gamma radiation.

### 2.3.2 Synchrotron Radiation

In the presence of magnetic fields, moving charged particles are deflected from their initial trajectory. When charged particles begin to gyrate in magnetic fields they produce synchrotron radiation. Electrons are much more efficient at emitting energy through gyration than heavier charged particles, therefore electrons are primarily responsible for astrophysical synchrotron. Many astrophysical non-thermal X-ray sources display synchrotron, but the process is not efficient up to very high gamma-ray energies. However, synchrotron becomes relevant at very high energies in conditions when gyrating electrons radiate X-ray emission and those same electrons up-scatter these emitted X-rays to higher energy, in a process called synchrotron-self-Compton (SSC). A localized signature of gamma-ray emission, coincident with non-thermal X-ray emission, is a signpost for a population of accelerated electrons traversing through strong magnetic fields.

To understand the nature of astrophysical gamma-ray emission, it is informative to study related X-ray emission, especially its energy distribution. The synchrotron radiation spectrum of a single electron peaks at critical frequency

$$\omega_c = \frac{3}{2}\beta\gamma^2\frac{eB}{m_e}sin(\theta) \tag{2.23}$$

where $\theta$ is the pitch angle of the electron. Therefore, a power law spectrum describes the energy distribution of an isotropic population of synchrotron emitting electrons. Over averaged pitch angles and velocities, the average power is derived as

$$P = \frac{4}{3}\sigma_t c\beta^2\gamma^2 U_B \tag{2.24}$$

Here $\sigma_t$ is the Thomson cross section. The energy loss rate dependence on $U_B$, the magnetic field energy density, shows that the energy loss rate increases for greater magnetic field strength. Additionally, dependence on $\beta^2\gamma^2$ shows that TeV electrons emitting X-ray synchrotron lose energy faster than radio emitting one (Rybicki and Lightman, 2004).

Since synchrotron emission occurs in magnetic fields, we can combine observed spectrum with the previous equations to infer local magnetic field strength, which in turn tells us about the nature of confinement of charged particles in SNR. Figure 2.5 is an image of the Tycho SNR, where the blue rims trace X-ray synchrotron radiation in the shockwaves. However, the complex nature of supernova shocks creates a difficult scenario for determining magnetic field strength without also making assumptions about the magnetic field morphology and amplification.

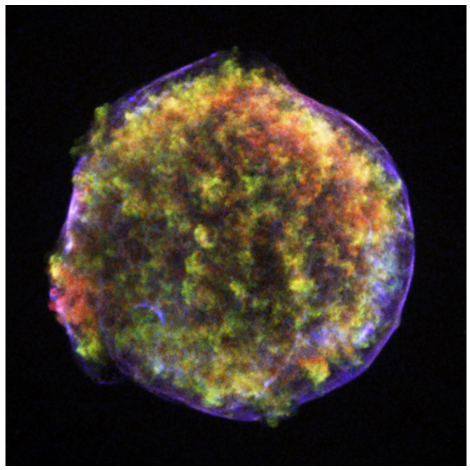

Figure 2.5: Three-color composite Chandra image of Tycho's SNR from (Warren et al., 2005). The blue color (4.1–6.1 keV) highlights a narrow synchrotron filament along the main shock (Credit: NASA/CXC/Rutgers/J.Warren J.Hughes et al.)

### 2.3.3 Inverse Compton Scattering

Inverse Compton (IC) scattering depends on two conditions, a relativistic leptonic particle population and dense radiation fields. The interaction goes as follows: when a photon encounters an electron, there is a probability the electron will up-scatter the photon. A fraction of the electron's kinetic energy is transferred to the photon. The average energy gained by a single photon in the laboratory frame is

$$\bar{E}_f = \frac{4}{3}\gamma^2\beta^2 E_i \tag{2.25}$$

where $\beta$ and $\gamma$ are the relativistic terms of the electron.

Due to the $\gamma^2$ factor in Equation 2.1, for populations of ultra-relativistic electrons, IC is an efficient process for boosting low energy photons (cosmic-microwave background (CMB), infrared, and optical) up to gamma-ray level energies detectable by IACTs, such as VERITAS. An ultra-relativistic electron with $\gamma$=1000 will up-scatter a 100 keV X-ray photon to 100 GeV, within the energy range of IACT detectors.

Since the energy of scattered photons depends on the energy of electrons, we can derive spectral models of IC emission from the electron spectrum. A full view of the gamma-ray IC spectrum requires looking at the transition from the relativistic regime to ultra-relativistic regime of electrons, otherwise called Thomson (classical) regime and Klein-Nishina regime, respectively.

In the Thomson regime, the energy of the photon is less than the rest energy of the electron, $E_\gamma \ll m_e c^2$, in the electron's reference frame. The spectral index of the scattered radiation spectrum depends on the power-law distribution of electron energies, $\frac{dN_e}{dE_e} = E_e^{-\Gamma_e}$. In the Thomson regime that relationship is $\Gamma_{IC} = (\Gamma_e - 1)/2$ for the photon spectral energy distribution.

In the Klein-Nishina regime, where $E_\gamma \gg m_e c^2$, the Compton interaction cross section decreases. Inverse Compton scattering becomes less efficient in the Klein-Nishina regime, leading to a softer spectrum at higher energies. Also, the energy loss rate of electrons increases with higher energy; therefore, a steep cutoff is a feature of IC spectra.

### 2.3.4 Neutral Pion Decay

When protons and atomic nuclei, accelerated to high energy, collide with one another, they annihilate and the interaction produces a particle shower. Each secondary particle in the shower also carries high energy. The most commonly produced secondary hadrons of proton-proton collisions are pions (Engel et al., 2011). Hadronic interactions also produce large numbers of neutrinos, whereas leptonic interactions produce none. Therefore, neutrinos observed in SNR shocks would provide significant evidence for accelerated protons. Astrophysical neutrinos have been observed by detectors such as IceCube. However, due the extremely small neutrino interaction cross-section the sample size remains small, localization is poor, and no astrophysical neutrinos have been traced back to individual SNR. Distinguishing between leptonic and hadronic generated VHE emission relies heavily on modeling various gamma-ray spectrum and comparing theory to energy distribution data.

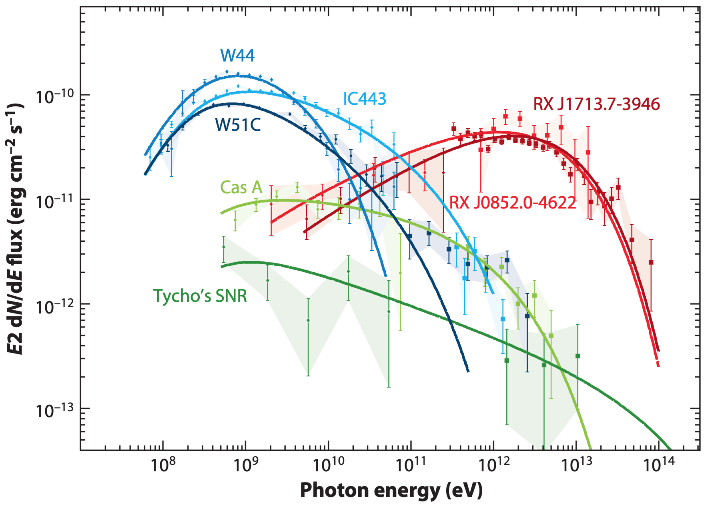


Figure 2.6: Overlapping gamma-ray energy spectra for multiple SNRs. Very young SNR (<1000 years) spectral points are shown in green, young SNR (∼2,000 years) are shown in red, and middle-aged SNRs (∼20,000 years) are shown in blue. Solid lines are hadronic fits to the data points (Funk, 2015).

Neutral pions almost instantly decay into a minimum of two photons. The neutral pion's rest mass sets a lower limit on the total energy of the resulting radiation: 135 MeV. Therefore, a gamma-ray spectrum produced from neutral pion decay must have a low energy cutoff higher than 135 MeV. The high energy end of a gamma-ray spectrum produced by proton-proton collisions will extend to TeV energies.

## 2.4 Current Gamma Ray Observations of Cosmic Rays from Supernovae

The study of astrophysical cosmic rays originating from supernova remnants is a research area currently undergoing development. This section summarizes the current state of the field and the remaining gaps in our understanding. Most of the contents of this chapter are taken from (Blasi, 2013).

It is well known that supernova remnants are in fact sites of astrophysical particle acceleration; the presence of synchrotron emission confirms this. What remains up for debate is whether cosmic rays are accelerated in supernova remnants up to, and beyond, the energy of the cosmic ray spectrum knee. Which environmental conditions and evolution phases create conditions favorable to acceleration to these energies is also under investigation in high energy astrophysics.

Acceleration of electrons to TeV energies has long been confirmed by the presence of X-ray synchrotron emission. X-ray synchrotron is also a signpost of magnetic field amplification along supernova shock waves, up to hundreds of micro-Gauss. The Fermi-LAT collaboration reported evidence of hadronic gamma-ray emission from the SNRs IC 443 and W44. Both sources exhibit a pion-decay feature in the gamma-ray spectra, providing direct evidence that these two SNR accelerate protons to VHE. The correlation between the spectral features and the interaction of IC 443 and W44 with molecular clouds suggests that proton acceleration is more likely in SNR interacting with dense molecular regions (Ackermann and et al., 2013a). Gamma-ray emission from both the Tycho SNR (Morlino and Caprioli, 2012) and Cassiopeia A SNR (Ahnen and et al., 2017) are also associated with hadronic origin. However, the maximum energy is below that needed to qualify either Tycho or Cassiopeia as accelerators of cosmic rays to PeV energies.

The evolution of SNR impacts the timescale and maximum accelerated energy of cosmic rays. X-ray synchrotron emission is detected from the rims of nearly all young SNR, proving that acceleration is possible at young ages. While the sample size is small, the SNR type most commonly associated with hadronic emission are middle aged SNRs ($\sim$10,000 years) interacting with molecular clouds (Blasi, 2013). HAWC has detected multiple sources with energies above 100 TeV, some associated with SNRs (Albert, 2020)(Albert and HAWC Collaboration, 2020). However, as of this writing, there is no proof that this emission detected from individual supernova remnants is largely hadronic in origin. Therefore, the question of whether SNRs can accelerate cosmic ray protons to PeV energies remains an open question.

# CHAPTER 3. THE VERITAS INSTRUMENT

VERITAS (**V**ery **E**nergetic **R**adiation **I**maging **T**elescope **A**rray **S**ystem) is an array of four 12-meter Imaging Atmospheric Cherenkov Telescopes located at the Fred Lawrence Whipple Observatory (FLWO) in southern Arizona (31 40N, 110 57W, 1.3km a.s.l.). The current array configuration is optimized to detect air showers generated from astrophysical gamma rays with energies from ~85 GeV to > 30 TeV, with an energy resolution between 15-25% and an angular resolution $< 0.1°$ at 1 TeV for 68% containment. A Crab-like source with 1% Crab gamma-ray flux can be detected by VERITAS with $5\sigma$ significance at several hundred GeV after 50 hours of observing time, with a pointing accuracy error of < 50 arc-seconds (Park, 2016).

Since the array's commission in 2007, VERITAS has had several minor and two major improvements to hardware, analysis methods, calibration, and operation. The VERITAS telescope level trigger system was replaced and upgraded in 2012 (Otte, 2009)(Zitzer and VERITAS Collaboration, 2013). During summer of 2009, telescope 1 was moved to its current location, adjacent to FLWO's public parking, resulting in a more symmetric array as shown in Figure 3.1 (Perkins et al., 2009). In 2012, the 499 photomultiplier tubes (PMTs) in each camera were replaced with new high-Quantum Efficiency PMTs that increased the photon detection efficiency of the camera by approximately 50% (Kieda, 2013). These two major upgrades divide VERITAS's operation from 2007 to the present into three separate epochs:

- **V4 (09/01/2007 - 08/31/2009):** The seasons where VERITAS operated with all four telescopes and before the relocation of telescope 1.
- **V5 (09/01/2009 - 08/31/2012):** The seasons after telescope 1's relocation and before the camera upgrade.
- **V6 (09/01/2012 - present):** All seasons after the camera upgrade.

This chapter details the components of VERITAS optimized to detect flashes of Cherenkov light generated from electromagnetic (EM) air showers. The first section describes the physics of atmospheric air shower generation and propagation. The remaining sections describe the workings of each major component of VERITAS's hardware and operating software, followed by sections on the data analysis software.


Figure 3.1: **Top:** Aerial view of the VERITAS array, pre-T1 move. The dashed red line indicates the relocation of Telescope 1 that was carried out in Summer 2009 (Ong and et al., 2009). **Bottom:** The VERITAS 4-reflector array and cameras in the current configuration, 2018

## 3.1 Atmospheric Air Showers

High energy astrophysical particles, which comprise gamma rays and cosmic rays (relativistic hadrons and electrons), do not pass through the Earth's atmosphere unaffected. After traversing some depth in the atmosphere an astrophysical gamma ray will interact electromagnetically through pair production and, for energies above $\sim 10$ GeV, produce a cascade of relativistic particles. The mean free path of pair production is $\frac{9}{7}X_o$, where $X_o$ is radiation length, which for air $X_o \sim 37$ g cm$^{-1}$. One radiation length translates to an altitude above sea level of about 20 km (Weekes, 2003).

Eventually in the shower's progression, the number of produced particles reaches a maximum number. Since the maximum size of the shower is proportional to the incident astrophysical particle's initial energy, it is vital that an instrument capture the Cherenkov light emitted around the shower's point of maximum particle production. The lower the energy of the initiating particle, the higher in the atmosphere the shower's maximum particle production occurs. To lower the minimum detection energy, IACT telescopes are located at elevations at least 1000 meters above sea level.

### 3.1.1 Electromagnetic Air Showers

Photons with energies greater than $2m_ec^2$ produce an electron-positron pair ($e^{\pm}$) when encountering the field of a nucleus. Astrophysical gamma-rays interacting with air nuclei ($N_2$, $O_2$, Ar) certainly meet this criteria for pair-production. The relativistic $e^{\pm}$ will subsequently produce bremsstrahlung radiation and an EM particle shower cascade consisting of the following particles: **electrons**, **positrons**, and **gamma-rays** and the following alternating interactions: **bremsstrahlung** and **pair-production**. Since the trajectory of the initial pair-production tends to aim parallel to the gamma-ray's direction, EM air showers tend to be more collimated compared to hadronic generated showers. Coulomb scattering of $e^{\pm}$ is most responsible for broadening the overall shape of the particle cascade (Longair, 2011). The steps of these interactions are described in further detail in Chapter 2.

As the shower propagates, major energy losses are due to bremsstrahlung, with a fraction of energy loss also due to ionization and momentum transferred to atmospheric nuclei. Ionization losses increase with lower particle energy. The energy at which the losses due to bremsstrahlung and ionization are equal is called the critical energy, ($E_{crit}$). In air, $E_{crit} \sim 84$ MeV. Below $E_{crit}$, Compton scattering begins to dominate shower evolution and particle production falls off (Grieder, 2010).

Cosmic ray electrons also produce EM air showers, nearly indistinguishable from gamma-ray induced EM showers, thus creating an irreducible background. Because astrophysical electrons experience significant energy losses from inverse compton and synchrotron radiation in the time scale it takes to traverse galactic scale distances, the cosmic ray electron flux drops off steeply around 1 TeV (Grieder, 2010).

### 3.1.2 Hadronic Air Showers

The vast majority of energetic atmospheric air showers (>99%) originate from high-energy hadrons. Usually the hadron will be a proton, however cosmic rays up to iron ions will interact in the Earth's atmosphere via the strong force to initially produce pion particles, both neutral and charged. Neutral pions rapidly decay to two photons that subsequently produce the electromagnetic component of the shower. On the other hand, high energy charged pions do not decay before interacting to produce other charged particles, mesons, muons, and neutrinos. This sequence makes up the hadronic component of the air shower (Engel et al., 2011).

The composition and multiple strong interactions in hadronic showers create a shower evolution much harder to model compared to showers with only EM interactions. In addition, the initial hadronic interaction in the shower has a greater lateral dispersion of the initial pions than the initial pair-production in EM showers. Secondary pions also exhibit large transverse momenta relative to the shower axis. This has the effect of creating a broader and irregular overall shower shape, as shown in Figure 3.2.

### 3.1.3 Cherenkov Radiation

A charged particle traveling faster than the speed of light in a dielectric medium (v=c/n, where n is the refractive index, always greater than 1) produces a reaction in the surrounding

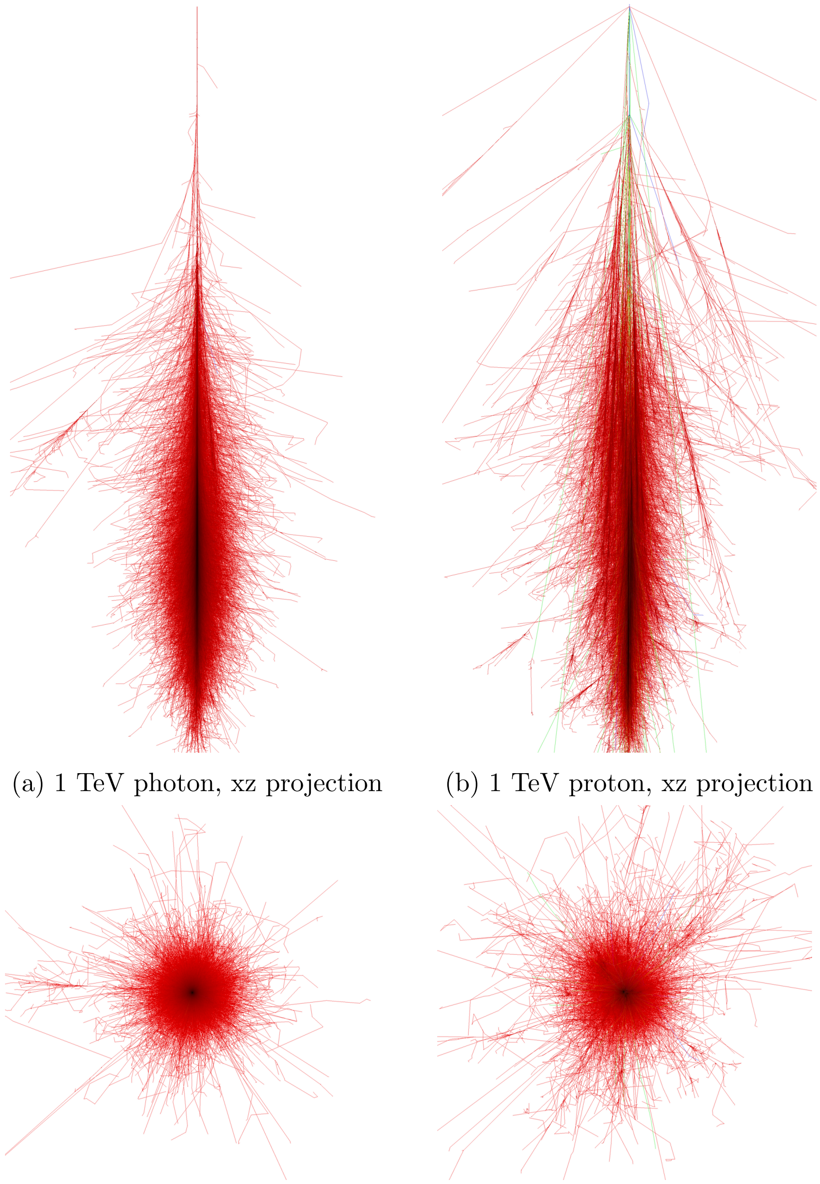

(a) 1 TeV photon, xz projection (b) 1 TeV proton, xz projection

(c) 1 TeV photon, xy projection (d) 1 TeV proton, xy projection

Figure 3.2: Proton and photon induced air showers with initial energy 1 TeV, simulated with the **CO**smic **R**ay **SI**mulations for **KA**scade (CORSIKA) simulation package (Karlsruhe Institute of Technology and Fabian Schmidt, 2020). Images compiled by Fabian Schmidt, University of Leeds, UK.

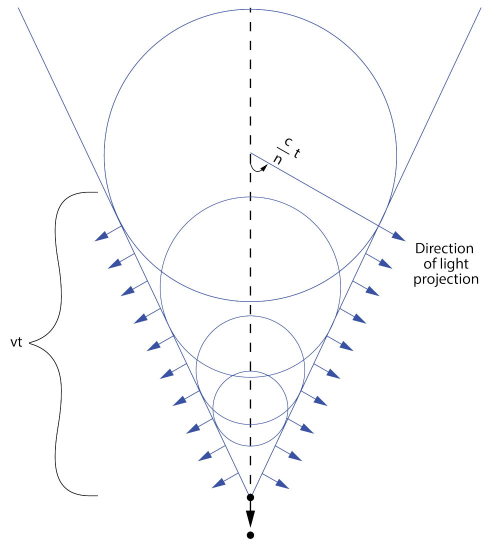


Figure 3.3: Model image of Cherenkov radiation wavefront.

atoms. Any moving charged particle induces dipoles in the surrounding material. The transition of dipoles emits radiation from the surrounding material. Normally the multiple wavelets interfere destructively. However, when a charged particle moves with $v_{phase}$ > c/n, the radiation emitted by dipole transitions is in phase along a certain angle. Therefore, relativistic particles traveling through medium produce a cone-shaped wave-front, transverse to the direction of travel (Grieder, 2010).

Figure 3.2 shows that the wavefront angle of Cherenkov light depends on the density of material and velocity of the traveling particle, where $\theta = \arccos(c/nv)$ and $n$ increases with greater density. Emitted wavelengths are optical and near ultraviolet components ($250 \geq \lambda \geq 600$ nm) (Grieder, 2010). Further Cherenkov light properties observed by IACTs are discussed in Section 3.4.1

## 3.2 Telescope Array Components

### 3.2.1 Structure and Camera

Each of VERITAS's four 12-meter, Davies-Cotton optical design telescopes has 345 hexagonal mirror facets, built to reflect atmospheric Cherenkov light to a camera located at the focal plane.

Figure 3.4: Telescope 1 of the VERITAS array and the OSS that supports the mirrors and camera.

The mirrors are made of polished glass that has been coated with aluminum and anodized. Each mirror has a collection area of 0.322 $m^2$, for a single telescope's total mirror collection area of 110 $m^2$. A steel optical support structure (OSS) holds the mirrors and camera in place through altitude-azimuth motion and while stowed in position (Holder and et al., 2013)(McCann et al., 2010).

Each telescope has a camera consisting of 499 photo-multiplier tubes (PMTs), each with an angular size of 0.15°, for converting optical-UV light to electronic signal. The optical point spread function (PSF) (different from the gamma-ray PSF) is $\sim$0.05° with 80% containment while observing at typical elevations (McCann et al., 2010). The entire camera has a field of view (FoV) of 3.5°. Over each pixel's front is a light concentrator, with a Winston cone at the exit surface and a hexagonally shaped entrance window. These light concentrators increase light collection in PMTs by 30% (Krennrich, 2007).

Before September 2012, the PMTs used were Photonis XP2970. From September 2012 on-wards the cameras consist of R10560-100-20 MOD from Hamamatsu, a one inch PMT with a UV glass entrance window and a superbialkali photocathode. The basic operation of the PMTs is

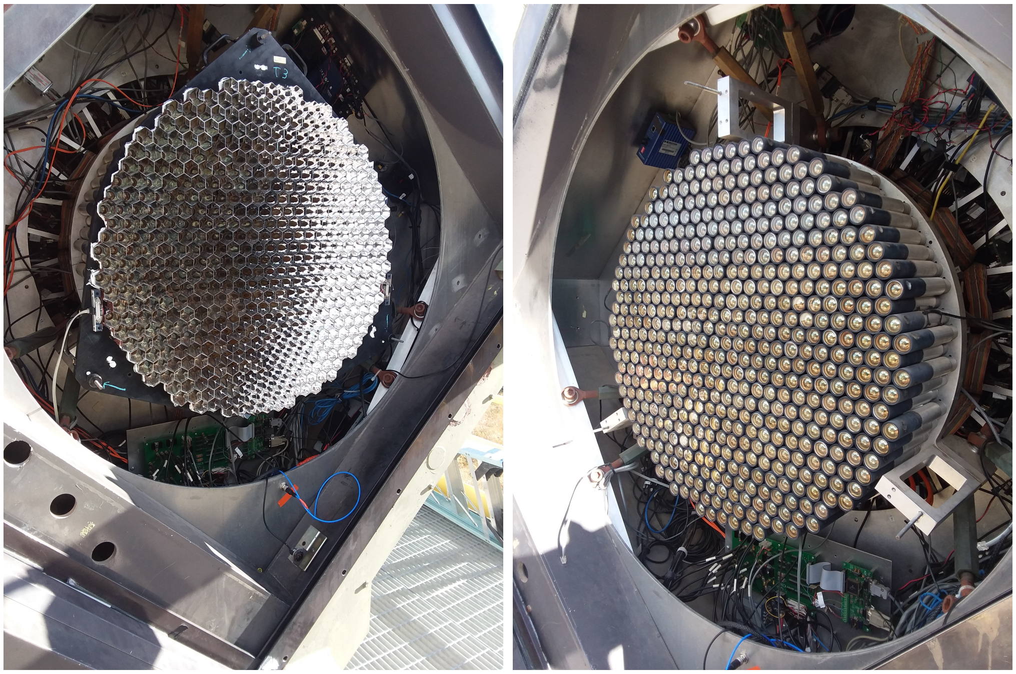

Figure 3.6: The VERITAS T3 camera, with (left) and without (right) lightcones. Photo credit: Jack Musser

the same: light interacting with a photocathode produces electrons via the photoelectric effect. The photoelectrons are directed by an electric field through a series of dynodes to amplify the number of electrons, before an anode converts the electrons to signal current.

*Gain* is a word used to refer to the ability of a PMT to convert Cherenkov photon signal to an electric current. It varies for different PMTs and fluctuates from night to night. The nominal operating gain of the VERITAS cameras, $2 \cdot 10^5$, remains the same across different epochs (Otte et al., 2011).

The upgraded PMTs produce narrower pulse shapes and have greater quantum efficiency compared to their previous counterparts. These characteristics increase the trigger rate, reduce the energy threshold for gamma-ray events, and produce ∼20-30% increase in detection area for energies above threshold (Kieda, 2013).

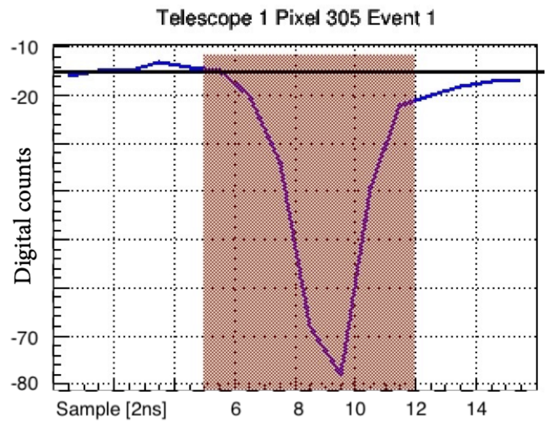


Figure 3.7: The trace from a single channel with a high flux signal. The red shading marks the 7 sample readout window.

### 3.2.2 Telescope Data Acquisition

High-bandwidth preamplifiers, integrated into the PMT base mounts, amplify the PMT signals. During operation currents are monitored and operations for dark fields are less than 10 $\mu$A. The signals are sent along RG59 stranded cable to the telescope trigger, consisting of a charged fraction discriminator (CFD) described in Section 3.2.2, and data acquisition electronics. Custom-build VME boards housing flash to analog digital converters (FADCs) digitize PMT signals with 2 ns sampling. The high gain setting is the default path for signal traces to the FADC. When the trace exceeds the 8 bit dynamic range an analog switch connects the FADC chip to a delayed low gain channel, extending the dynamic range for a single sample from 256 digital counts (dc) to 1500 (Holder, 2005).

Each PMT waveform converted to FADC signal has a readout window and an integration window over which all the charge is integrated. The nominal readout window is 24 samples (48 ns) (Holder, 2005). The current nominal integration window is 7 samples.

Electronic noise and night sky background (NSB) produce both positive and negative signal fluctuations, therefore an artificial signal is injected into the signal trace so the PMT signal never crosses zero, referred to in this work and VERITAS publications as the *pedestal*. The pedestal value is nominally 16 dc. The term *pedvar* refers to the pedestal's RMS deviation (Bird, 2015). An example of a signal trace is shown in Figure 3.7.

### 3.2.3 Trigger System

The multiple sources of night sky background (NSB) and muon products of hadronic air showers overwhelm light from potential electromagnetic air showers. Therefore, it was necessary to develop a trigger system for the VERITAS array in order to eliminate a part of the overwhelming background sources. The trigger system consists of three threshold levels that a signal must attain to be read out as data: a threshold signal in a single pixel (L1), a number of adjacent pixels which also meet this threshold in a narrow time window (L2), and multiple telescopes satisfying the previous two criteria in a time window (L3). With this applied trigger system the rates for a nominal dark field observation is $\sim$300 Hz and the deadtime is $\sim$10% (Weinstein, 2007).

The Constant Fraction Discriminator (CFD) trigger threshold, L1, consists of PMT output routed to custom-build CFDs for each pixel. The CFDs produce an output pulse if the sum of the voltages from the PMT pulse and a time-delayed copy reaches a set threshold. The typical darktime CFD threshold for observations is 45 mV, which can be raised by an equipped rate feed-back (RFG) to a maximum of 60 mV, as noise level rises.

The single telescope trigger, L2, consists of a coincidence between at least three adjacent pixels, with a coincidence window for CFD signals of $\sim$5ns (Zitzer and VERITAS Collaboration, 2013). The L2 trigger system underwent an upgrade in November 2011. For the latest pixel neighborhood coincidence, the systems use 400MHz Xilinix Virtex-5 field-programmable gate arrays (FPGAs). The L2 trigger reduces signals from single-pixel fluctuations, therefore improving rejection of NSB and reducing the energy threshold at this level of the trigger system. (Otte, 2009).

The multi-telescope array trigger, L3, requires that L2 triggers from at least two telescopes coincide within 50 ns time windows (Zitzer and VERITAS Collaboration, 2013). Multiple sources of time delay are taken into consideration before comparing time difference between L2 triggers. Firstly, time delay is produced by the air shower itself, depending on the Cherenkov wavefront's width and curvature. An approximate calculation is made based on the pointing of the telescope. Secondly, each telescope has different signal transmission times due to varying optical fiber and cable length. This is corrected for exactly (Weinstein, 2007).

For events passing the L3 trigger all PMTs and all cameras in the array read out in 32 ns windows from the FADCs to a data acquisition (DAQ) system. Readout is the largest contribution to deadtime, the operating time where the the array does not collect data. The deadtime typically scales linearly with array trigger rate and readout window width and is 10-11% for an array trigger rate of 225Hz. Knowing the array's deadtime is important, because it directly affects source flux calculation (Weinstein, 2007). During deadtime the array is reading out events, not recording new events, and therefore deadtime must be subtracted from the observing time to determine the exposure on gamma ray sources.

## 3.3 Maintenance and Calibration

### 3.3.1 Data Quality Monitoring

Each observing run goes through preliminary analysis to produce a set of data quality monitoring (DQM) plots, detailing telescope operation, hardware responses, weather, and early stage event parameterization. In order to monitor for issues, a person from the collaboration reviews these diagnostic plots and submits a report. The main objectives of the review process are to summarize the night, grade the quality of each run, report any hardware or software anomalies, and perform time cuts on the data in the case of brief clouds or transient sources of artificial light, such a satellites, vehicle lights, or air traffic.

### 3.3.2 Regular Calibrations

In each observing season, VERITAS carries out a series of observations for instrument calibration and performance studies. The Crab is VERITAS's most ideal gamma-ray source for calibration and being a steady flux source it is regularly monitored at low and high zenith angles for several months out of the year. Standard calibrations in a typical season are:

- **VERITAS Pointing Monitor/On-axis PSF:** During observing, the telescopes scan a grid of points centered in the direction of bright stars at multiple different zeniths. These measurements identify misaligned mirror facets (McCann et al., 2010).

- **Whole-dish reflectivity:** A wide-field CCD camera, located near the mirror's center, measures the brightness of a reference star is the sky FOV simultaneously with the star image reflected by the primary mirror (Archambault et al., 2013).

- **Single Photo-electron:** The light from the flasher LED is attenuated with a perforated plate installed in front of the camera, in order to match a single electron charge to a single photo-electron, where the proportionality constant is the gain of the system. The flashers are run for several minutes for multiple runs, split between the nominal and increased voltage (110%).

- **Bias curves:** The CFD threshold is adjusted in 2mV steps between 20-100 mV. This is performed while pointed at dark and bright fields. This is done to monitor the changing trigger rate of the array.

Each telescope in the array has a CCD camera mounted on the OSS, known as the VERITAS Pointing Monitor (VPM). During observations the camera tracks both stars in the FoV and LEDs mounted on the camera plating. Comparing the fixed positions of the LEDs to positions of stars in the FoV improves the telescope pointing and PSF. The VERITAS source location accuracy, determined by VPM calibrations, is 50 arcseconds or 0.014 degrees [1].

More recently, a compilation of Crab data taken over the entire V6 epoch reveals that the Crab flux observed by VERITAS has been gradually decreasing since the time of the last upgrade. Since no other instruments have detected flux changes in Crab emission at TeV energies this flux

[1] Details on VERITAS performance, including source location accuracy, can be found at https://veritas.sao.arizona.edu/about-veritas/veritas-specifications.

change is the fault of hardware. The most likely determined cause is continual degradation of the mirror reflectivity in all four telescopes. Until mirror re-coating and re-polishing takes place, a solution has been implemented in the software. The simulations used to generate the original instrument response functions for the entire V6 epoch will have their fluxes degraded to match the fraction of light loss in each season of V6. New IRFs will be generated for each season in V6 and used for the corresponding season's data analysis. The implementation of production is further discussed in Appendix A.

## 3.4 Offline Data Analysis

The goal of an IACT data analysis is to reverse engineer the development of a gamma-ray into an atmospheric air shower, the subsequent propagation, and the readout of Cherekov photons into electronic signal. At the end of a complete data analysis is a reconstructed energy and position for each event. Since several factors are impossible to measure directly, especially related to shower development through the Earth's atmosphere, electromagnetic shower simulations, which have known parameters, are a crucial component of data analysis.

The VERITAS collaboration currently uses GrISUDet simulations, which incorporates gamma-ray air shower simulations performed with CORSIKA (Cosmic Ray Simulation for KASCADE)[2], models the VERITAS telescopes and hardware, and outputs instrument response functions. Lookup tables created with these simulations sort gamma-ray air showers according to energy. In the course of data analysis, an event's parameters are cross-referenced with the contents of a corresponding lookup table. The collaboration is in the process of transitioning to **CA**mera and **RE**adout (CARE)[3] simulations for use with V6 data. Work done to validate these simulations is shown in Appendix A.

The VERITAS collaboration currently maintains two separate software packages for independent data analysis: Eventdisplay (ED) and **VE**ritas **G**amma-ray **A**nalysis **S**uite (VEGAS). Both analyses reconstruct the incident particle's energy by referencing shower image

[2] https://www.iap.kit.edu/corsika/
[3] http://otte.gatech.edu/care/

brightness and the shower's impact distance in look-up tables generated from simulations of atmospheric air showers. Most VERITAS publications require an independent analysis with both ED and VEGAS. As the work in this thesis is entirely based on VEGAS, out of the two analysis packages only VEGAS will be considered here.

### 3.4.1 Data Run Calibration

At least once per observing night, for a few minutes, observers point the telescopes at a dark sky field and turn on a flasher system consisting of blue light-emitting diodes (LEDs), mounted on each telescope's OSS and facing the camera (Hanna et al., 2010). The light pulse from the LEDs is a few ns in width in order to be similar to the pulses produced by Cherenkov photons from air showers. The uniform light measured by the cameras in a flasher run are used to measure the relative gain in each PMT and timing differences between pixels. The gains for each pixel are applied to data runs in the standard analysis.

In the first stage of VEGAS data analysis, the pedestal and relative gain are calculated in order to account for fluctuations on a run by run basis before determining if a PMT readout contains a Cherenkov signal. The pedestal and pedestal deviation, *pedvar*, are calculated by artificially triggering the telescopes during an observing run and integrating a special FADC readout over enough events to generate pedestal statistics for each data channel. The pedestal events are then The calibration of data runs with flasher runs and evaluation of FADC traces are performed in VEGAS stage2. In this step of the data reduction the event are gain corrected and the pedestal is removed (Cogan and VERITAS Collaboration, 2007).

### 3.4.2 Image Reconstruction

#### 3.4.2.1 Image Cleaning

For a given event that passes all the trigger thresholds described in Section 3.2.2, the entire camera is read out. This includes many pixels with only background signal that has nothing to do with an air shower event and must be removed in data reduction. This background signal, usually referred to as night-sky-background (NSB), is a combination of starlight, zodiacal light, light pollution, and, when present, moonlight. Image cleaning is the removal of channels that do not make up the atmospheric air shower image in the camera. After cleaning, the images are much less noisy and therefore easier to characterize with quality Hillas parameters.

The current criteria in standard analysis for discriminating between those channels that only have NSB signal and those with signal from Cherenkov light are multiple signal-to-noise (S/N) cuts. In VEGAS stage2, the default cleaning method is called *EventDisplayCleanUp*, which performs three levels of cleaning. First, the S/N is calculated for each pixel by summing the digital counts in a 7 sample integration window for the trace and dividing it by the pedestal variance. All pixels with S/N greater than a default threshold value of 5.0 are flagged as *picture* pixels. This value is selected so as to be high enough to remove the vast majority of pixels that do not make up a shower image, but not so high that it removed pixels on shower edges. The second criteria is for pixels that have at least a S/N of 2.5 and are adjacent to a *picture* pixel. These pixels are flagged as *boundary* pixels. After flagging, *EventDisplayCleanUp* removes single, isolated pixels, even if they have S/N $> 5.0$. Any other pixels that have not passed the criteria are removed and the remaining pixels constitute the event's image and are ready for Hillas parameterization (Bird, 2015).

After cleaning, there is an additional set of quality standards. To reduce the effects of pixels triggered by fluctuations in NSB, images with PMTs $\leq 5$ and total image charge (*size*) $\leq 400$ digital counts are removed for a standard analysis. To remove truncated images, an angular distance cut in the camera of 1.43 degrees is applied.

#### 3.4.2.2 Gamma-Hadron Separation

After cleaning and quality cuts in a data run, cosmic rays events still dominate over any source of gamma rays. In the development of the field of TeV astrophysics this presented a significant hurdle against source detection. The solution came when Michael Hillas presented parameters, derived from from Monte-Carlo air shower simulations, for discriminating between

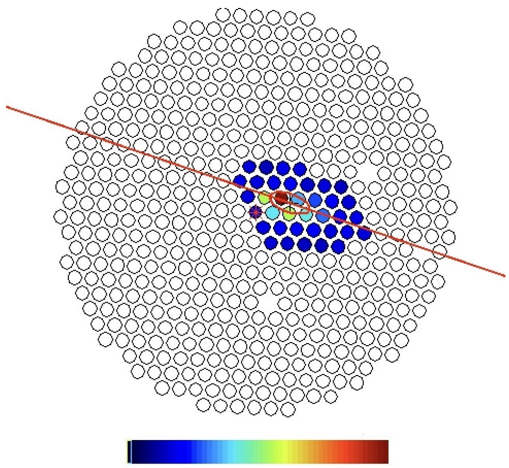

(a) Event image, before all cleaning

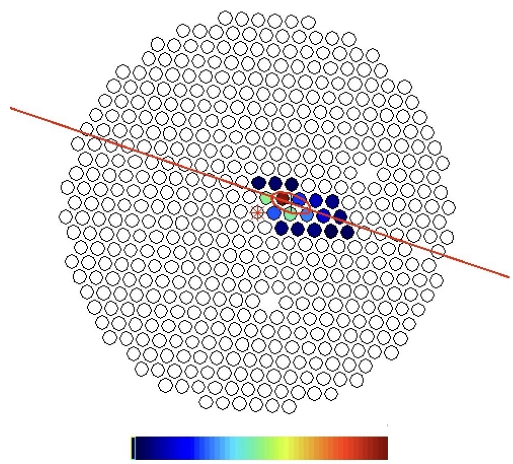

(b) After cleaning

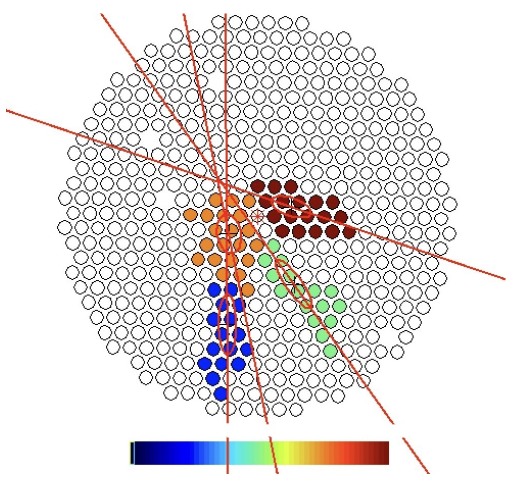

(c) All four telescope images

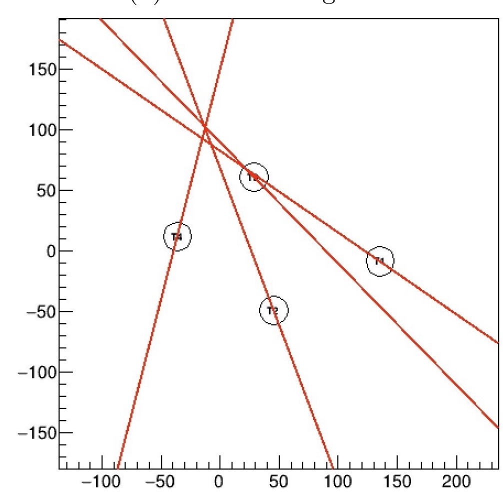


(d) Ground plane

Figure 3.8: The first three plots are shower images in the camera, all from one single event, displayed with the image software vaDisplay. Plot d) shows the reconstructed impact distance relative to each telescope location.

electromagnetic showers and hadronic showers (Hillas, 1985). As shown in Figure 3.2, cosmic rays have different development compared to gamma rays. Hadronic induced air-showers typically initiate with much more transverse momentum and the shower propagation consists of many more types of particle interaction than gamma-ray induced air-showers. Gamma-ray induced air showers only go through electromagnetic interactions between the initial particle production and the point of losses due to ionization. These differences have a great effect on the shape of the developing shower and the shape of the Cherenkov light in the VERITAS PMT cameras. A gamma-ray induced air-shower has a defined transverse width and length, whereas a hadronic induced shower has no well defined shape. As a consequence, the images of Cherenkov signals of gamma-ray-like events have roughly ellipsoidal shapes in a PMT camera, as shown in Figure 3.9. Hillas recognized the potential for eliminating hadronic produced images that are typically far from ellipsoidal and and characterized shower images with the following parameters:

- **width:** The RMS spread of light parallel to the shower image major axis.
- **length:** The RMS spread of light perpendicular to the shower image minor axis.
- **distance:** The angular distance of the image centroid from the center of the camera FOV.
- **miss:** The perpendicular angular distance of the image axis from the center of the camera FOV.
- **azimuth-width:** The RMS image width relative to an axis drawn from the image centroid to the center of the camera FOV.

The VERITAS standard analysis defines additional parameters for characterizing shower images, which are applied in event reconstruction.

- **size:** The total number of digital counts from all the pixels making up the shower image.
- **nTubes:** The total number of pixels that make up the shower image.

In addition, Hillas also defined a parameter *Frac2* in order to measure light concentration. *Frac2* is the fraction of total integrated charge of all pixels in a shower image that is concentrated

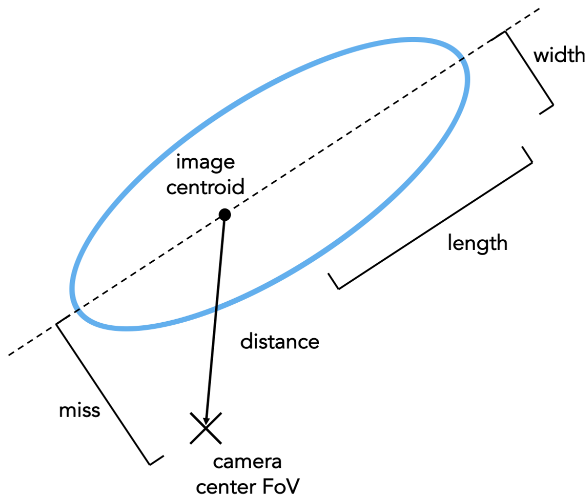


Figure 3.9: Illustration of a gamma-ray induced shower image in a single imaging focal plane camera, with shower parameters labeled.

in the two brightest PMTs (Fegan, 2019). Historically, these parameters are referred to collectively as Hillas parameters. Historically, these parameters are referred to collectively as Hillas parameters. They are also referred to as telescope parameters, since the parameterization is limited to the camera image in a single telescope.

There are rare cases where the shower image, even if the event is a gamma-ray, will not have a distinctive shape appropriate for characterizing with Hillas parameters. One such case occurs when both the shower propagation axis and telescope pointing axis are aligned.

The transverse momentum of the initial secondary shower particles and the lateral distribution in the shower propagation are the major determining factors of the shower shape. Therefore, width and length are the most important telescope parameters used to derive quantities that characterize showers observed by multiple IACTs. Width is used to derive the shower parameter mean scaled width (MSW), and likewise, length is used to derive mean scaled length (MSL). The calculation of MSW and MSL is done by the following

$$MSP = \frac{1}{N_{tel}} \sum_{i=1}^{N_{tel}} \frac{p_i}{\bar{p}_{sim}(\theta, size, r)}$$

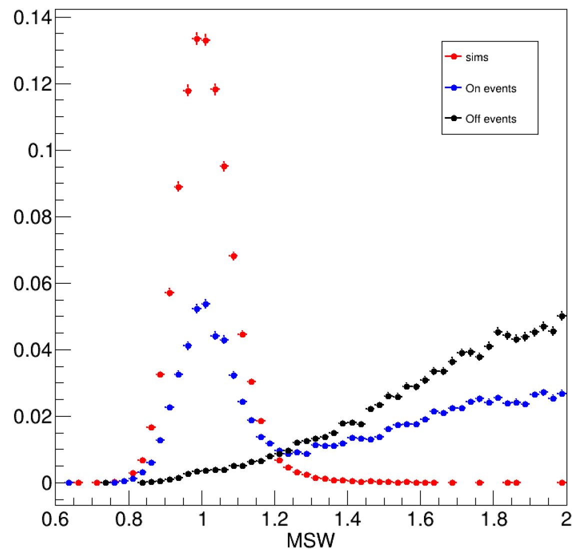


Figure 3.10: Mean scaled width distributions, normalized to equal area, for gamma-ray simulations (red), a cosmic ray dominated region of a data sample (Segue1, black), and data centered on a gamma-ray source (Crab, blue). The MSW of gamma-rays peaks around 1, while most of the background distribution lies above MSW=1.0

where $p_i$ corresponds to width or length, $i$ is the telescope number, and $\bar{p}_{sim}(\theta, size, r)$ is the mean length/width for a given image *size*, impact distance ($r$), and zenith angle $\theta$ predicted by air shower simulations. Electromagnetic air showers have a distribution of MSW and MSL peaking at 1; therefore, standard box cuts for selecting the gamma-ray like events are $0.05 \leq$ MSW $\leq 1.1$ and $0.05 \leq$ MSL $\leq 1.3$ (Daniel, 2007). On a regular basis cut values on MSL and MSW go through re-optimization to take into account factors such as telescope aging and scientific results focused on a specific energy range.

#### 3.4.2.3 Position Reconstruction with Stereo Imaging

Given the geometry of the shower image in the camera, the incoming particle's position in the camera FoV must lie at some point along a line drawn through the image's major axis. A single telescope can determine the point along the line which coincides with the particle's incoming trajectory. However, the use of multiple telescopes drastically improves the angular resolution.

Taking into account the scale of air showers upon impact on the ground, reflectors placed apart from one another on the order of 100 meters can observe the same shower simultaneously, while also producing images with different orientations in each telescope's camera. By overlapping two or more shower images on the same sky map, the multiple image axes intersect at the position where the event originated (Fegan, 2019). Although Jelly and Porter suggested stereoscopic imaging in 1963, it was not until the 1990s when two Cherekov telescopes, HEGRA, first successfully employed the stereoscopic method (Weekes, 2003). Figure 3.8 depicts the stereoscopic method in practice with VERITAS data.

The trajectory of an electromagnetic shower core is similar to the trajectory of the originating astrophysical gamma-ray had it not interacted. For a hadronic shower image this is much less the case. Therefore, stereoscopic imaging of showers also improves background rejection, especially for muons. Overall, telescope arrays improve flux sensitivity and energy resolution, reduce energy threshold, and increase effective area and angular resolution. With multiple telescopes, it is possible to determine a geometric reconstruction of the shower's direction, impact position, and, with a degree of precision, the source position on the sky.

#### 3.4.2.4 Energy Reconstruction

The astrophysical gamma-ray's energy can be estimated from the total amount of Cherenkov light emitted by the total number of particles in the cascade and collected by the telescope camera. Additional factors apart from energy determine the total amount of light detected by the camera. With greater distance of the shower core's impact from an individual telescope and/or shower development higher in the atmosphere, the subsequent camera image is dimmer. A shower arriving at a large zenith angle will traverse through more atmosphere and therefore low energy events that would have appeared if the shower were coming in at a small zenith angle disappear.

Energy reconstruction is possible with lookup tables, created from air shower simulations, which catalog energy correlated with image parameters such as size and impact distance, and observing parameters, such as zenith, azimuth, and night sky background. With simulations and a lookup table it is also possible to derive plots that predict the telescope array collection area (effective area) and energy resolution as a function of energy and other observing parameters. Effective area and energy resolution are two VERITAS instrument response functions (IRFs) which will be described in more detail in Section 4.4.

### 3.4.3 Background Estimation Methods

Even after running through every selection criteria for gamma-ray-like events, there remains a substantial background. The number of gamma-ray events, $N_s$, can be estimated by subtracting a background region from a region of interest with the following calculation,

$$N_s = N_{on} - \alpha N_{off}$$

where $N_{on}$ is the number of events in an observed region searching for a gamma-ray signal, $N_{off}$ is the number of events in a region with no gamma-ray signal. The constant $\alpha$ is the relative acceptance of two regions, determined by the fraction of observing time on the $N_{on}$ region versus the $N_{off}$ region and the relative camera sensitivities between the two regions.

There are multiple methods for selecting a background region and calculating $\alpha$. One background estimation method utilized by the Whipple 10-meter, and less frequently by the current generation IACTs, is **ON/OFF** observations and analysis. In this scenario, the gamma-ray source is observed, with the source position located at the center of the camera, for 20-30 minutes. An OFF region that does not contain the target gamma-ray source in the FoV, is then or also observed. For best results, the OFF region is taken immediately after the ON region, for at least equal observing time, and where the ON and OFF regions have similar azimuth, zenith, and NSB. Slight differences in NSB may still exist between ON and OFF regions, however, these can be corrected with software padding (Fegan, 2019). The implementation of padding is explained further in Section 6.3.

The major downside of ON/OFF observations is the large investment of observing time on background. Current and future generation IACTs perform OFF observations only for a few, very extended targets with unknown morphology, such as the Galactic Center.

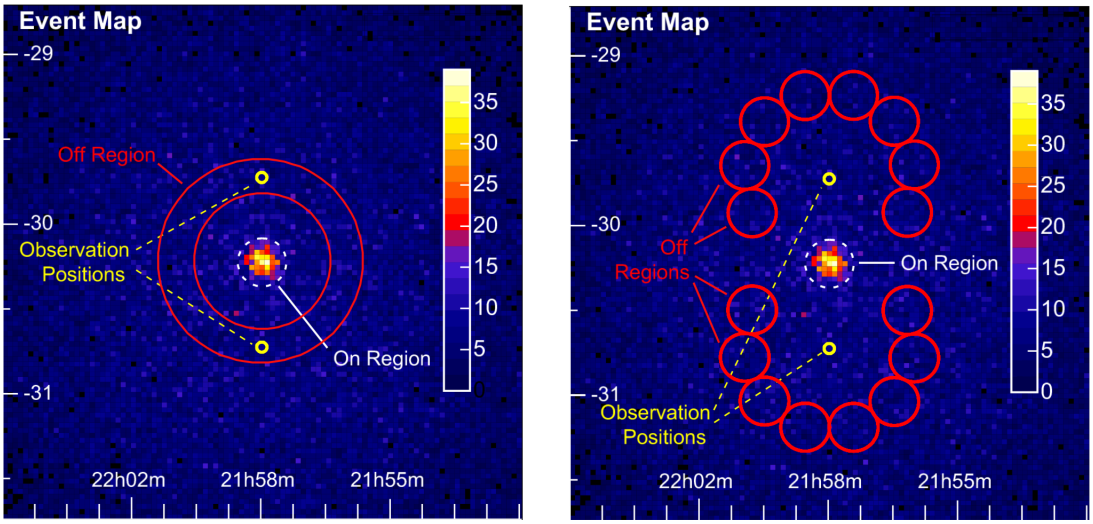


Figure 3.11: Counts maps of H.E.S.S. observations, with the two standard background methods, *ring* (**left**) and *reflected region* (**right**) illustrated. The gamma-ray source is a point-like source and located in the ON region. The OFF regions for background selection are outlined in red. Image taken from (Berge et al., 2006).

The **Ring Background** method (RBM) selects an annulus OFF region, drawn around a circular ON region, within the same FoV. An exclusion region encompassing a larger area than the size of the ON region is selected to reduce any source contamination of the background region. The parameter $\alpha$ is approximately the ratio of the solid angles of the ON versus OFF region. The ON and OFF regions, both compared to one another and across the OFF region annulus, have different radial distances from the camera center, and therefore, the acceptance is not constant. An acceptance correction is used in each radial position on the annulus. Even though RBM is a robust method for determining significance, since the acceptance curve changes with energy, the RBM is disfavored for energy spectra analysis (Berge et al., 2006).

The **Reflected Region** or *wobble* method (RR) also selects background in the same FoV as the gamma-ray target. To keep same sensitivity between background and source regions in the same FoV, observations are performed in wobble mode, where the source position is offset from the camera center by 0.5°. The central position of moderately extended sources tends to be placed further than 0.5° to reduce the chance that source emission overlaps background regions.

Since the source position is offset from the camera center there is a small reduction in sensitivity of sources with RR. Multiple background regions, of the same angular size and camera offset position as the ON source regions, are placed where there is no exclusion regions of overlap with the ON region. The correction factor between ON and OFF exposure is simply $\alpha = 1/n_{OFF}$, where $n_{OFF}$ is the number of OFF regions (Berge et al., 2006). Both RBM and RR methods are displayed in Figure 3.11.

### 3.4.4 Significance and Flux Calculation

In general, background events can be determined by accounting for the number of events in a region where there is high confidence there is no gamma-ray emission associated with the source of interest, followed by the application of scale factors that account for different exposure and changes to sensitivity across the camera size. However, statistical fluctuations in background rates can produce a positive signal after subtraction, and this need to be taken into account when calculating a significance for source detection. A signal measurement that includes estimates of statistical reliability was created by Ti-Pei Li and Yu-Quin Ma and tested on Monte Carlo simulations (Li and Ma, 1983). In what is called the Li&Ma formula, the signal significance for a single observation is calculated with

$$\sigma_S = \sqrt{2}\{N_{on}ln[\tfrac{1+\alpha}{\alpha}(\tfrac{N_{ON}}{N_{on}+N_{off}})] + N_{off}ln[(1+\alpha)\tfrac{N_{off}}{N_{off}+N_{on}}]\}^{1/2}$$

The off region in this calculation can be a separate observing field with no gamma-ray signal. However, to maximize observing time on gamma-ray sources, the background region is typically taken from the same FoV as the target gamma-ray source. In a standard analysis, there are two ways to select background regions in the same FoV as the gamma-ray signal, Ring Background and Reflected Region, explained with more detail in Section 3.4.3.

A bright star in the FoV increases the noise in a few pixels in the camera. This leads to higher energy threshold for these pixels and poorer event reconstruction in this part of the image. To counter this, regions around star positions or other expected gamma-ray sources that are not the target are excluded from background calculations. If the source significance does not meet criteria, usually $5\sigma$ post trials, then an upper limit is calculated instead.

To determine the source **flux**, both the gamma-ray rate and the effective collection area of the telescope array need to be known. The gamma-ray rate, $R_\gamma$ is

$$R_\gamma = \frac{R_{ON} - \alpha R_{OFF}}{\tau}$$

where, $R_{ON}$ is the rate of events in the ON region, $R_{OFF}$ is the rate of events in the OFF regions, and $\tau$ is the livetime of the telescope array, after correcting for deadtime and performing time cuts on data runs.

For a radio or optical telescope, collection area is proportional to the telescope's primary dish area. For IACTs, this is not the case. Instead, the collection area of IACTs is proportional to the area centered around a telescope in which, if a gamma-ray induced air shower impacts, a telescope reconstructs the event. Therefore, the collecting power of the array depends on multiple factors unrelated to hardware: NSB, weather, zenith angle, azimuth, camera offset, and energy of the primary astrophysical gamma-ray, and is thus, referred to as *effective area*. Effective areas are generated from gamma-ray simulations for a set of array configurations and night sky conditions. The simulated events for a given energy are distributed around the simulated array at random positions in a sufficiently large area. The effective area at an energy, E, is calculated by comparing all generated events versus the number of events passing all data analysis selections, given by

$$A(E) = A_{generated}\left(\frac{\text{events passing selections at E}}{\text{total events at E}}\right)$$

The general shape of effective areas for different zenith angles is shown in Figure 4.1. The effective area goes to zero at lower energies as air showers fail to produce light with enough intensity for detection. At high energies, the effective area drops off due to the FoV and distance cuts in the camera (Mohanty et al., 1998). For larger zenith angles, the effective area decreases at low energies. However, for high energies, gamma rays at large zenith angles the effective area increases and the relative intensity decreases. This is a geometric effect: with greater angular displacement from zenith angle of zero, the air shower traverses through more atmosphere and photons have larger distribution on the ground. With larger zenith angle, more light is absorbed and lower energy showers are fainter. Higher energy events ($> 5$ TeV) yield a larger light pool at the detector, even as photons are distributed over a larger area, increasing the area over which the array can reconstruct events.

### 3.4.5 Shower-Image Template Stereo Reconstruction

There are multiple advanced analysis methods aiming to improve VERITAS's sensitivity. They usually come down to improving event reconstruction and/or improving background rejection. A recent addition to the standard VERITAS data analysis is stereo reconstruction with shower-image templates (Christiansen and VERITAS Collaboration, 2017).

Templates of photoelectrons expected to be detected by VERITAS cameras have been derived from large numbers of simulations and stored as a function of energy, zenith angle, core location (x,y), and depth of first interaction in the atmosphere. These templates were created by Stephane Vincent using CORSIKA simulations of gamma-ray atmospheric showers (Vincent and VERITAS Collaboration, 2015). The software reconstruction code performs the likelihood between the template prediction to the observed number of photoelectrons in each pixel of the image. The maximized likelihood finds the optimal gamma-ray parameters. The end result is improvement on the standard VERITAS analysis to angular and energy resolution (Christiansen and VERITAS Collaboration, 2017).

# CHAPTER 4. MAXIMUM LIKELIHOOD METHOD COMPONENTS

This chapter begins with an overview of **maximum likelihood**, a method for estimating model parameters meant to reproduce a set of experimental data. Maximum likelihood calculations have an advantage in scenarios where a background subtraction region cannot be selected from the data field of view, which is often the case when VERITAS observes extended sources. To analyze VERITAS data, the main dimensions of the maximum likelihood are energy, the 2D spatial distributions of events, both background and gamma-rays, and a gamma-hadron separation parameter, mean scaled width (MSW). Therefore, this technique has been termed the **4D Maximum Likelihood Method** (4D-MLM).

Previous work in Cardenzana (2017) developed a 3D-MLM, where an unbinned likelihood was performed using two-dimensional spatial models and a gamma-hadron separation parameter template. Energy dependence was treated by performing the likelihood fit simultaneously over multiple course bins of reconstructed energy. The 3D-MLM demonstrated application on multiple VERITAS sources. The computed likelihood on regions with no significant emission should favor a null result. However, the results of 3D-MLM performance studies in Cardenzana (2017) with extended source spatial models on blank data fields reported significant emission. The author concluded that incorrect background models were the most probable cause for the large erroneous significance values and proposed improvements. Mismatch between the background model and the background emission present in data arises from large statistical errors of the background models themselves.

Major changes to the 3D-MLM presented in this work address the statistical error in the test models arising from the input of limited background and Monte-Carlo (MC) events. This was partially accomplished by creating broader bins in cases where narrow binning on a background systematic parameter was not needed. The greatest change was to move away from using two finely binned MSW distributions which were implemented to separate source and background components from total emission. In the newest implementation of the 3D-MLM, now the 4D-MLM, the fit is performed between what are referred to in this work as **event classes**. The separation of events between two event classes is based on MSW values: gamma-ray dominated range, $0.8 \leq MSW \leq 1.1$, and the background dominated range, $1.1 < MSW \leq 1.3$.

The following sections in this chapter and the next two chapters describe the derivation of instrument response functions (IRFs) and background models for each of the two event classes and their application in the 4D-MLM. The IRFs are effective area, energy distribution, and point spread function (PSF) and are used to derive the 2D spatial distribution of gamma-rays. The 2D spatial background model is derived from source-free fields, with observation parameters matched between data and background fields. The development and validation of the new PSF is presented in Chapter 5. Studies of background systematics and techniques to mitigate or eliminate the effect of statistical uncertainty in background models, are presented in Chapter 6.

## 4.1 The Likelihood Method

Several experiments, past and current, in gamma-ray astronomy and other science fields, employ a likelihood technique in the course of data analysis. For a given set of data, consisting of N events, we also have have a set of parameters, $a_1$, $a_2$,...$a_m$, within a function modeling the data, typically a probability density function (PDF). In order to fit the function to the data, we need to obtain values for these parameters. We do so by taking the likelihood equation, the product of all PDFs modeling the data,

$$L = \prod_{i=1}^{N} P_i \tag{4.1}$$

where

$$P_i = P(\vec{x}_i; a_1, a_2, ...a_m) \tag{4.2}$$

and $\vec{x}_i$ represents the independent variables of the function.

Finding the parameter values which maximize L is the same as determining the parameter values of the modeling equation which maximize the likelihood of the fit matching the data (Robinson, 2003).

Taking the logarithm of $L$ and maximizing $-2ln(L)$ makes for an easier mathematical formulation. This is especially useful for the case where there are multiple different datasets on the same source, but with different conditions that require a joint-likelihood between the different datasets. Most often all VERITAS data on one source is observed across a variety of observing conditions: multiple observing seasons, zenith ranges, atmospheric conditions, etc. Therefore, different set of IRFs are required and a joint-likelihood is essential for the 4D-MLM to perform on more than a few runs of data. A joint-likelihood is the product of multiple likelihood formula. After taking the logarithm, the joint-likelihood of $N$ likelihoods can be written as

$$-2Ln(L_{joint}) = -2Ln(L_1 L_2 L_3 ... L_N) = -2\Big(Ln(L_1) + Ln(L_2) + Ln(L_3) + ... + Ln(L_N)\Big). \quad (4.3)$$

## 4.2 Event Classes

The background in IACT analysis is extremely sensitive to systematics. Therefore, the 4D-MLM utilizes the power of the MSW distribution, in addition to the radial acceptance of the instrument. The MSW distribution shape is different for gamma-rays versus background, especially above MSW=1.1, as shown in Figure 3.10. In past development of the 4D-MLM, a fit was performed on the MSW distribution in conjuncture with the spatial model, with models for the gamma-ray and background MSW distributions; this was the method's third dimension. One drawback of this method however was that the MSW distribution was finely binned in order to preserve the shape and given the limited samples of background data, sparse statistics in the edge bins became an issue (Cardenzana, 2017). This work bypasses the statistics problem by dividing events into fewer bins, or event classes: gamma-ray dominated MSW values (0.8-1.1) and background dominated MSW values (1.1-1.3). Instrument response functions and the data events were also separated between these bins of MSW.

It is crucial to include, in the overall fit, a background dominated event class and a normalization applied to this class. A sufficiently large range of MSW values constrains the overall difference between the distribution shape of gamma-ray versus hadronic.

## 4.3 Overview of Data Selection

Both the background and gamma-ray MSW distribution shape are highly sensitive to multiple factors. Before performing the likelihood analysis, separate datasets with corresponding background models are created for the following: zenith, azimuth, and observing season. The following is the current binning for which the MSW distribution for background has been determined to be consistent:

- **Zenith (degrees):** 0-15,15-25, 25-30, 30-35, 35-40
- **Azimuth (degrees):** 180-270, 270-180
- **Observing season:** 2009-2010, 2010-2011, 2011-2012
- **Telescope Multiplicity:** Three and four telescope events.

## 4.4 Instrument Response Functions

For a set of observing configurations and conditions, Instrument Response Functions (IRFs) describe the instrument performance modeled to the expected number of detected events, given a certain sky flux and integration time. This work uses the IRF equation implemented in (Deil and et al., 2017; Nigro and et al., 2019; The Gammapy Developers),

$$R(p, E|p_{true}, E_{true}) = A_{eff}(p_{true}, E_{true}) \times PSF(p|p_{true}, E_{true}) \times E_{disp}(E|p_{true}, E_{true}) \tag{4.4}$$

where:

- $A_{eff}(p_{true}, E_{true})$**:** Effective Area
- $PSF(p|p_{true}, E_{true})$**:** Point Spread Function

- $E_{disp}(E|p_{true}, E_{true})$**:** Energy Dispersion

Additionally, for the purposes of the technique implemented in this work for extended sources, the likelihood also needs a background model. The background model is derived from multiple source-free data runs and is described in Section 4.2.

The gamma-ray IRFs are derived from gamma-ray simulations after they are run through the data reduction steps of VERITAS, as VERITAS software analysis. Air-shower shape changes not only for different energy, but also zenith, noise, and camera position. There is also some dependence on azimuth due to deviation of charged particle trajectories in the Earth's magnetic field, an affect which increases for observations at larger zenith angles. Therefore, the instrument response functions are derived from gamma-ray simulations generated for a given epoch, atmosphere, azimuth, zenith,and camera offset. Additional selection is done based on optimization cuts, selections of two ranges of mean scaled width, and telescope multiplicity. For this work, the selections are

- **Epoch:** Array configuration V5
- **Season:** ATM21 (Nov.-Apr.), ATM22 (May-Oct.)
- **Zenith:** 0°, 20°, 30°, 35°, 40°
- **Azimuth:** 0°, 45°, 90°, 135°, 180°, 225°, 270°, 315°
- **Offset:** 0°, 0.25°, 0.50°, 0.75°, 1.00°, 1.25°, 1.50°, 1.75°, 2.00°
- **Telescope Multiplicity:** Only use events reconstructed with 3 or 4 telescopes.
- **Shower Image cuts:** medium cuts

  [•]**Size cut:** 400 digital counts

  [•]**Minimum tubes cut:** 5

  [•]**Distance upper cut:** 1.43

- **MSW:** 0.8-1.1 (gamma-ray dominated), 1.1-1.3 (background dominated)

The two telescope events are removed in a 4D-MLM analysis in order to work with a narrower point spread function and improve the energy resolution.

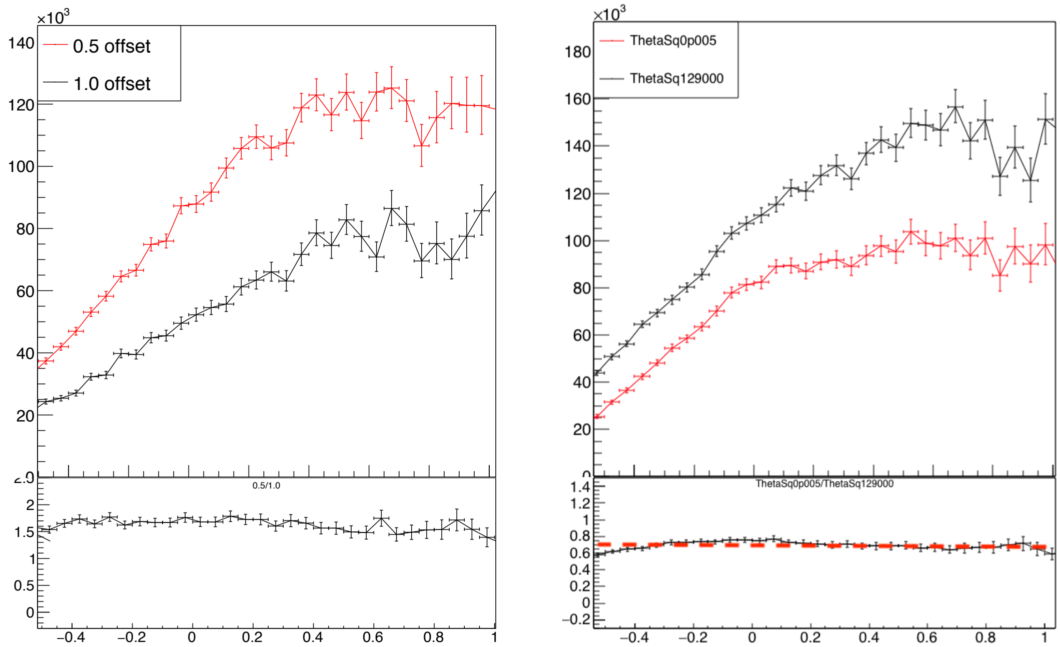


(a) 0.5° versus 1.0° offset

(b) $\Theta^2$=0.005 versus no cut on $\Theta^2$

Figure 4.1: The overlay and ratio between two effective areas. **Left:** Effective areas at 20° zenith, generated with no $\Theta$ cut, at 0.5° offset and 1.0° offset. VERITAS is roughly 50% more sensitive at 0.5° offset than 1.0° offset. **Right:** Effective areas at 20° zenith and 0.5° offset with $\Theta^2$=0.005 versus no cut on $\Theta^2$. The red line denotes $\sim 0.68$ on the ratio plot.

### 4.4.1 Effective Area

In order to answer how a gamma-ray source's flux changes with energy it is essential to account for how the VERITAS performance changes with energy. This can be done by studying the response of the telescope array to a simulated gamma-ray source with a known spectrum and flux. Comparing the number of measured counts to the number of simulated counts, in fine bins of true energy, accounts for the array's effective collection area as a function of energy and observing conditions. Therefore, passing effective areas to VERITAS data analysis is essential to reconstruct or forward fold a source spectrum and compare for the likelihood energy dependent parameters.

The effective areas used in the 4D-MLM were generated from corsika+GrISUDet simulations, which were produced with a power-law spectrum of index=2.0. Since the 4D-MLM is built to search for largely extended sources the effective areas were produced with no theta squared cut and an upper cut on the field of view of 2.0 degrees.

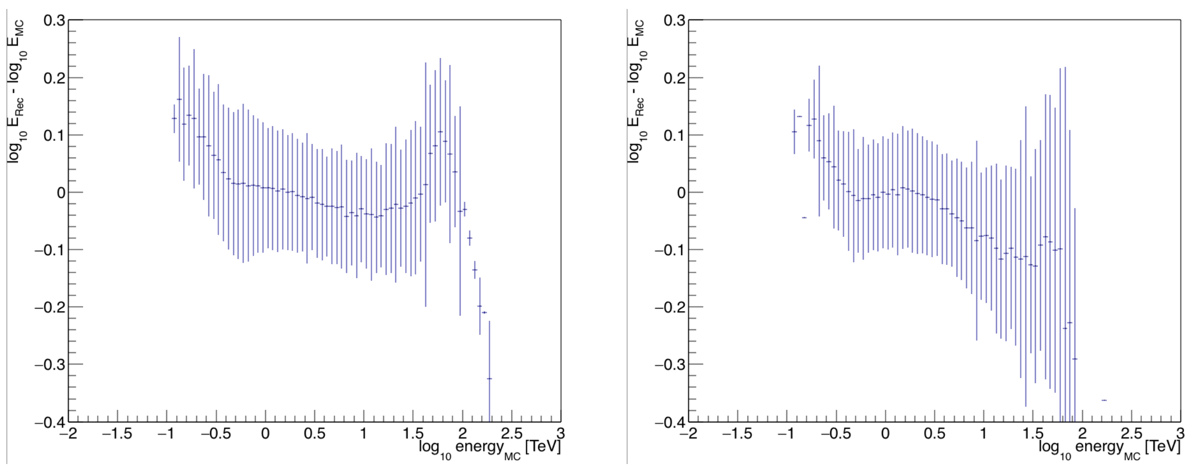


(a) Offset 0.5

(b) Offset 1.5

Figure 4.2: The energy bias curves for CORSIKA-GrISUDet simulations produced at 35° zenith, with average night sky background equal to 6.08, and under winter atmosphere conditions in the V5 epoch.

### 4.4.2 Energy Dispersion

Since the energy of gamma rays, before they interact with the Earth's atmosphere, is unknown, and must be reconstructed in data analysis, the reported quantity is referred to as *reconstructed energy*. Accumulated errors over the shower propagation, telescope hardware, and analysis chain result in imprecise measurements of event energy. Therefore, the reconstructed energy has some probability to migrate between different true energy bins in effective areas and each event's reconstructed energy has an associated error due to offset from true energy (energy bias) and standard deviation around true energy (energy resolution).

Quantifying energy bias and energy resolution is made possible by analyzing Monte Carlo simulations of gamma-ray showers and comparing reconstructed energy to the known true energy. In order to perform spectral analysis, the probability that an event with a given reconstructed energy migrates across bins of given true energy must be passed to the spectral analysis.

# CHAPTER 5. POINT SPREAD FUNCTION

To model the two-dimensional distribution of gamma-ray events at a given position in the field of view each instrument response needs a probability distribution function. Previous work in Cardenzana (2017) fit several functions to spatial distribution of gamma-ray simulations in order to find the best model of the VERITAS gamma-ray point spread function (PSF), settling on the 2D symmetric King function. Though the symmetric King function was used in Cardenzana (2017) evidence presented in his thesis suggested there were shortcomings to this PSF model. One of the major drawbacks is present in skymaps produced from a full likelihood analysis of Crab data, which display over-subtraction and under-subtraction features, as shown in Figure 5.1. This is due to different spatial distribution correlated with different mean scaled width (MSW) values.

Since Cardenzana's work concluded, multiple changes have been implemented to the 4D-MLM PSF model, including a division of events into a gamma-ray dominated class ($0.8 < MSW < 1.1$) and background dominated class ($1.1 < MSW < 1.3$). With the addition of event classes, previous validation studies performed in Cardenzana (2017) have been repeated, separately for each event class, and are presented here.

## 5.1 Symmetric vs Asymmetric

Initial comparisons to the gamma-ray simulation 2D distribution were performed between the 2-D distribution of gamma-ray simulations and the symmetric King-function. Asymmetry is observed at large camera offset ($> 0.75°$) and greater energy ($> 1$ TeV), shown in Figures B.2, B.3, B.4, B.5, B.6, and B.7 and Figures B.14, B.15, B.16, B.17, B.18, and B.19. A King function with parameters characterizing both the x and y directions was fit to the spatial distribution of events and is a better match in both MSW bins, shown in Figures B.8, B.9, B.10, B.11, B.12, and B.13 and Figures B.20, B.21, B.22, B.23, B.24, and B.25.

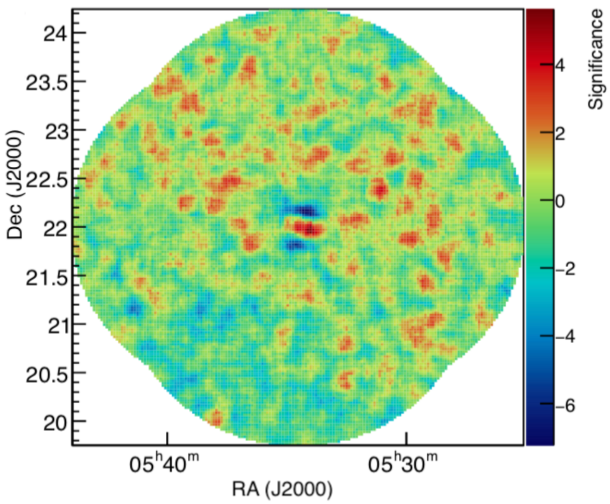


(a) $0.8 < MSW < 1.1$

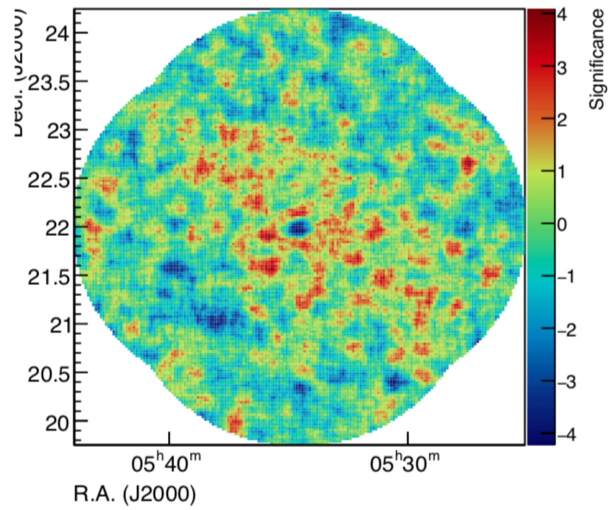


(b) $1.1 < MSW < 1.3$

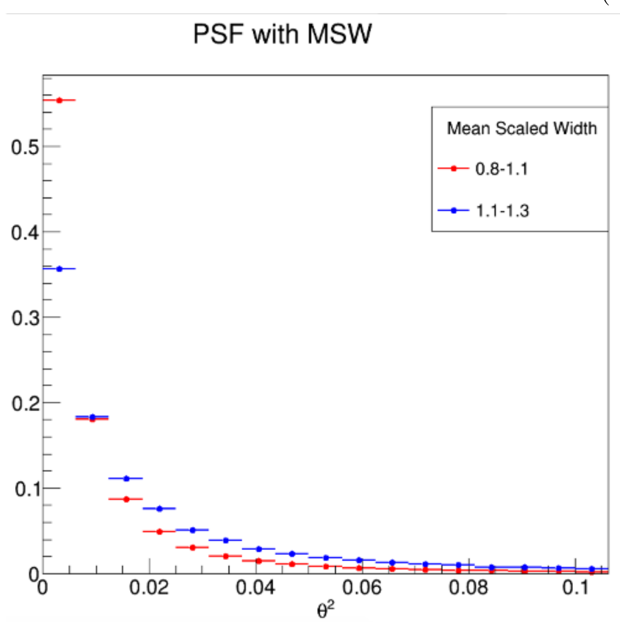


(c) Theta-squared distribution of gamma-ray simulations.

Figure 5.1: **Top plots:** 3D-MLM residual sky maps of Crab analysis, binned in two ranges of MSW. **Bottom plot:** A $\Theta^2$ distribution of $0.5°$ offset gamma-ray simulations, binned in two ranges of MSW.

Therefore, the asymmetric King-function is the best function fit to the VERITAS PSF, with the following form:

$$PSF(x, y, \sigma_x, \sigma_y, \lambda) = \frac{1}{2\pi\sigma_x\sigma_y}\left(1 - \frac{1}{\lambda}\right)\left[1 + \frac{1}{2\lambda}\cdot\left(\frac{x^2}{\sigma_x^2} + \frac{y^2}{\sigma_y^2}\right)\right]^{-\lambda}. \tag{5.1}$$

The parameters $\sigma_x$ and $\sigma_y$ characterize the size of the angular distribution in the x or y direction and parameter $\lambda$ determines the weight of distribution in the tails (Ackermann and et al., 2013b). The x and y directions can be written is terms of the rotation angle of the distribution major axis in camera coordinates, given in Equation 5.2 and Equation 5.3. Validation of the King function was repeated in two separate bins of MSW values. The fits were obtained for values of $\sigma_x$ and $\sigma_y$ in narrow bins of $log_{10}(E_{true})$. The $\lambda$ parameter was not allowed to float and was fixed at $\lambda = 2.5$. In previous work, allowing the $\lambda$ parameter to vary while fitting to the distribution caused the extrapolated $\lambda$ values to become unstable (Cardenzana, 2017).

Figures 5.5 and **??** show that not only is the 2D spatial distribution asymmetric, but also broadens in the y-direction at larger camera offset and greater energy. This is important because one inquiry about extended sources is energy dependent morphology. Therefore, understanding and accounting for the cause of PSF dependence on both energy and offset is important. While the overall behavior is likely impossible to eliminate, event selections that diminish the effect and decrease the PSF should be performed.

The Image Template Method (ITM) is a shower reconstruction algorithm that utilizes the likelihood method with shower image templates generated from simulations. Published studies demonstrate that ITM leads to an overall narrower PSF (Christiansen and VERITAS Collaboration, 2017). Fitting of the King-function to the 2-D distribution of simulations processed with ITM also shows the narrower PSF, presented in Figure 5.2. With or without applying ITM, the general trends of PSF dependency on offset and energy remain similar.

Two sets of PSF studies were carried out to determine the cause of spatial distribution broadening with increasing offset at large energy. One study compared the PSF of events observed by only 3 telescopes versus events observed by all 4 telescopes in the VERITAS array.

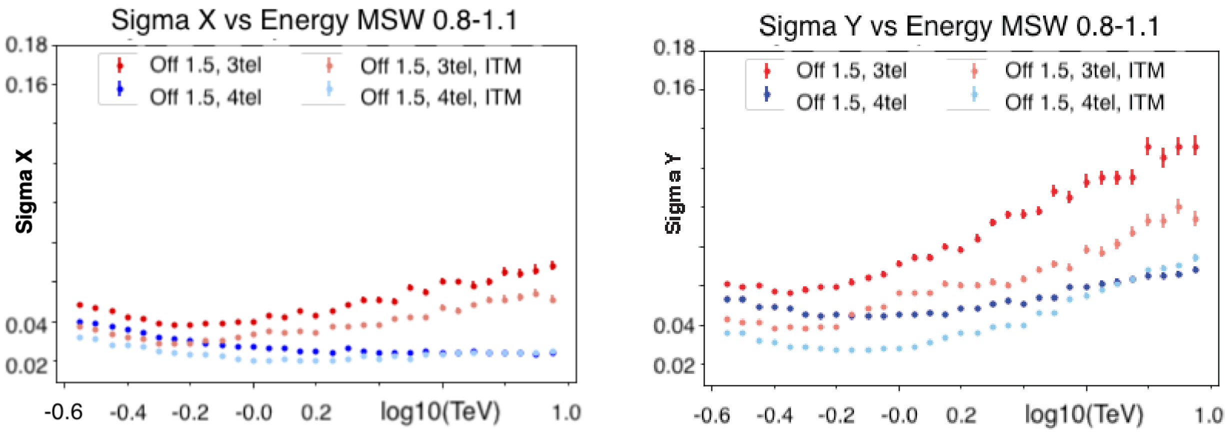


Figure 5.2: Distribution of $\sigma_x$ (left) and $\sigma_y$ (right) versus energy after a fit of the asymmetric King function to simulations produced at 1.5 offset, reconstructed with either 3 or 4 telescope events, ITM or without ITM.

The results are in Figure 5.2 and show a much narrower PSF for 4 telescope events versus 3 telescope events. The second study performed two separate event selections to remove events truncated at the edge of the camera: 1) a cut on camera distance of 1 degree or 2) a cut on the loss parameter. The cut on the loss parameter removed all shower images with a fraction of the total charge in the outer pixels of the camera greater than 0.1. Both of these event selections remove truncated images. Figure 5.3 shows the PSF of simulations produced at 1.5 offset, processed with standard parameters, or a loss cut of 0.1, or a distance cut of 1.0 degree.

Both Figures 5.2 and 5.3 demonstrate that event truncation is a primary cause of the broader PSF at large offset and large energy. Truncated images, especially when truncation removes a part of the core image, creates a poorly reconstructed shower image major axis. A single truncated image in an event observed by multiple telescopes negatively impacts position reconstruction and impacts 3 telescope events more than 4 telescope events. Removal of truncated images improves the PSF and should be performed in analyses searching for energy dependent morphology. However, removing 3 telescope events or applying a loss cut significantly reduces statistics of the gamma-ray simulations. Therefore, only ITM is applied to data and background samples. The IRFs are derived from simulations processed with ITM.

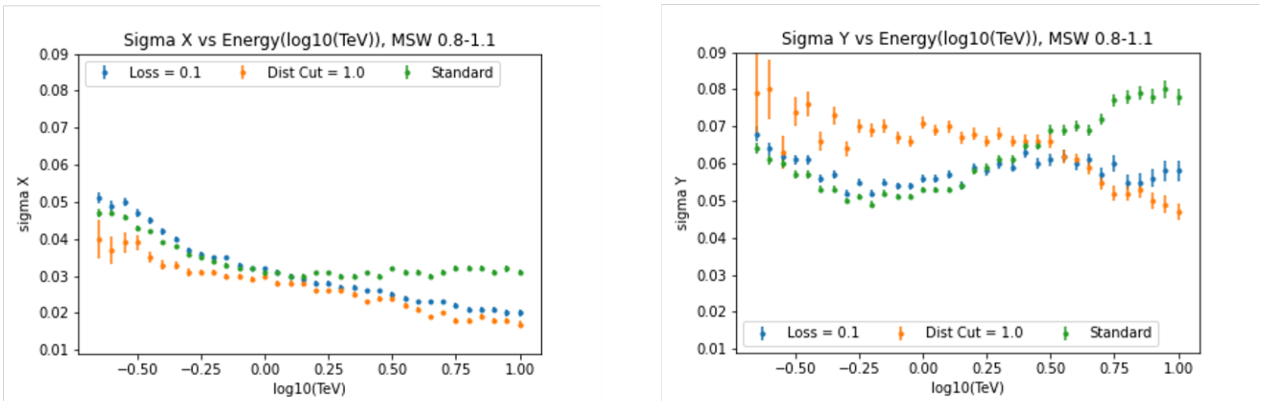


Figure 5.3: Distribution of $\sigma_x$ (left) and $\sigma_y$ (right) versus energy after a fit of the asymmetric King function to simulations. These simulations were produced at 20 degrees zenith, 1.5 offset, and reduced with either a loss cut or a distance cut.

Since the 2D distribution of events is asymmetric, the orientation of the distribution relative to Cartesian coordinates needs to be included in the PSF calculation. Before the fit, the coordinate system is rotated into the frame where the major and minor axes of the PSF align with y and x Cartesian coordinate axes. The rotation equations are

$$x^{'} = xcos\theta - ysin\theta \tag{5.2}$$

and

$$y^{'} = xsin\theta + ycos\theta. \tag{5.3}$$

The values of sin$\theta$ and cos$\theta$ passed to the PSF function are taken from the eigenvectors and eigenvalues of the given 2D distribution of simulation events.

Although the asymmetric King function is the best fit to the VERITAS PSF, the final choice of PSF format in the 4D-MLM in this analysis is the symmetric King Function. This decision was made to accommodate the 4D-MLM with the current iteration of the software analysis Gammapy. Usage of the 4D-MLM with Gammapy is explained in Section 7.4. A few technical details related to VERITAS PSF validation are in Appendix B.

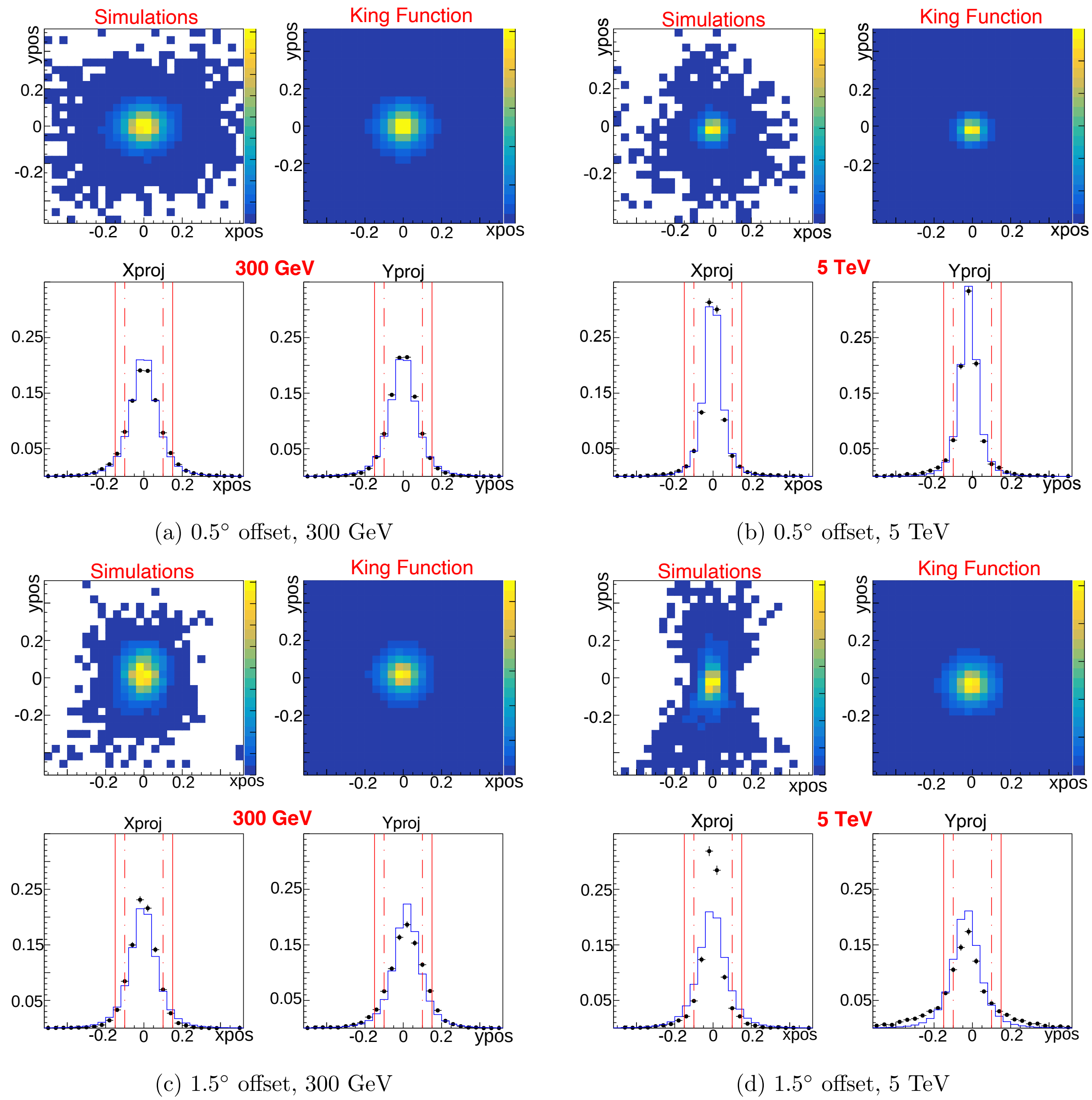


Figure 5.4: Plots of 2-D distributions and projections in x and y for a set of GrISUDet V5 simulations with average noise 6.41, binned in two energies and two offsets. Each set of four plots has the 2-D distribution of simulation events, the resulting 2-D plotted King function after fitting, and the overlaid data and fitted King function, projected in x and y. These plots are all fit with the symmetric King function, for events $0.8 < MSW < 1.1$.

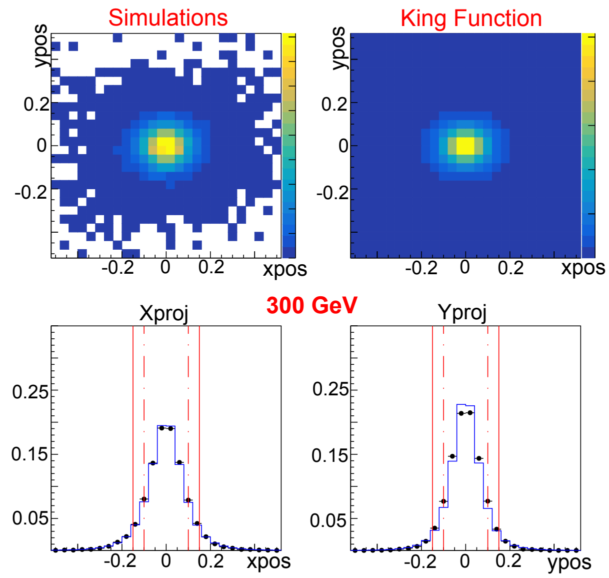


(a) 0.5° offset, 300 GeV

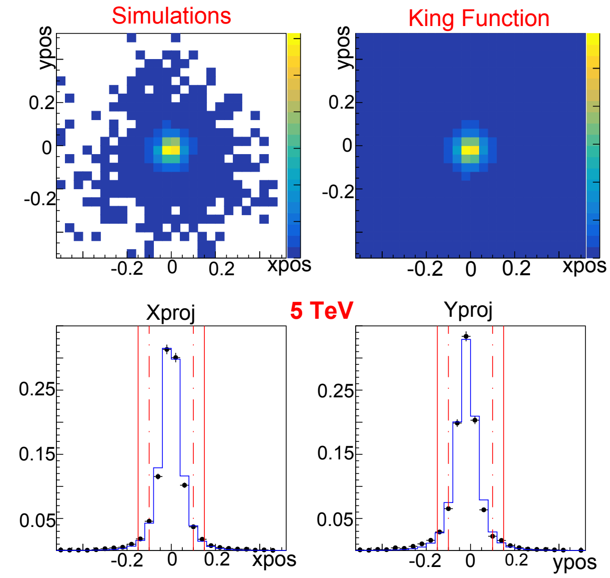


(b) 0.5° offset, 5 TeV

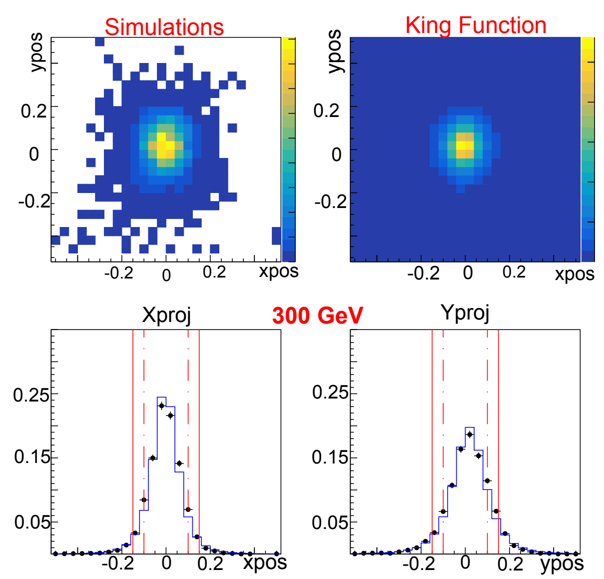


(c) 1.5° offset, 300 GeV

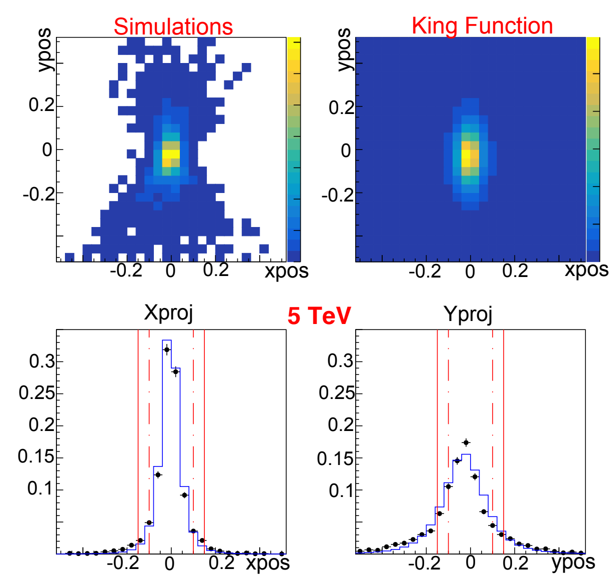


(d) 1.5° offset, 5 TeV

Figure 5.5: Plots of 2-D distributions and projections in x and y for a set of GrISUDet V5 simulations with average noise 6.41, binned in two energies and two offsets. Each set of four plots has the 2-D distribution of simulation events, the resulting 2-D plotted King function after fitting, and the overlaid data and fitted King function, projected in x and y. These plots are all fit with the asymmetric King function, for events $0.8 < MSW < 1.1$.

## 5.2 Observation Parameter Dependence

Division of simulated gamma-ray events into finer bins of observation parameters leads to fewer statistics and unreliable fits, especially for events with $1.1 < MSW < 1.3$. Therefore, a series of validations were performed on the dependence of the PSF on the following observation parameters: noise, azimuth, and offset. This was done in order to gauge the degree of dependence and determine an appropriate binning for observation parameters.

The plots in Figure 5.6 show the PSF dependence on noise for a set of gamma-ray simulations, for parameters characterizing both the major and minor axis of the fitted asymmetric King function. Noise levels which are largely distinct from each other show appreciably different King-function parameter values. However, adjacent noise levels show very little difference between parameters after fitting. Thus, simulated gamma-ray events with adjacent noise levels are combined before performing a fit on the spatial distribution on a set of binned events. The following GrISUDet noise levels were used: 100MHz, 150MHz, 200MHz, 250MHz, 300MHz, 350MHz, 400MHz, 490MHz, 605MHz, and 730MHz.

The plots in Figure 5.7 show PSF dependence on azimuth for a set of gamma-ray simulations with two different zeniths and two different camera offsets after fitting with an asymmetric King function. The azimuth is split between two bins, north and south directions. The difference between the two azimuth bins is greatest for simulations at 40° zenith and least different at 20°, as expected. However, the dependence of PSF on azimuth is less than the dependence on offset. Dividing the simulations into two bins of azimuth also reduces statistics, which impacts the reliability of fitting the PSF for events with $1.1 < MSW < 1.3$ and energies approaching 5 TeV. Therefore, there is no azimuth binning of the PSF IRF format in this current iteration of the 4D-MLM.

## 5.3 Impact of Shower Reconstruction on the Point Spread Function

The gamma-ray PSF width and degree of elongation shows significant dependence on offset at energies above about 2 TeV. The spatial distribution dependency on energy at large offset needs

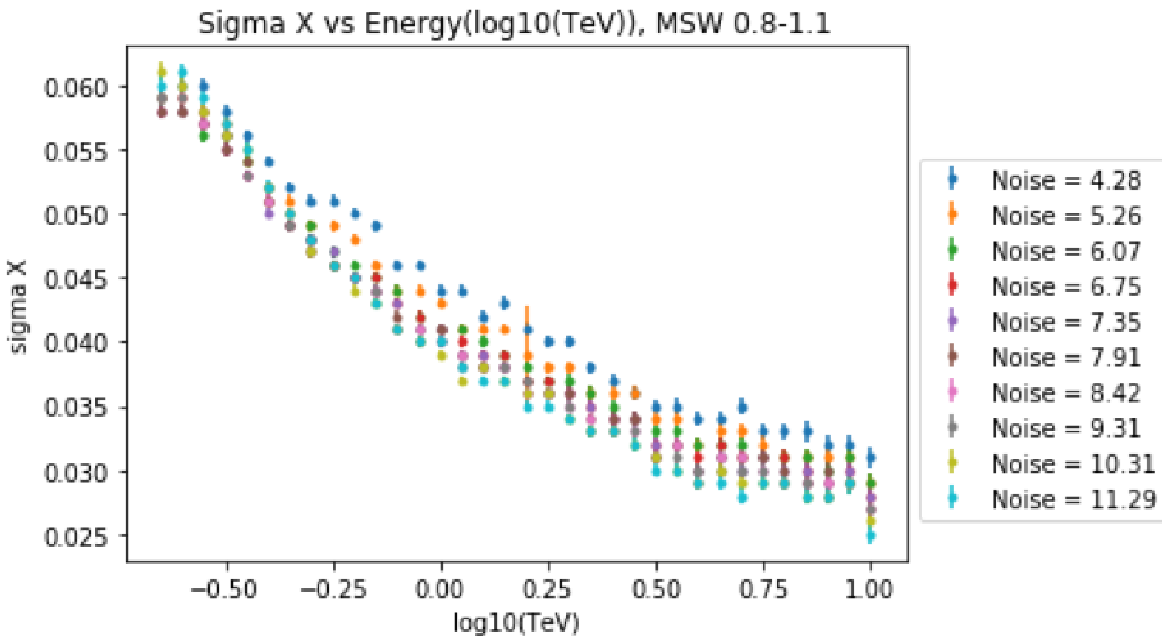


(a) Sigma X

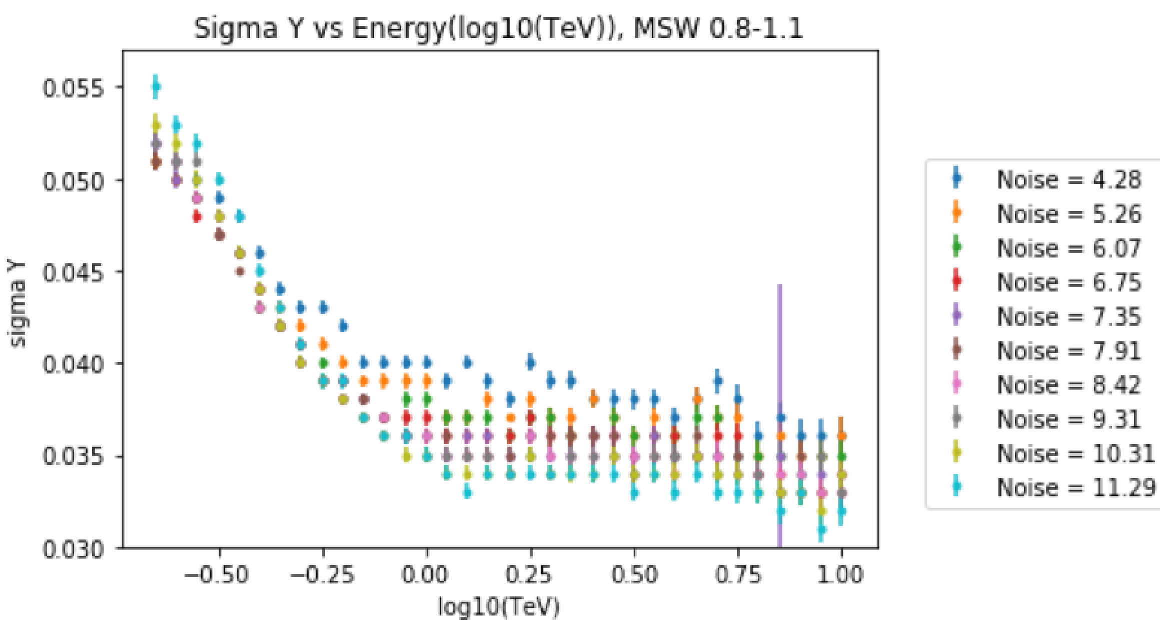


(b) Sigma Y

Figure 5.6: The asymmetric King-function sigmax and sigmay parameters after fitting with 10 different simulated noise levels.

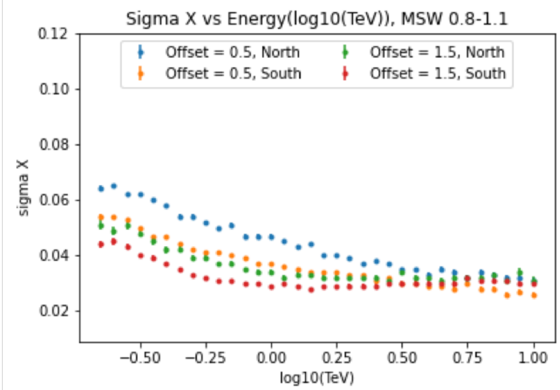


(a) 20° zenith, sigmaX

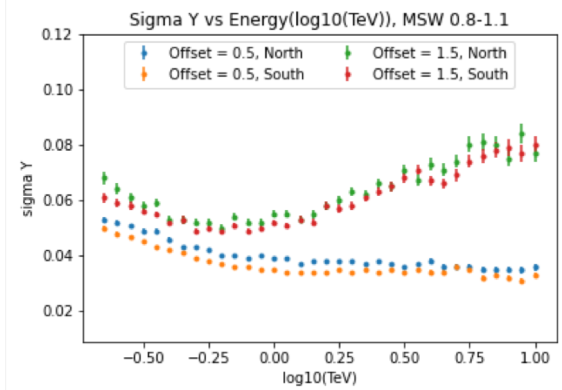


(b) 20° zenith, sigmaY

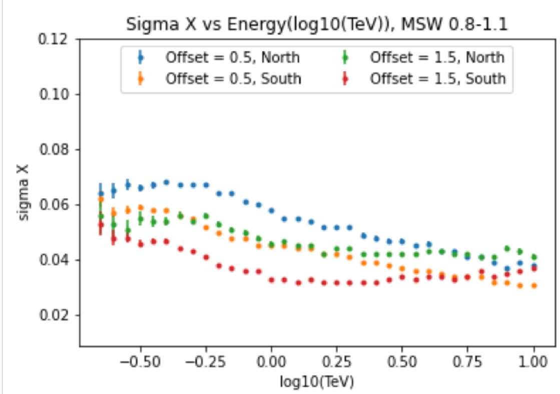


(c) 40° zenith, sigmaX

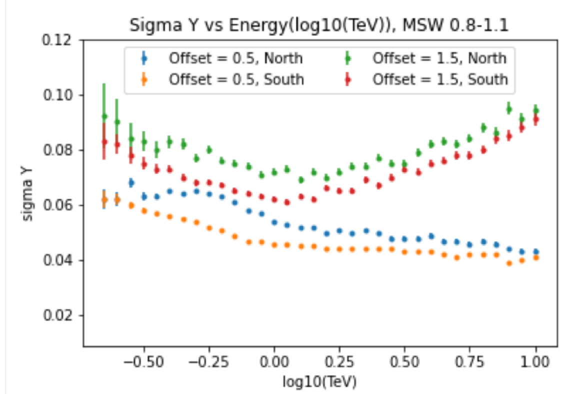


(d) 40° zenith, sigmaY

Figure 5.7: The asymmetric King-function major and minor axis parameters (sigmaY and sigmaX) after fitting with two different zeniths, two different offsets, and north and south azimuths, for events $0.8 < MSW < 1.1$.

to be better understood. After fifteen years of observations the VERITAS catalog now includes several sources or potential sources observed at large camera offset or sources with emission in the outer camera. Most of these sources are extended and exhibit energy dependent morphology. In order to better distinguish the PSF dependence on energy from a source energy dependent morphology the cause of PSF asymmetry has been determined and, where possible, event selection performed to reduce the PSF size.

The most likely cause of the increasing and elongated asymmetric PSF at larger offset and greater energy is truncation of images at the edge of the camera and the poor reconstruction of position this produces. Section 3.4.2.2 describes parameters which define shower images in an IACT camera. These shower parameters are essential for reconstructing a gamma-ray's energy and FOV position. The shower parameters themselves are calculated in the VERITAS data analysis and reduction software, either EventDisplay or VEGAS. In VEGAS, the shower parameters width, length, distance, etc., are calculated in vaStage4.

In VEGAS vaStage4, calculation of shower parameters depends on the determination of the shower image's primary axis, which gives its position and orientation, and the image centroid. The image centroid is determined by looping over all the channels with charge after cleaning. The x-position and y-position of the centroid are calculated by summing the x and y position of each nonzero channel, weighted by the charge of the corresponding channel, and then dividing by the total summed image charge, or image *size*. The major shower axis is determined by the location of the image centroid relative to the center of the camera.

The shower source location in the FoV is determined by a weighted minimization of the perpendicular distance of the source location to each image axis. The weight on each distance value corresponds to the image size. If there is a shower seen by more than two telescopes, the source location is computed for each pair of image axes. The location in the FOV is then calculated by a weighted average of the multiple source locations. The weight in this calculation favors image pairs with larger angular separation and image size versus pairs of images that are fainter and more parallel to each other (Cogan, 2006). Therefore, truncation on one or more images will produce a poor position reconstruction and a larger PSF.

Reconstruction of a gamma-ray source position in the FOV depends on reconstruction between multiple telescope images. Therefore, dependency on the number of telescopes capturing a shower image was investigated. Splitting the 2-D distribution between images seen by only three telescopes and images seen by four telescopes is show in Figure 5.2. Overall, 3 telescopes events produce a broader PSF. The PSF elongation at larger offset and greater energy is in much greater effect for three telescope events than four telescope events. Reconstruction with four telescope events has less impact from a truncated image.

# CHAPTER 6. BACKGROUND

Previous development of the 3D Maximum Likelihood Method (3D MLM) in Cardenzana (2017) modeled the background spatially and with mean scaled width (MSW) templates. The spatial component is the radial distribution of events in bins of angular offset from the camera center. For both this work and Cardenzana (2017) MSW is an additional dimension in the likelihood calculation. This parameter has a very different distribution for a pure gamma-ray signal versus a hadronic signal and is therefore essential for modeling a separate background component from source emission. In Cardenzana (2017) there are separate MSW templates for for background and gamma-ray emission, consisting of a MSW distribution for $0.8 < MSW < 1.3$. The background MSW template was derived from dark matter targets or fields with low flux blazars.

The major drawback to the approach in Cardenzana (2017) was the impact of limited statistics due to binning across multiple parameters: zenith, azimuth, and the spatial model binned in angular offset from the camera center. The MSW distribution itself is a binned distribution. This multiple division of data with already limited statistics from background led to multiple bins with few events. Nuisance parameters were introduced to account for Poisson statistical fluctuations in bins with the lowest counts while the uncertainty in bins with more statistics is not assumed and the MSW distribution is assumed to be constant.

The introduction of nuisance parameters was a solution in theory, but could not be applied in practice. Nuisance parameters greatly increased the number of free parameters in the likelihood, leading to scenarios where the fit would not converge. This work takes a different approach to the application of MSW with the maximum likelihood. First, event classes were created based on a range of values of MSW. Currently, there is a gamma-ray event class ($0.8 < MSW < 1.1$) and a hadronic event class ($1.1 < MSW < 1.3$). There are now separate effective areas, energy distributions, and point spread functions created for each event class. A spatial model of the background component is derived across the entire camera for each event class. This approach reduced the number of divided bins, increasing statistics. A likelihood is performed across both event classes, where the different, but related background normalization between the two event classes will changed depending on the significance of gamma-ray emission. Results of a study on Crab data employed with event classes are shown in Chapter 7. Second, terms which account for uncertainty in models were added to the likelihood equations. Results of this method performed on a single parameter, MSW, are shown in the next section. Future work will combine event classes with Barlow Beeston terms.

## 6.1 Background Selection and Modeling

The signal in an Imaging Atmospheric Cherenkov Telescope (IACT) observing field is dominated by hadronic-induced air showers. While there is current software available to simulate extensive air showers generated by hadrons, current programs are not considered robust enough for separating background from real gamma-ray data. Therefore, the background models created for this thesis's work are derived from events in VERITAS blank field observations. These blank fields used for background modeling are primarily dark matter targets, weak blazars, or blazars with only upper-limit values. The fields are also at least 5 degrees off the galactic plane in order to avoid a significant gamma-ray background component.

Background fields are selected based on a set of observing conditions matched to a data set. These background samples are passed to Gammapy in order to produce models of the VERITAS instrument's radial acceptance, which are then written to data fits files.

## 6.2 Single Parameter Likelihood

In order to examine background systematics separately from the full analysis, multiple likelihood ratio tests (LRTs) were performed only on the distribution of the gamma-hadron separation parameter, MSW. A series of single parameter LRTs were performed on data from blank field targets to confirm null results and on a bright gamma-ray source, the Crab. When analyzing the Crab, the LRTs were performed in two separate camera regions, an inner region encompassing the Crab source position and an outer region, containing no known gamma-ray sources.

The likelihood was performed on binned histograms of the MSW distribution, with lower and upper bounds on the distribution of MSW=0.8 and MSW=1.3. In each LRT the data were modeled with two components, a MSW distribution for the gamma-ray signal, derived from gamma-ray simulations, and a MSW distribution for the background, derived from observations taken on fields dominated by hadronic emission. A set of data, simulations, and background MSW distributions are shown in Figure 6.1.

Background dependency on changing zenith, azimuth, camera offset, and energy was controlled through event selection prior to generation of MSW distribution histograms. Each parameter binning is listed in the previous subsection. A strategy of accounting for noise, another known dependent background parameter, was found through these single parameter studies. Mitigation of differences between night sky brightness systematics between separate fields is described in Section 6.2.

These single parameter studies were also concerned with determining the effect of limited statistics in both the data and the background model. Small event numbers near the lower bound of MSW distributions were a concern from the beginning of these single parameters tests. In order to account for statistical error, single parameter likelihood fits included Barlow Beeston terms.

### 6.2.1 The Barlow Beeston Method

The previously introduced likelihood formula described in Section 4.1 does not include error intrinsic to models in the fit. For model parameters derived from simulations, there will be some dispersion around the mean. Statistical error is minuscule when models are derived from enormous numbers of simulations. However, in some scenarios, statistical error cannot be ignored in an analysis utilizing the likelihood method. For situations of limited simulation production time or where Monte Carlo events subdivide across large multidimensional space, statistical error does factor into modeling. Where real data is used for modeling, such as is the case for this work, statistical error in background models is also extremely relevant.

In 1993 Roger Barlow and Christine Beeston derived and presented terms to add to the maximum likelihood equations when statistics are finite and subject to fluctuations. Their derivation of the binned likelihood finds the best model of predicted events, $f_i$, to the number of events $d_i$, where $d_i$ is a set of Poisson distributed real data that fall in bin $i$. Under this framework the likelihood may be written as follows:

$$L = e^{-f_i}\frac{f_i^{d_i}}{d_i!}. \tag{6.1}$$

The predicted number of counts, $f_i(P_1, P_2, ...P_m)$, is given by the respective model source probability, $P_j$, and the numbers of Monte Carlo events $a_{ji}$ from source $j$ and in bin $i$, resulting in

$$f_i = N_D \sum_{j=1}^{m} \frac{P_j a_{ji}}{N_j}. \tag{6.2}$$

The probabilities must sum to unity. The values $N_D$ and $N_j$ are the total number of events in the data sample and the total number in the MC sample for source $j$, respectively. Calculating the likelihood is more numerically stable on the natural logarithm scale, which gives the following:

$$lnL = \sum_{i=1}^{n} d_i ln f_i - f_i \tag{6.3}$$

where $n$ is the total number of bins.

To account for statistical fluctuations in the Monte Carlo samples, each model source is expressed not based on the number of Monte Carlo events, $a_{ji}$, but on some expected, yet unknown number of events $A_{ji}$. The predicted number of data events in a bin $i$ and in $j$ models is

$$f_i = \sum_{j=1}^{m} p_j A_{ji}, \tag{6.4}$$

where the likelihood becomes

$$lnL = \sum_{i=1}^{n} d_i ln f_i - f_i + \sum_{i=1}^{n}\sum_{j=1}^{m} a_{ji} ln A_{ji} - A_{ji}. \quad (6.5)$$

After rewriting $a_{ji}$ in terms of $A_{ji}$ and for a model with two components, a background model, $B_i$, and a source model, $S_i$, the likelihood for $n$ number of bins is as follows:

$$lnL = \sum_{i=1}^{n} d_i ln f_i - f_i + \sum_{i=1}^{n} p_b B_i + p_s S_i \quad (6.6)$$

,

where $f_i$ is $p_b B_i + p_s S_i$. In each bin $i$, the probabilities, $p_b$ and $p_s$ are calculated such that, the number of model events, $S_i$ and $B_i$, and data events, $d_i$, maximize the likelihood.

### 6.2.2 Single Parameter Fit Results

Table 6.1: Test statistic (TS) of single parameter likelihood ratio tests on the MSW distribution of Ursa Minor, in both the inner (0.0-1.2 degrees) and outer camera (1.2-1.7 degrees). The fit was performed for three different background models derived from source-free events and in four different energy bins. Zenith matching was done between 35 to 40 degrees zenith and all events are within the northern half of the sky. The exposure ratio is the number of data events divided by the number of background events.

| **Energy (TeV)** | **Background** | **TS (0.0-1.2 deg)** | **TS (1.2-1.7 deg)** | **exposure ratio** |
|---|---|---|---|---|
| 0.3-0.6 | M82 | 0.03 | 2.49E-07 | 0.35 |
| | 1ES 0502+675 | 0.46 | 0.01 | 0.68 |
| | 1ES 0502+675 and M82 | 0.001 | -8.98E-06 | 0.23 |
| 0.6-1.0 | M82 | -8.00E-06 | 0.49 | 0.31 |
| | 1ES 0502+675 | 0.74 | 0.01 | 0.71 |
| | 1ES 0502+675 and M82 | -3.73E-07 | 0.44 | 0.21 |
| 1-2 | M82 | 6.40E-08 | -6.41E-07 | 0.32 |
| | 1ES 0502+675 | 4.95E-07 | -7.60E-06 | 0.71 |
| | 1ES 0502+675 and M82 | -1.16E-07 | -3.37E-06 | 0.22 |
| 2-5 | M82 | 4.66E-09 | 0.01 | 0.32 |
| | 1ES 0502+675 | -1.55E-06 | 0.34 | 0.70 |
| | 1ES 0502+675 and M82 | -9.94E-06 | 0.10 | 0.22 |

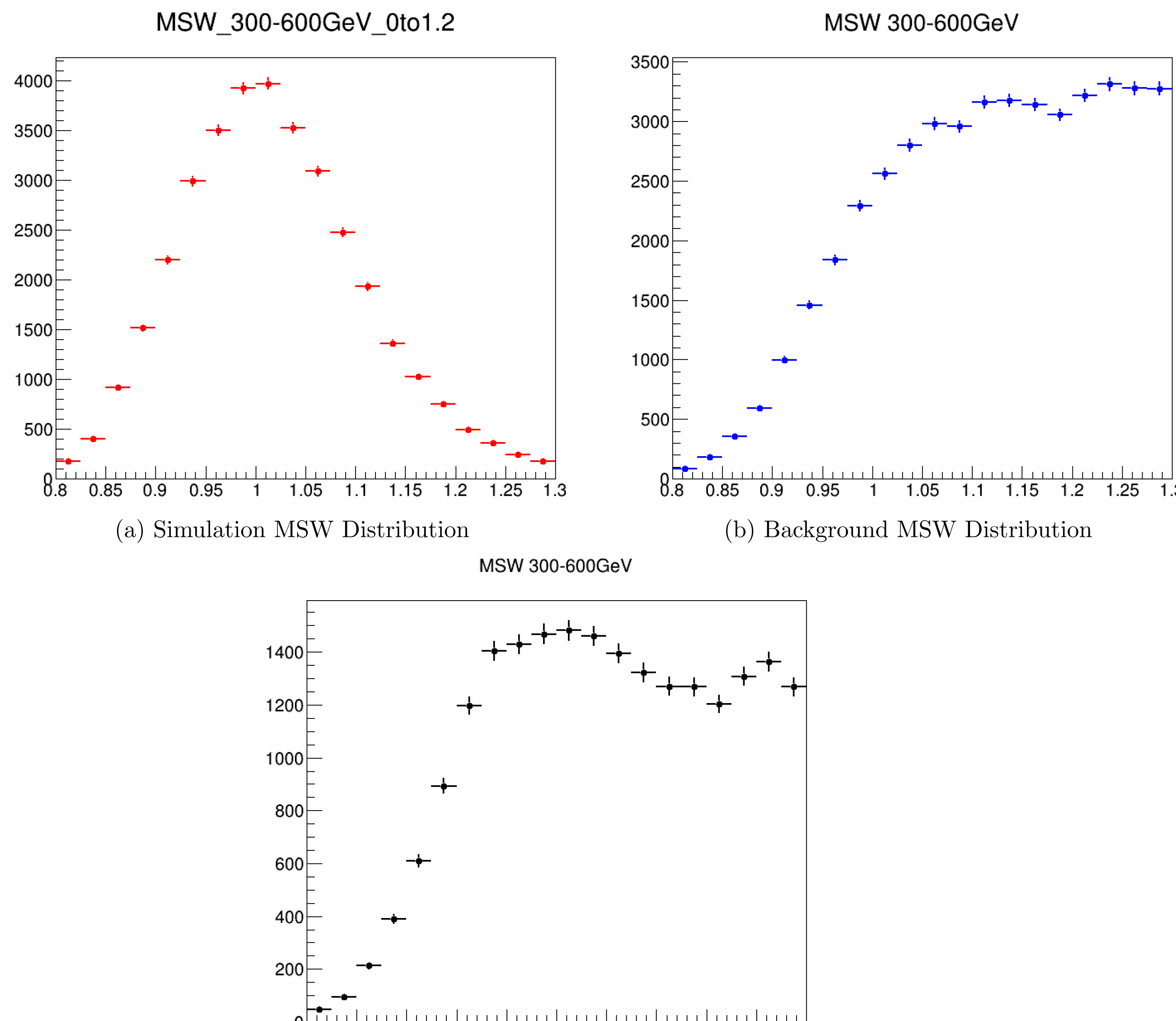


(a) Simulation MSW Distribution

(b) Background MSW Distribution

(c) Crab Data MSW Distribution

Figure 6.1: A sample of a MSW distributions, the two models and the data, for a single parameter likelihood fit performed in the inner camera (0.0-1.2 degrees) and in energy bin 300-600GeV.

Table 6.2: Test statistic (TS) of single parameter likelihood ratio tests on the MSW distribution of Segue1. The fit was performed for three different background models derived from source-free events and in four different energy bins. Zenith matching was done between 15 to 25 degrees zenith. The exposure ratio is the number of data events divided by the number of background events.

| **Energy (TeV)** | **Background** | **TS (0.0-1.2 deg)** | **TS (1.2-1.7 deg)** | **exposure ratio** |
|---|---|---|---|---|
| 0.3-0.6 | 1ES0229 | 6.1 | 2.63 | - |
| | 1ES0229/M87/1ES1218 | -1.10E-05 | 0.39 | - |
| | 1ES0229/M87/1ES1218/1ES1440 | 0.02E-02 | 0.13 | - |
| 0.6-1.0 | 1ES0229 | 1.89 | -2.74E-09 | - |
| | 11ES0229/M87/1ES1218 | 0.25 | -4.66E-10 | - |
| | 11ES0229/M87/1ES1218/1ES1440 | 0.57 | 0.13 | - |
| 1-2 | 1ES0229 | -4.12E-07 | -2.11E-06 | - |
| | 1ES0229/M87/1ES1218 | -2.49E-08 | -5.820E-11 | - |
| | 1ES0229/M87/1ES1218/1ES1440 | -1.57E-09 | 0.08 | - |
| 2-5 | 1ES0229 | 0.12 | -1.09E-07 | - |
| | 1ES0229/M87/1ES1218 | -5.10E07 | -1.37E-09 | - |
| | 1ES0229/M87/1ES1218/1ES1440 | 0.17 | -4.07E-10 | - |

The likelihood, with Barlow Beeston terms, was performed on the gamma-hadron separation parameter, MSW, of two blank field data sets observed in the V5 epoch. The first of the two blank field tests used M82 and 1ES0502 data to model the background signal of a dark matter target, Ursa Minor. Separate likelihood tests were performed for events from the inner camera (0.0-1.2 degrees) and the outer camera (1.2-1.7 degrees). To create a clean sample for the background model, events at point source and star positions were subtracted before creating the background MSW distributions. Table 6.1 shows the likelihood results. The second blank field test used four low flux active galactic nuclei sources, 1ES 0229+200, M87, 1ES 1218+304, and 1ES 1440+122, to model the background signal of a dark matter target, Segue1. Table 6.2 shows the likelihood results.

Both blank field tests return test statistic (TS) values << 9 in both the inner and outer camera, consistent with null results, as expected. Instances where TS values lie between 1 and 6 only occur where the background to data event ratio is less than 2:1; therefore, limited statistics of background compared to data can explain these values.

Table 6.3: Average noise of Galactic Plane versus Off Plane data sets. Source galactic longitude taken from http://simbad.u-strasbg.fr/simbad/.

| **Source** | **Average Noise** | **Galactic Longitude** |
|---|---|---|
| Crab | 4.94 | -05.78 |
| IC 443 | 5.01 | +03.24 |
| Gamma Cgyni | 5.42 | +02.27 |
| TeV J2032+4130 | 5.44 | +01.11 |
| Segue1 | 4.18 | +50.42 |
| Ursa Minor | 4.21 | +44.80 |
| 1ES 0229+200 | 4.41 | -36.61 |
| 1ES 1218+304 | 4.02 | +82.73 |

### 6.2.3 Fit Results Before and After Noise Padding

A series of LRTs, with Barlow Beeston terms, were performed on Crab data observed in the V5 epoch during winter atmosphere conditions. The Crab position in this data is located 0.5° offset from the camera center. For a bright source like the Crab, LRTs in the camera center (0.0-1.2 degrees) should favor the presence of source over a null result, even for the likelihood of a single parameter. The background models in the likelihood were derived from dark matter targets and faint blazar observations. Figure 6.1 shows one set of initial data and model MSW distributions to be passed to the binned likelihood.

Table 6.4 shows the results of the likelihood fit performed on the MSW distribution of Crab data. The likelihood results from the inner camera are consistent with a bright source of gamma-ray emission. In the outer camera, the results should indicate no significant gamma-ray emission and near zero TS. However, the TS results of the LRT on Crab data in the outer camera, while within acceptable limits, have values sufficiently larger than zero, which led to further investigation.

Since the Crab nebula is located in the galactic plane, the source field has many more stars than observations far off plane; therefore, a larger average night sky brightness. Consistently, observations in the galactic plane have a larger average night sky background compared to observation targets located far from the galactic plane, as shown in Table 6.3.

Table 6.4: Test statistic (TS) of single parameter likelihood ratio tests on the MSW distribution of the Crab. Underlined red text denotes likelihood performed with background that has been padded to match the average night sky background of the Crab. Zenith matching was done between 10 to 20 degrees zenith.

| **Energy (TeV)** | **Background** | **TS (0.0-1.2 deg)** | **TS (1.2-1.7 deg)** |
|---|---|---|---|
| 0.3-0.6 | Segue1 | 396 | 0.32 |
| | Segue1/M87/1ES1218/1ES1440 | 555 | 0.90 |
| | Segue1 | 429 | -2.52E-07 |
| | 1ES0229 | 436 | -3.50E-06 |
| | Segue1/1ES0229 | 535 | -2.60E-06 |
| 0.6-1.0 | Segue1 | 407 | -1.58E-06 |
| | Segue1/M87/1ES1218/1ES1440 | 564 | 1.57E-07 |
| | Segue1 | 520 | -1.83E-07 |
| | 1ES0229 | 479 | -2.40E-07 |
| | Segue1/1ES0229 | 847 | -1.00E-07 |
| 1-2 | Segue1 | 563 | 4.82E-06 |
| | Segue1/M87/1ES1218/1ES1440 | 708 | 0.69 |
| | Segue1 | 699 | 0.02 |
| | 1ES0229 | 448 | -8.80E-06 |
| | Segue1/1ES0229 | 724 | -1.20E-07 |
| 2-5 | Segue1 | 289 | 6.03 |
| | Segue1/M87/1ES1218/1ES1440 | 399 | 5.47 |
| | Segue1 | 380 | 0.66 |
| | 1ES0229 | 300 | -5.19E-06 |
| | Segue1/1ES0229 | 424 | -1.47E-07 |

The analysis software VEGAS has a tool for injecting artificial noise into event files in the early stages of data reduction. Sets of Segue1 and 1ES0229+200 data were padded with additional noise to match the average noise of the Crab data set. After running the single parameter likelihood fit on Crab data with a background model now derived from padded events, likelihood analysis in the outer camera returned consistently lower TS values. Based on these results came the policy to pad all background samples with artificial noise to match the average camera noise of data to be analyzed with the 4D-MLM.

### 6.3 Mitigation of Night-Sky Brightness Systematics with Padding

Fluctuations in the pixelated camera image arise primarily from electronic noise and optical night-sky background emission. Observations in the galactic plane have greater night-sky background than observations taken far off plane. When noise level is low most pixels will pass the threshold test performed in the image cleaning stage of data reduction and be included in the post-cleaning shower image. If the noise level is high the threshold for cleaning is also increased, increasing the probability that negative fluctuations will cancel genuine signal components. Therefore, differences between a background or OFF region and a source or ON region could introduce biases.

A software technique, known as software padding, was developed during the era of first generation IACTs to correct for these biases (Lessard et al., 2001). This technique is applicable in VEGAS at the image cleaning stage. Software padding adds artificial noise into events for the OFF or background sky regions.

For a particular pixel, $P_{on}P_{off}, \sigma_{on}\sigma_{off}$ are the ON(OFF) pedestal and pedestal deviation values. The signal component due to Cherenkov light and Cherenkov fluctuations are $C_{on}C_{off}, \sigma_{C_{on}}\sigma_{C_{off}}$. The noise component due to night-sky emission in a region is

$$N = \sigma Gauss(0:1), \tag{6.7}$$

where $Gauss(0:1)$ is a random number drawn from a Gaussian distribution of zero mean and unit variance. This quantity accounts for random fluctuations in background noise.

In the case where $N_{on}$ is larger than $N_{off}$ and to add artificial noise, $N_{add}$, such that

$$N_{on}^2 = N_{off}^2 + N_{add}^2 \tag{6.8}$$

the total OFF (background) signal, after adding artificial noise, is

$$OFF = P_{off} + \sigma_{off}Gauss(0:1) + C_{off} + \sigma_{C_{off}}Gauss(0:1). \tag{6.9}$$

# CHAPTER 7. TESTS OF THE 4D-MAXIMUM LIKELIHOOD APPROACH

This chapter details a series of studies performed on different VERITAS datasets to test the overall approach of the 4D-Maximum Likelihood Method (MLM). Independent validation studies on the VERITAS point spread function (PSF) and background model were performed and presented in previous chapters. Chapter 5 established a strategy for predicting the spatial distribution of photons in VERITAS observations. Previous studies performed in Chapter 6 established a strategy for modeling background emission in the VERITAS field of view (FoV). In the current 4D-MLM, the PSF is modeled with a symmetric King function. Likelihood analyses performed only on the mean scaled width (MSW) distribution found good prediction of the background level when a background sample is selected with zenith and azimuth similar to the source parameters and padded to a similar night sky background level.

Likelihood analyses on VERITAS data were performed with a complete source model and a model of background rates. The gamma-ray emission is dispersed in a 2D-plane and was modeled with instrument response functions (IRFs): effective area, energy resolution, and PSF. The background model is binned in energy and camera offset. In order to effectively scale the background separately from the gamma-ray emission, events were binned between two event classes, gamma-ray dominated and hadronic-dominated. Gamma-ray emission peaks at MSW=1, therefore one event class is $0.8 < MSW < 1.1$. Hadronic emission increases above MSW=1.1, therefore the second event class is $1.1 < MSW < 1.3$. All data events and IRFs are binned in two bins of MSW, therefore this parameter is the fourth dimension of the 3D-MLM. The two MSW bins still share the same scale factor in order that the background level in the gamma-ray dominated event class benefits from the scaling of the hadronic dominated event class.

All IRFs and data files, separated by event class, are analyzed through the framework of Gammapy, a Python software developed for gamma-ray analysis, including current and next generation IACTs. Gammapy performs likelihood fits in set bins of energy. Therefore, it is appropriate to call the 3D-MLM (spatial+MSW) applied in Gammapy a four-dimensional MLM (spatial+energy+MSW). The following performance studies support whether or not the use of two event classes is adequate to scale the background level and further validate the PSF and background modeling strategy. This chapter concludes with discussion on further improvements to the overall model, raised both by the results in this chapter and previous chapters.

The initial 4D-MLM data analysis in this chapter focuses on a bright point source, the Crab Nebula. Another analysis on a source free field of view (FoV), Ursa Minor, was performed with a search for significant gamma-ray emission when a null result is expected. All observations reduced to Gammapy datasets already went through a VERITAS data reduction which applied the Image Template Method (ITM) for event reconstruction. For crosscheck on the Crab results, a standard analyses was performed on the same data and is also presented in this chapter.

These studies were limited to the following observing criteria:

- **Observations during the V5 epoch (September 2009 through July 2012)**
- **Events reconstructed with 3 or 4 telescopes**
- **All four telescopes operational**

## 7.1 Implementation with Gammapy

The 4D-MLM has been implemented with Gammapy[1], an open-source Python package for gamma-ray astronomy analysis. Gammapy is the official data analysis software for the Cherenkov Telescope Array (CTA) and is also compatible with other Imaging Atmospheric Cherenkov Telescopes (IACTs), Water Cherenkov telescopes, and space based gamma-ray instruments, such as the *Fermi*-Large Area Telescope (Deil and et al., 2017; Nigro and et al., 2019).

[1] Version 0.19

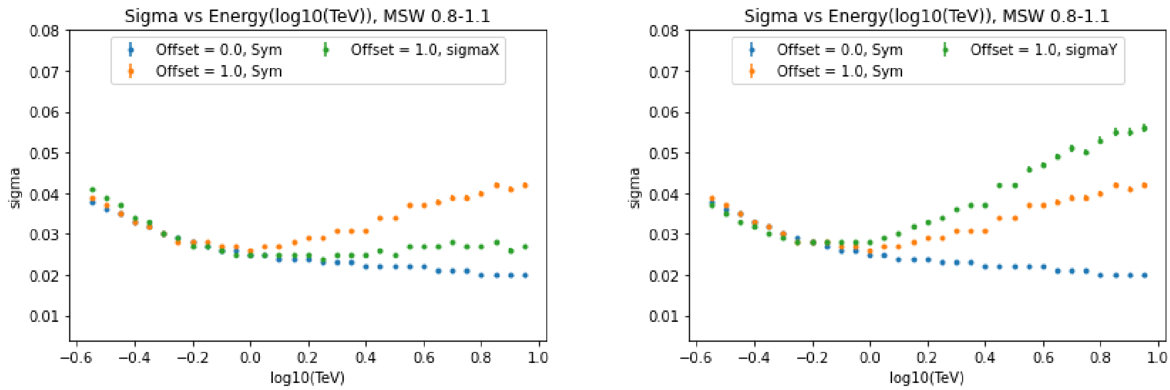


(a) $\sigma$ and $\sigma_x$ vs energy

(b) $\sigma$ and $\sigma_y$ vs energy

Figure 7.1: Symmetric king function parameter $\sigma$ and asymmetric parameters $\sigma_x$ and $\sigma_y$ versus energy, derived from simulations at 20° zenith.

Gammapy supports modeling a binned dataset using Poisson maximum likelihood fitting. Multiple datasets can be combined to perform a joint-likelihood analysis. This section covers the development and implementation of the likelihood performed with the gamma-hadron separation parameter, MSW, in Gammapy.

### 7.1.1 Point Spread Function Model Implementation

The initial tests of PSF parameterization were performed with Gammapy's symmetric King function:

$$PSF(r,\sigma,\lambda) = \frac{1}{2\pi\sigma^2}\left(1-\frac{1}{\lambda}\right)\left[1+\frac{1}{2\lambda}\cdot\left(\frac{r^2}{\sigma^2}\right)\right]^{-\lambda}. \tag{7.1}$$

Each data fits file compatible with Gammapy contains a PSF format with $\sigma$ and $\lambda$ parameters derived from simulations and matched to the average noise and average zenith of the data. Examples of the PSF containment is shown in Figures 7.2 and 7.1. Changes to the calculations of the containment in Gammapy are explained in Appendix B.

Attempts were made to add a class and functions in Gammapy to support the asymmetric format. However, an asymmetric format requires more than one camera dimension in the PSF kernel and the current memory capabilities of Gammapy cannot manage multiple PSF

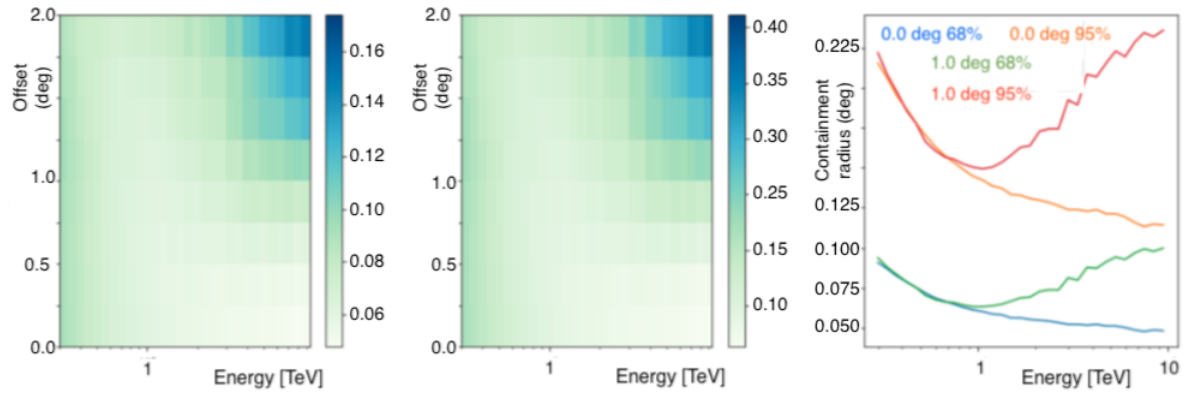


Figure 7.2: The containment radius calculated with Gammapy functions and the symmetric King function parameters. *Left*: 68% containment radius. *Center*: 95% containment radius. *Right*: 68% containment radius and 95% containment radius at 0.0° and 1.0° offset, plotted versus energy.

dimensions. Future work will develop an asymmetric PSF kernel outside Gammapy for later import to work around this issue.

### 7.1.2 Background Model Implementation

In Gammapy, the background estimate depends on a given model of the background rate, as a function of energy and camera offset and a scale factor for the entire field of view. The background scale factor is a free parameter in the likelihood.

The Gammapy template background model is formatted in each each data fits file to store the background rate per solid angle, $s^{-1}MeV^{-1}sr^{-1}$, as a function of reconstructed energy and offset angle from the FoV center. Observations of source-free regions, off the galactic plane, are passed to a python multi-step algorithm which calculates the differential background rate. The class that performs the background rate computation, BackgroundModelEstimator, is provided through the Gammapy package. Circular regions with radius 0.3° centered on the positions of bright stars are also subtracted from runs selected for background. Figure 7.3 shows a resulting two-dimensional radially symmetric background template in bins of energy and offset, **Background2D**.

Before the data is passed to the algorithms, background runs have been padded to match the average noise level between background observations and observations taken on a source of interest. Background has also been selected to match the same observing season (2009-2010, 2010-2011, or 2011-2012) and similar azimuth ($90° < \phi < 270°$ or $270° < \phi < 359°$, $0° < \phi < 90°$). Background events are also separated in bins of zenith. Determination of the differential background rate, in each bin of reconstructed energy and offset, is calculated by counts divided by exposure. Exposure in this case is observing time, after taking into account the respective energy bin width and solid angle. The models are then written out to Header/Data Units (HDU) tables and data fits files with similar observation parameters. In the likelihood analysis in this work performed with Gammapy the binning in reconstructed energy matches the energy binning of the likelihood overall. In general, the exposure of observation runs used to derive a background model is at least twice the exposure for each dataset. In addition, any combination of offset and energy bins in the background model must contain a nonzero background rate value.

In Gammapy, a python class called FoVBackgroundModel contains the correction parameter or scale factor applied to the input template background model and outputs the FoV background model. The likelihood fits the background model correction parameter according to defined regions in the datasets. The default background energy spectrum of FoVBackgroundModel is a single power-law with the same correction factor across all energies. The correction parameter reported by the likelihood is applied across the entire FoV and makes possible the calculation of the number of background events to gamma-ray events.

For the purposes of the 4D-MLM, there is a dataset for each event class defined by MSW, $0.8 < MSW < 1.1$ and $1.1 < MSW < 1.3$. Therefore, a different background template is created for each event class. Each pair of event classes has a shared FoVBackgroundModel and scale factor. This is done in order to utilize the normalization of the event class dominated by background events, $1.1 < MSW < 1.3$, to constrain the background component of the gamma-ray dominated event class, $0.8 < MSW < 1.1$.

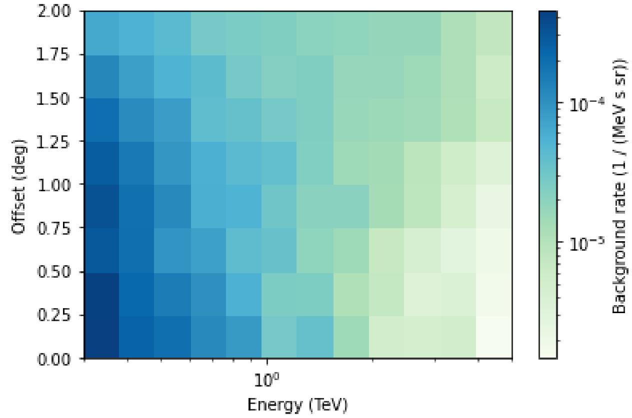


Figure 7.3: Rate versus energy and offset, binned in 12 bins of energy and eight bins of offset, and produced from source-subtracted Crab V5 runs.

### 7.1.3 Gammapy Joint Likelihood

Gammapy datasets consist of a set of reduced data, IRFs, and models (spatial, spectral, and background), which are used to perform a likelihood analysis. The 4D-MLM depends on additional binning based on the gamma-hadron separation parameter MSW in order to constrain the background normalization. Since MSW is not a dimension internal to Gammapy, a user applied binning is required. A separate dataset is required to adequately scale the level of background emission, using events dominated by hadronic emission (MSW > 1.1). In all joint-likelihood analyses performed in this work there are separate Gammapy datasets for each range of MSW, $0.8 < MSW < 1.1$ and $1.1 < MSW < 1.3$. There are also separate datasets for conditions where the background normalization is expected to be different, such as between different wobble pointings, zeniths, and observing seasons.

A single dataset with a complete field model consists of one spatial model, one spectral model, and a scaled FoV background model. There are eight parameters in a spatial+powerlaw model of each dataset, three of which are always free parameters: spectral index ($\Gamma$), spectral amplitude ($F_0$), and background normalization. The background normalization parameter is shared across each pair of datasets which have been divided between $0.8 < MSW < 1.1$ and $1.1 < MSW < 1.3$. Initially, the source coordinates (right ascension and declination) are set also free parameters. In case where fits do not converge the spatial parameters are fixed at either a known source position or the position of maximum significance reported from a standard analysis.

## 7.2 Point Source Analysis with Gammapy

The Crab Nebula is the brightest steady source visible by IACTs. Therefore, this source is used to validate simulations, calibrate instruments, and test the performance of new analysis methods. The Crab provides a good opportunity to assess the 4D-MLM implementation through Gammapy, even with just a few hours of Crab exposure.

The point source analysis selected $\sim 8.16$ hours of Crab data processed with ITM, taken at four cardinal pointings, a narrow zenith range (10-20 degrees), and one observing season (2010-2011). Two sets of background IRFs were created, one derived from combined 1ES 0229+200 and Segue1 runs, padded to match the noise level of the Crab fields. The second background IRF was derived from source subtracted Crab runs. In both cases events regions around bright star positions were subtracted before the creation of the background models. The background IRFs were also confined to zenith range 10-20 degrees and the 2010-2011 observing season. These selections were performed to control background systematics. The reasonable assumption was made that the background normalization does not appreciably change between different nights in the same observing season. Two Crab analyses were done on all $\sim 8.16$ hours of Crab data, one with the Crab derived background rates and one with the 1ES 0229+200 and Segue1 derived background rates.

Each joint-analysis performed on Crab data divided the events between two datasets in two different ranges of MSW: $0.8 < MSW < 1.1$ and $1.1 < MSW < 1.3$. Datasets were further divided between the four different wobble pointings, north, south, east, and west, creating a total of eight datasets. The full model for the fit includes one point source spatial model, one power-law spectral model, and eight scaled FoV background models. During initial runs of the likelihood the Crab position converged on the following position: right ascension=83.635($\pm$0.001) and declination=22.004($\pm$0.001). In subsequent analyses on the Crab the position was fixed at

Table 7.1: Table of Crab spectral parameters. The left hand columns are from analysis done with Crab derived background. The right hand columns are from analysis done with Segue1 and 1ES0229+200 derived background.

| **Dataset** | **Index** | **Flux** $\times 10^{-10}$ $\text{TeV}^{-1}\text{s}^{-1}\text{cm}^{-2}$ | Index | **Flux** $\times 10^{-10}$ $\text{TeV}^{-1}\text{s}^{-1}\text{cm}^{-2}$ |
|---|---|---|---|---|
| Joint dataset | 2.60±0.03 | 1.02(±0.02) | 2.60±0.03 | 1.01(±0.02) |
| Joint $0.8 < MSW < 1.1$ | 2.62±0.03 | 0.99(±0.02) | 2.62±0.03 | 0.98(±0.02) |
| Joint N dataset | 2.56±0.06 | 1.09(±0.04) | 2.56±0.06 | 1.08(±0.04) |
| Joint S dataset | 2.62±0.06 | 0.96(±0.04) | 2.62±0.06 | 0.95(±0.04) |
| Joint E dataset | 2.65±0.06 | 1.10(±0.04) | 2.64±0.06 | 1.09(±0.04) |
| Joint W dataset | 2.57±0.06 | 0.96(±0.03) | 2.57±0.06 | 0.95(±0.03) |
| VEGAS RR analysis | 2.51±0.03 | 0.87(±0.02) | - | - |

these values. Since the total Crab exposure is less than 10 hours the flux normalization energy was selected and frozen at a flux level populated with more events, 0.7 TeV. Overall, a typical Crab joint-likelihood analysis consisted of six free parameters.

Gammapy's minimizer for finding the best-fit model parameters to data is *iminuit*[2]. In order to achieve convergence and avoid the minimizer becoming stuck near 0 or infinity, limits were set on the spectral index (min=1.0, max=5.0) and background normalization (min=0.1, max=10.0). The fit on $\sim 8.16$ hours of Crab datasets also kept the source position free within a few tenths of a degree from initial position inputs (R.A=83.633, Dec=22.015).

The best fit spectral parameters were found to be, for data with background derived from Crab runs, $\Gamma = 2.601(\pm 0.029)$ and $F_0 = 1.024(\pm 0.018) \times 10^{-10}\text{TeV}^{-1}\text{cm}^{-2}\text{s}^{-1}$, evaluated at $E_0 = 0.7$ TeV. For Crab data with background derived from 1ES 0229+200 and Segue1 the post-fit spectral parameters are $\Gamma = 2.597(\pm 0.030)$ and $F_0 = 1.008(\pm 0.018) \times 10^{-10}\text{TeV}^{-1}\text{cm}^{-2}\text{s}^{-1}$, evaluated at $E_0 = 0.7$ TeV. The Crab power-law spectrum, binned in 12 bins of energy, is shown in Figure 7.4. Both 4D-MLM Crab spectrum are consistent within the errors, which demonstrates that both background inputs, from the same fields or different fields, are appropriate starting models for the likelihood. The spectral results also demonstrate that the usage of event classes

[2]Version 1.5.4

provides a good approximate of background levels of emission. All post-fits spectral flux and test statistic (TS) values are presented in Table 7.2.

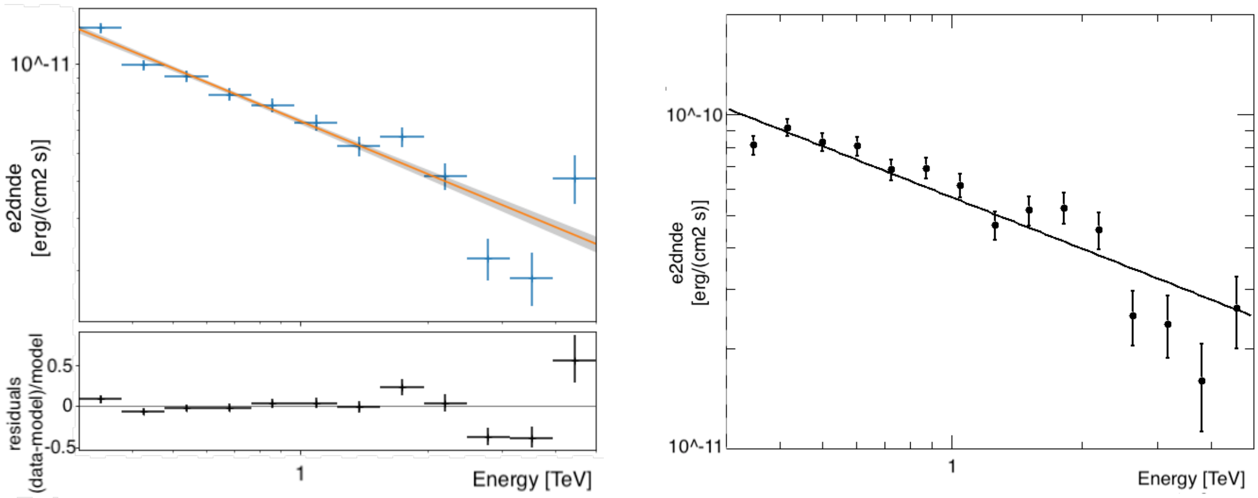


(a) Gammapy Crab

(b) VEGAS Crab

Figure 7.4: Best fit spectrum for $\sim$ 8.16 hours of Crab V5 data observed in 2010-2011, modeled with a point source at the Crab position. Left: The best fit power-law model, flux points, and residuals after analysis with Gammapy. Right: Flux points and best fit power-law model after analysis with VEGAS.

A complete Crab analysis provides an opportunity to assess the implementation of the 4D-MLM through Gammapy. How well the source and background model setup matches the Crab data field, after the likelihood fit converged, is assessed through 2D and 1D residuals. Before creating residual maps, datasets that makeup the joint dataset are stacked together. Residual plots which show the $\sqrt{TS}$ and percent difference between models and data, Figures 7.5 and 7.7 b), reveal that the post-fit models account for a substantial portion of the Crab emission. The largest discrepancy between data and the full model is in the lowest energy bin, 0.30-0.379, as shown in Figure 7.6.

Figure 7.8 contains residual plots of individual datasets which show that certain over and under-subtraction patterns change appearance, correlated with the different wobble pointings and two MSW ranges. For the $0.8 < MSW < 1.1$ datasets there are pairs of under and over-subtraction features, adjacent to one another and overlapping the Crab position, in the same

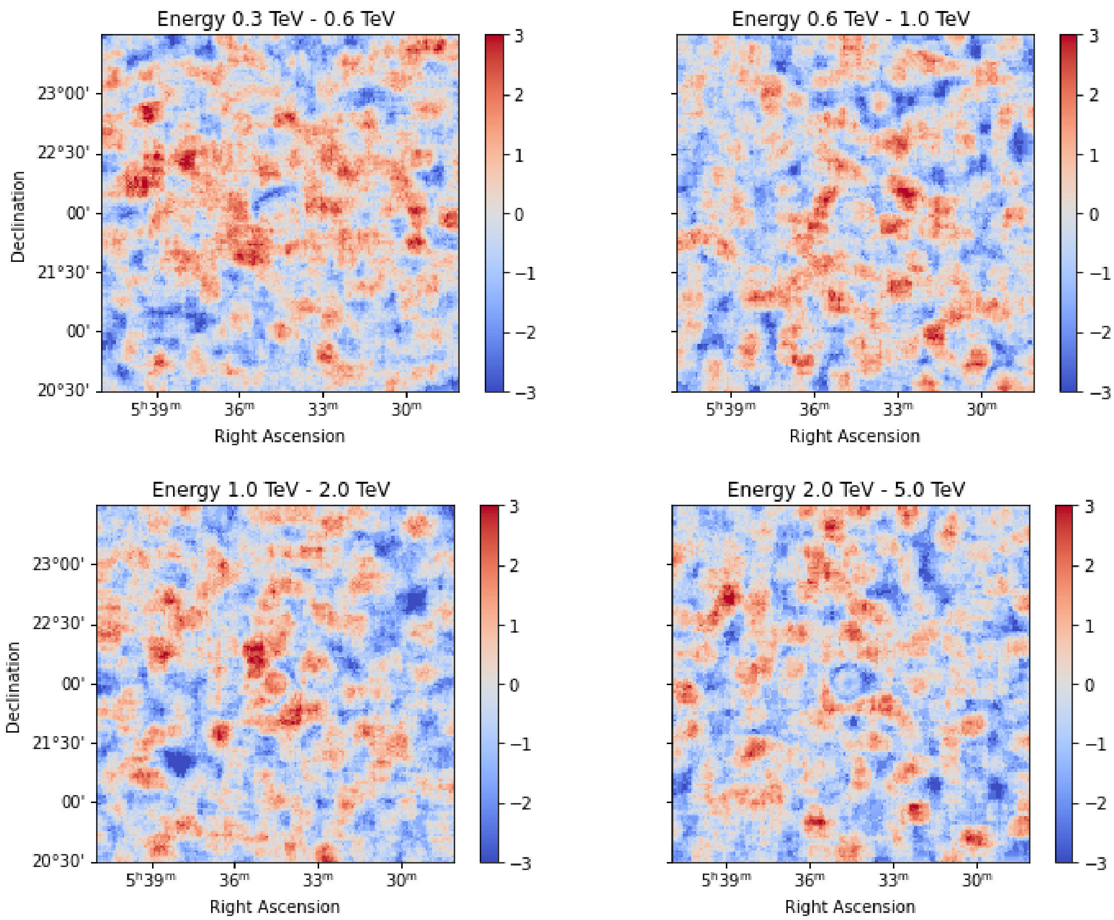


Figure 7.5: Two-dimensional residual $\sqrt{TS}$ maps of a joint-likelihood point source analysis of Crab data separated in four bins of energy.

map, as shown in Figure 7.9. The orientation of the features are sensitive to the wobble direction, indicating there may be imperfect pointing offset calibrations. For the $1.1 < MSW < 1.3$ datasets, the same pair of features is present, as shown in Figure 7.10, but is much reduced due to the Crab's low flux in this event class. These features are negligible in the residual $\sqrt{TS}$ maps and percent difference maps. When a joint-likelihood analysis is performed on two event classes in only a single wobble offset, either north, south, east, or west, the bipolar feature vanishes. There are no other obvious features in the residual maps, nor any features which could point to an inconsistency in the PSF modeling and the position of the Crab, located 0.5° from the camera center.

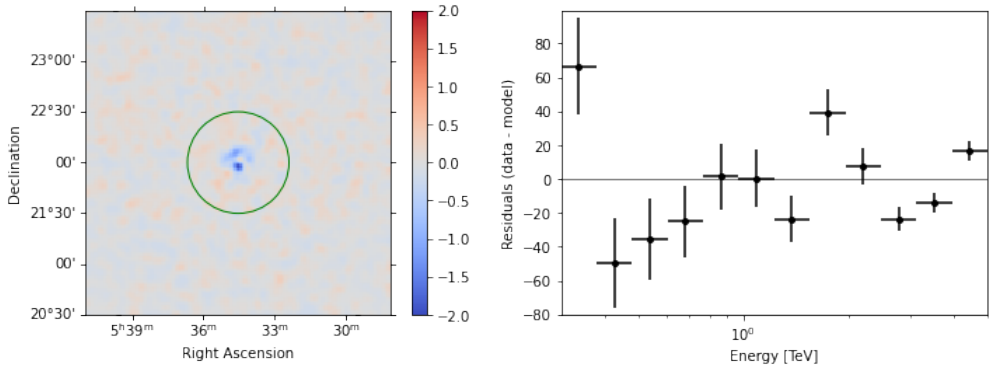


(c) $0.8 < MSW < 1.1$

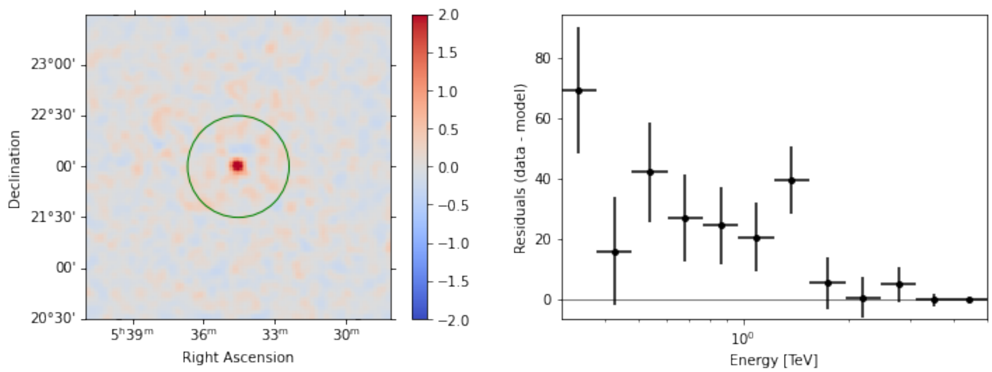


(c) $1.1 < MSW < 1.3$

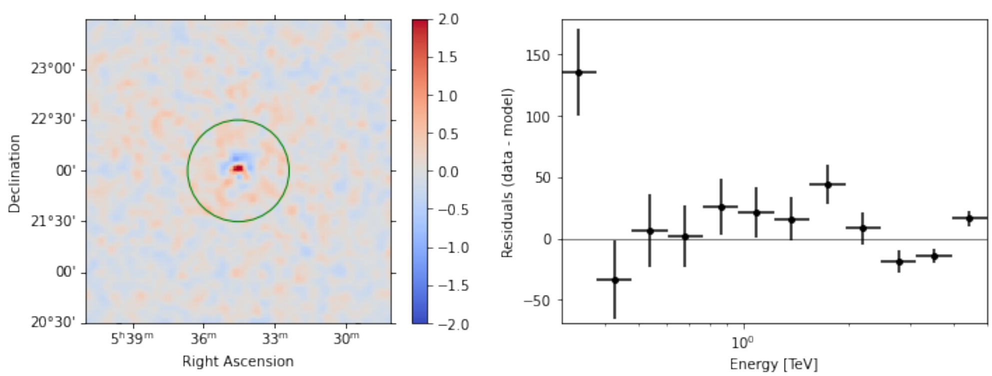


(c) Data-Model, all datasets

Figure 7.6: Two-dimensional residual maps created by subtracting model counts from data and smoothing with a 0.035° radius gaussian kernel. The top and middle row shows the 2D residual map and 1D versus energy residual for the stacked datasets for each event class separately. The bottom plot shows all datasets stacked. The 1D versus energy residual counts are calculated from a 0.5° radius circle centered on the Crab position.

Table 7.2: Table of flux points for ∼8.16 hours of Crab V5 data, processed with Gammapy, in 12 bins of energy, and employing a background IRF derived from Segue1 and 1ES0229+200 subtracted background.

| $E_{min}$ **[TeV]** | $E_{max}$ **[TeV]** | **Flux** $\mathrm{TeV^{-1}s^{-1}cm^{-2}}$ | **Flux** [error] $\mathrm{TeV^{-1}s^{-1}cm^{-2}}$ | $\sqrt{TS}$ |
|---|---|---|---|---|
| 0.30 | 0.379 | $6.71^{-10}$ | $2.96^{-11}$ | 53.3 |
| 0.379 | 0.479 | $3.65^{-10}$ | $1.39^{-12}$ | 56.3 |
| 0.479 | 0.606 | $1.99^{-10}$ | $8.49^{-12}$ | 55.6 |
| 0.606 | 0.766 | $1.08^{-10}$ | $5.19^{-13}$ | 51.0 |
| 0.766 | 0.969 | $5.88^{-11}$ | $3.24^{-13}$ | 48.1 |
| 0.969 | 1.548 | $3.20^{-11}$ | $2.00^{-12}$ | 42.8 |
| 1.225 | 1.225 | $1.74^{-11}$ | $1.28^{-12}$ | 34.1 |
| 1.548 | 1.957 | $9.46^{-12}$ | $9.22^{-13}$ | 32.3 |
| 1.957 | 2.475 | $5.15^{-12}$ | $5.41^{-13}$ | 25.8 |
| 2.475 | 3.128 | $2.80^{-12}$ | $2.83^{-13}$ | 15.1 |
| 3.128 | 3.955 | $1.52^{-12}$ | $1.96^{-13}$ | 12.5 |
| 3.955 | 5.0 | $8.28^{-13}$ | $2.41^{-13}$ | 16.0 |

Table 7.3: Table of the first flux points for ∼8.16 hours of Crab V5 data, analyzed with the 4D-MLM and analyzed with reflected region analysis.

| $E_{RR}$ **[TeV]** | $E_{MLM}$ **[TeV]** | $Flux_{MLM}$ $\mathrm{TeV^{-1}s^{-1}cm^{-2}}$ | $Flux_{MLM}$ [error] $\mathrm{TeV^{-1}s^{-1}cm^{-2}}$ | $Flux_{RR}$ $\mathrm{TeV^{-1}s^{-1}cm^{-2}}$ | $Flux_{RR}$ [error] $\mathrm{TeV^{-1}s^{-1}cm^{-2}}$ |
|---|---|---|---|---|---|
| 0.337 | 0.347 | $6.71^{-10}$ | $2.96^{-11}$ | $4.22^{-10}$ | $2.79^{-11}$ |
| 0.426 | 0.417 | $3.65^{-10}$ | $1.39^{-12}$ | $3.30^{-10}$ | $1.99^{-11}$ |

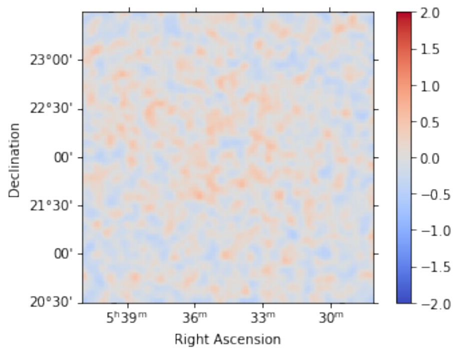


(a) (Data-Model)/$\sqrt{Model}$

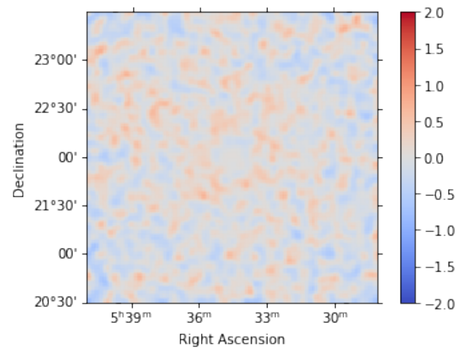


(b) (Data-Model)/Model

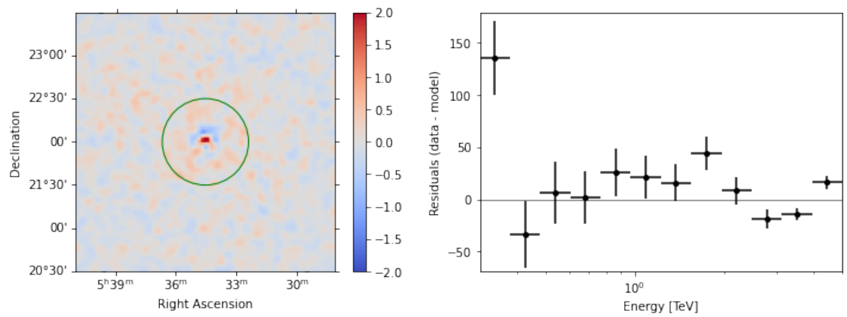


(c) Data-Model

Figure 7.7: Two-dimensional residual maps, smoothed with a 0.035° radius gaussian kernel. The top right plot is percent deviation from model. The bottom plots are residuals, (data-model), subtracted from a 0.5° radius circular region centered on the Crab position.

## 7.3 Comparisons to RBM and RR Analysis

The Crab is a source that has undergone intense study with standard analysis techniques such as the ring background method (RBM) and reflected region (RR), methods detailed in Section 3.4.3. Any new analysis strategies performed on point sources should be consistent with standard analysis in order to prove reliability of the new technique. An RBM analysis and an RR analysis were performed on the same $\sim 8.16$ hours Crab data, covering the same energy range, 300 GeV to 5 TeV and processed with ITM. In order to optimize the gamma-ray signal, the following cuts on telescope parameters were performed: MSW [0.8,1.1], MSL [0.05,1.3], and shower max height [7,100]. The 4D-MLM analysis has two bins of MSW values, $0.8 < MSW < 1.1$ and

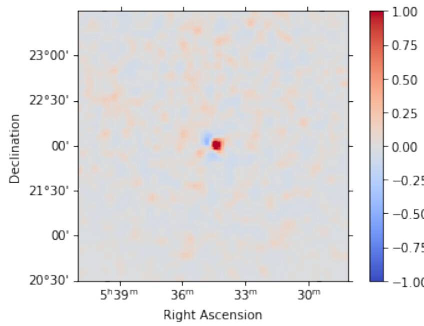


(a) North wobble, in joint likelihood

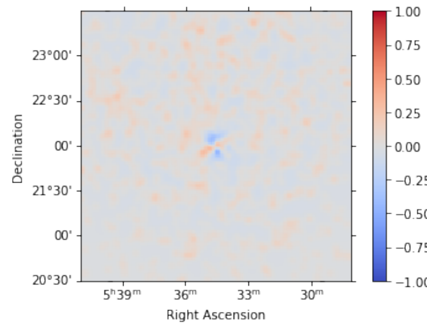


(b) North wobble only

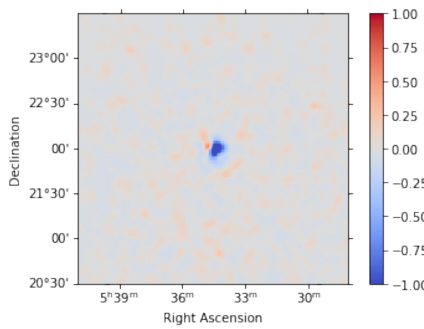


(a) South wobble, in joint likelihood

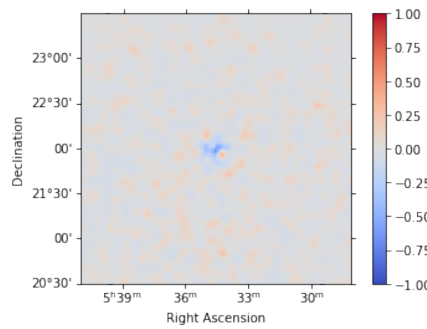


(b) South wobble, only

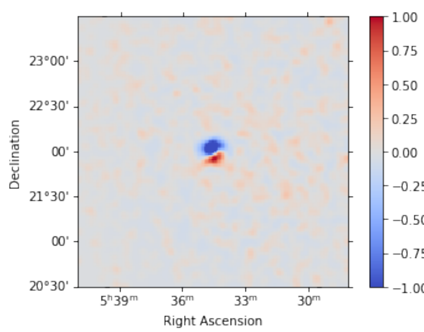


(a) West wobble, in joint likelihood

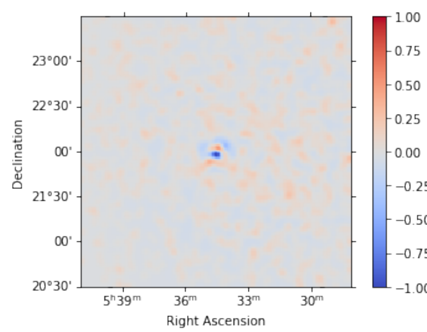


(b) West wobble, only

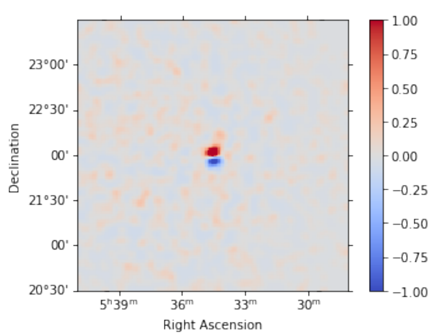


(a) East wobble, in joint likelihood

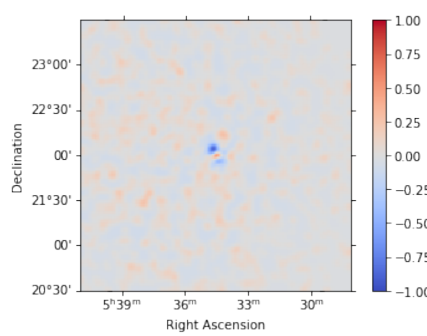


(b) East wobble, only

Figure 7.8: Data-model maps of separate Crab datasets, in the $0.8 < MSW < 1.1$ event class, after a joint-likelihood. These maps have been smoothed with a $0.035°$ radius gaussian kernel.

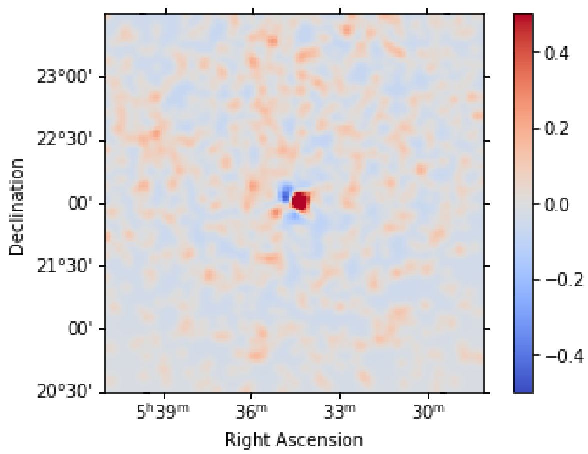


(a) North wobble

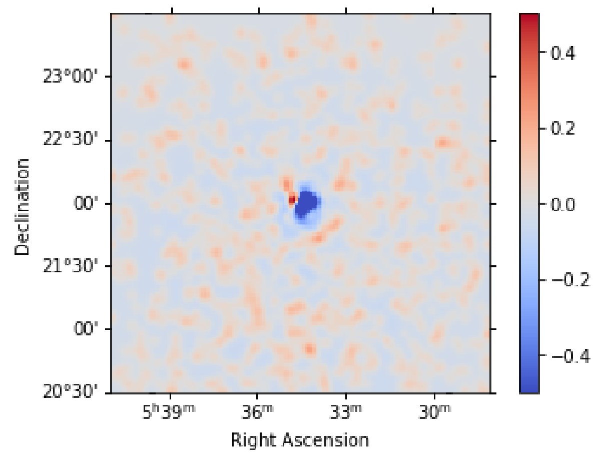


(b) South wobble

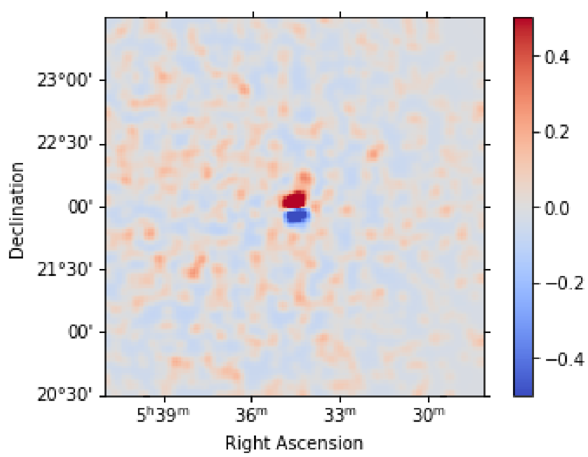


(c) East wobble

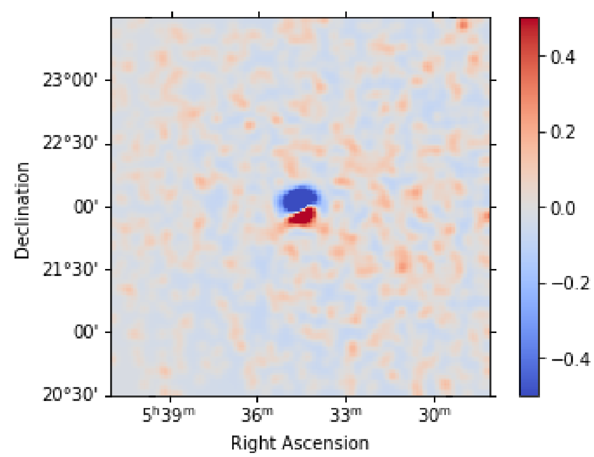


(d) West wobble

Figure 7.9: Data-model maps of $0.8 < MSW < 1.1$ Crab datasets. These maps have been smoothed with a 0.035° radius gaussian kernel. The scale has been set small to exaggerate the effect and show it is visible in both event classes.

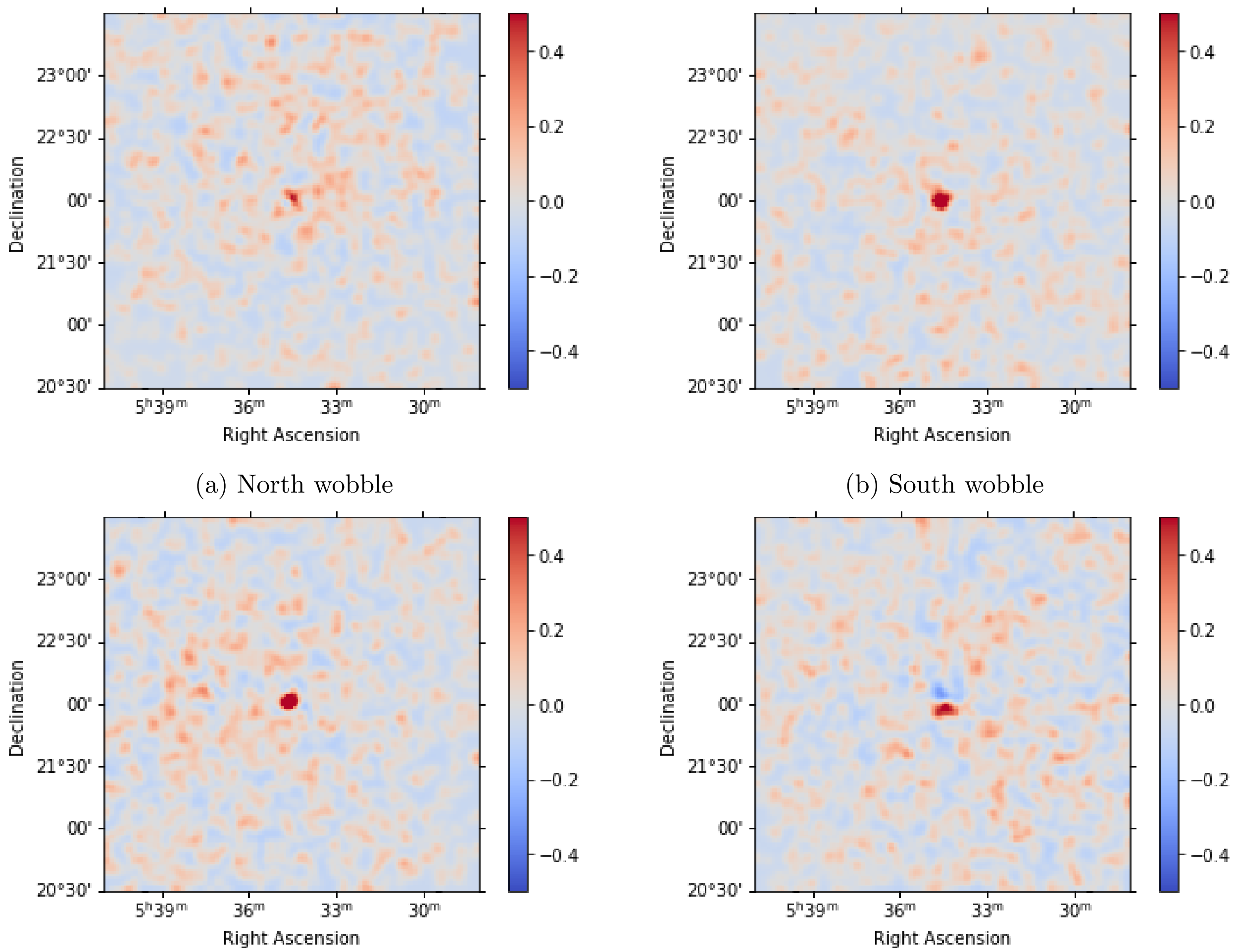


(a) North wobble

(b) South wobble

(c) East wobble

(d) West wobble

Figure 7.10: Data-model maps of $1.1 < MSW < 1.3$ Crab datasets. These maps have been smoothed with a 0.035° radius gaussian kernel. The scale has been set small to exaggerate the effect and show it is visible in both event classes.

$1.1 < MSW < 1.3$, where the second bin allowing events with $MSW > 1.1$ is included to better characterization the background signal.

The significance values (RBM) and best fit spectral parameters (RR) of VEGAS analysis are $\sigma$=104, $\Gamma = 2.51(\pm 0.03)$, and $F_{0.7} = 0.87(\pm 0.02) \times 10^{-10}\mathrm{TeV}^{-1}\mathrm{cm}^{-2}\mathrm{s}^{-1}$, evaluated at $E = 0.7$ TeV. The best fit spectral parameters of a 4D-MLM analysis, performed with only the four $0.8 < MSW < 1.1$ datasets, are $\Gamma = 2.62(\pm 0.03)$ , and $F_{0.7} = 0.99(\pm 0.02) \times 10^{-10}\mathrm{TeV}^{-1}\mathrm{cm}^{-2}\mathrm{s}^{-1}$, evaluated at $E = 0.7$ TeV. The indices do not agree within errors and are different by about $4\sigma$. The VEGAS RR flux normalization is different from the flux normalization returned by the joint-likelihood by $\sim 12.1\%$. Both Crab power-law spectrum are shown in Figure 7.4. A table of VEGAS RR spectral parameters, alongside the spectral parameters returned from analyses performed with Gammapy, are shown in Table 7.1. A table of the Gammapy spectral bins for the full joint-dataset is shown in Table 7.2.

Inconsistencies between the flux normalization values are worth further discussion. The VEGAS RR analysis uses effective areas optimized to search for point sources. These particular effective areas are derived from simulations which assume that the 68 containment radius of a point source is $\Theta \sim 0.07°$. Since the likelihood performed in Gammapy models the entire FoV, the effective area table, converted to a V2DL3 format readable by Gammapy, was derived from effective areas not optimized for point sources. They were optimized for extended source analysis with no cut on $\Theta$ and an upper cut on the field of view of 2.0°. Differences between the two effective areas and energy biases can lead to a difference in spectral flux and index. In addition, the Gammapy effective area tables were generated with an FoV upper cut of 2.0° whereas no cut on the FoV was applied to the Crab data files. Since the Crab is offset only 0.5° from the camera center it is expected that a mismatch between cuts on the FoV will have a minimal impact on the number of gamma-ray events near the Crab position.

There are differences between the point source effective areas used in the standard analysis versus the extended source effective areas written out to the data file format used by Gammapy. A comparison between two different effective areas is shown in Figure 4.1 b). Effective areas without a cut on $\Theta$ will include the tail of the point source PSF, where effective areas with $\Theta \sim 0.07^\circ$ will only include core emission. Therefore, impact on the flux and index of the spectrum is reasonable to expect. Nonuniform differences across all energy bins will also impact the source spectral index. The effective areas in Figure 4.1 b) show both features. Near $\sim 300$ GeV the sensitivity of the $\Theta \sim 0.07^\circ$ effective decreases compared to the rest of the energy range which impacts the spectral index of the overall spectrum. Figure 7.4 and Table 7.3 shows the different between likelihood and RR flux in the lowest energy bins. As shown in Figure 7.7, the data-model residuals of the Crab likelihood disagree most at the lowest energy bins, which will impact the overall spectral index. All of these features are likely contributing to the discrepancy between the flux normalization and index values of the RR analysis and likelihood Crab analysis.

Table 7.4: Table of right ascension and declination after performing joint likelihood fit on Crab data. The right-most column is the separation between the each individual wobble dataset position and the Crab position reported in NASA's High Energy Astrophysics Science Archive Research Center (RA:83.633, 22.015). The middle column is the separation between each individual wobble dataset position and the joint likelihood post-fit position (RA:83.635, 22.004).

| **Wobble** | R.A. (J2000) | Dec[°] (J2000) | separation(deg) | separation(deg) |
|---|---|---|---|---|
| West | 83.633(±0.002) | 21.993(±0.001) | 0.011° | 0.022° |
| East | 83.636(±0.002) | 22.013(±0.002) | 0.009° | 0.003° |
| North | 83.630(±0.002) | 22.005(±0.002) | 0.005° | 0.010° |
| South | 83.643(±0.002) | 22.006(±0.002) | 0.008° | 0.013° |

## 7.4 Blank Field Study with Gammapy

The greatest concern in the development of the 4D-MLM is false detection of emission. If the likelihood fit reports significant emission for a dataset which contains no known gamma-ray source there are likely issues with the background model. In Cardenzana (2017), a series of tests were performed on blank fields modeled with uniform disk templates. The blank field studies in Cardenzana (2017) reported no significant emission when the background was derived from the same field, but reported false positives when the background was derived from separate fields taken from dark matter targets and low-flux blazars.

In order to evaluate the performance of the 4D-MLM in Gammapy a series of analyses were performed on a set of Ursa Minor data. A background IRF was derived from Ursa Minor data and a separate background IRF was derived from M82 data. Emission in the Ursa Minor datasets was only modeled with background models. A separate 4D-MLM analysis was performed for each different background IRF. When the background models fit well to the data the resulting residuals, either excess maps or significance maps, will show no significant spatial features across all energy bins.

### 7.4.1 Ursa Minor

About 15.2 hours of Ursa Minor data were divided between two datasets for the two event classes, $0.8 < MSW < 1.1$ and $1.1 < MSW < 1.3$, and four datasets for north, south, east, and west wobble directions. About 24.3 hours of Ursa Minor data, after removal of events located within 0.3 degrees of a bright star, were used to create a background IRF for the Ursa Minor analysis. About hours of M82 data, after removal of events within 0.3° of a bright star and M82 itself, were used to create a separate background IRF for the Ursa Minor analysis. All Ursa Minor and M82 runs have average zenith between 35° to 40°.

Joint-likelihood analyses, performed from 300 GeV to 5 TeV, were carried out for each different background IRF. Each of the eight datasets in the joint-likelihood was modeled only with spatial background models. The normalization parameter for each corresponding dataset corresponding to a different telescope pointing was shared between the datasets separated by MSW.

The goodness-of-fit of post-likelihood fit models was determined by reviewing data-model residual maps and $\sqrt{TS}$ residuals, both for separate datasets, shown in Figures 7.14, 7.15, 7.16, and 7.17 and combined datasets, shown in Figures 7.11 and 7.13. The plots in these figures show the residuals from a likelihood performed with the Ursa Minor derived background IRFs and a separate likelihood performed with the M82 derived background IRFs. The residual excess maps show that above $\sim$500 GeV data and model are consistently within $1\sigma$ error bars. In $\sqrt{TS}$ residuals above 500 GeV, the fluctuations are homogeneous and at the level of $\pm 3\sigma$.

Between 300 and $\sim$500 GeV, the post-fit models underestimate the data, both for the analysis performed with a background IRF derived from Ursa Minor observations and for the analysis performed with a background IRF derived from M82 observations. In the significant distributions of Ursa Minor, between 300 and 500 GeV, shown in Figure 7.12, there is a positive bias $\mu > 0.3$, whereas between 1 and 2 TeV there is no longer a positive bias. The level of discrepancy between the two analyses performed with different background IRFs is consistent, suggesting that the unreliability of the background model at these low energies has little to do with matching different observing field parameters, such as zenith, azimuth, and season.

There are a few other systematics to consider when determining the cause of background discrepancies. Certain spatial information is lost when background IRFs are derived from a set of observations. The steps for deriving Gammapy background IRFs are described in Section 7.1.2. The Gammapy format for 2D background IRFs, binned in energy and radial offset, assumes azimuthal symmetry in the camera FoV. Information about the background rate in the north versus south versus east versus west quarter of the camera FoV is lost in the process of deriving background IRFs from real data. There is a 3D background model in Gammapy which consists of 2D FoV binning called **Background3D**. However, there are currently no working algorithms for deriving such a background model from source-free observations.

Therefore, there is good reason to assume that background rate gradients across the FoV and the inability of the present background IRFs to model this effect causes data versus model discrepancy seen in the post-fit analysis on Ursa Minor between 300 and $\sim$500 GeV. Some of the residuals show evidence of spatial gradients, most prominently between south versus north runs, as shown in Figure 7.18. At larger zenith angles greater air mass absorbs more Cherenkov light and therefore the VERITAS low energy threshold increases. Therefore, zenith threshold effects become pronounced between 35° to 40° zenith and 300 GeV. At large zenith angles the low energy background rate will significantly change across only a few degrees and, therefore, in the same FoV, there will be a non-radial gradient.

Studies performed and presented in Mohrmann et al. (2019) derived background models from archival H.E.S.S. data binned across multiple observing factors. The background rate in energy bins near the low threshold are also shown to be non-radially asymmetric. Figure 7.19 from Mohrmann et al. (2019) shows a strong dependence of the background energy spectrum on zenith angle, especially at low energy. The most relevant point coming out of this plot for the Ursa Minor studies is the background energy spectrum between 35° to 40° zenith. Just below 500 GeV the variation of the background rate with energy is large, therefore a background model with only a one energy spectral index will fail to constrain the background component close to the low energy threshold. In the Ursa Minor 4D-MLM analyses the energy bins with the largest discrepancy between model and data are also between 300 and 500 GeV. A model which assumes that the background energy spectrum is a single power-law, which is what is applied in the 4D-MLM, will struggle account for a rapid change in the background rate with energy, show in Figure 7.19. Mohrmann et al. (2019) also shows non-radial background rates in low energy bins. Therefore, a background model that takes into account a non-radial background rate and a changing background spectral index is likely to correct for the discrepancy at low energy.

The next step towards improving the background model at low energies will be to add a spatial correction component to the background IRFs. As of the writing of this work there is no mechanism to do so in the current version of Gammapy. However, the post-fit model counts and data counts agree quite well above 479 GeV for all datasets, both event classes, and both joint datasets with M82 and Ursa Minor derived background models. These higher energy residual maps suggest that the usage of two event classes and the current source and background models largely account for emission in a background dominated field, Ursa Minor, above 479 GeV.

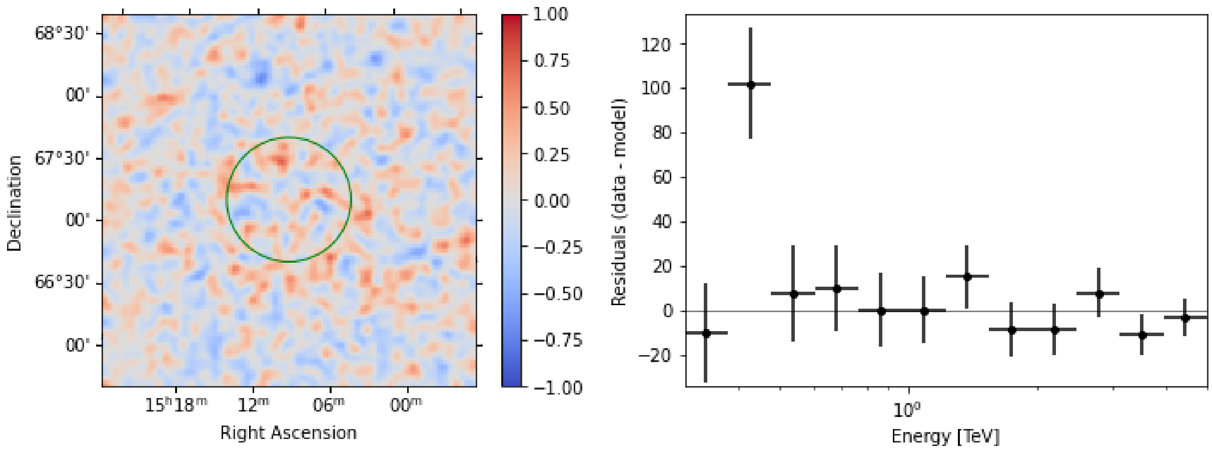


(a) Ursa Minor bkg

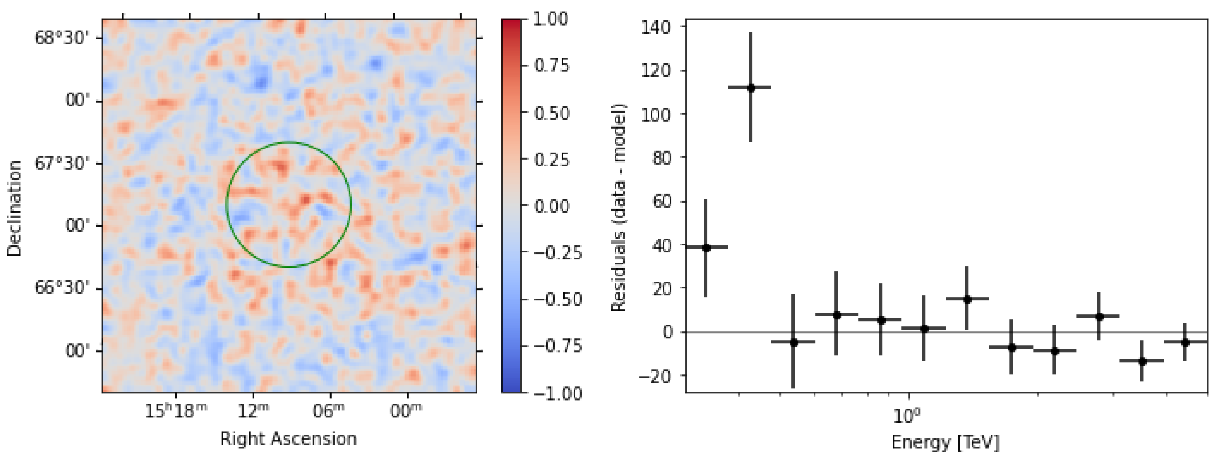


(a) M82 bkg

Figure 7.11: Data-model plots of all combined Ursa Minor datasets from all wobbles and both event classes, smoothed with a 0.035° radius gaussian kernel. The residual counts per energy are derived from within a 0.5° radius circle centered on the source position.

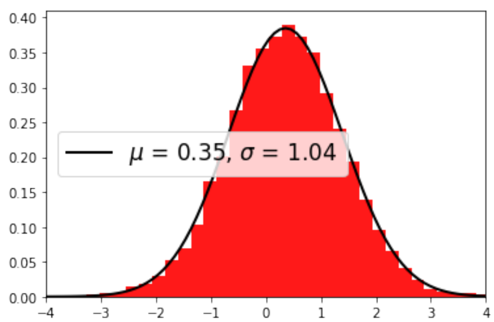


(a) 300-500 GeV, with Ursa Minor background

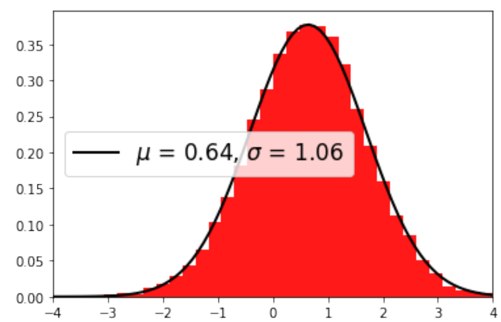


(b) 300-500 GeV, with M82 background

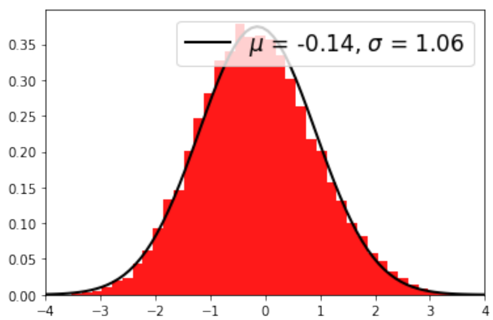


(c) 1-2 TeV, with Ursa Minor background

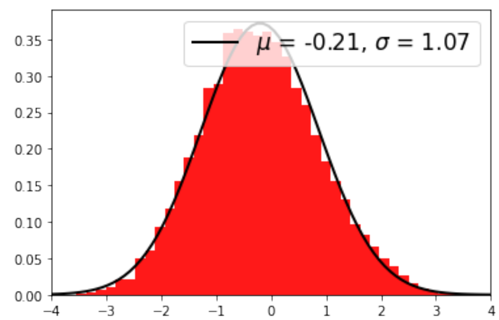


(d) 1-2 TeV, with M82 background

Figure 7.12: Significance distributions of residuals of all combined Ursa Minor datasets from all wobbles and both event classes. The top row is 300-500 GeV. The bottom row is 1-2 TeV. The left column plots are datasets with Ursa Minor derived background templates. The right column plots are datasets with M82 derived background templates.

## 7.5 Discussion

The previous sections of this chapter detailed a series of studies on multiple different datasets in order to test the 4D-MLM implemented in Gammapy. In previous chapters, the background and PSF were validated separately from the overall method. In this chapter, all IRFs and data have been run through the Gammapy software to perform a complete data analysis. The initial test studies on the robustness of the 4D-MLM were performed on a known point source, the Crab, and on blank fields with no known gamma-ray emission.

A series of analyses with the 4D-MLM were performed on $\sim 8.16$ hours of Crab data observed in a narrow zenith range ($10^\circ$ to $20^\circ$) and one observing season (2010-2011). Datasets were divided between two event classes, $0.8 < MSW < 1.1$ and $1.1 < MSW < 1.3$. The source model

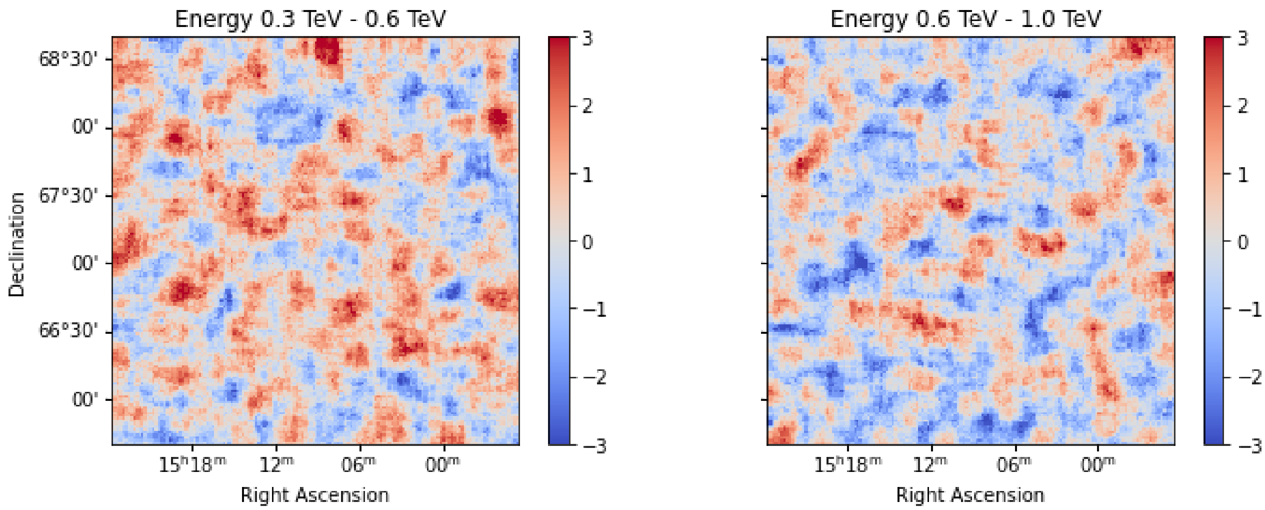


Figure 7.13: Residual $\sqrt{TS}$ plots of all combined Ursa Minor datasets from all wobbles and both event classes. The plots are separated into two energy bins: 0.3 TeV - 0.6 TeV and 0.6 TeV - 1.0 TeV.

passed to the likelihood was a single point source with a power-law spectrum. Results from a likelihood performed with background models and one source modeled located at the position of the Crab were consistent with a high flux point source. Two different likelihood analyses were performed on the Crab, one with background derived from source-subtracted Crab runs and a second with background derived from Segue1 and 1ES0229+300 runs. Post-fit spectral parameters and residual maps from both analyses were consistent within $2\sigma$, indicating that the background rates derived from separate fields were appropriate for the Crab. These result supports the current 4D-MLM performance, especially the newest addition to the method: two separate event class that share the same background normalization parameter.

Residual maps were also produced to judge how well the post-fit model matched the Crab data. All post-fit Crab residual maps display largely uniform emission, demonstrating that there are very minimal discrepancies in the modeling of the source. Out to 0.5° offset from the camera center the symmetric King function is a good match to the PSF and the background model accounts for the majority of background emission.

The standout features in the Crab residuals are in the data-minus-model residual maps, produced after a joint likelihood fit on all four different Crab telescope pointings. These residual plots are in Figures 7.9 and 7.10. The residual plots for separate datasets for different pointings contain pairs of under and over-subtraction features. Depending on which dataset is viewed, the direction of the bipolar feature is different, which suggests the discrepancy between data and model is dependent on the different cardinal direction VERITAS pointed relative to the Crab position. When a likelihood fit is performed on the north, south, east, or west offset data individually the bipolar feature disperses, shown in Figure 7.8. The post-fit right ascension and declination positions returned for each individual wobble were all different. The greatest difference between the joint-fit position and each four direction datasets is between the west wobble, 0.022°. When all Crab data is combined into a single joint likelihood there is only one final source position for the entire joint-dataset. For a perfect instrument, the source position would be the same for each different wobble pointing and there would no longer be a bipolar feature in the individual datasets of the joint-dataset. However, IACTs have finite position localization accuracy. The VERITAS source location accuracy, determined by VERITAS Pointing Monitor (VPM) calibrations, is 50 arcseconds or 0.014°, detailed in Section 3.3.2. The accuracy of the VERITAS VPM is consistent with the separation between the post-fit positions of each Crab wobble dataset and the HEASARC Crab source position.

A search for extended source emission in a blank field was performed in order to further validate the handling of the background in the 4D-MLM with two event classes and background IRFs derived from real data. Two different likelihood analyses were performed on Ursa Minor, one with background derived from the Ursa Minor data runs themselves and a second with background derived from source-subtracted M82 runs. Both M82 and Ursa Minor observations had similar zenith, azimuth, noise level, and observing season. The post-fit significance distribution of both analyses performed with different background IRFs are consistent, demonstrating that the discrepancy that is present in the residuals at low energy is not due to the observation fields used to derive the background model. In both analyses, there is a bias in the significance distribution towards positive fluctuations, but the discrepancy is only present in the lowest energy bin. There are also gradients across the FoV in some of the data minus model residual maps. Above about 479 GeV there is good agreement between the post-fit model of the region to the Ursa Minor data.

The discrepancies seen in the Ursa Minor studies are also in agreement with the behavior of background modeling near the low energy threshold, where the background is non symmetric. Also, more than a single power-law is needed to characterize the background energy spectrum. Especially at larger zenith angles the background rate changes rapidly at low energy, as shown in the top plot in Figure 7.19 (Mohrmann et al., 2019). For purposes of confirming that this trend in background rate over energy is true for the data samples in these Crab and Ursa Minor studies the background flux was plotted in bins of energy for both Crab and Ursa Minor runs and is shown in the bottom plot of Figure 7.19. At small zenith angles a single power-law is a reasonable approximation to the background energy spectrum from 300 GeV to 5 TeV. At large zenith angles this conclusion is less acceptable. Both plots in Figure 7.19 are consistent, which strongly suggests that the background dependency on zenith and camera azimuth at the low energy threshold, described in Mohrmann et al. (2019), is causing the deviations between model and data in the previous sections.

A robust solution to these issue would require the development of a background model that has both azimuthal asymmetry and zenith angle dependence. A background model needs to also take into account a changing background energy spectral index. In the current version of the software there is no known Gammapy algorithm taking into account the dependency of rates due to a zenith gradient across the camera. There is a 3D background model in Gammapy which stores background rates in bins of energy and 2D camera coordinates. However, there are currently no working algorithms for deriving a 3D background model model from source-free observations.

Given the improvement that the Barlow Beeston terms made to the likelihood performed on the distribution of MSW values, detailed in Section Section 6.2, future development of the

4D-MLM will add terms to the likelihood equations containing information on the statistical uncertainty. Certain hurdles exist which are intrinsic to Gammapy that make the implementation of Barlow Beeston terms in Gammapy likelihood functions difficult. The Gammapy IRF format does not currently have parameters which store statistics of each bin of energy and offset. One strategy for implementing Barlow Beeston that does not require extensive editing of the Gammapy software is what shall be termed *Barlow Beeston-lite*. A single term, for each bin, in the likelihood accounts for the combined uncertainty of all models in that particular bin. Reduction of multiple Barlow Beeston terms down to one is acceptable since it is assumed that the background statistical uncertainty dominates.

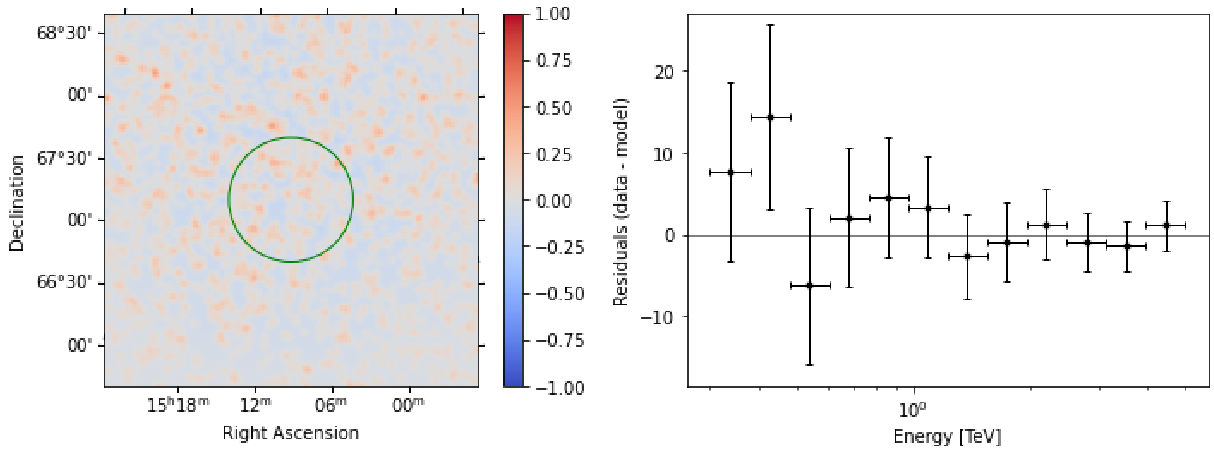


(a) North wobble, $0.8 < MSW < 1.1$

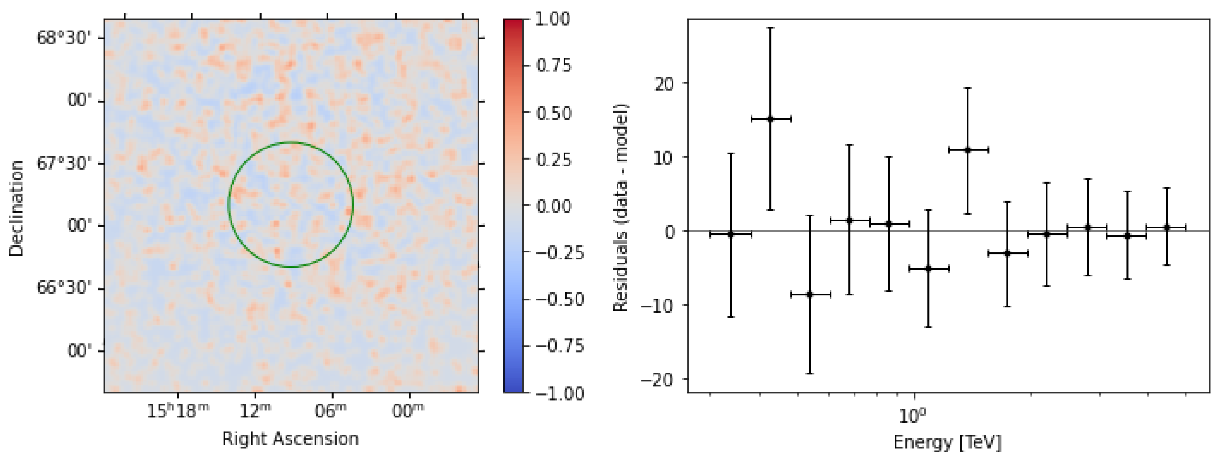


(b) North wobble, $1.1 < MSW < 1.3$

Figure 7.14: Data-model plots of north offset datasets using the Ursa Minor derived background IRFs. The residual counts per energy are derived from within a 0.5° radius circle centered on the source position.

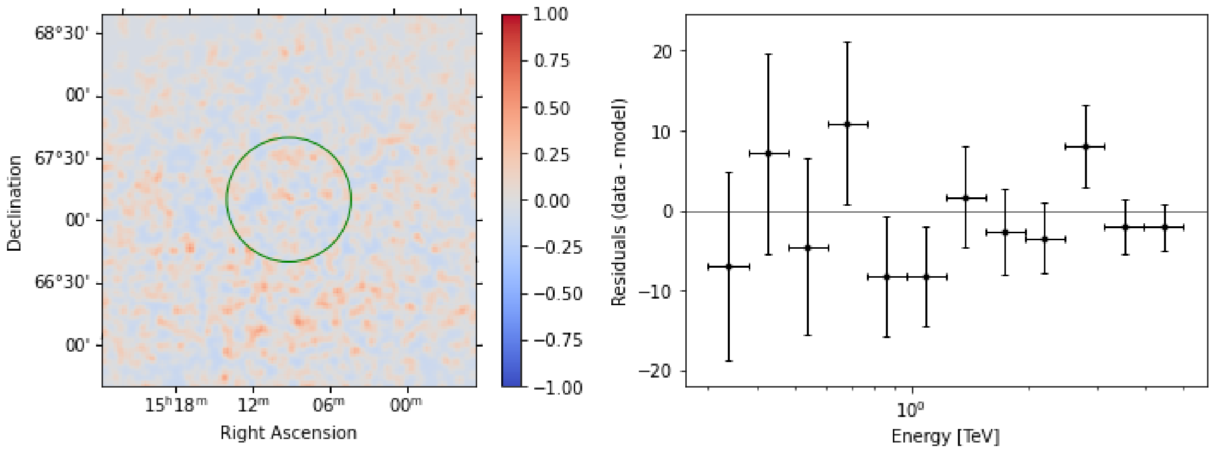


(a) South wobble, $0.8 < MSW < 1.1$

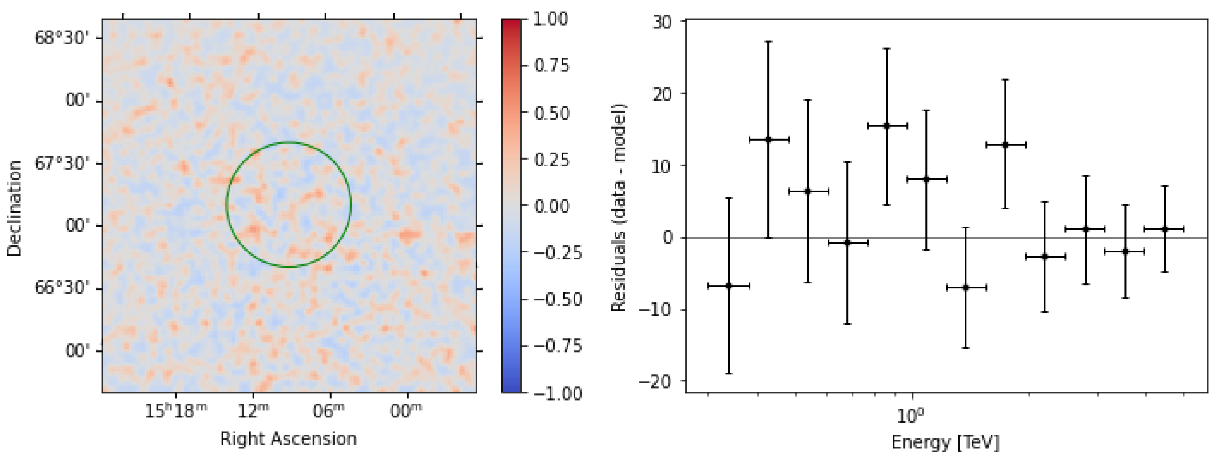


(b) South wobble, $1.1 < MSW < 1.3$

Figure 7.15: Data-model plots of south offset datasets using the Ursa Minor derived background IRFs. The residual counts per energy are derived from within a 0.5° radius circle centered on the source position.

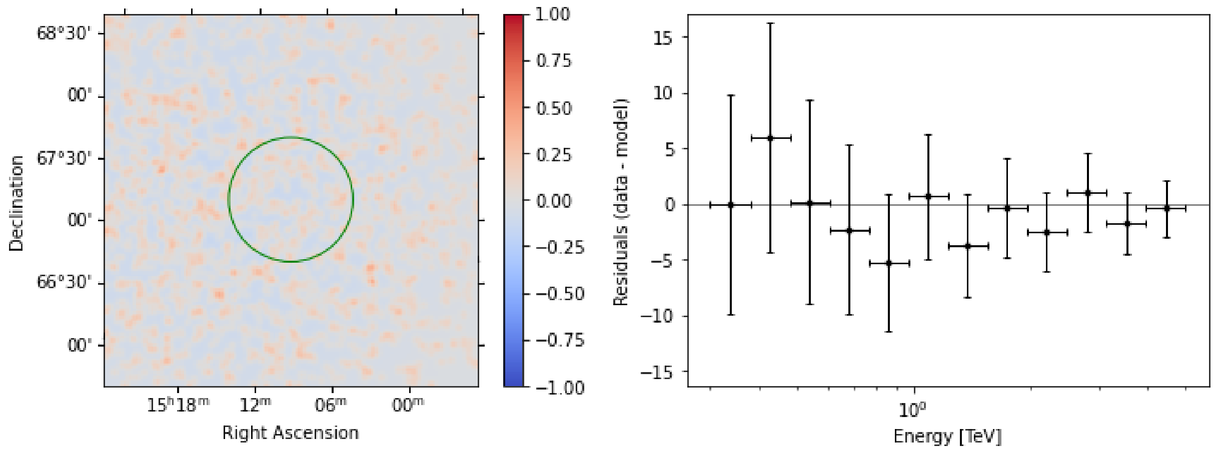


(a) East wobble, $0.8 < MSW < 1.1$

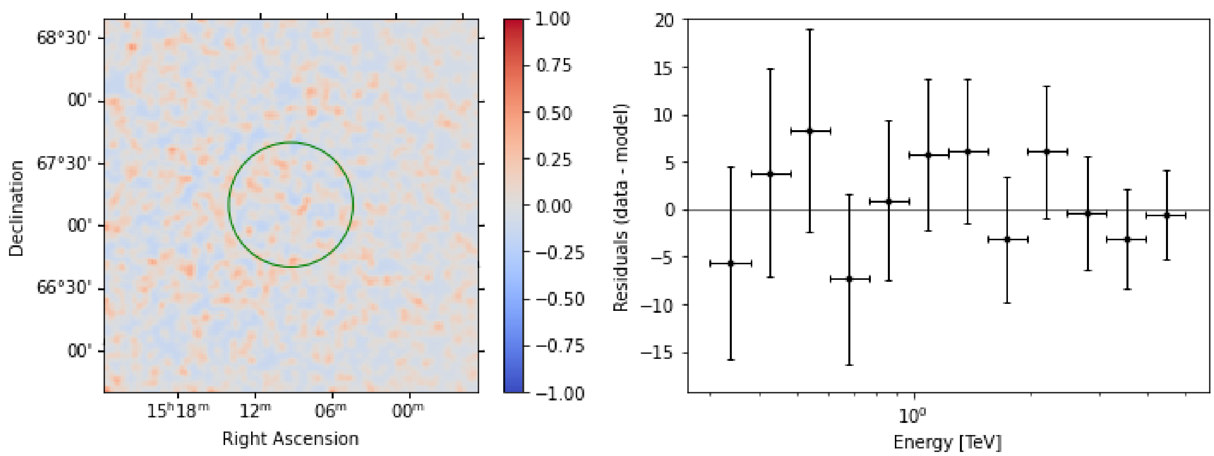


(b) East wobble, $1.1 < MSW < 1.3$

Figure 7.16: Data-model plots of east offset datasets using the Ursa Minor derived background IRFs. The residual counts per energy are derived from within a 0.5° radius circle centered on the source position.

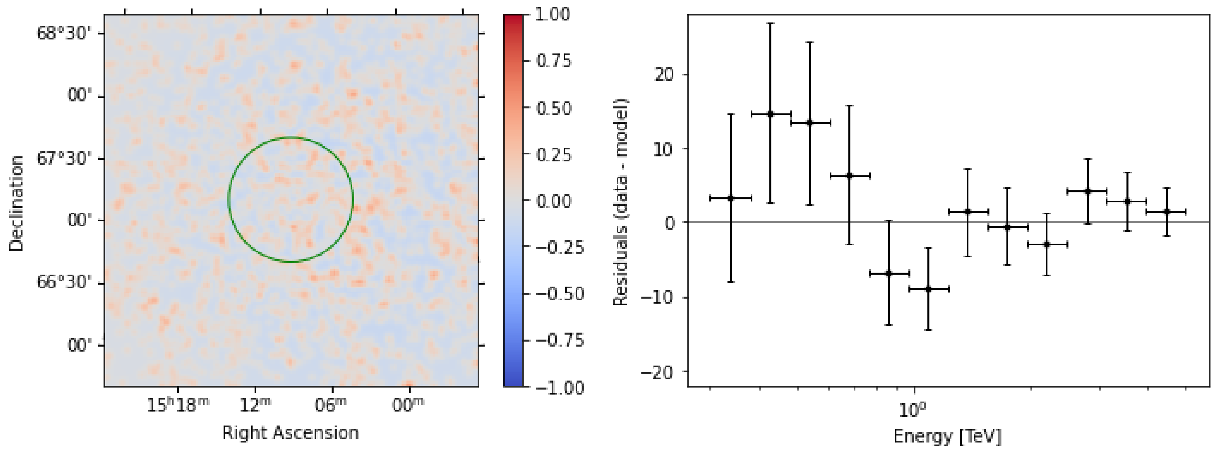


(a) West wobble, $0.8 < MSW < 1.1$

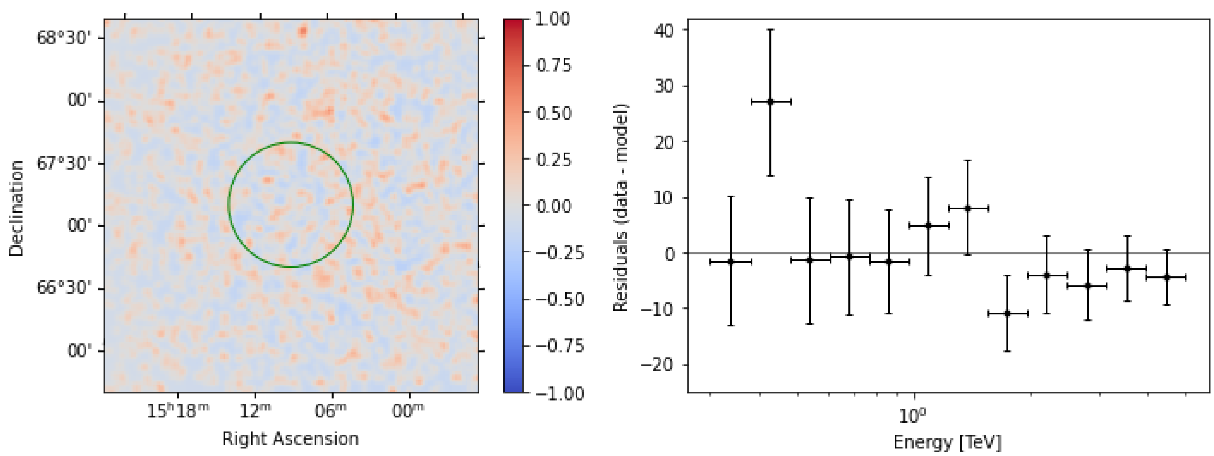


(b) West wobble, $1.1 < MSW < 1.3$

Figure 7.17: Data-model plots of west offset datasets using the Ursa Minor derived background IRFs. The residual counts per energy are derived from within a $0.5°$ radius circle centered on the source position.

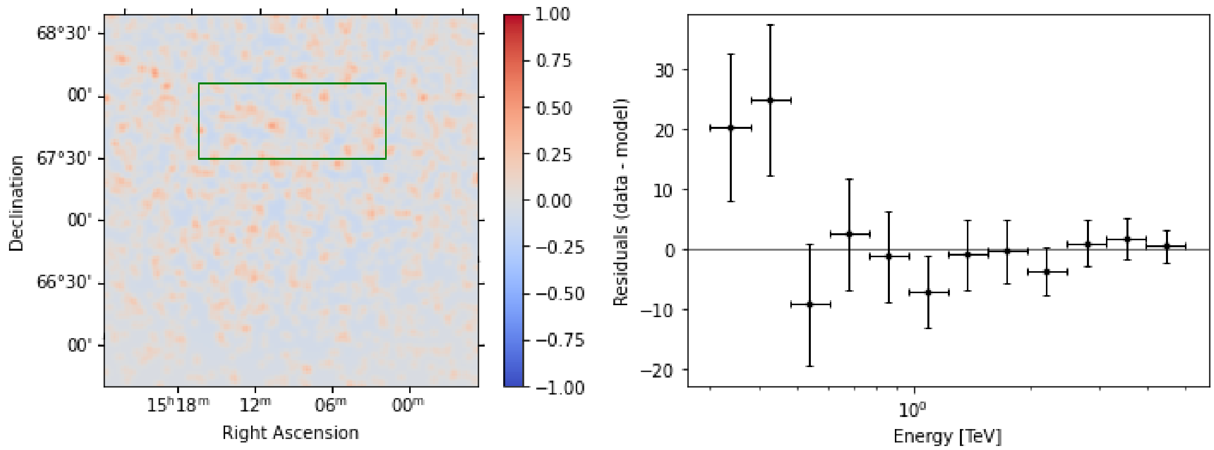


(a) North wobble, $0.8 < MSW < 1.1$

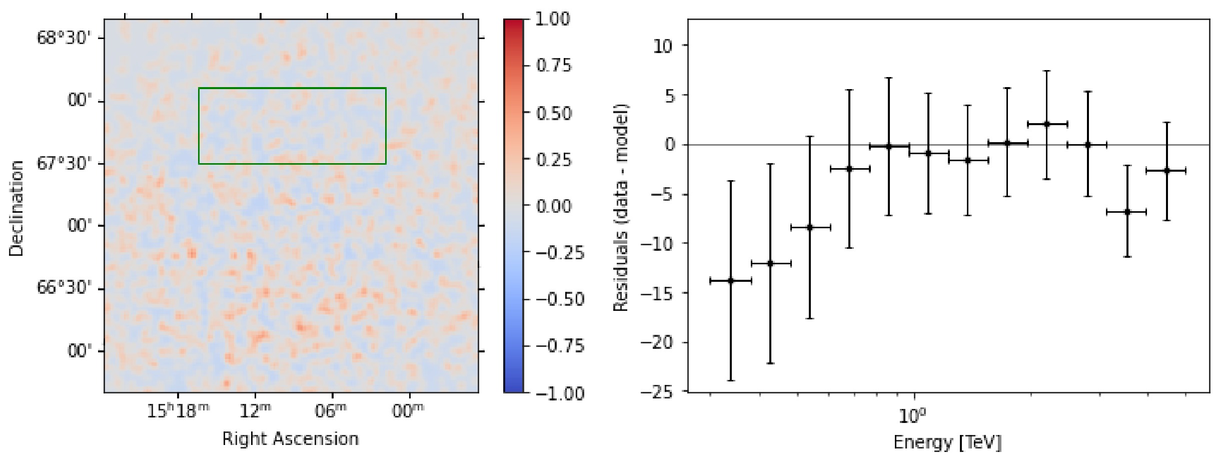


(b) South wobble, $0.8 < MSW < 1.1$

Figure 7.18: Data-model plots of datasets using the Ursa Minor derived background IRFs, north versus south fields. The residual counts per energy are derived from rectangular sections placed north.

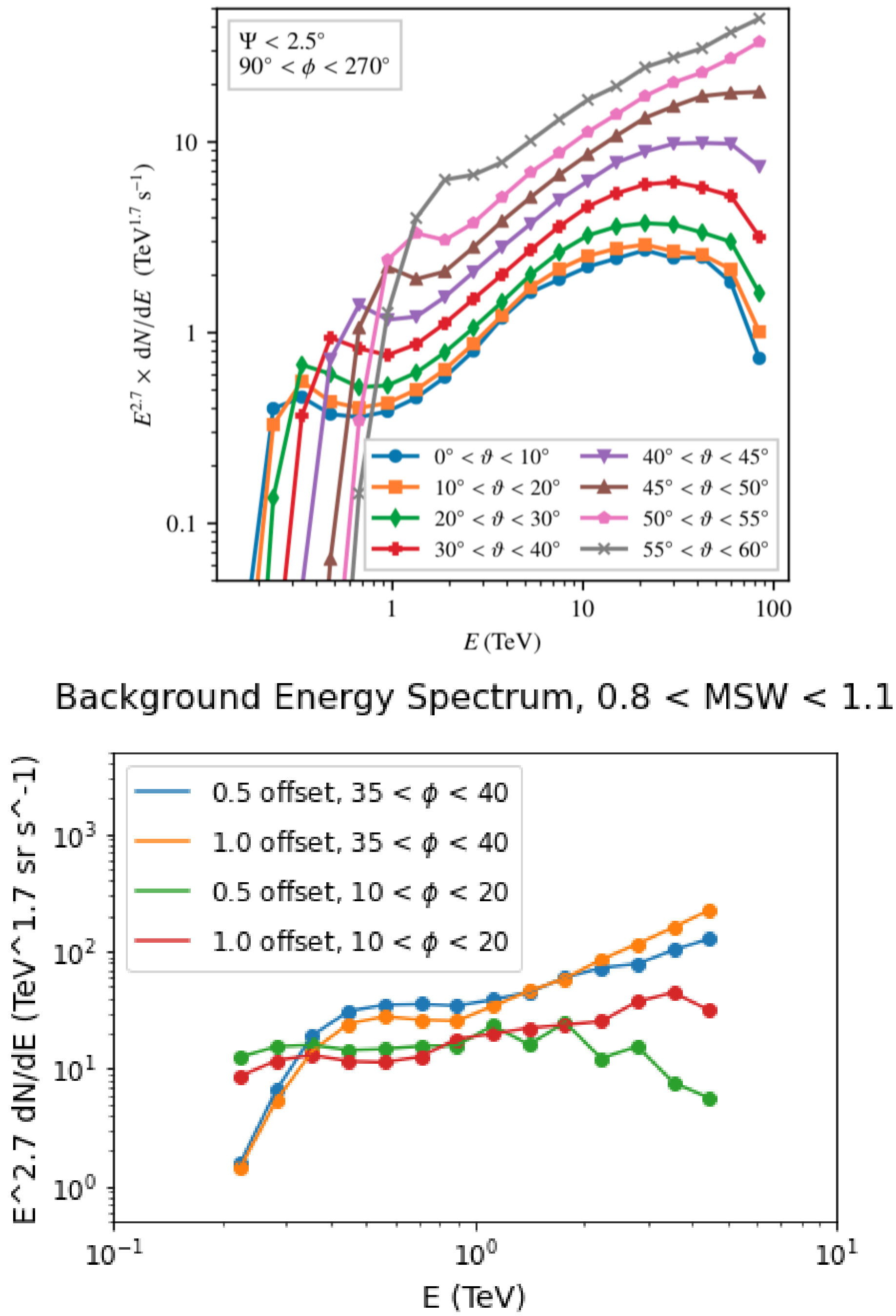


Figure 7.19: **Top:** H.E.S.S. background model energy spectrum from Mohrmann et al. (2019) in different bins of zenith angle, for azimuth angles $90° < \phi < 270°$. The rate is integrated in a circle with radius 2.5° around the pointing position. **Bottom:** Ursa Minor runs between 35° to 40° zenith and Crab runs between 10° to 20° zenith. To enhance the spectral features, the vertical axis in both plots are multiplied by $E^{2.7}$.

# CHAPTER 8. GAMMA-CYGNI

The shell-like supernova remnant (SNR) Gamma-Cygni (SNR G78.2+2.1), located in the Cygnus star-forming region, is visible in gamma rays up to TeV energies. A review on current emission models of Gamma-Cygni and the remnant's surrounding environment is given in Section 1.2.4. At very high energy (VHE), VERITAS has observed emission along the northwestern rim of the shell-like radio structure. There have been two VERITAS publications on Gamma-Cygni using standard analysis methods which detect an extended VHE source associated with the northwestern rim of the radio shell. The IACT telescope MAGIC also reports three different regions of extended VHE emission associated with the radio SNR. Results from *Fermi*-LAT also report a gamma-ray source associated with Gamma-Cygni, however the *Fermi*-LAT source extension is larger than the VERITAS source. Spectral parameters of the *Fermi*-LAT source strongly suggest that VERITAS should be able to detect the larger extended source (Fraija and Araya, 2016).

This chapter details new VERITAS analysis on Gamma-Cygni, with the aim of better characterizing the extent and morphology of the VHE gamma-ray emission. Two analyses are performed, one with standard methods and the other performed with the 4D-Maximum Likelihood Method (4D-MLM). The first analysis entails including substantially more exposure and, most critically, employs a recent improvement in VERITAS data reduction, image template method (ITM) for gamma-ray stereo reconstruction. Data reduction performed with image templates, described in further detail in Section 3.4.5, improves event angular resolution and reduces bright star effects. The second analysis is performed with the 4D-MLM on a subset of the total Gamma-Cygni dataset, observed during fall 2009. The Gamma-Cygni results from the 4D-MLM presented in this thesis point to morphology consistent with previous studies. Future application of this method on the larger Gamma-Cygni dataset is likely to characterize morphologies and spectra of different regions across the entire Gamma-Cgyni extension and immediate surrounding regions.

## 8.1 Standard Methods with Image Templates

The first VERITAS scientific results on Gamma-Cygni were published in 2013. This study includes a spectral and morphological analysis on observations performed in 2009, with a total livetime of 18.6 hours and a low energy threshold of 320 GeV. Significant, extended emission was detected at a post-trials significance of 7.5 standard deviations, localized near the northwestern rim of the radio remnant. This source is named VER J2019+407. The source extension was modeled as a symmetric two-dimensional Gaussian, convolved with the VERITAS PSF and fitted with an extension $0.23^{\circ} \pm 0.03^{\circ}_{stat}{}^{+0.04^{\circ}}_{-0.02^{\circ}_{sys}}$ (Aliu and et al., 2013).

A VERITAS publication released in 2018 presented a survey of the Cygnus region from observations conducted by VERITAS between 2007 April 2007 and June 2012. The spectral and morphological results included the VERITAS source associated with Gamma-Cygni, VER J2019+407. This publication reported that the VER J2019+407 extension is asymmetric, unlike the reported morphology in the earlier publication The extended emission was fit with an asymmetric Gaussian with major axis $0.29 \pm 0.02_{stat} \pm 0.02_{sys}$ and minor axis $0.19 \pm 0.01_{stat} \pm 0.02_{sys}$ (Abeysekara and et al., 2018).

The analyses in these two previous publications used standard methods, reflected region (RR) and ring background method (RBM). These two methods are also used in the first new Gamma-Cygni analysis performed and presented in the immediate following sections, with two major improvements to sensitivity; additional exposure and use of ITM. Observations from the V4 epoch were excluded due to the lower sensitivity of the instrument in the configuration when T1 and T4 were in close proximity.

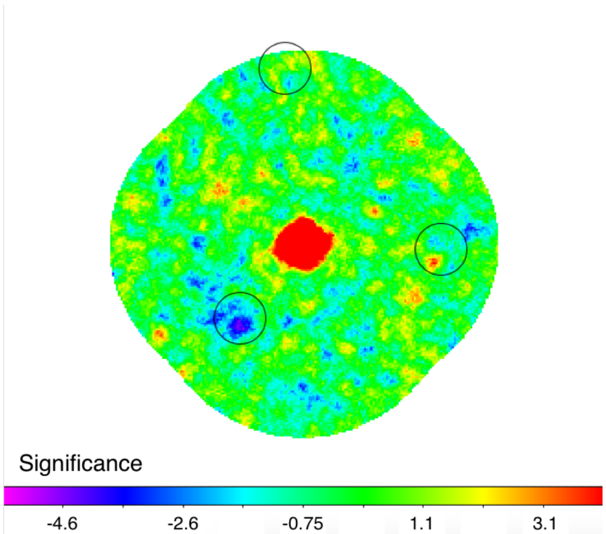


(a) $0.8 < MSW < 1.3$, without ITM

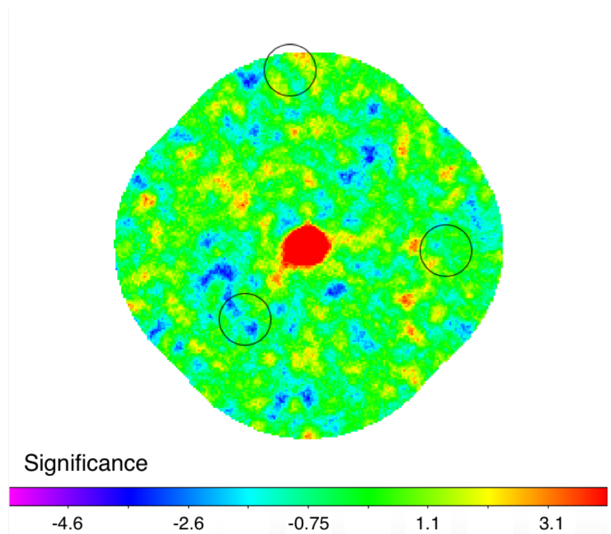


(b) $0.8 < MSW < 1.3$, with ITM

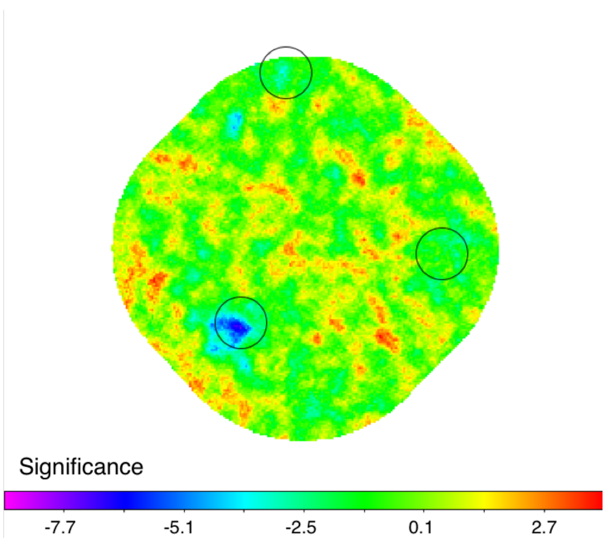


(d) $1.3 < MSW/L < 1.6$, without ITM

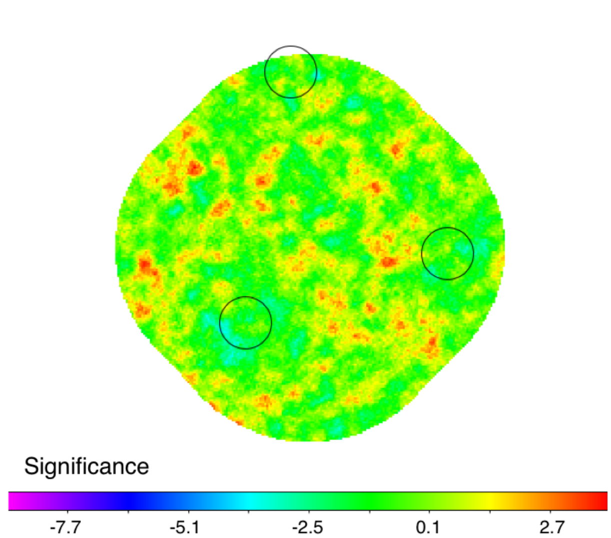


(e) $1.3 < MSW/L < 1.6$, with ITM

Figure 8.1: Significance maps of Crab data. The top row of maps have cuts on MSW applied to select gamma-rays. The bottom row of maps have cuts on MSW and MSL applied to only select background events. The three black circles denote the positions of stars with $M_B$ <6.0.

### 8.1.1 Justification for Image Template Method

A bright star ($\gamma$-Cygni, mag_B=2.90) overlaps the *Fermi*-LAT reported extension of the SNR, Gamma-Cygni. Optically bright stars produce constant, enhanced signal in clusters of camera pixels and the brightest stars will suppress pixels. These features in the pixelated camera will impact the shape of the shower image and therefore bias shower image reconstruction at and near the star position. In standard analysis, a circular region around the star position is subtracted from all possible background regions. In the construction of 2D maps, excess counts and significance are still calculated at bright star positions. Since poor event reconstruction occurs near bright star regions compared to dark regions far fewer events will pass the cuts optimized for gamma rays. The number of **ON counts** versus **OFF counts** factors into the calculation of significance, therefore significance maps will have over-subtraction features at the position of bright stars, as shown in the left column of plots in Figure 8.1.

Furthermore, a local region around a bright star cannot be excluded for instances where the star position overlaps a gamma-ray source, as is the case for Gamma-Cygni. Results from analyses performed with ITM show great improvement on image reconstruction at bright star positions, as shown in Figure 8.1. This fact greatly informed the decision to perform all analysis going forward on Gamma-Cygni with ITM, presented in this chapter.

## 8.2 Ring Background Analysis Results

A series of ring background method (RBM) analyses were performed on observations with positions overlapping the Gamma-Cygni remnant extension. An initial analysis focuses solely on data taken in the V5 epoch, and compares and contrasts applying ITM versus not applying ITM, with livetime adding up to 16.5 hours.

Data taken on a gamma-ray source near Gamma-Cygni, TeV J2032+4130, has also been added to the total dataset passed through the standard analysis. The outer region of the field of view (FoV) of those data runs taken on TeV J2032+4130 overlap with the southern rim of the *Fermi*-LAT extension of Gamma-Cygni. The addition of TeV J2032+4130 runs is not expected to considerably contribute to the overall effective exposure on Gamma-Cygni due to the greatly reduced sensitivity of the VERITAS camera at the edge of the FoV. These runs will become crucial for future VERITAS studies of the larger *Fermi*-LAT source, the Cygnus Cocoon, which extends between the positions of Gamma-Cygni and TeV J2032+4130.

A second analysis adds in VERITAS V6 epoch data that has not been analyzed previously, with either standard methods or the 4D-MLM. The livetime of V6 data, centered the Gamma-Cygni remnant, adds up to 31.7 hours. Most of the new data centered around the remnant was observed between May-November 2019. The total livetime of observations directed at Gamma-Cygni positions in each analysis are shown in Table 8.1.

### 8.2.1 VER J2019+407

The position of maximum significance resulting from an RBM analysis performed on V5 runs with ITM (R.A.=305.06°, Dec=40.93°) coincides with the fitted centroid coordinates of VER J2019+407, localized along the northwestern rim of the radio remnant. The position of VER J2019+304 does shift slightly between an ITM analysis versus an analysis without ITM, as shown in Table 8.3. Analysis on the same data reduced with ITM reveals a more compact source versus without ITM, as shown in Figures 8.2, 8.3, and 8.4. Furthermore, the V5 ITM analysis reports greater significance when the integration radius, localized at the source position, is $r = 0.1°$. The nominal ITM 68% containment is 0.07°; this defines the VERITAS point source dimensions. Therefore, the source emission located on the northwestern rim remains best characterized by a slightly extended source model.

About 31.7 hours of V6 data from Gamma-Cygni and several V6 runs of TeV J2032+4130 were added to the V5 dataset. The position of max significance resulting from an RBM analysis performed on V5 and V6 runs with ITM (R.A.=304.97°, Dec=40.88°) also coincides with the centroid coordinates of VER J2019+407 and is consistent with the V5 position, as shown in Table 8.3. The RBM significance was performed with an $r = 0.1°$ circular integration radius and the final significance is $8.3\sigma$. The Gamma-Cygni source significance from RBM analyses performed only on observations taken directly on Gamma-Cygni are in Table 8.1. The Gamma-Cygni source significance from reflected region (RR) analyses are in Table 8.2.

Table 8.1: Total livetime of observations taken only directly on Gamma-Cygni positions. The significance values are derived from ring background method analysis performed on runs processed with ITM.

| **Analysis** | significance | total livetime [hr] |
|---|---|---|
| **(Aliu and et al., 2013)** | 7.5 $\sigma$ | 18.6 hr |
| **V5, only $\gamma$-Cygni** | 6.0 $\sigma$ | 16.5 hr |
| **V5+V6, only $\gamma$-Cygni** | 7.3 $\sigma$ | 48.2 hr |

Table 8.2: Spectral parameters of different VERITAS analyses at each study's respective position of highest significance in the Gamma Cygni remnant. The spectral parameters are derived from reflected region analysis. The significance values are derived from RR analysis. The V5 analysis was only performed on observations taken directly on Gamma-Cygni while the V5+V6 analysis also included observations from the nearby source TeV J2032+4130.

| **Analysis** | significance [$\sigma$] | Flux[1 TeV] $\times 10^{-13}$ [$\mathrm{TeV}^{-1}\mathrm{cm}^{-2}\mathrm{s}^{-1}$] | index | energy threshold |
|---|---|---|---|---|
| **(Aliu and et al., 2013)** | 7.5 $\sigma$ | 11.5[$\pm$6.0] | 2.37[$\pm$0.34] | 320 GeV |
| **(Abeysekara and et al., 2018)** | 7.6 $\sigma$ | 5.01[$\pm$1.93] | 2.79[$\pm$0.59] | 400 GeV |
| **V5, with ITM** | 6.4 $\sigma$ | 6.44[$\pm$1.31] | 2.26[$\pm$0.34] | 288 GeV |
| **V5+V6, with ITM** | 9.1 $\sigma$ | 5.04[$\pm$0.7] | 2.37[$\pm$0.18] | 347 GeV |

### 8.2.2 SNR Shell

The main motivation of a 4D-MLM analysis of the Gamma-Cygni region observed by VERITAS, as well as requests for further exposure on the source, is the detection of largely extended emission, observed across the entire radio-shell, by two other gamma-ray instruments, *Fermi*-LAT and HAWC. Given the significance and spectral parameters reported from these two instruments VERITAS should be able to collect gamma rays emitted from a larger Gamma-Cygni region than currently reported.

An overall positive significance in three different regions associated with Gamma-Cygni has been reported by the IACT MAGIC (Acciari and MAGIC Collaboration, 2020). In a study on 87

Table 8.3: Position of highest significance in the Gamma-Cygni remnant.

| **Analysis** | R.A. (J2000) | Dec (J2000) |
|---|---|---|
| **(Aliu and et al., 2013)** | 20hr 20min 04.8sec | +40 45' 36" |
| **(Abeysekara and et al., 2018)** | 20hr 20min 04.8sec | +40 45' 36" |
| **V5, without ITM** | 20hr 19min 39.84sec | +40 43' 50.5" |
| **V5, with ITM** | 20hr 20min 13.44sec | +40 55' 49.8" |
| **V5+V6, without ITM** | 20hr 19min 45.60sec | +40 49' 26.8" |
| **V5+V6, with ITM** | 20hr 20min 01.44sec | +40 56' 29.0" |

hours of good-quality data the MAGIC collaboration modeled the Gamma-Cygni remnant with three sources, a disk matching the extension of the radio remnant, a Gaussian associated with VER J2019+407, and an annular sector tracing out the rim adjacent to and west of VER J2019+407. Patchy features located outside the vicinity of both VER J2019+407 and the west annular sector, while still within the radio extension, are at the level of $3\sigma$. These significant features add up to a significant detection ($6.1\sigma$) by MAGIC of a source modeled with a disk template and closely matching the position and extension the Gamma-Cygni SNR radio shell. The report of an adjacent annulus of emission extending from the localization of VER J2019+407 supports previous VERITAS publications reporting extended emission (Aliu and et al., 2013) and an asymmetric extension (Abeysekara and et al., 2018).

An RBM analysis was performed on VERITAS data which excluded a $0.4°$ overlapping region around VER J2019+407 and calculated the significance of a source at the position and extension of the *Fermi*-LAT disk. The combined V5 and V6 exposure added up to about 48.2 hours of data taken on Gamma-Cygni and TeV J2019+407 observations. The resulting RBM significance is $3.32\sigma$. A meaningful spectral study cannot be performed and an affirmative source detection cannot be claimed from only the RBM analysis given the low significance ($< 5\sigma$). However, the overall positive significance bias across the disk extension, as shown in Figures 8.6 and 8.5, strongly supports the presence of VHE gamma-ray emission. The mean value of the standard distribution of bins within the *Fermi*-LAT disk extension, minus an exclusion region centered

Table 8.4: Table of Gamma-Cygni spectral parameters, both standard analysis and the 4D-MLM performed in Gammapy. The previous analyses, Aliu and et al. (2013) and Abeysekara and et al. (2018), were performed across a larger energy range and at a flux normalization of 1 TeV. The energy range of Albert (2020) is 0.7-14.8 TeV, with a flux normalization at 7 TeV.

| **Analysis** | **Index** | $\mathbf{Flux}_{0.7}\times10^{-13}$ $\mathrm{TeV}^{-1}\mathrm{s}^{-1}\mathrm{cm}^{-2}$ |
|---|---|---|
| **(Aliu and et al., 2013)** | $2.37\pm0.34$ | - |
| **(Abeysekara and et al., 2018)** | $2.79\pm0.59$ | - |
| **(Albert, 2020)** | $3.11\pm0.07^{+0.08}_{-0.04}$ | - |
| V5, with ITM | $2.15\pm0.37$ | - |
| Gammapy point source | $2.82\pm0.25$ | 23.8($\pm$3.21) |
| Gammapy disk source | $2.78\pm0.11$ | 158.6($\pm$9.97) |

around the position of VER J2019+407, is $\mu$=0.9798, demonstrating the trend towards positive fluctuations in this region.

### 8.3 Reflected Region Spectral Analysis

Two RR analyses were performed on VERITAS Gamma-Cygni observations, processed with ITM, in order to produce a spectrum, fit with a power-law. The analysis was performed with a 0.1 degree integration radius located at the position of maximum significance. This position is localized to the northwestern rim of the remnant and is associated with the previously reported source VER J2019+407. The first analysis was performed on $\sim$ 16.5 hours of V5 data. The second analysis was performed on $\sim$ 48.2 hours of combined V5 and V6 data. The second analysis also included TeV J2032+4107 observations, however these runs have minimal impact on improving sensitivity on the remnant, and even lesser impact near the position of VER J2019+407.

The V5 effective areas were reproduced from GrISUDet simulations, with ITM reconstruction, for the purposes of performing this spectral analysis. The V6 effective areas were produced from CARE simulations that have been modified with GT factors, which are described in Appendix A. The GT factors used were derived from summer 2019 VERITAS calibrations. Due to the time cost of table production only one season of simulations were produced and the V6 dataset was limited to runs taken from 20180609 to 20191101.

The energy spectrum plots of only V5 runs and combined V5 and V6 runs are shown in Figure 8.7. The spectral parameters are organized in Table 8.2, along with spectral parameters from previous VERITAS studies of VER J2019+407. The V5 and V5+V6 power-law spectral parameters resulting from the RR analyses are consistent within errors with the previous VERITAS study spectral parameters.

## 8.4 Likelihood Analysis

The primary goal of the development of a 4D-MLM likelihood is the detection of extended sources observed by VERITAS, both morphology and energy distribution. Gamma-Cygni is a source with some known extended emission already detected in the energy range of IACTs. Therefore, Gamma-Cygni is a source where a consistency check between 4D-MLM results to previous studies performed with standard methods is possible. In addition, Gamma-Cygni has additional extended emission detected at gamma-ray energies above and below the ranges sensitive to IACTs. Furthermore, a discovery of larger extended emission by VERITAS would offer an independent test to MAGIC's claims of extended emission and possibly constitute a new scientific result.

A series of 4D-MLM likelihood analyses, within the analysis framework of *Gammapy*, are performed on a set of Gamma-Cygni runs observed in fall 2009, during the VERITAS V5 epoch. The background IRFs were derived from Gamma-Cygni and TeV J2032+4130 observations in fall 2009, after subtracting all known gamma-ray sources. All Gamma-Cygni runs with average zenith between $10°$ to $20°$ and observed in fall 2009 have a total livetime of $\sim 7.6$ hours. All Gamma-Cygni runs with average zenith between $20°$ to $30°$ and observed in fall 2009 have a total livetime of $\sim 8.8$ hours. The total livetime of all datasets in the 4D-MLM is $\sim 16.4$ hours.

Source templates in the 4D-MLM analyses were initially centered on the position of maximum significance contained within V5 Gamma-Cygni data, a position associated with the VERITAS source VER J2019+407. All runs were divided between four cardinal wobble directions, 0.6° north, south, east, and west and also divided between two bins of zenith angles: 10°-20° and 20°-30°. In addition, Gamma-Cygni events were divided between the two event classes, $0.8 < MSW < 1.1$ and $1.1 < MSW < 1.3$. Therefore, sixteen separate datasets make up the joint-likelihood analysis on Gamma-Cygni, performed between 300GeV-5TeV.

An initial 4D-MLM analysis on Gamma-Cygni modeled the region associated with VER J2019+407 as a point source. The initial position was set at right ascension = 305.056 and declination = 40.931 and the two position parameters were allowed to float in the likelihood. The likelihood fit converged and returned a position of 305.01 ±0.009 and 40.871 ±0.007. The following spectral parameters from this analysis are $\Gamma = 2.601(\pm 0.029)$ and $F_{0.7} = 1.024(\pm 0.018) \times 10^{-10}\text{TeV}^{-1}\text{cm}^{-2}\text{s}^{-1}$, evaluated at $E_0 = 0.7$ TeV.

A likelihood analysis was also performed with a uniform disk modeling the source emission associated with VER J2019+407. The disk extension was initialized at position right ascension = 305.056 and declination = 40.931 and the position left to float between a few tenths of degree. The disk extension was left a free parameter. The likelihood fit converged and returned spectral parameters $\Gamma = 2.777(\pm 0.108)$ and $F_{0.7} = 1.918(\pm 0.117) \times 10^{-11}\text{TeV}^{-1}\text{cm}^{-2}\text{s}^{-1}$, evaluated at $E_0$ = 0.7 TeV. The post-fit extension is r=0.510 ±0.004, located at right ascension = $304.96 \pm 0.01$ and declination = $40.64 \pm 0.01$. The disk template is not meant to report that the morphology is in the shape of a disk, but is rather to characterize the localization and extent of gamma-ray emission.

Residual maps in Figures 8.18 and 8.17 show that the likelihood performed with a disk model accounts for a greater amount of excess emission than a point source model alone. The excess emission present in the residual maps is also concentrated along the northern rim, with some morphology extending just beyond the *Fermi*-LAT extension. Caution should be had when making conclusions about small scale source morphology, especially since the PSF is modeled with a symmetric King function, which is not the most preferred model for the PSF at larger offset. Nevertheless, there is consistency between the location of the enhanced extended emission and the localization of emission in previous VERITAS publications.

Figure 8.8 shows $\sqrt{TS}$ residual maps with only the background models subtracted. As long as the post-fit background models account for all components of background emission what should remain are random fluctuations and gamma-ray emission. The region with greatest significant emission is consistent with the localization of highest gamma-ray emission reported from RBM analysis on V5 and V5+V6 Gamma-Cygni observations.

The greatest significant emission in the background subtracted residuals overlaps a level of enhance 1420 MHz contours along the northern rim of the radio emission. The enhanced gamma-ray flux reported by the 4D-MLM also overlaps the 408 MHz radio contour and extends just beyond the northern 408 MHz rim. A 2020 MAGIC publication on Gamma-Cygni also concluded that VHE emission along the northern rim also extends outside the radio shell (Acciari and MAGIC Collaboration, 2020). Figure 8.9 shows the MAGIC relative flux map and 4D-MLM background subtracted $\sqrt{TS}$ residual side by side. There is consistent structure in both plots, even though the 4D-MLM residual map was created from less exposure than the plots generated from MAGIC data.

The flux points and power-law fit of both the likelihood with a point source model and the likelihood with a disk source model are shown in Table 8.2 and Figure 8.7. While the point source spectrum is somewhat consistent with a power-law, when the likelihood is performed only with a disk template multiple flux points show significant deviation from the power-law fit. The deviation of flux points from the power-law indicate that either a different spectral model is preferred or point to the presence of more than one source. Another possibility is that since the morphology of the extended emission is not a perfect flat disk the fluctuations are also visible in the spectral fit. Attempts were made to fit the disk emission with a log-parabola and exponential-cutoff spectrum, but there was no convergence in those cases.

A separate likelihood on the same Gamma-Cygni datasets searched for the significance of modeling the Gamma-Cygni region with both a disk and point source. The initial spatial source model is a point source with the position frozen at post-fit parameters. A disk template was added to the spatial model, also fixed at the position and extension values returned from the likelihood performed with only a disk source. The spectral index and flux normalization of both the disk and point source were left to float in the subsequent likelihood analysis of the Gamma-Cygni region modeled with both a point and a disk spatial model.

According to Wilks theorem, for composite or nested models a likelihood ratio test can be performed (Wilks, 1938). A likelihood ratio test statistic (TS) evaluates the preference of one source model versus a different source model. For example, the TS of finding two sources in the same dataset, both a disk and a point source, versus only finding a point source at the given position, is

$$TS = S_{point} - S_{point+disk}, \tag{8.1}$$

where $S$ is the fit statistic, $-2 * log(L)$ , the output of the log likelihood:

$$S = -2 * log(L). \tag{8.2}$$

The square-root of the TS for modeling the Gamma-Cgyni region with a model that includes a point source versus a model that includes only background emission is $\sqrt{TS} = 10.1$. The square-root of the TS for modeling the region with a model that includes a disk source versus a model that includes only background emission is $\sqrt{TS} = 19.3$. A likelihood was performed on a combined disk and point source model, where the point source was fit first, then the point source position fixed and the disk model added. The disk model had position and extension fixed at the post-fit positions of the disk only fit. The square-root of the TS for modeling the region with a model that includes both a disk and a point source versus a model with only a point source is $\sqrt{TS} = 25.1$. The square-root of the TS for modeling the region with a model that includes both a disk and a point source versus a model with only a disk source is $\sqrt{TS} = 19.0$. Both of the later two results indicate that the region is best modeled with some extended emission. This affirmation of extended emission from a likelihood analysis result matches the reports from previous VERITAS and recent MAGIC conclusions concerning extended emission.

## 8.5 Discussion

Both results from the new standard analysis performed with ITM and the 4D-MLM analysis support the conclusions of previous publications from IACTs that the Gamma-Cygni SNR produces enhanced VHE emission primarily along the north-western rim of the remnant. The extended gamma-ray morphology reported from the 4D-MLM results is consistent with certain regions of gamma-ray emission reported in a recent MAGIC publication on Gamma-Cygni. The fact that the 4D-MLM analysis was able to find some areas of emission consistent with a study performed by a separate instrument is evidence that the 4D-MLM is more sensitive than standard methods given that the exposure provided to the 4D-MLM (16.4 hrs) is less than the exposure of MAGIC publication (87 hrs). A 4D-MLM analysis on Gamma-Cygni will still benefit from datasets with more exposure since the extended source results do not report emission from the entire radio remnant, which the MAGIC study does. The significance distribution of the total Gamma-Cygni remnant, minus the region of enhanced emission associated with VER J2019+407, shown in Figure 8.6 d) indicates that there is VHE emission in regions of the remnant other than along the northern rim. A much deeper exposure is needed to say anything further about extended emission across the entire radio remnant.

A major goal of VHE studies of SNRs is interpretation of morphology and spectra in regards to the nature of particle acceleration. Improvements need to be made to the 4D-MLM spectral modeling before employing cosmic ray emission models to explain the data. Some inferences can be made through spatial coincidence between gamma-ray emission, other radiation, and potential target material. The circular shape of the remnant strongly suggests that the SNR has not been greatly affected on a large scale by interaction with surrounding medium. In radio, the most intense region is along the south-east rim, where there is no high significance VHE emission in the same region. There is weaker, but still enhanced radio emission along the north-west rim, in correlation with the localization of VHE emission (Ladouceur and Pineault, 2008). There are also multiple clumps of hard X-ray emission along the northern part of the remnant (Uchiyama et al., 2002). Gamma-ray source significance contours were overlay on CO J=1←0, 100 $\mu m$ intensity, and HI emission maps in Acciari and MAGIC Collaboration (2020). The CO emission is near the border of a significance contour, but not coincident with gamma-ray emission. The 100 $\mu m$ emission, which traces dust, and some H1 emission does coincide with significant MAGIC gamma-ray emission along the northwestern rim. The morphology of the gamma-ray emission and association with other radiation and coincidence with some molecular material supports a hadronic scenario where the supernova shock-waves are slamming into local abundances of protons. However, without confident distance measurements of molecular structures interaction of the SNR with surrounding material cannot be claimed at this point. Better understanding of the region local to Gamma-Cygni would benefit from future observations of molecular material (Acciari and MAGIC Collaboration, 2020).

Conclusions that can be made in this work about the morphology of Gamma-Cygni are limited due to a few concerns. Firstly, the VERITAS PSF is asymmetric and the PSF asymmetry is energy and offset dependent. In the likelihood performed previously, the PSF model is symmetric. Therefore, this work refrains from making any detailed conclusions about small scale morphology in Gamma-Cygni. This includes distinguishing separate regions of emission and energy dependence of the emission regions. The lowest energy range, from 300-479 GeV, continues to demonstrate significant mismatch between data and the source region model, as seen in residual maps in Figure 8.17. This trend of deviation is consistent with the validation studies performed in Chapter 7, where it was concluded that the background rates change more rapidly with energy at low energy. The true background rate is likely no longer azimuthally symmetric (Mohrmann et al., 2019), the background template is azimuthally symmetric. In order to implement improvements to the 4D-MLM and produce confident results down to 300 GeV changes need to be make to the Gammapy software. New tools need to be added to create multidimensional PSF and background models. Statistical uncertainties needs to be added to the IRF format and likelihood terms.

Future analysis with the 4D-MLM and Gammapy framework will include observations taken on Gamma-Cygni during the V6 epoch. The V6 epoch Gamma-Cygni runs were used in standard analysis, with results presented in Section 8.2.1. The increase of exposure produced a higher significance of emission associated with VER J2019+407 and results in Figures 8.6 and 8.5 point to the presence of additional sources and regions of VHE emission across the radio remnant. Data from the V6 epoch was not included in the likelihood analysis presented in this work due to the overhead time taken to generate IRFs for both event classes in the V6 epoch. There are 40 hours of additional time allocated for VERITAS observations on Gamma-Cygni during the spring and summer months of 2022. With combined V5 and V6 data there now exists a substantial VERITAS exposure on Gamma-Cygni. A combined analysis of Gamma-Cygni and TeV J2032+4107 can also be performed with the 4D-MLM to search for VHE orginating from the Cygnus Cocoon, an extended source visible to both HAWC and *Fermi*-LAT that extends across and between Gamma-Cygni and TeV J2032+4107.

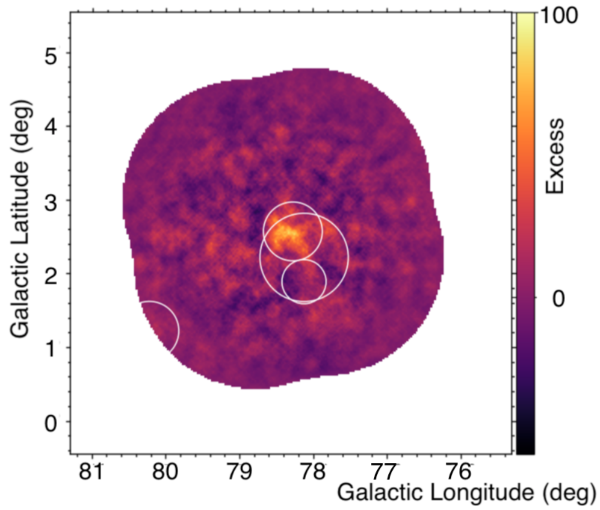


(a) Gamma Cygni, without ITM

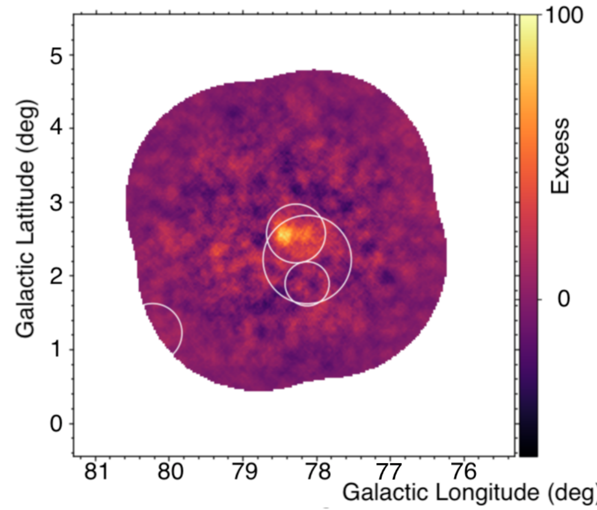


(b) Gamma Cygni, with ITM

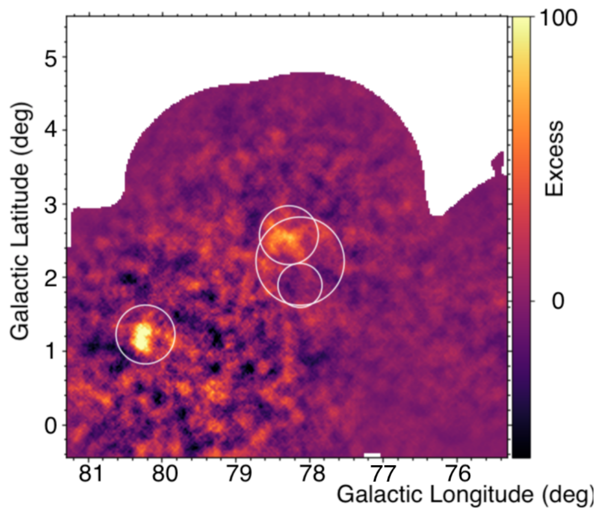


(a) all runs, without ITM

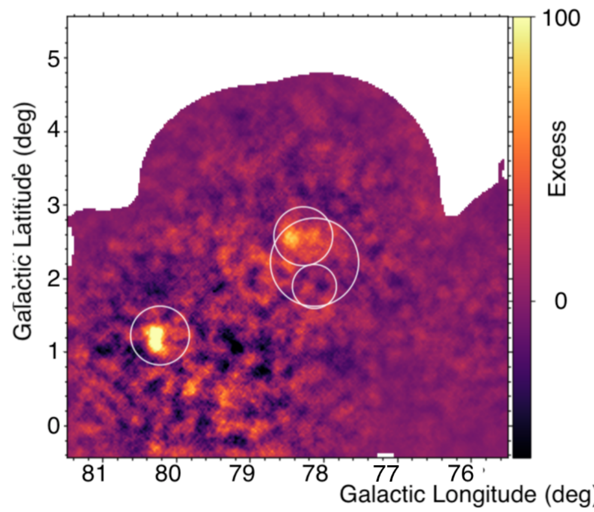


(b) all runs, with ITM

Figure 8.2: Excess count maps of observations taken on Gamma Cygni and surrounding regions in the V5 epoch, without applying ITM versus with ITM. The large white circle denotes the Fermi-LAT extended source, which has been excluded from background regions. The white circle at the left lower edge of the map is centered on another gamma-ray source, TeV J2032+4130. The top row of plots includes V5 runs only taken directly on Gamma-Cygni. The bottom row contains additional V5 runs surrounding and overlapping the Gamma-Cgyni extension.

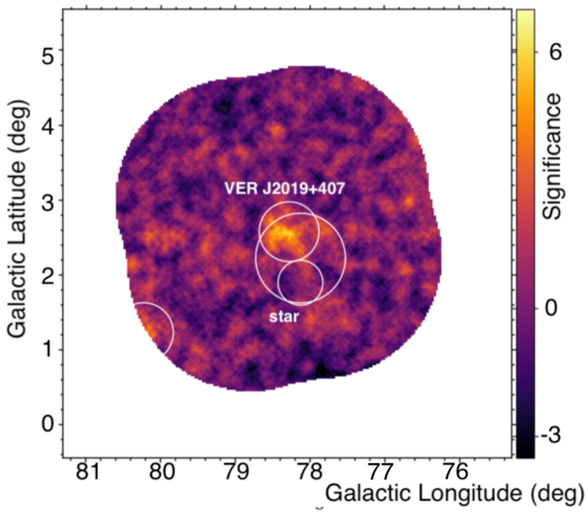


(a) Gamma Cygni, without ITM

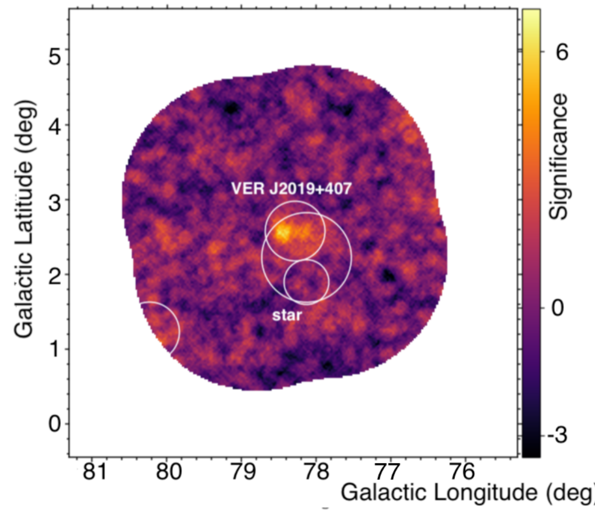


(b) Gamma Cygni, with ITM

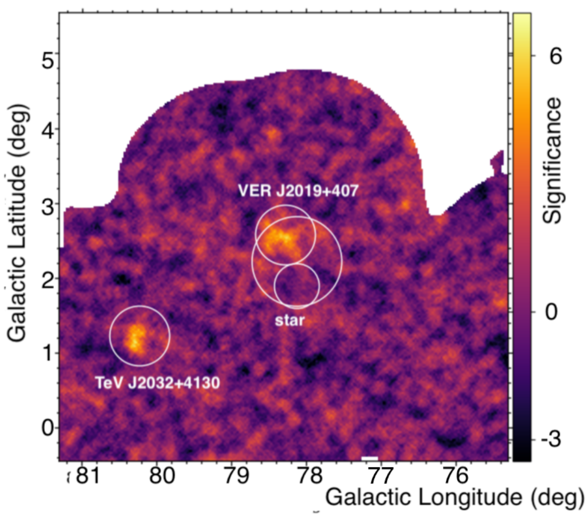


(a) all runs, without ITM

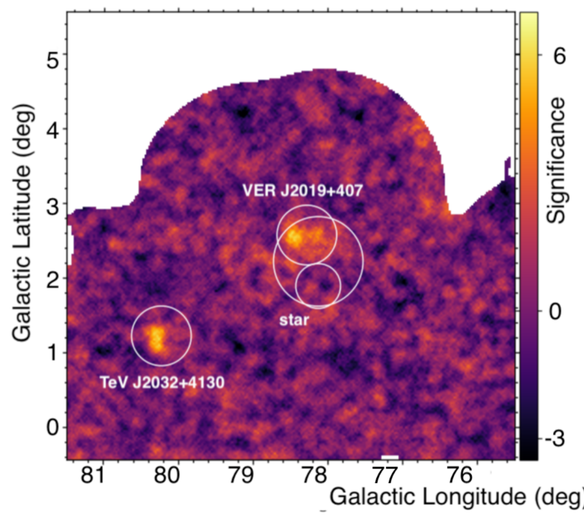


(b) all runs, with ITM

Figure 8.3: Significance maps of observations taken on Gamma Cygni and surrounding regions in the V5 epoch, without applying ITM versus with ITM. The large white circle denotes the Fermi-LAT extended source, which has been excluded from background regions. The white circle at the left lower edge of the map is centered on another gamma-ray source, TeV J2032+4130. The top row of plots includes V5 runs only taken directly on Gamma-Cygni. The bottom row contains additional V5 runs surrounding and overlapping the Gamma-Cgyni extension.

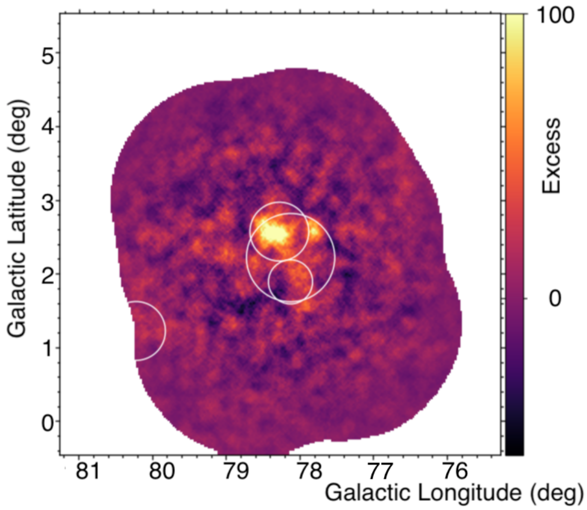


(a) excess counts, without ITM

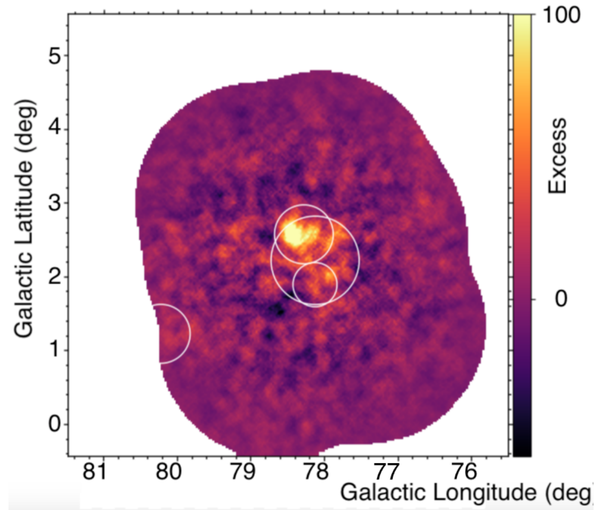


(b) excess counts, with ITM

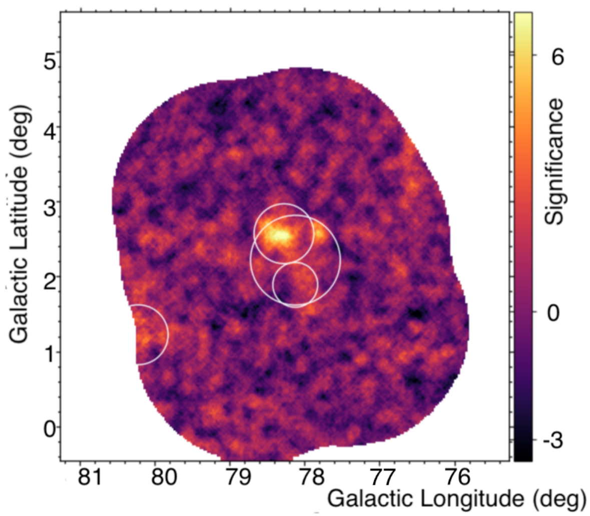


(a) significance, without ITM

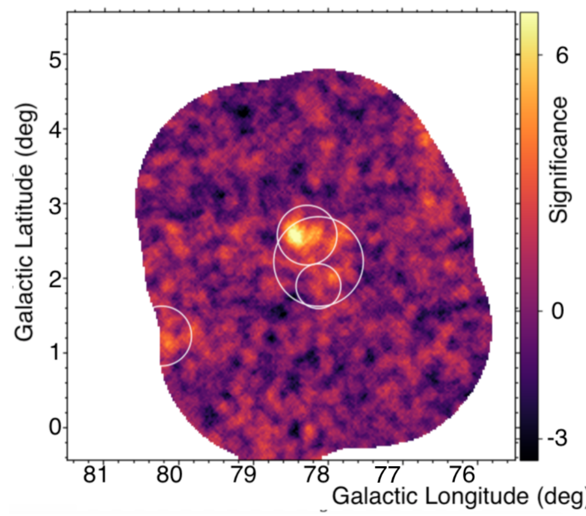


(b) significance, with ITM

Figure 8.4: Significance maps of observations only on Gamma-Cygni from combined V5 and V6 data, without applying ITM versus with ITM. The large white circle denotes the Fermi-LAT extended source, which has been excluded from background regions. The white circle at the left lower edge of the map is centered on another gamma-ray source, TeV J2032+4130.

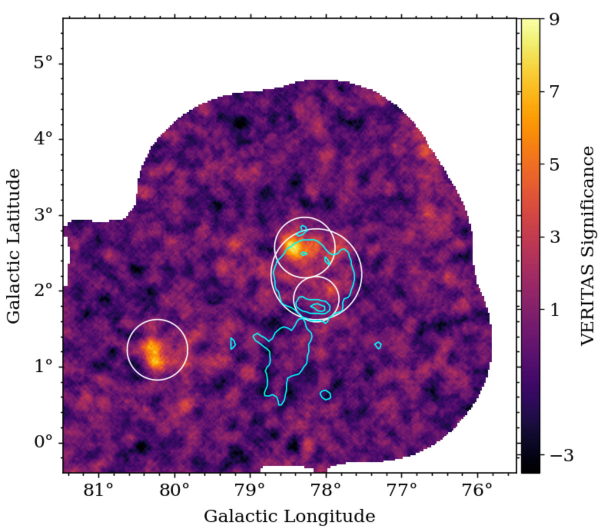


(c) Scale -3 to 9

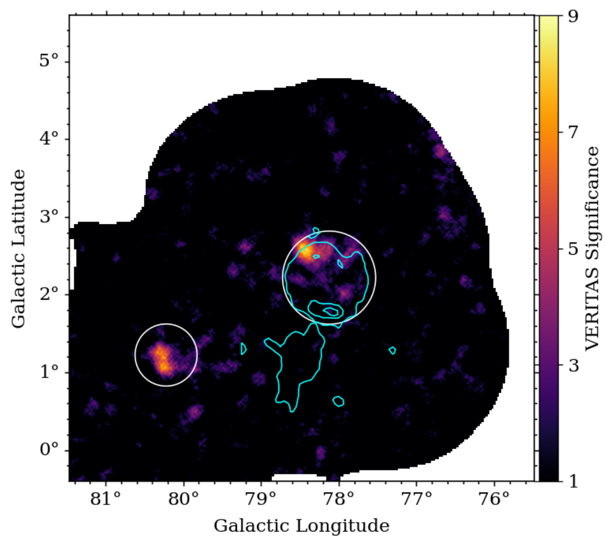


(d) Scale 1 to 9

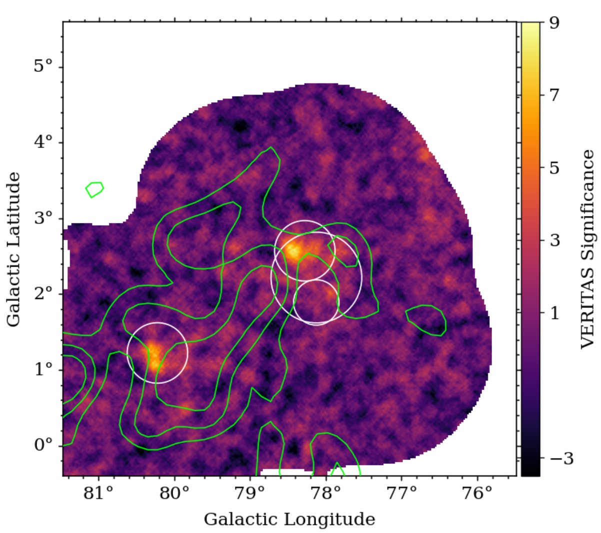


(c) Scale -3 to 9

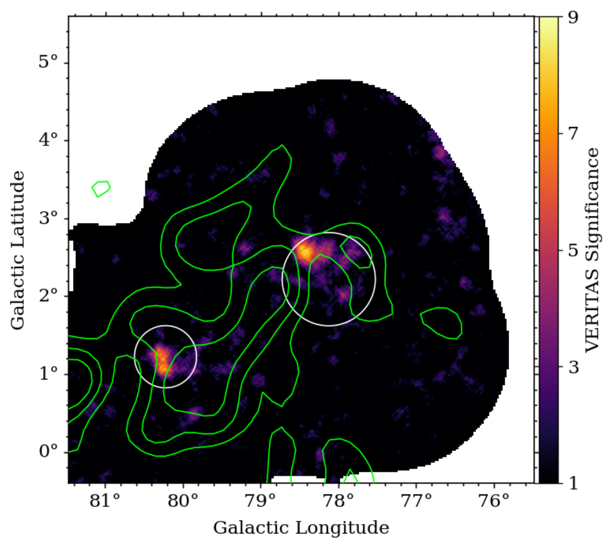


(d) Scale 1 to 9

Figure 8.5: Significance maps of combined V5 and V6 observations on Gamma-Cgyni and TeV J2032+4130. The right maps are scaled down to one to clearly show bins with significance greater than one. The top and bottom rows have the same significance maps with different contours. The green contours are photon counts of the *Fermi*-LAT Cygnus Cocoon from 10 to 100 GeV Ackermann and et al. (2011). The cyan contours are radio contours of the 408 MHz observation by the CGPS.

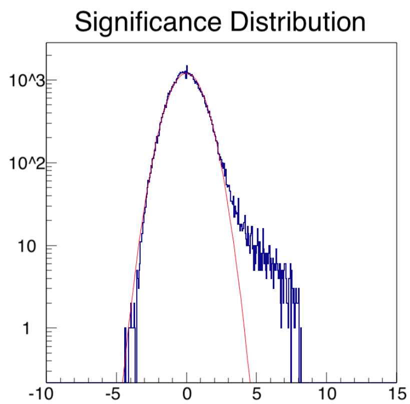


(a) No exclusions

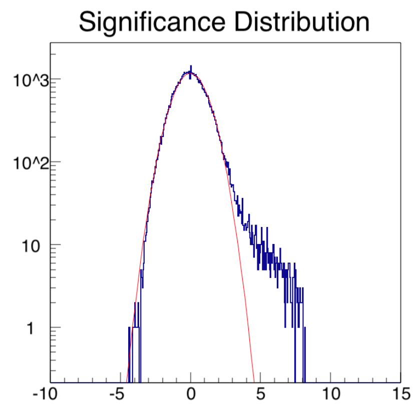


(b) Exclude TeV J2032+4130

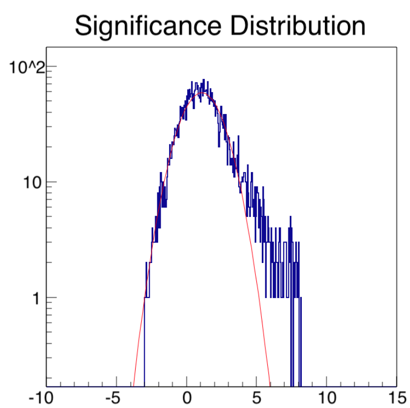


(c) Disk and VER J2019+407

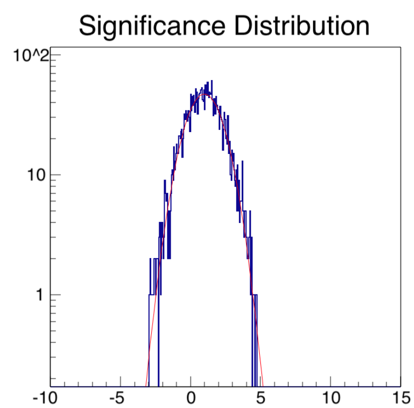


(d) Disk Only

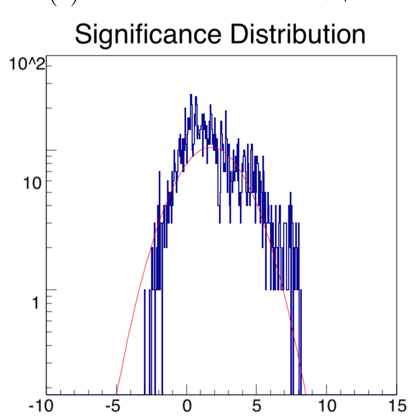


(e) VER J2019+407

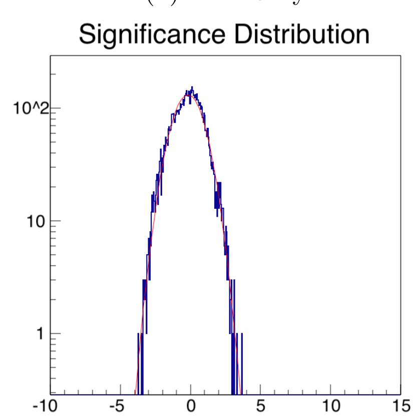


(f) No known gamma-ray sources

Figure 8.6: Significance distributions of combined V5 and V6 observations on Gamma-Cgyni and TeV J2032+4130. The significance distribution plot f) is filled from bins in a 0.6° radius circle in a source-free region of the skymap.

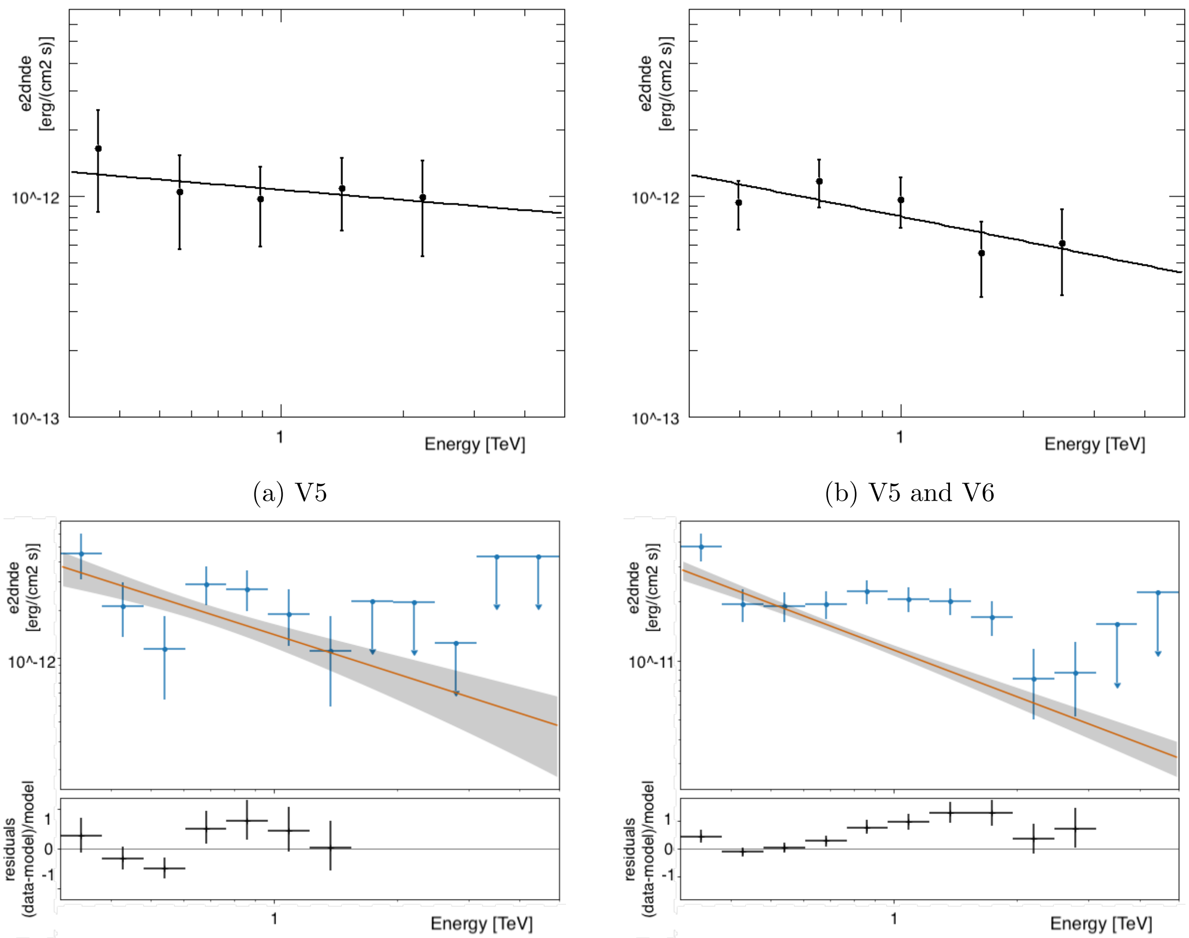


Figure 8.7: Gamma-Cygni spectrum, fit with a power-law. The top row is the spectrum from a slightly extended source resulting from reflected region analysis. The bottom plots are the spectrum of a point source located at VER J2019+407 or a disk source, after the likelihood performed with Gammapy. An upper limit is plotted when the test statistic of the flux point is less than 4.

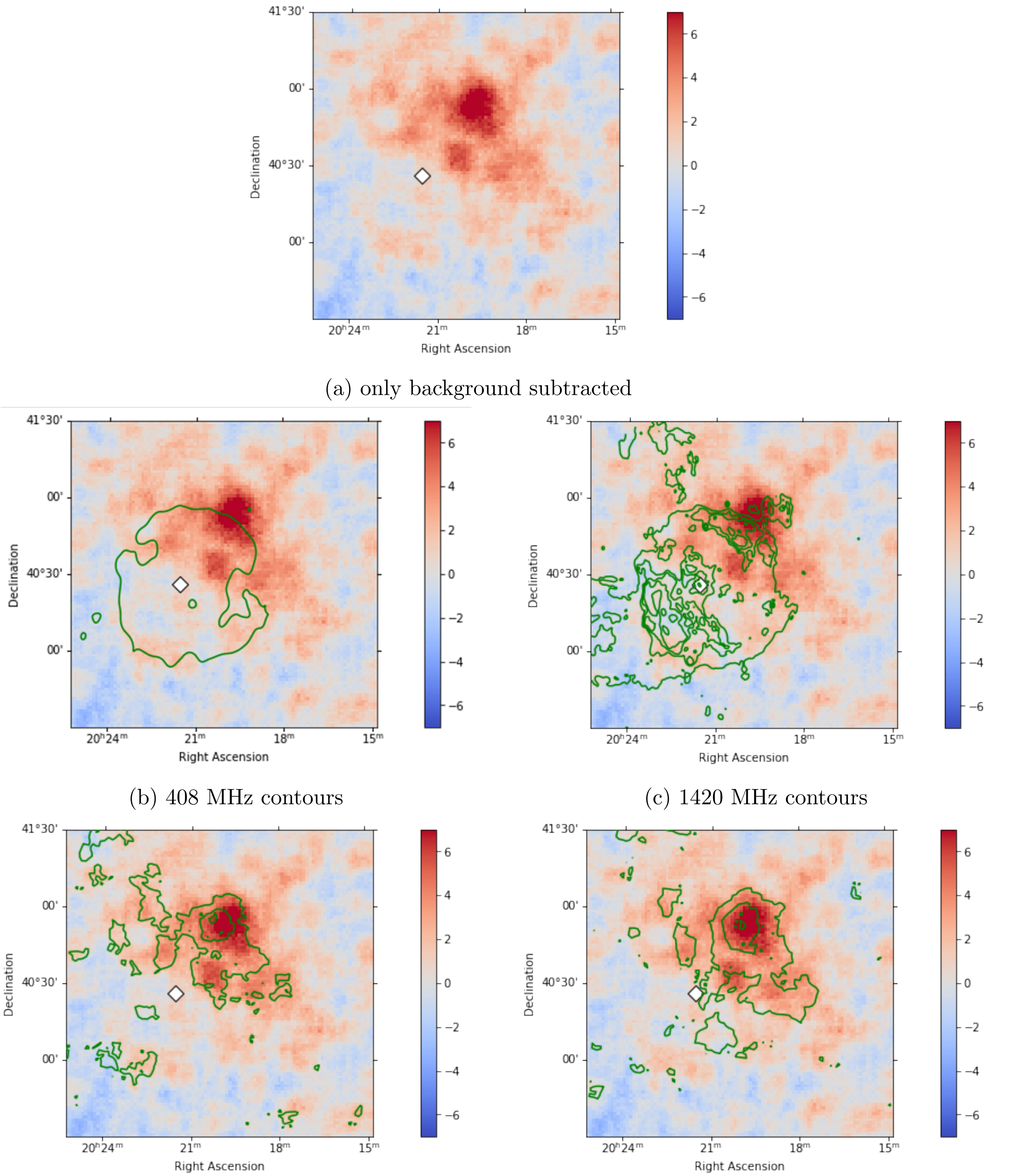


(a) only background subtracted

(b) 408 MHz contours

(c) 1420 MHz contours

(d) RBM V5 contours

(e) RBM V5+V6 contours

Figure 8.8: Residual maps of $\sqrt{TS}$, within 300-5000 GeV. The maps are overlay with green contours derived from the significance maps of RBM analyses and Canadian Galactic Plane Survey 1420 MHz and 408 MHz observations. The significance levels of V5 and V5+V6 contours are 2,4,5.5 and 2,5,8. The black circle or white diamond marks the position of the pulsar 4FGL J2021.5+4026.

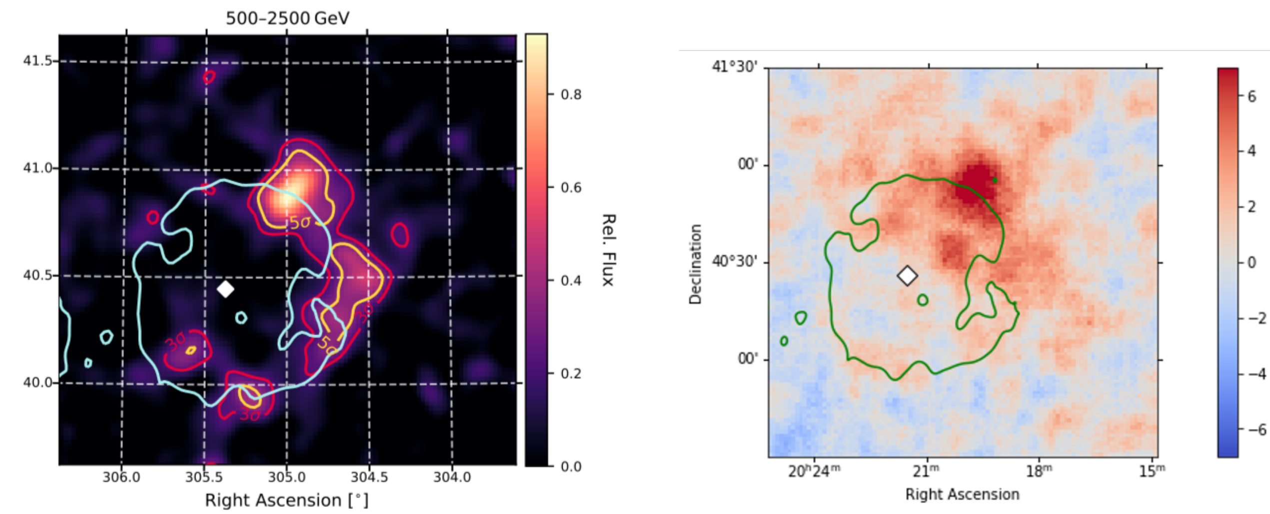


Figure 8.9: **Left:** A MAGIC Gamma-Cygni sky map in units of relative flux, $E > 250GeV$. Regions exceeding 3 (5) local, pre-trial significance for a point source are indicated by red (yellow) contours Acciari and MAGIC Collaboration (2020). **Right:** Residual map of $\sqrt{TS}$, within 300-5000 GeV. Both plots are overlaid with contours derived from Canadian Galactic Plane Survey 408 MHz observations. The white diamond marks the position of the pulsar 4FGL J2021.5+4026.

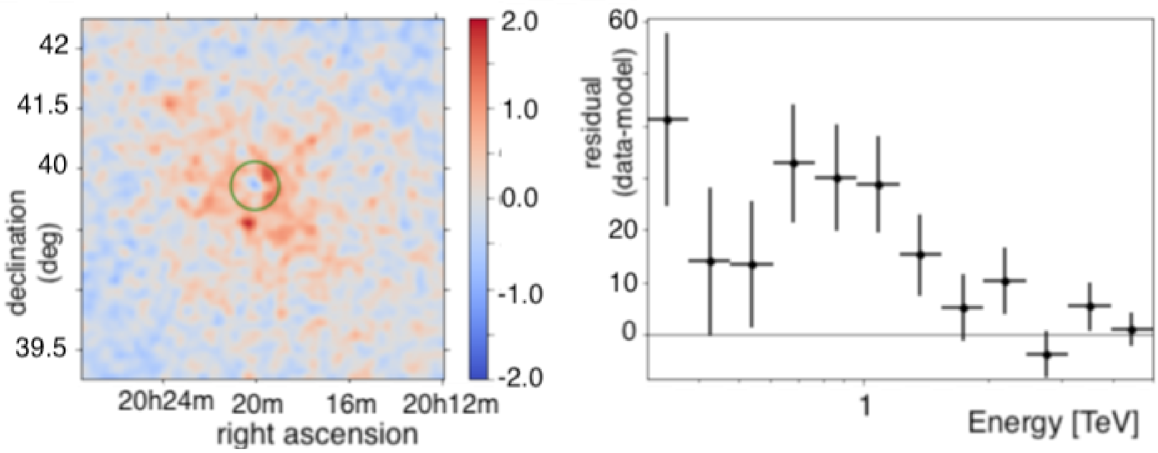


(a) Point Source Fit

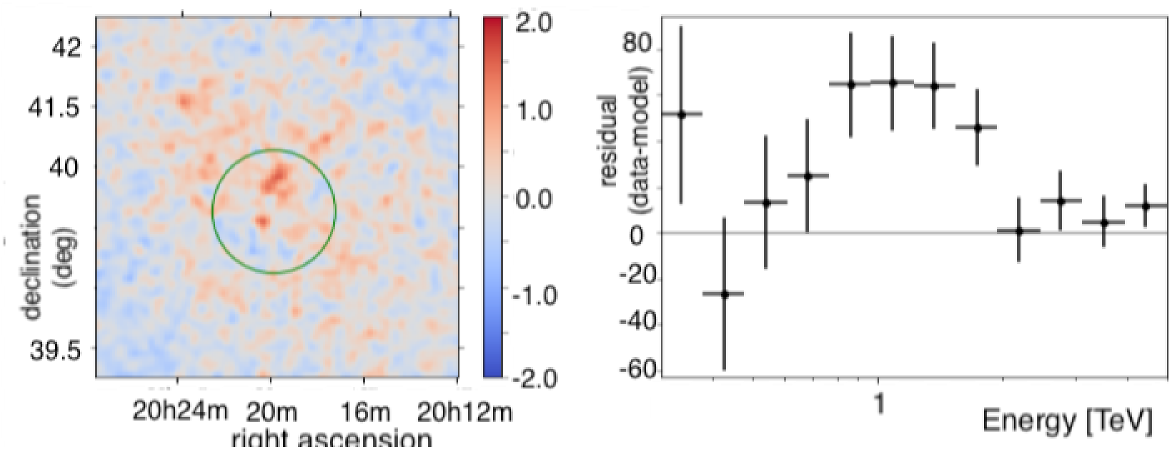


(b) Disk Source Fit

Figure 8.10: Energy dependent residual plots smoothed with a 0.035° Gaussian kernel. Plots a) and b) are overlaid with a circle centered on the source position. The circle in plot b) matches the fit extension of the disk, $r \sim 0.5°$.

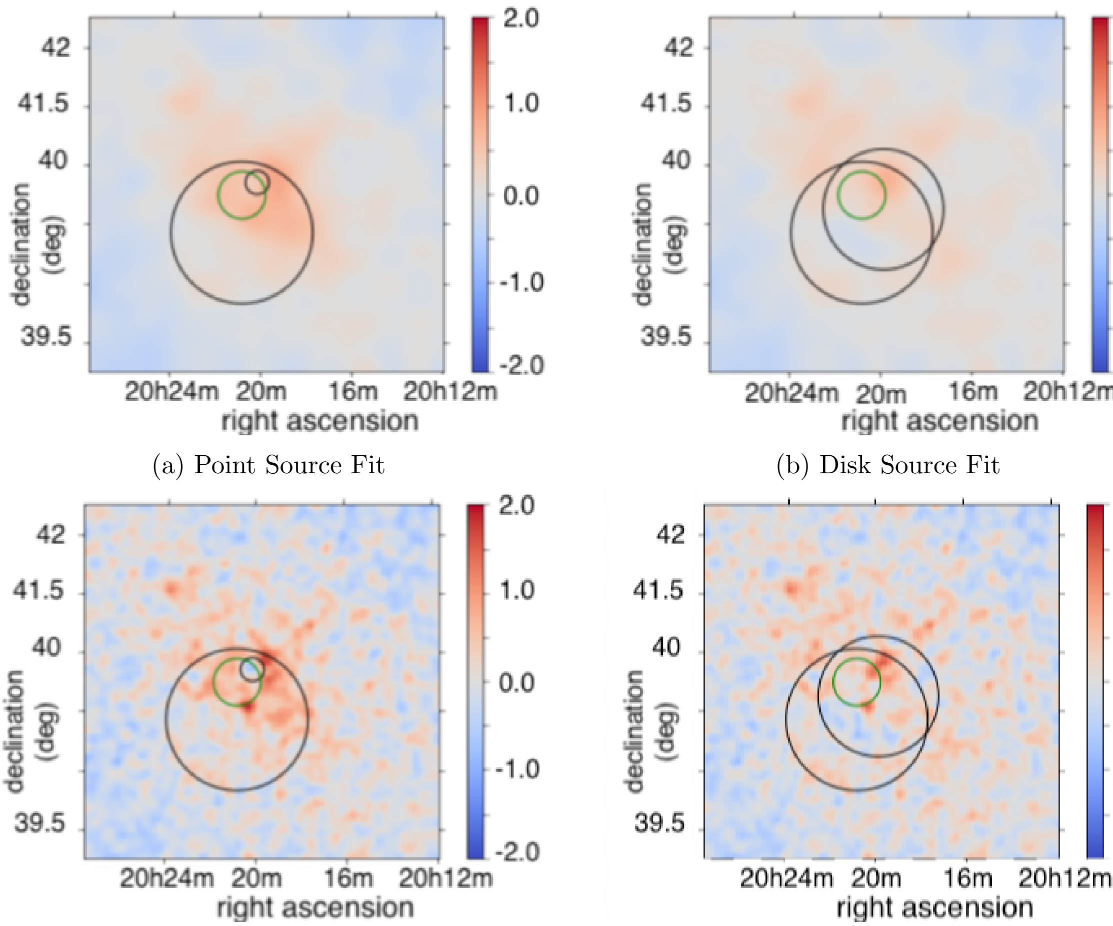


(a) Point Source Fit

(b) Disk Source Fit

(c) Point Source Fit

(d) Disk Source Fit

Figure 8.11: Residual plots. Plots c) and d) are smoothed with a 0.035° Gaussian kernel and plots a) and b) are smoothed with a 0.1° Gaussian kernel. The circle in plots b) and d) matches the fit extension of the disk, $r \sim 0.5°$. In plots a) and c), the small black circle marks the position of the point source. The green circle marks the position of VER J2019+407 and the large black circle marks the *Fermi*-LAT extension.

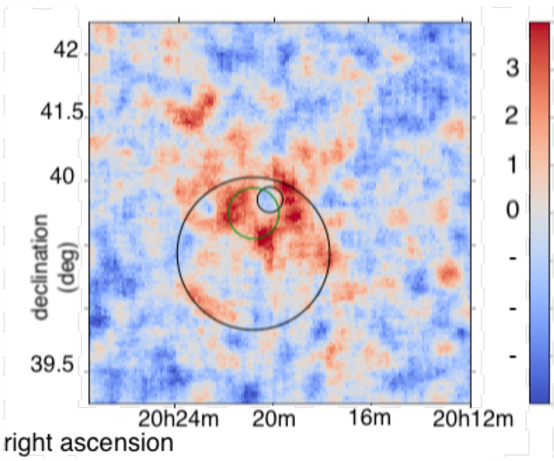


(a) point source, 300-600 GeV

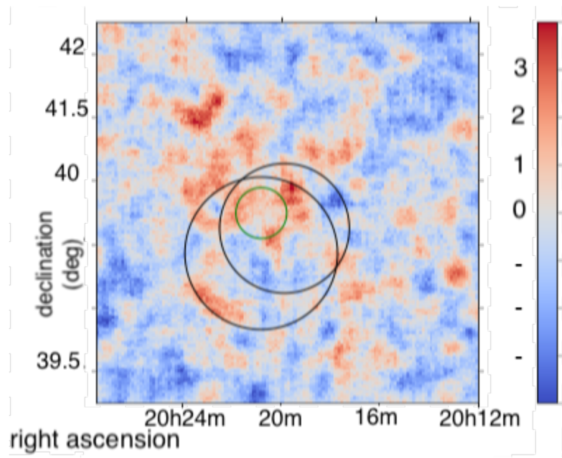


(b) disk source, 300-600 GeV

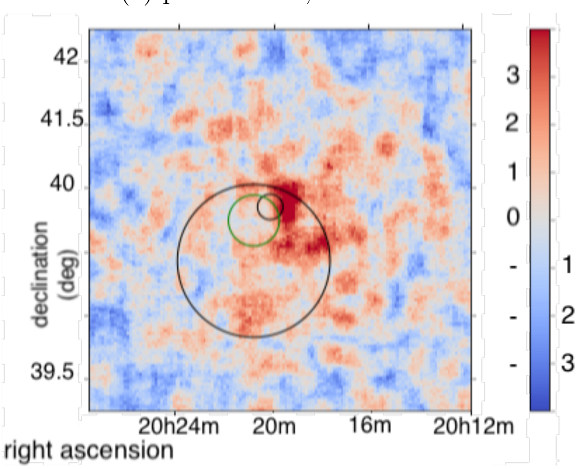


(c) point source, 600-1000 GeV

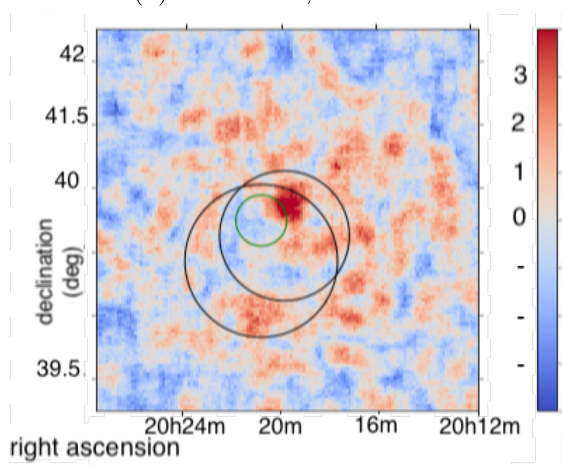


(d) disk source, 600-1000 GeV

Figure 8.12: Maps of $\sqrt{TS}$, point source versus disk fit, divided in bins of energy: 300-600 GeV and 600-1000 GeV. The small black circle marks the position of the point source, the green circle marks the position of VER J2019+407, and the large black circle marks the extent of the *Fermi*-LAT disk extension. The smaller black circle marks the extension of the fitted disk, $r \sim 0.5$.

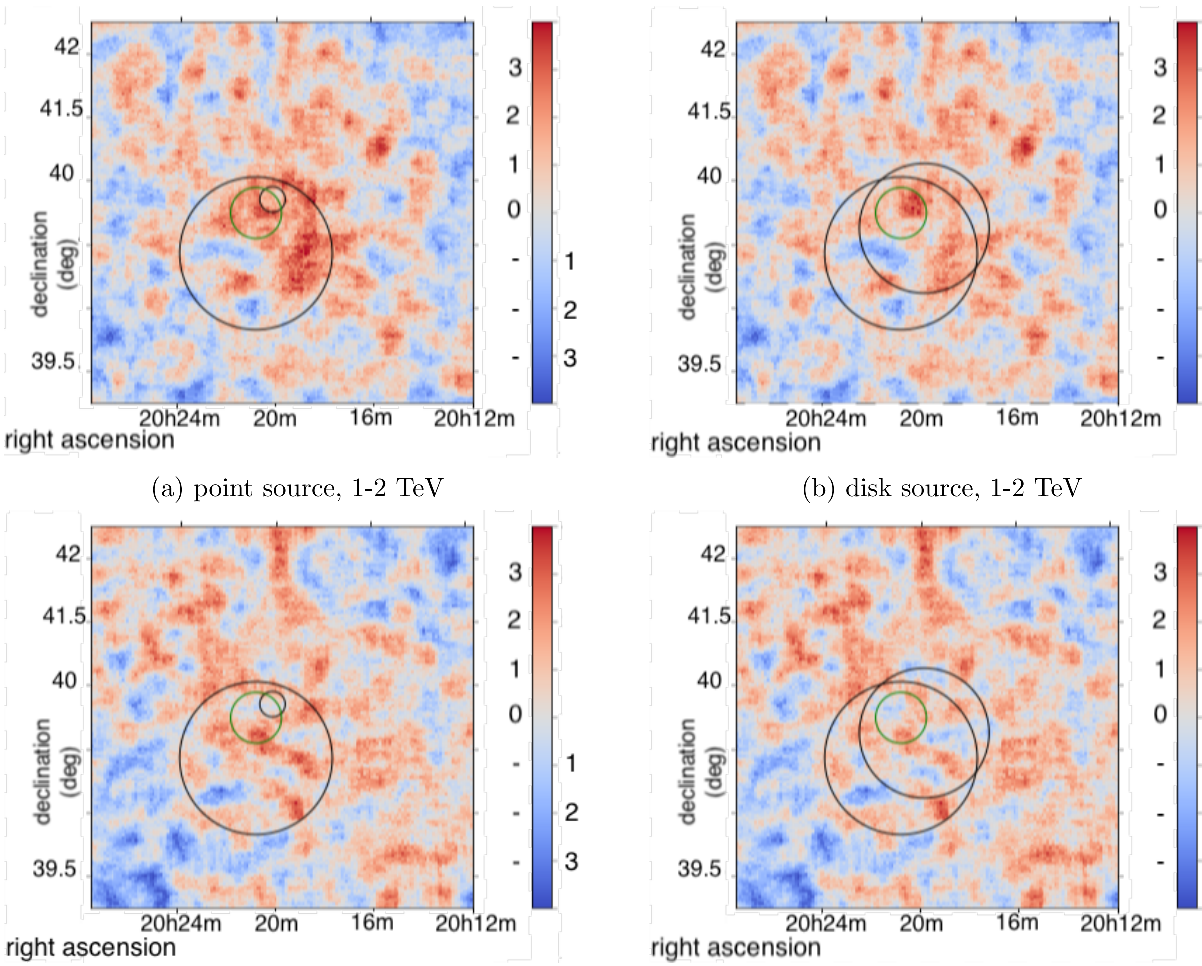


(a) point source, 1-2 TeV

(b) disk source, 1-2 TeV

(a) point source, 2-5 TeV

(b) disk source, 2-5 TeV

Figure 8.13: Maps of $\sqrt{TS}$, point source versus disk fit, divided in bins of energy: 1-2 TeV and 2-5 TeV. The small black circle marks the position of the point source, the green circle marks the position of VER J2019+407, and the large black circle marks the extent of the *Fermi*-LAT disk extension. The smaller black circle marks the extension of the fitted disk, $r \sim 0.5$.

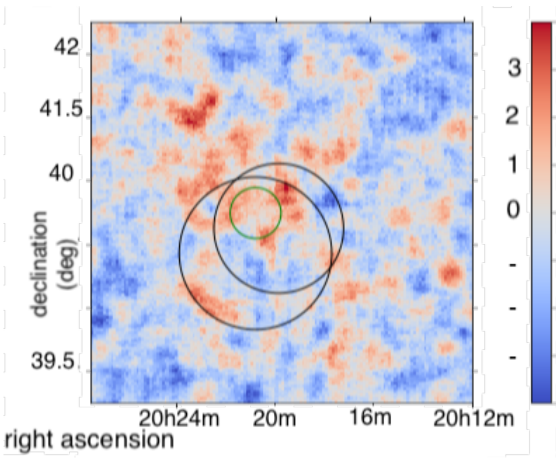


(b) disk source, 300-600 GeV

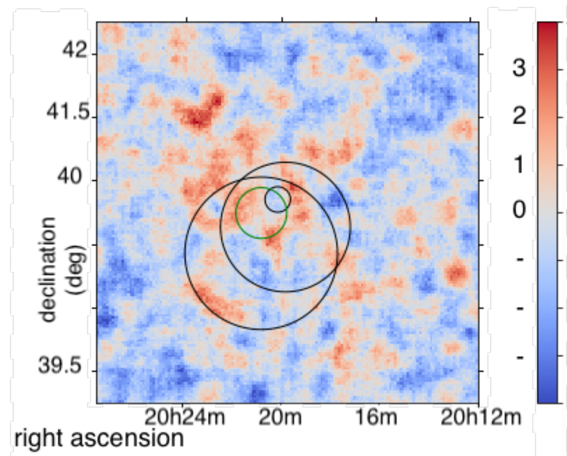


(c) disk+point source, 300-600 GeV

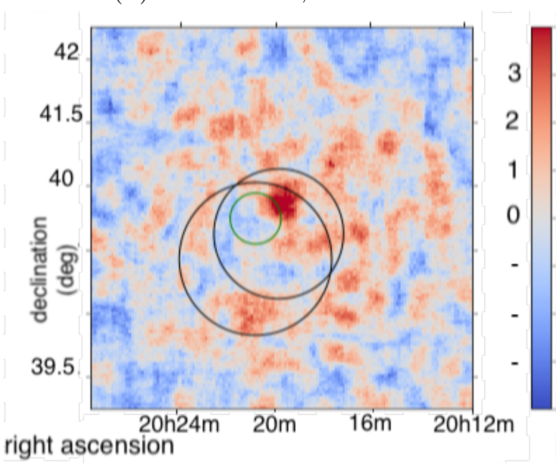


(b) disk source, 600-1000 GeV

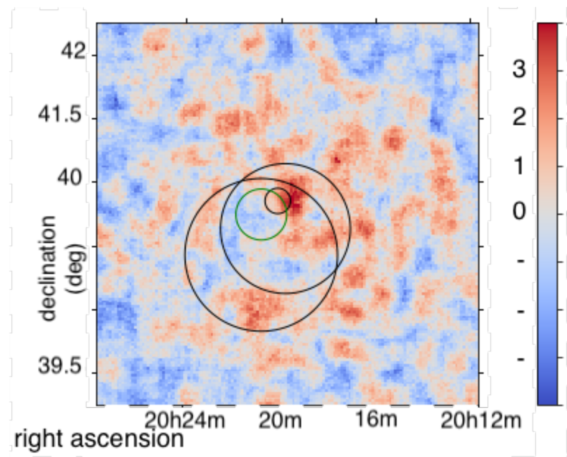


(c) disk+point source, 600-1000 GeV

Figure 8.14: Maps of $\sqrt{TS}$, disk source versus disk+point fit, divided in bins of energy: 300-600 GeV and 600-1000 GeV. The small black circle marks the position of the point source, the green circle marks the position of VER J2019+407, and the large black circle marks the extent of the *Fermi*-LAT disk extension. The smaller black circle marks the extension of the fitted disk, $r \sim 0.5$.

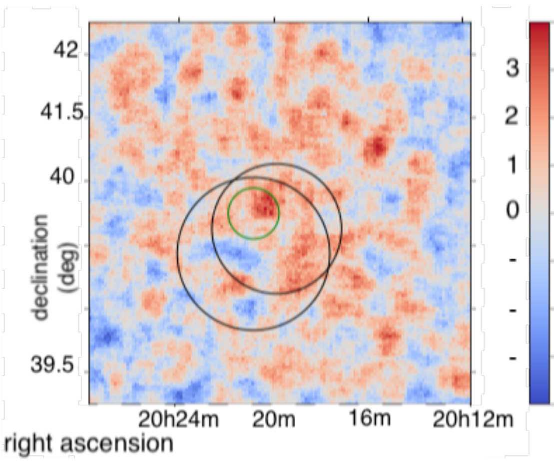


(b) disk source, 1-2 TeV

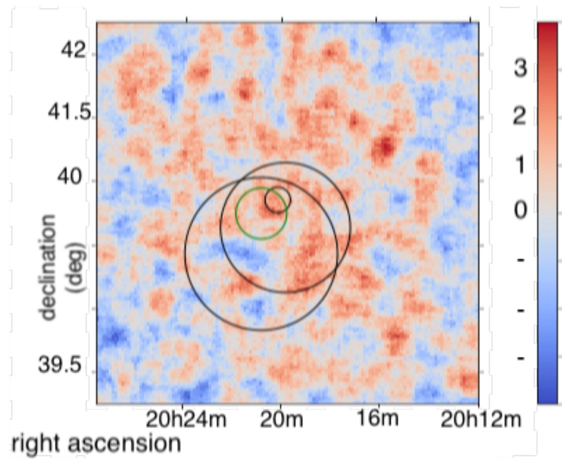


(c) disk+point source, 1-2 TeV

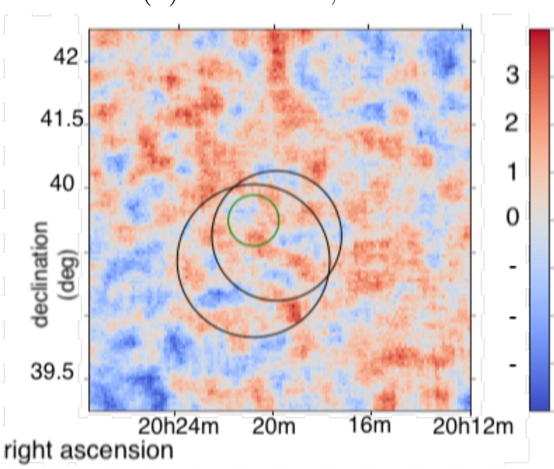


(b) disk source, 2-5 TeV

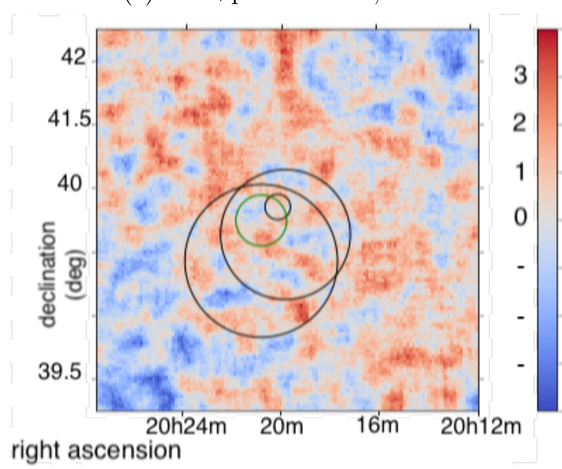


(c) disk+point source, 2-5 TeV

Figure 8.15: Maps of $\sqrt{TS}$, disk source versus disk+point fit, divided in bins of energy: 1-2 TeV and 2-5 TeV. The small black circle marks the position of the point source, the green circle marks the position of VER J2019+407, and the large black circle marks the extent of the *Fermi*-LAT disk extension. The smaller black circle marks the extension of the fitted disk, $r \sim 0.5$.

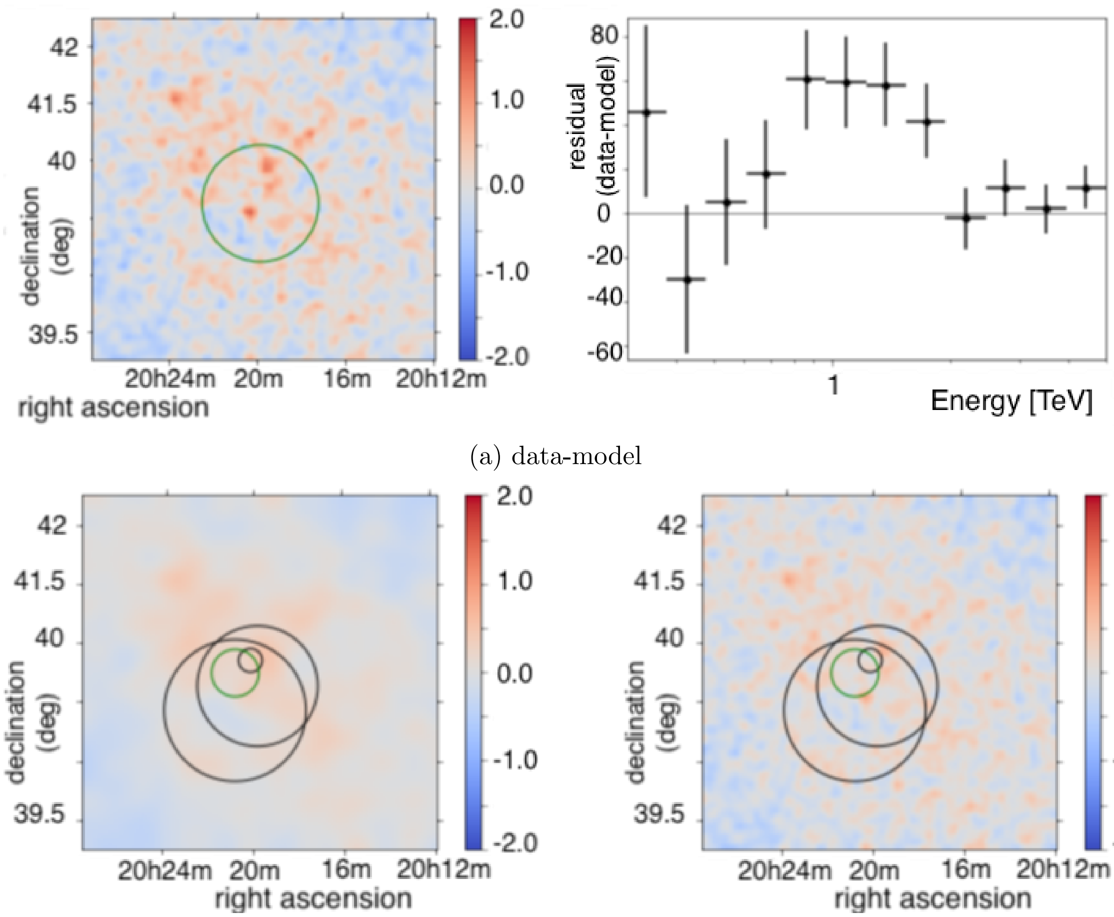


(a) data-model

(b) data-model

(c) data/$\sqrt{model}$

Figure 8.16: Residual plots for Gammapy analysis on Gamma-Cygni data fit with both a point source and disk, after smoothing with a 0.035 Gaussian kernel or a 0.1° Gaussian kernel. Plot a) is overlaid with a circle centered on the source position and matching the fit extension of the disk, $r \sim 0.5°$. In plots b) and c), the small black circle marks the position of the point source, the green circle marks the position of VER J2019+407, and the large black circle marks the *Fermi*-LAT extension. The medium black circle marks the extension of the fitted disk, $r \sim 0.5°$.

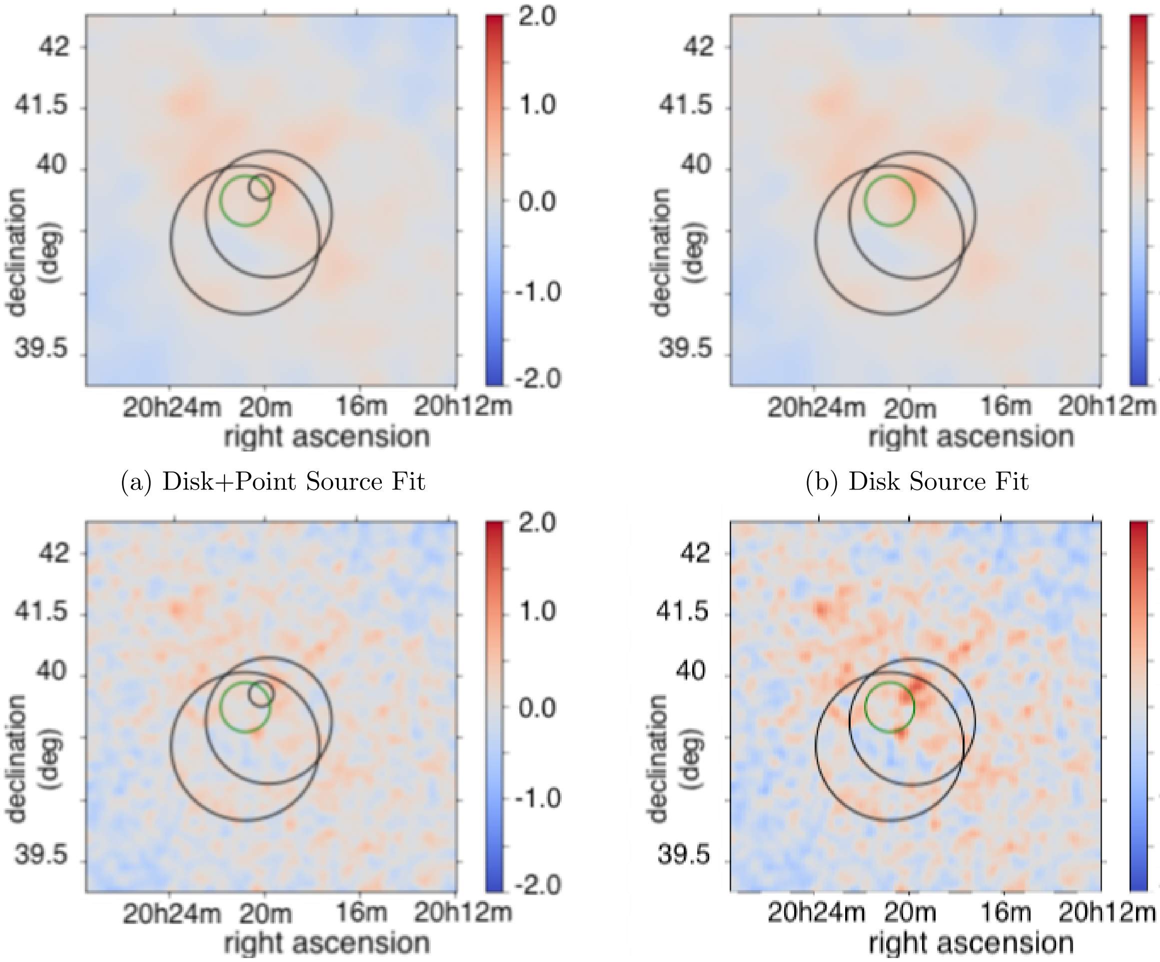


(a) Disk+Point Source Fit

(b) Disk Source Fit

(c) Disk+Point Source Fit

(d) Disk Source Fit

Figure 8.17: Gamma-Cygmi residual plots for disk and disk+point spatial models. Plots c) and d) are smoothed with a 0.035° Gaussian kernel and plots a) and b) are smoothed with a 0.1° Gaussian kernel. The small black circle marks the position of the point source, the green circle marks the position of VER J2019+407, and the large black circle marks the *Fermi*-LAT extension. The medium black circle marks the extension of the fitted disk, $r \sim 0.5°$.

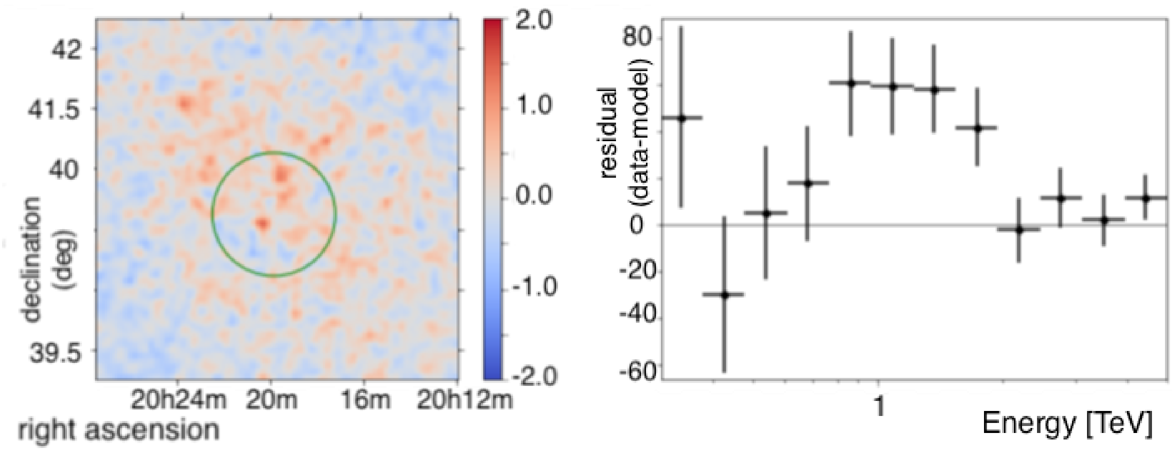


(a) Disk+Point Source Fit

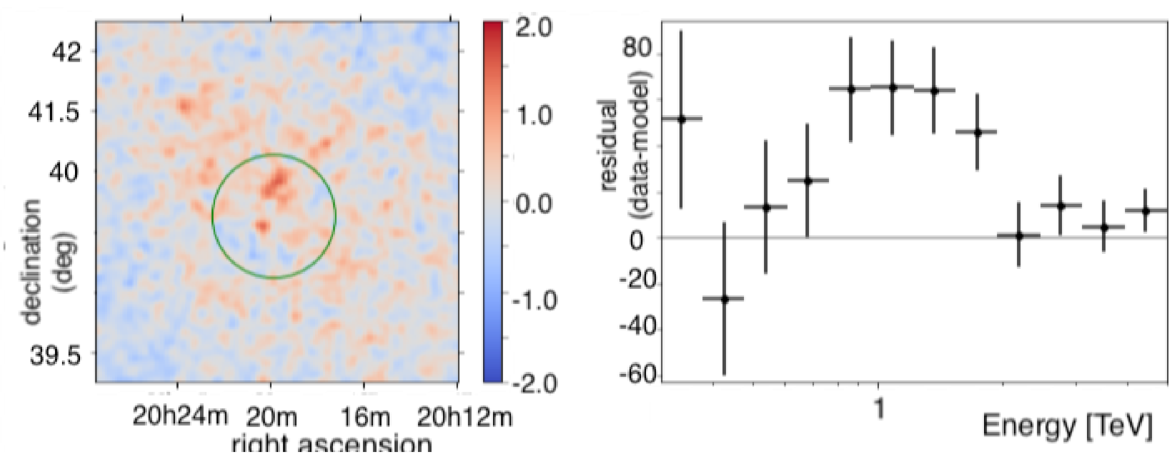


(b) Disk Source Fit

Figure 8.18: Energy dependent Gamma-Cygmi residual plots for disk and disk+point spatial models. Plots a) and b) are smoothed with a 0.035° Gaussian kernel and are overlaid with a circle centered on the source position and matching the fit extension of the disk, $r \sim 0.5°$.

# CHAPTER 9. SUMMARY AND CONCLUSION

This thesis has presented validation of multiple components of and the full implementation of a 4D-Maximum Likelihood Method (4D-MLM). The motivation behind the development of this new technique are the several VERITAS galactic targets with complex, largely extended sources, sometimes multiple sources and sometimes overlapping. Standard background estimation techniques that measure the background rates within in the same field of view fail in these cases. A likelihood technique which models the hadronic emission component in the VERITAS field of view will account for the remaining gamma-ray component and will therefore exhibit a superior performance to the standard methods for extended source analysis.

A series of chapters in the first part of this thesis summarized the telescope functionality, the challenges of accounting for overwhelming background emission, and the reasons for utilizing the symmetric King function to model the VERITAS point spread function (PSF). The maximum likelihood in three dimensions (2D coordinates and gamma-hadron separation parameter) was performed in the open analysis framework *Gammapy*, adding an additional dimension of energy. Analysis on real data was performed with a complete 4D-MLM. Initial results show consistency with standard analysis results. However, there are some areas where compromises on accuracy needed to be made and where deficiencies were discovered. A majority of this chapter focuses on the strategies for future improvement to the 4D-MLM as implemented in *Gammapy*.

## 9.1 Future Work

### 9.1.1 Point Spread Function Uncertainty

The VERITAS gamma-ray PSF is best fit with an asymmetric King function, as shown in Chapter 5. However, the need to store more than one dimension of the PSF kernel increases the demands on the temporary Gammapy software memory. Current versions of Gammapy are incapable of constructing a higher dimension PSF kernel at this time. A possible work around the limited memory of Gammapy is to develop the asymmetric King Function PSF kernel outside Gammapy operations, to be imported during the data analysis.

In the validation studies of the 4D-MLM performed on Crab data, taken at 0.5 degree wobble offset, none of the residuals maps contained asymmetries associated with an incorrect PSF model. However, the difference between the symmetric and asymmetric model increases at larger offset. Therefore, it stands to reason that a systematic error must be associated with small scale changes in morphology at large offset. For models of largely extended sources with no fine structure a symmetric PSF is sufficient.

A concern when fitting the King function to the VERITAS gamma-ray PSF is the lack of information about the PSF dependence on wobble direction in the camera. The CORSIKA-grISUdet simulations are produced only along one wobble direction, North of the source position(Cardenzana, 2017). Since the 2D spatial distribution is asymmetric at large offsets, the PSF shape is dependent on both North-South directions and East-West directions, suggesting the possibility of dependence on azimuth in the camera. Due to the production of simulations at only one offset direction, this dependence is difficult to study.

During the 2021-2022 observing season, VERITAS has a high priority task to observe the Crab at 1.0° and 1.5° offset from the camera center. A completed allocation will greatly increase the Crab exposure at large offset and make possible Monte Carlo-to-data comparisons of the PSF at those offsets. A MC-to-data comparison has never been performed before on the VERITAS PSF above 0.5° offset. The main objectives to look for are how well the simulated asymmetry in the VERITAS PSF, both GrISUDet and CARE, matches the 2D distribution of Crab data.

### 9.1.2 Background Models

Previous work on the 3D-MLM, presented in Cardenzana (2017), expressed the limitations of the background models to sufficiently separate background emission from gamma-ray emission. The author of that work presented evidence that this was likely due to two reasons: falling short of controlling for all parameters that determine cosmic ray distribution across the VERITAS FoV and Poisson fluctuations in statistically limited background events. Systematic uncertainty is controlled by both matching observation parameters between select background fields and data. Software padding is also applied to the background runs in order that the average background noise matches the average noise of data runs.

In the previous iteration of the 3D-MLM the background discrimination template included finely binned MSW distributions; histograms bins ranging from 0.8-1.3, where gamma-ray emission peaks at MSW$\sim$ 1.0. Values of $MSW > 1$ were included in the template so that the background scaling factor could operate on events with little to no gamma-ray emission. Limited statistics and therefore statistical uncertainty was highly prevalent in the finely binned MSW distributions. Figure 6.1 shows examples of MSW templates used in the previous iteration of the 3D-MLM.

The Barlow Beeston method adds terms to the likelihood calculation which take into account the statistical errors of models. In section 6.2, performance studies of the likelihood, modified with Barlow Beeston terms, were carried on the distribution of a gamma-hadron separation parameter, MSW. The results of these single parameter studies demonstrated that Barlow Beeston does mitigate against the likelihood returning a false signal when a null result is the expected outcome. Since limited statistics will always be a factor in likelihood analysis in cases where real data is employed to model the background, the full 4D-MLM needs to include additional terms in the likelihood for an analysis with Gammapy. As of the writing of this work Barlow Beeston terms have not been applied due to the lack of infrastructure in Gammapy to store and pass statistical information for each model offset and energy bin.

In the meantime, an approach was taken to reduce the binning of the MSW template. In the current iteration of the 4D-MLM MSW values are split between two event classes: $0.8 < MSW < 1.1$ and $1.1 < MSW < 1.3$. When the likelihood is performed the two event classes share the same scale factor so that the scaling in the event class what contains trace amounts of gamma-ray emission will correctly scale the background level in the event class containing the vast majority of gamma-ray emission.

Both the use of the 4D-MLM with two event classes and, separately, applying Barlow Beeston terms to a likelihood on MSW templates, have been shown to produce a better fits between data and models. With the inclusion of a mechanism that will store and pass statistics it is possible to include Barlow Beeston terms in the likelihood for an analysis with Gammapy. Therefore, in the future, a complete and robust 4D-MLM will combine Gammapy tools with Barlow Beeston terms.

## 9.2 Final Conclusions

Validation of the 4D-MLM performance was determined by joint-likelihood on a bright point source, the Crab, and a blank field target, Ursa Minor. Future validation studies will be carried out to test how well the method reproduces the morphology and spectrum of other point sources and extended sources. These next studies will entail further blank field tests and an analysis on a slightly extended source with known morphology, IC 443. The blank field tests are of particular importance since they establish the robustness of background models in the likelihood. These validation studies will be performed for both likelihoods with and without Barlow Beeston terms.

A 4D-MLM is currently functioning and works with *Gammapy*, a software framework that will be the primary analysis tool for the next generation of IACTs, the Cherenkov Telescope Array (CTA). The preliminary results obtained from analyses on a point source and a blank field demonstrate that the post-fit likelihood results of combined background+source models exhibit good agreement with data for energy above 500 GeV. Below 500 GeV there is discrepancy between the data and models which is understood to be largely caused by an azimuthally symmetric background model being fit to data where the background rate is not azimuthally symmetric and a greater dependence background rate with on energy near the low energy threshold. Results of the likelihood performed on a moderately extended source, Gamma-Cygni, show large scale morphology which agrees well with results from previous IACT publications. A study with the 4D-MLM will be performed on the larger Gamma-Cygni dataset in the near future.

Multiple proposed improvements to the 4D-MLM IRFs have been described previously in this chapter. Once these improvements are tested and implemented the 4D-MLM will have reached its full potential as a VERITAS analysis method for gamma-ray sources of various extensions and morphology down to 300 GeV. The approach to analysis of extended gamma-ray sources, described in this work and in future improvements, may be useful to strategies for extended source analysis with CTA, especially since the 4D-MLM operates with *Gammapy*, the core library for the CTA science tools.

## BIBLIOGRAPHY

Abdo, A. A. and et al. (2012). Observation and Spectral Measurements of the Crab Nebula with Milagro. , 750(1):63.

Abdollahi, S. and et al. (2020). Fermi Large Area Telescope Fourth Source Catalog. , 247(1):33.

Abeysekara, A. U. and The HAWC Collaboration (2017). The 2HWC HAWC Observatory Gamma-Ray Catalog. , 843(1):40.

Abeysekara, E. and et al. (2018). A Very High Energy $\gamma$-Ray Survey toward the Cygnus Region of the Galaxy. , 861(2):134.

Acciari, V. A. and MAGIC Collaboration (2020). Study of the GeV to TeV morphology of the $\gamma$-Cygni SNR (G78.2+2.1) with MAGIC and Fermi-LAT. *arXiv e-prints*, page arXiv:2010.15854.

Ackermann, M. and et al. (2011). A Cocoon of Freshly Accelerated Cosmic Rays Detected by Fermi in the Cygnus Superbubble. *Science*, 334(6059):1103.

Ackermann, M. and et al. (2013a). Detection of the Characteristic Pion-Decay Signature in Supernova Remnants. *Science*, 339(6121):807–811.

Ackermann, M. and et al. (2013b). Determination of the Point-spread Function for the Fermi Large Area Telescope from On-orbit Data and Limits on Pair Halos of Active Galactic Nuclei. , 765(1):54.

Ahnen, M. L. and et al. (2017). A cut-off in the TeV gamma-ray spectrum of the SNR Cassiopeia A. , 472(3):2956–2962.

Albert, A. and HAWC Collaboration (2020). HAWC J2227+610 and Its Association with G106.3+2.7, a New Potential Galactic PeVatron. , 896(2):L29.

Albert, A. e. a. (2020). 3hwc: The third hawc catalog of very-high-energy gamma-ray sources. *The Astrophysical Journal Supplemental Series*, 247(1):33.

Aliu, E. and et al. (2013). Discovery of TeV Gamma-Ray Emission toward Supernova Remnant SNR G78.2+2.1. , 770(2):93.

Anderhub, H. and et al. (2010). FACT – the First Cherenkov Telescope using a G-APD Camera for TeV Gamma-ray Astronomy (HEAD 2010). *arXiv e-prints*, page arXiv:1010.2397.

Archambault, S., Hanna, D., and Griffin, S. (2013). In-situ measurements of whole-dish reflectivity for VERITAS. In *International Cosmic Ray Conference*, volume 33 of *International Cosmic Ray Conference*, page 3076.

Atwood, W. B. and et al. (2009). The Large Area Telescope on the Fermi Gamma-Ray Space Telescope Mission. , 697(2):1071–1102.

Baade, W. and Zwicky, F. (1934). Remarks on Super-Novae and Cosmic Rays. *Physical Review*, 46(1):76–77.

Beck, R. and Wielebinski, R. (2013). *Magnetic Fields in Galaxies*, volume 5.

Berge, D., Funk, S., and Hinton, J. (2006). Background modelling in very-high-energy gamma-ray astronomy. *Astronomy and Astrophysics*, 466.

Bird, R. A. (2015). *Probing Cosmic Rays with VERITAS: Observations of M31 and the Positron Fraction*. PhD thesis, University College Dublin.

Blasi, P. (2013). The origin of galactic cosmic rays. , 21:70.

Cardenzana, J. V. (2017). *A 3D Maximum Likelihood Analysis for Studying Highly Extended Sources in VERITAS Data*. PhD thesis, Iowa State University.

Christiansen, J. and VERITAS Collaboration (2017). Characterization of a Maximum Likelihood Gamma-Ray Reconstruction Algorithm for VERITAS. In *35th International Cosmic Ray Conference (ICRC2017)*, volume 301 of *International Cosmic Ray Conference*, page 789.

Cogan, P. (2006). *Nanosecond Sampling of Atmospheric Cherenkov Radiation Applied to TeV Gamma-Ray Observations of Blazars with VERITAS*. PhD thesis, University College Dublin.

Cogan, P. and VERITAS Collaboration, f. (2007). VEGAS, the VERITAS Gamma-ray Analysis Suite. In *30th International Cosmic Ray Conference (ICRC2007)*, International Cosmic Ray Conference.

Daniel, M. (2007). The veritas standard data analysis. volume 3, page 1325.

Deil, C. and et al. (2017). Gammapy - A prototype for the CTA science tools. In *35th International Cosmic Ray Conference (ICRC2017)*, volume 301 of *International Cosmic Ray Conference*, page 766.

Di Mauro, M., Manconi, S., and Donato, F. (2019). Detection of a $\gamma$ -ray halo around Geminga with the Fermi-LAT data and implications for the positron flux. , 100(12):123015.

Engel, R., Heck, D., and Pierog, T. (2011). Extensive Air Showers and Hadronic Interactions at High Energy. *Annual Review of Nuclear and Particle Science*, 61(1):467–489.

Fegan, D. (2019). *Cherenkov Reflections, Gamma-Ray Imaging and the Evolution of TeV Astronomy*. World Scientific Publishing Co. Pte. Ltd., Hackensack, NJ.

Fermi, E. (1949). On the Origin of the Cosmic Radiation. *Physical Review*, 75(8):1169–1174.

Fraija, N. and Araya, M. (2016). The Gigaelectronvolt Counterpart of VER J2019+407 in the Northern Shell of the Supernova Remnant G78.2+2.1 ($\gamma$ Cygni). , 826(1):31.

Funk, S. (2015). Ground- and Space-Based Gamma-Ray Astronomy. *Annual Review of Nuclear and Particle Science*, 65:245–277.

Gaensler, Bryan M.; Slane, P. O. (2006). The evolution and structure of pulsar wind nebulae. *Annual Review of Astronomy and Astrophysics*, 44(1):17–47.

Gaisser, T. K., Engel, R., and Resconi, E. (2016). *Cosmic Rays and Particle Physics, 2nd Edition*. Cambridge University Press, New York.

Ginzburg, V. L. and Syrovatskii, S. I. (1964). *The Origin of Cosmic Rays*.

Greisen, K. (1966). End to the Cosmic-Ray Spectrum? , 16(17):748–750.

Grieder, P. (2010). *Extensive air showers. High energy phenomena and astrophysical aspects. A tutorial, reference manual and data book. Vol. I and II*, volume 1.

Hanna, D., McCann, A., McCutcheon, M., and Nikkinen, L. (2010). An LED-based flasher system for VERITAS. *Nuclear Instruments and Methods in Physics Research A*, 612(2):278–287.

Hess, V. (2018). On the Observations of the Penetrating Radiation during Seven Balloon Flights. *arXiv e-prints*, page arXiv:1808.02927.

Higgs, L. A., Landecker, T. L., and Roger, R. S. (1977). The true extent of the gamma Cygni supernova remnant. , 82:718–724.

Hillas, A. M. (1984). The Origin of Ultra-High-Energy Cosmic Rays. , 22:425–444.

Hillas, A. M. (1985). Cerenkov Light Images of EAS Produced by Primary Gamma Rays and by Nuclei. In *19th International Cosmic Ray Conference (ICRC19), Volume 3*, volume 3 of *International Cosmic Ray Conference*, page 445.

Holder, J. (2005). Status and Performance of the First VERITAS telescope. In *29th International Cosmic Ray Conference (ICRC29), Volume 5*, volume 5 of *International Cosmic Ray Conference*, page 379.

Holder, J. and et al. (2013). The first veritas telescope. *Astroparticle Physics*, 25:391.

Hui, C. Y., Seo, K. A., Lin, L. C. C., Huang, R. H. H., Hu, C. P., Wu, J. H. K., Trepl, L., Takata, J., Wang, Y., Chou, Y., Cheng, K. S., and Kong, A. K. H. (2015). A Detailed X-Ray Investigation of PSR J2021+4026 and the $\gamma$-Cygni Supernova Remnant. , 799(1):76.

Karlsruhe Institute of Technology and Fabian Schmidt (2020). Corsika – an air shower simulation program.

Kieda, D. B. (2013). The Gamma Ray Detection sensitivity of the upgraded VERITAS Observatory. In *International Cosmic Ray Conference*, volume 33 of *International Cosmic Ray Conference*, page 1124.

Kraushaar, W., Clark, G. W., Garmire, G., Helmken, H., Higbie, P., and Agogino, M. (1965). Explorer XI Experiment on Cosmic Gamma Rays. , 141:845.

Krennrich, F. (2007). Status report from VERITAS. *Journal of Physics: Conference Series*, 60:34–39.

Ladouceur, Y. and Pineault, S. (2008). New perspectives on the supernova remnant G78.2+2.1. , 490(1):197–211.

Lagage, P. O. and Cesarsky, C. J. (1983). The maximum energy of cosmic rays accelerated by supernova shocks. , 125:249–257.

Leahy, D. A., Green, K., and Ranasinghe, S. (2013). X-ray and radio observations of the $\gamma$ Cygni supernova remnant G78.2+2.1. , 436(2):968–977.

Lessard, R. W., Buckley, J. H., Connaughton, V., and Le Bohec, S. (2001). A new analysis method for reconstructing the arrival direction of TeV gamma rays using a single imaging atmospheric Cherenkov telescope. *Astroparticle Physics*, 15(1):1–18.

Li, T. P. and Ma, Y. Q. (1983). Analysis methods for results in gamma-ray astronomy. , 272:317–324.

Lingenfelter, R. (2017). Cosmic rays from supernova remnants and superbubbles. *Advances in Space Research*, 62.

Longair, M. S. (2011). *High Energy Astrophysics, 3rd Edition.* Cambridge University Press, New York.

McCann, A., Hanna, D., Kildea, J., and McCutcheon, M. (2010). A new mirror alignment system for the veritas telescopes. *Astroparticle Physics*, 32:325–329.

Mohanty, G., Biller, S., Carter-Lewis, D., Fegan, D., Hillas, A., Lamb, R., Weekes, T., West, M., and Zweerink, J. (1998). Measurement of tev gamma-ray spectra with the cherenkov imaging technique. *Astroparticle Physics*, 9:15–43.

Mohrmann, L., Specovius, A., Tiziani, D., Funk, S., Malyshev, D., Nakashima, K., and Eldik, C. (2019). Validation of open-source science tools and background model construction in gamma-ray astronomy. *Astronomy Astrophysics*, 632.

Morlino, G. and Caprioli, D. (2012). Strong evidence for hadron acceleration in Tycho's supernova remnant. , 538:A81.

Nievas Rosillo, M. and VERITAS Collaboration (2021). The throughput calibration of the VERITAS telescopes. In *37th International Cosmic Ray Conference (ICRC2021)*, volume 301 of *International Cosmic Ray Conference*, page 789.

Nigro, C. and et al. (2019). Towards open and reproducible multi-instrument analysis in gamma-ray astronomy. , 625:A10.

Ong, R. A. and et al. (2009). Highlight Talk: Recent Results from VERITAS. International Cosmic Ray Conference, page arXiv:0912.5355.

Otte, A. (2009). Upgrade of the veritas cherenkov telescope array. *Proceedings of the 31st International Cosmic Ray Conference, ICRC 2009*.

Otte, A., Gebremedhin, L., Kaplan, K., and Long, D. (2011). The upgrade of veritas with high efficiency photomultipliers. *Proceedings of the 32nd International Cosmic Ray Conference, ICRC 2011*, 9:247–250.

Park, N. (2016). Performance of the VERITAS experiment. In *Proceedings of The 34th International Cosmic Ray Conference — PoS(ICRC2015)*, volume 236, page 771.

Perkins, J. S., Maier, G., and The VERITAS Collaboration (2009). VERITAS Telescope 1 Relocation: Details and Improvements. *arXiv e-prints*, page arXiv:0912.3841.

Piano, G., Cardillo, M., Pilia, M., Trois, A., Giuliani, A., Bulgarelli, A., Parmiggiani, N., and Tavani, M. (2019). AGILE Study of the Gamma-Ray Emission from the SNR G78.2+2.1 (Gamma Cygni). , 878(1):54.

Piddington, J. H. and Minnett, H. C. (1952). Radio-Frequency Radiation from the Constellation of Cygnus. *Australian Journal of Scientific Research A Physical Sciences*, 5:17.

Rector, T. A., Levay, Z. G., Frattare, L. M., English, J., and Pu'uohau-Pummill, K. (2007). Image-Processing Techniques for the Creation of Presentation-Quality Astronomical Images. , 133(2):598–611.

Reynolds, S. P. (2008). Supernova remnants at high energy. , 46:89–126.

Robinson, P. R. B. . D. K. (2003). *Data Reduction and Error Analysis for the Physical Sciences, 3rd Edition*. McGraw-Hill, New York.

Rybicki, G. B. and Lightman, A. P. (2004). *Radiative Processes in Astrophysics*.

Rygl, K. L. J., Brunthaler, A., Sanna, A., Menten, K. M., Reid, M. J., van Langevelde, H. J., Honma, M., Torstensson, K. J. E., and Fujisawa, K. (2012). Parallaxes and proper motions of interstellar masers toward the Cygnus X star-forming complex. I. Membership of the Cygnus X region. , 539:A79.

Sudoh, T., Linden, T., and Beacom, J. F. (2019). TeV halos are everywhere: Prospects for new discoveries. , 100(4):043016.

The Gammapy Developers. *Gammapy Documentation*, 0.19 edition.

Uchiyama, Y., Takahashi, T., Aharonian, F. A., and Mattox, J. R. (2002). ASCA View of the Supernova Remnant $\gamma$ Cygni (G78.2+2.1): Bremsstrahlung X-Ray Spectrum from Loss-flattened Electron Distribution. , 571(2):866–875.

Vincent, S. and VERITAS Collaboration (2015). A Monte Carlo template-based analysis for very high definition imaging atmospheric Cherenkov telescopes as applied to the VER. In *34th International Cosmic Ray Conference (ICRC2015)*, volume 34 of *International Cosmic Ray Conference*, page 844.

Vink, J. (2020). *Physics and Evolution of Supernova Remnants.*

Warren, J. S., Hughes, J. P., Badenes, C., Ghavamian, P., McKee, C. F., Moffett, D., Plucinsky, P. P., Rakowski, C., Reynoso, E., and Slane, P. (2005). Cosmic-Ray Acceleration at the Forward Shock in Tycho's Supernova Remnant: Evidence from Chandra X-Ray Observations. , 634(1):376–389.

Weekes, T. C. (2003). *Very High Energy Gamma-Ray Astronomy.* Institue of Physics Publishing, Bristol and Philadelphia.

Weekes, T. C. and et al. (1989). Observation of TeV Gamma Rays from the Crab Nebula Using the Atmospheric Cerenkov Imaging Technique. , 342:379.

Weinstein, A. (2007). The veritas trigger system. *Proceedings of the 30th International Cosmic Ray Conference, ICRC 2007*, 3.

Wilks, S. S. (1938). The large-sample distribution of the likelihood ratio for testing composite hypotheses. *The annals of mathematical statistics*, 9(1):60–62.

Zatsepin, G. T. and Kuzmin, V. A. (1966). Upper Limit of the Spectrum of Cosmic Rays. *Soviet Journal of Experimental and Theoretical Physics Letters*, 4:78.

Zitzer, B. and VERITAS Collaboration (2013). The VERITAS Upgraded Telescope-Level Trigger Systems: Technical Details and Performance Characterization. In *International Cosmic Ray Conference*, volume 33 of *International Cosmic Ray Conference*, page 3076.

# APPENDIX A. MONTE CARLO TO DATA COMPARISONS FOR GAIN-THRESHOLD FACTOR VALIDATION

Degradation of the VERITAS instrument, particularly the mirror reflectivity, has been occurring in the V6 epoch at a rate that needs to be taken into account in the collaboration science. Reduced mirror reflectivity leads to smaller shower image size collected in each telescope photo-multiplier tube camera. This in turn causes energy loss in each gamma-ray event and an increase of the VERITAS low energy threshold. This is a significant reason why data from the V6 epoch and CARE simulations were not included in this thesis.

In order to quantify the degradation, sets of gain and optical threshold (GT) factors were derived from each telescope's seasonal reflectivity and gain calibrations. The final result is a set of GT factors for each of the four telescopes in the array and for each season and atmosphere. A full validation of the GT factor derivation is described in Nievas Rosillo and VERITAS Collaboration (2021).

The degradation of the telescopes is significant and increasing to the point that current lookup tables (LTs) and effective areas (EAs) are no longer suitable for analysis, especially for more recent seasons of data. Reduced reflectivity decreases the observed shower size of events compared to events observed at the beginning of the V6 epoch. Therefore, energy values referenced from an old LT encoding the dependency of energy on size greatly underestimate the true energy.

To correct the level of degradation on observations, the VERITAS collaboration must produce a new set of simulations and tables which include the effects of degradation. To accomplish this, GT factors are applied directly to the simulation pedestal charge and pixel charge. Analysis of data collected in later seasons of the V6 epoch requires production of new LTs and EAs from simulations scaled with GT factors from calibrations taken in the respective seasons.

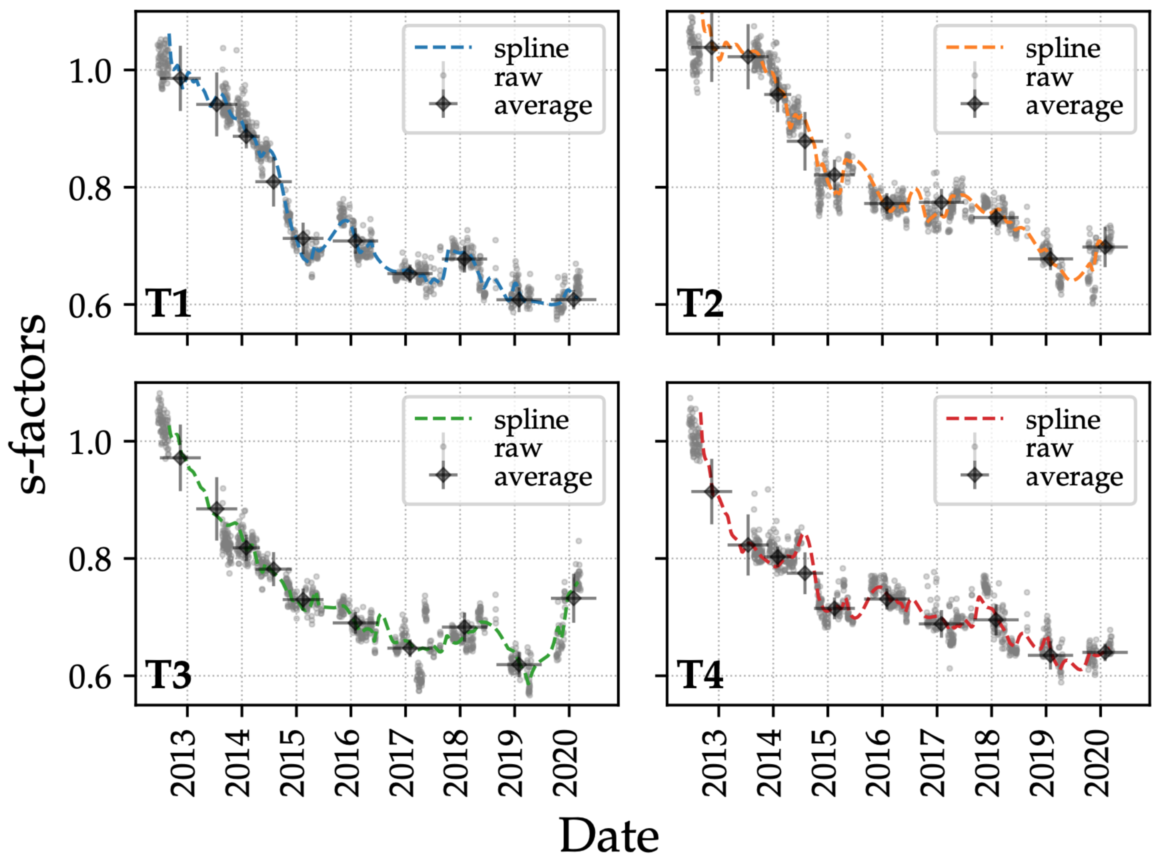


Figure A.1: Evolution of GT-factors (primary mirror+gain factors) for the four VERITAS telescopes (Nievas Rosillo and VERITAS Collaboration, 2021)

.

The process of validating GT factors has required extended periods of time for crosschecks and study. Primarily for this reason, data from the V6 epoch were not included in the main work of this thesis. One of the validation studies is a set of Monte Carlo to data comparisons performed to validate the performance of GT factor scaled LT tables. This work lead to a finalized table production pipeline and to the ongoing production of LTs and EAs for V6 data analysis. With future table production, analysis of V6 data with the 4D-Maximum Likelihood Method (4D-MLM) can proceed.

## Parameters for Comparison

The VERITAS standard data reduction derives and stores several parameter values meant for characterizing atmospheric air-showers and diagnosing telescope configuration. There are eight shower parameters: **mean scaled width** (MSW), **mean reduced scaled width** (MRSW), **mean scaled length** (MSL), **mean reduced scaled length** (MRSL), **shower max height**, **energy**, **energy difference**, and **theta squared**. There are sixteen telescope parameters: **width**, **length**, **size**, **distance**, **impact distance**, **size fraction low**, **asymmetry**, **minor asymmetry**, **loss**, **fraction 1**, **fraction 2**, **fraction 3**, **max 1**, **max 2**, **max 3**, and **number of tubes**. The gamma-hadron separation parameters have greater importance for diagnostics, parameters such as width, length, MSW, and MSL.

For the purposes of validating new simulations, the VERITAS collaboration carries out a comparison of parameters between a set of simulations and a Crab dataset. An example comparison between a normalized parameter, MSL, of simulations and data is shown in Figure A.2. When both simulation and data histograms sufficiently overlap and calculated efficiencies of both agree within reasonable error, usage of simulations in the generation of lookup tables and effective areas can proceed.

## Monte Carlo to Data Comparison with GT-factors

A series of validations studies with Monte Carlo to data comparisons were performed on simulations scaled with GT factors. The main goal of these studies was to demonstrate that the application of GT factors on CARE simulations, and the LTs and EAs produced from these simulations, lower the energy threshold and restore the spectrum of Crab data observed in later seasons.

A LT and EA production pipeline was edited to run the VEGAS analysis software on CARE simulations and apply GT factors; the pipeline utilizes a VEGAS Docker image. Validation studies applied with the pipeline were run at National Energy Research Scientific Computing Center (NERSC).

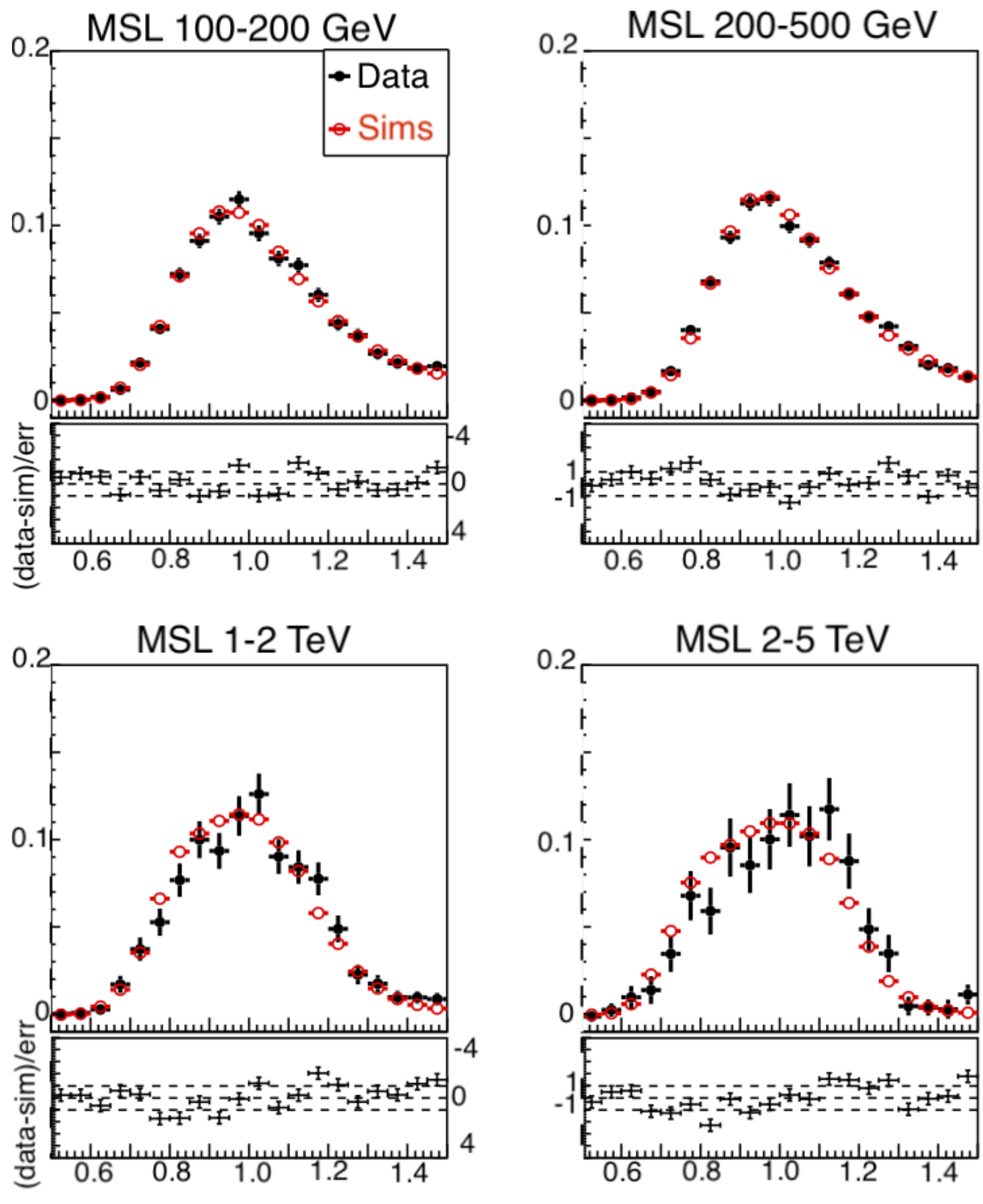


Figure A.2: Histograms of normalized MSL parameter distributions, derived from a set of CARE V6 simulations (black) and Crab V6 data (red) and overlaid. The four different plots are the parameters divided across four energy bins, from 100 GeV to 200 GeV, 200 GeV to 500 GeV, 1 TeV to 2 TeV, and 2 TeV to 5 TeV. The ratio plot is a calculation in each bin of data minus sims, divided by the cumulative error.

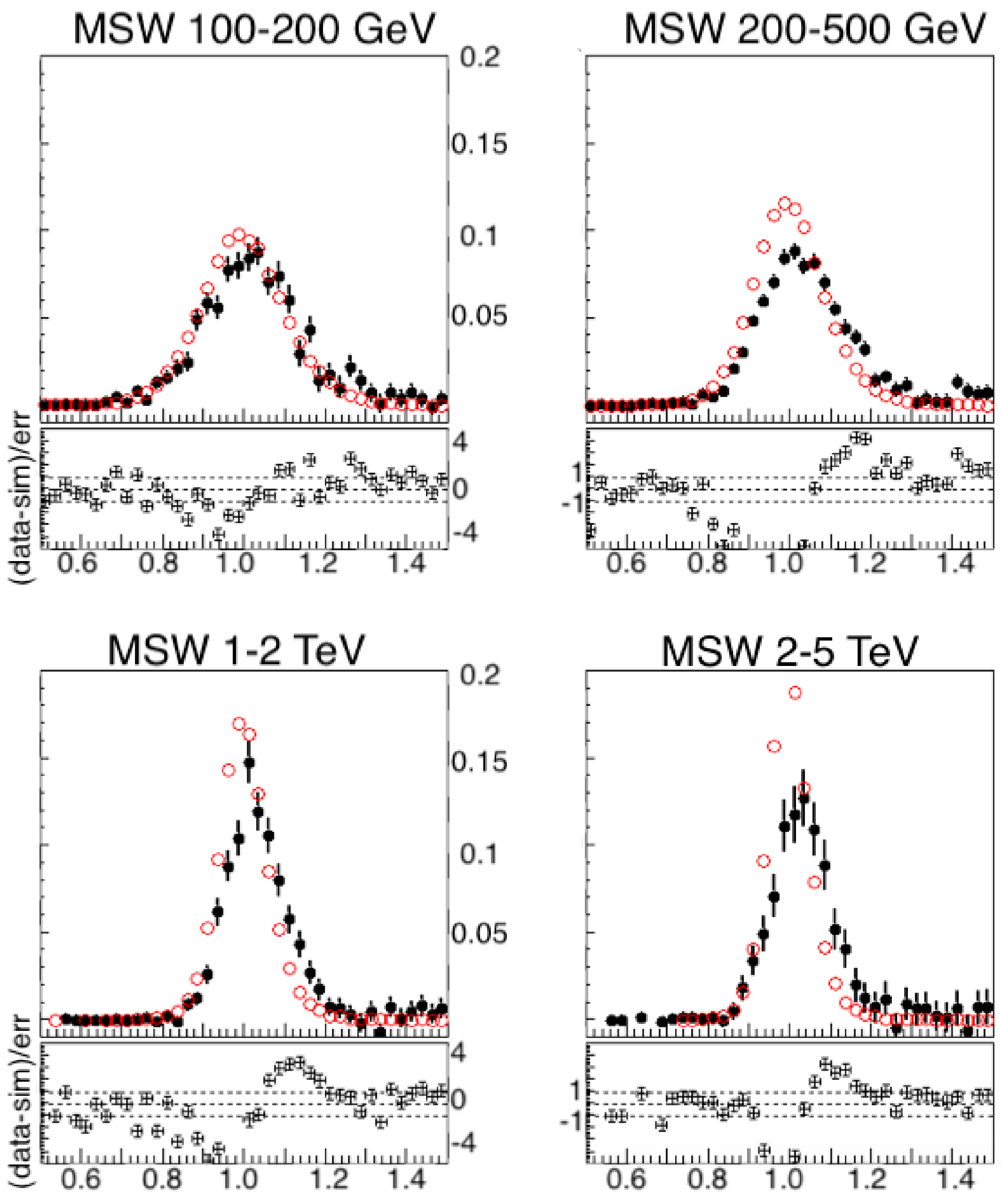


Figure A.3: MSW histograms of CARE simulations (red), with only the pixel charge scaled, versus Crab V6 (black). The six plots in each figure are MSW divided across six energy bins, from 100 GeV to 10 TeV. The Crab data has been analyzed with lookup tables generated from CARE simulations scaled with GT factors.

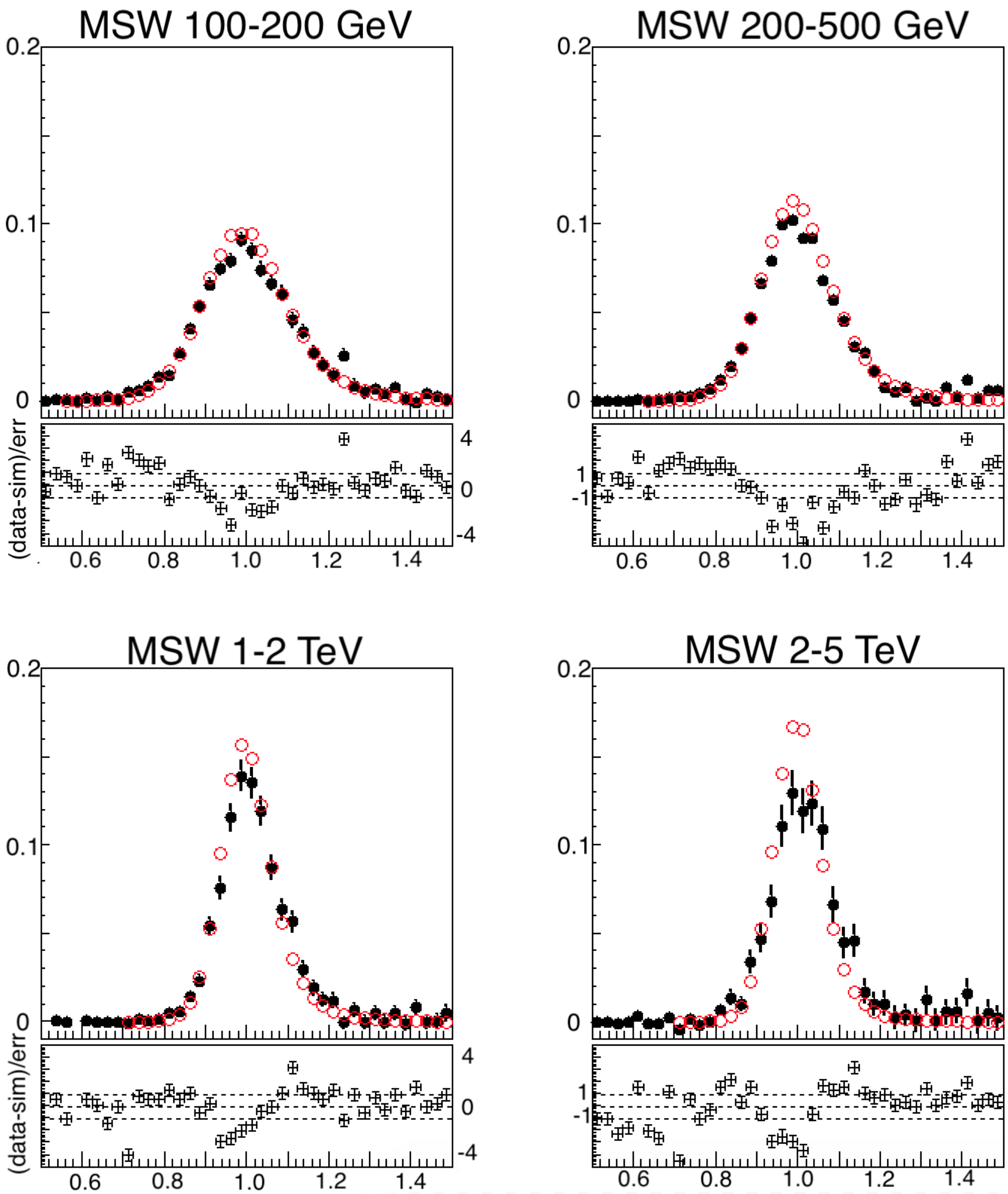


Figure A.4: MSW histograms of CARE simulations (red), with both the pixel charge and pedestal scaled, versus Crab V6 (black). The six plots in each figure are MSW divided across six energy bins, from 100 GeV to 10 TeV. The Crab data has been analyzed with lookup tables generated from CARE simulations scaled with GT factors.

In the pipeline, the simulated charge of all pixels in a shower image, for each telescope, are scaled by GT factors derived from the 2017-2018 seasons's calibrations. The new set of scaled CARE V6 simulations produce new LTs, which are then used in VEGAS analysis of Crab data observed in the 2017-2018 observing season.

Comparisons between histograms of telescope and shower parameter distributions showed significant discrepancies between the distributions derived from the Crab V6 2017-2018 season's data versus the CARE V6 simulations with scaled pixels, as shown in Figure A.3. These results strongly indicated that the GT factors were not applied correctly.

Consultation with validations performed with Event Display revealed what was missing in the initial GT factor application was scaling of the pedestal, in addition to the pixel charge. However, a repeat of the LT production with 2017-2018 GT factors scaling both charge and pedestal of CARE simulations also created an issue with the software performance. Before scaling, all four telescopes had similar camera noise levels. However, since each telescope has different reflectivity degradation, and therefore, different GT factors, the simulated noise level of each camera is significantly different after scaling. Part of the VEGAS lookup table production code needed to change. In VEGAS 259, the four telescope camera noise levels are kept separate through lookup table production. The resulting MSW distribution of the table production and data analysis with new tables is shown in Figure A.4. There is now good comparison of telescope and shower parameters, such as MSW, between Crab V6 2017-2018 data and CARE V6 scaled simulations.

# APPENDIX B. POINT SPREAD FUNCTION WITH ITM

This appendix covers issues that were touched on during the validation of the point spread function (PSF) with the symmetric and asymmetric King function. The parameters from the symmetric King function, $\sigma$ and *lambda*, are written out to each data fits file compatible with Gammapy. Before performing a full analysis, only the containment radius was returned for data with the King function PSF format. This diagnostic was done in order to check the performance of a rarely used tool in Gammapy. Counter to all expectations, for all energy and offset bins, the containment radius returned a single negative value. The cause of this error in the containment radius calculation came from Gammapy's integration formula for a symmetric King function. The correct polar integration for a radially symmetric, normalized King function was derived analytically and is

$$F(x, y, \sigma, \lambda) = 1 - \left(1 + \frac{r^2}{2\lambda\sigma^2}\right)^{1-\lambda}. \tag{B.1}$$

This formula replaces the previous integration formulation in the symmetric King function containment evaluation and was used for Gammapy analysis going forward. Trends in subsequent plots and values of percent containment, for example in Figure 7.2, are consistent with $\sigma$ parameter plots. Full documentation of this change and an official update to the released version of Gammapy will be in future work.

The Image Template Method (ITM) is a shower reconstruction algorithm that utilizes the likelihood method with shower image templates generated from simulations. Published results demonstrate that ITM leads to a narrower PSF (Christiansen and VERITAS Collaboration, 2017). Fitting of the King-function to the 2-D distribution of ITM processed simulations shows the narrower PSF for both 3 and 4 telescopes events, except for 3 telescope events at energies $> 4$ TeV. The overall PSF dependency on offset at large energy remains in ITM processed simulations.

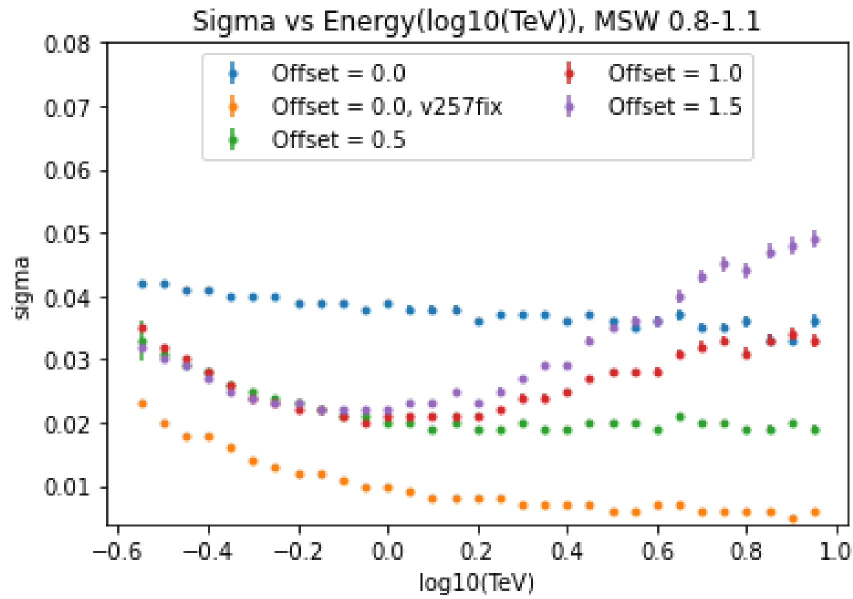


Figure B.1: Sigma versus energy after fitting the symmetric King function to ITM processed simulations produced at 0 degrees zenith. The orange points are sigma value produced from the fit of the symmetric King function to the simulations processed with the software after fixing the plane-to-plane conversion code. All other curves are produced from fits with simulations processed with the standard analysis.

In the course of PSF validation with ITM processed simulations the PSF was observed to be much worse for a specific set of simulations produced at 0 degrees zenith and 0 offset. This is due to a algorithm in the VEGAS analysis software that cuts off on events within a minimum angular distance from 0 zenith. In the standard software the minimum angular distance squared is 0.08 degrees squared. Since ITM processed simulations have a narrower PSF most events would fail this condition and the algorithm would not return a value. This is not an issue for real data because the telescope is never pointed at 0 degrees zenith. This error was fixed when the minimum angular distance squared was changed in one line of code from 0.08 to 0.0000008, so that ITM can be performed much closer to zenith=0°. Only simulations with 0° zenith and 0° offset needed to be reprocessed with the edited analysis software. Figure B.1 shows sigma parameters of the symmetric King function fitted to 0° zenith simulations, before and after the fix.

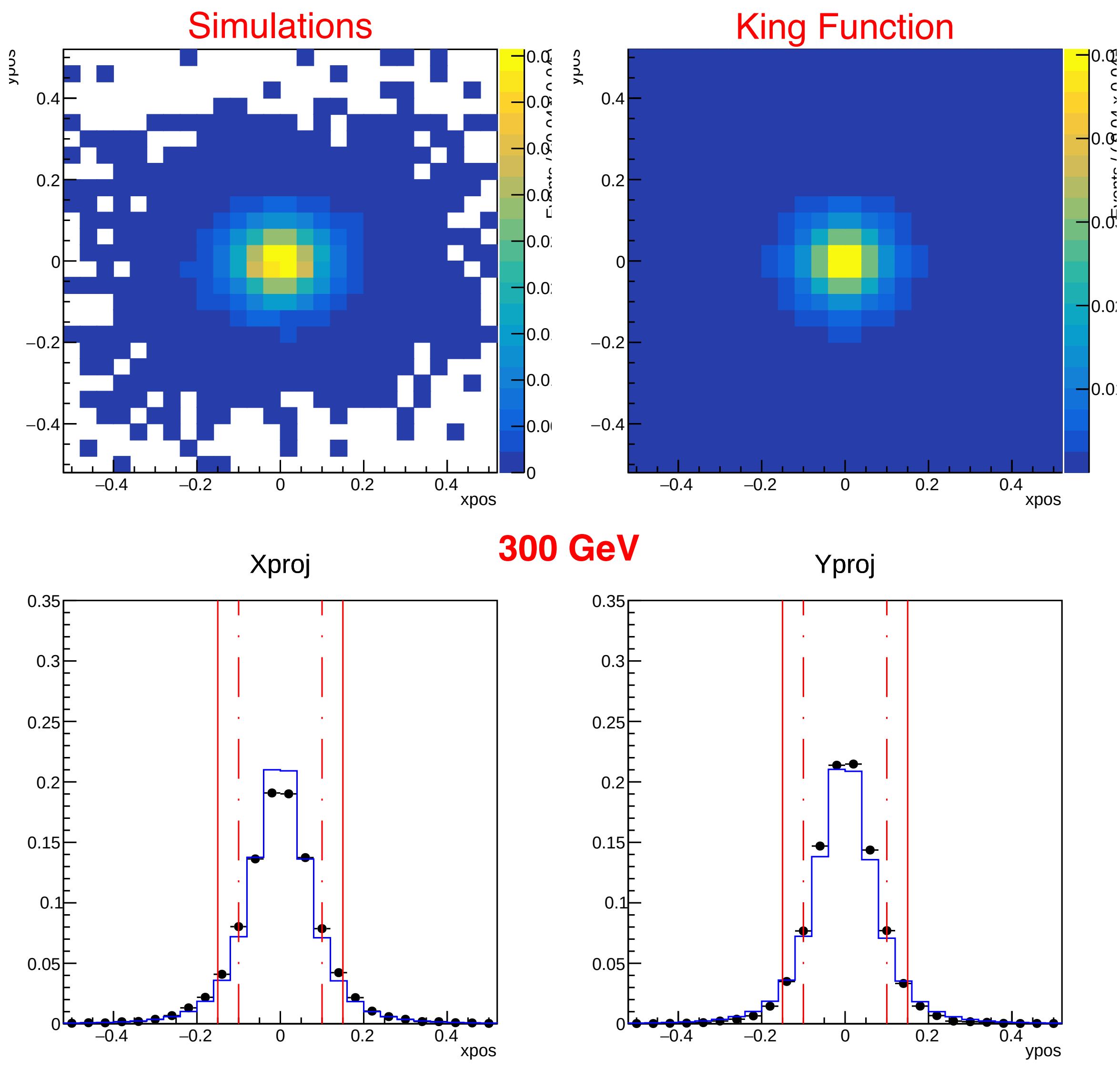


Figure B.2: A 2-D distribution of events simulated at 0.50° offset and 300 GeV, the resulting 2-D plotted King function post-fitting, and the overlaid data and fitted King function, projected in x and y. These plots are all fit with the symmetric King function, for events $0.8 < MSW < 1.1$.

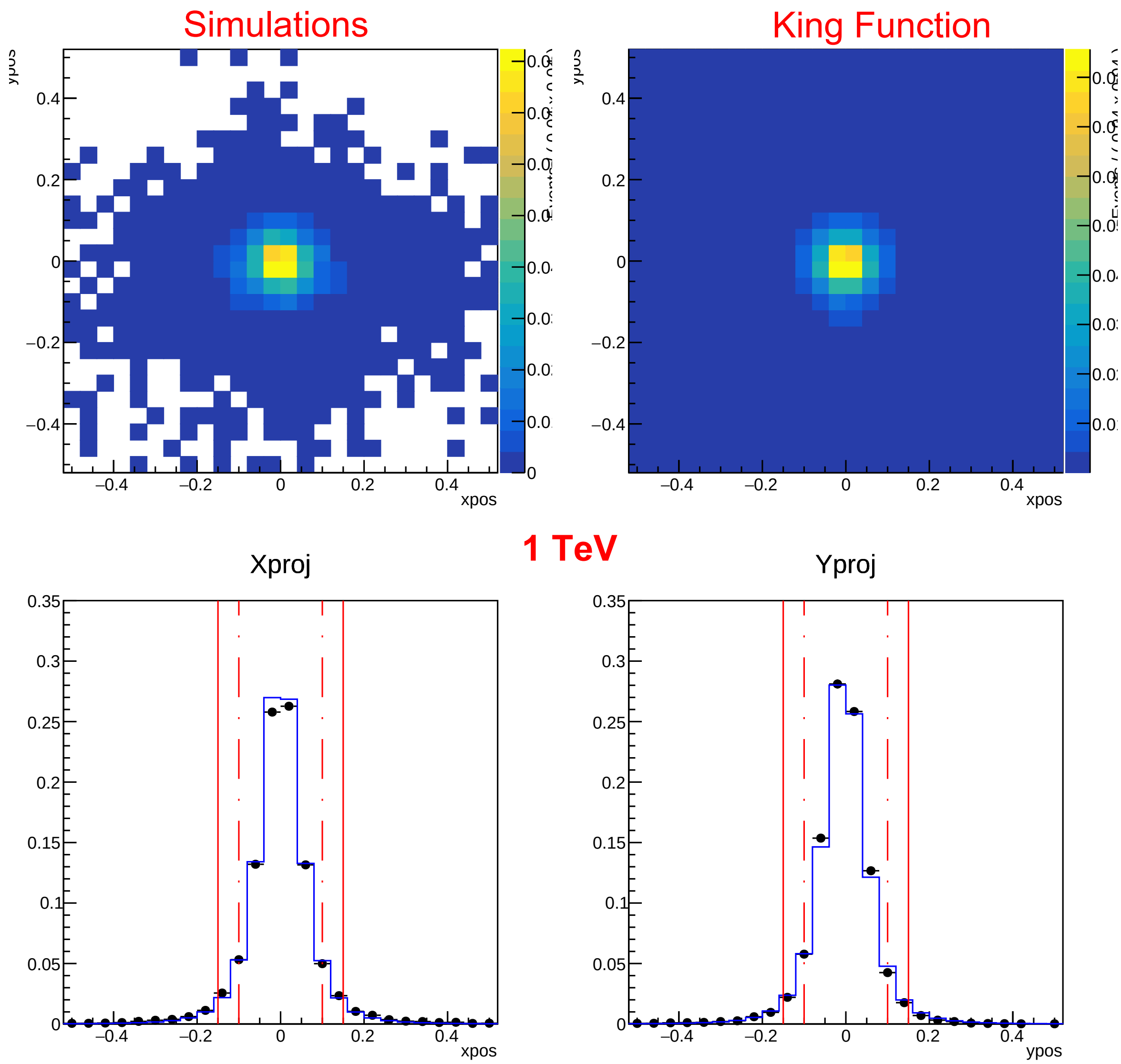


Figure B.3: A 2-D distribution of events simulated at 0.50° offset and 1 TeV, the resulting 2-D plotted King function post-fitting, and the overlaid data and fitted King function, projected in x and y. These plots are all fit with the symmetric King function, for events $0.8 < MSW < 1.1$.

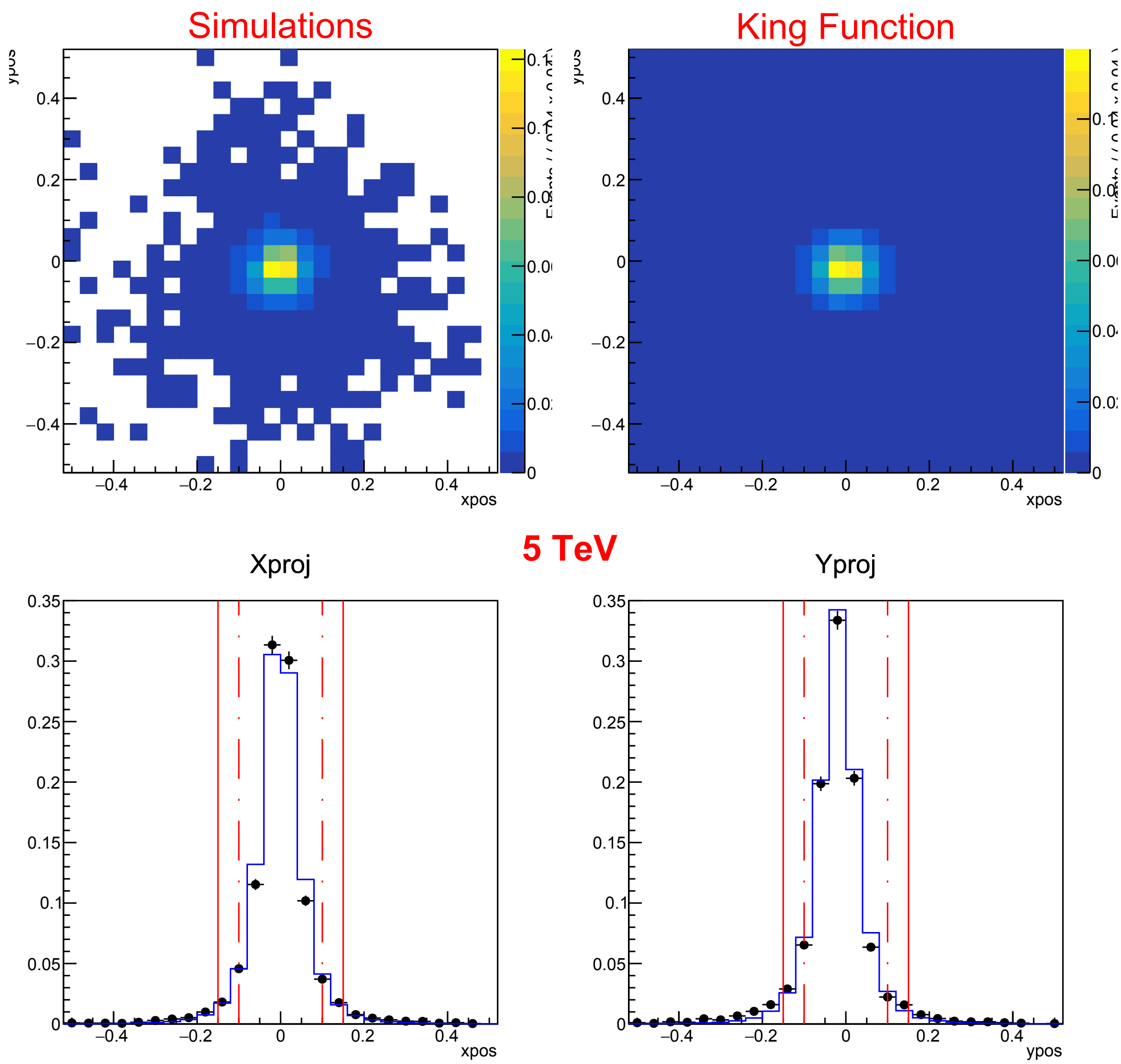


Figure B.4: A 2-D distribution of events simulated at 0.50° offset and 5 TeV, the resulting 2-D plotted King function post-fitting, and the overlaid data and fitted King function, projected in x and y. These plots are all fit with the symmetric King function, for events $0.8 < MSW < 1.1$.

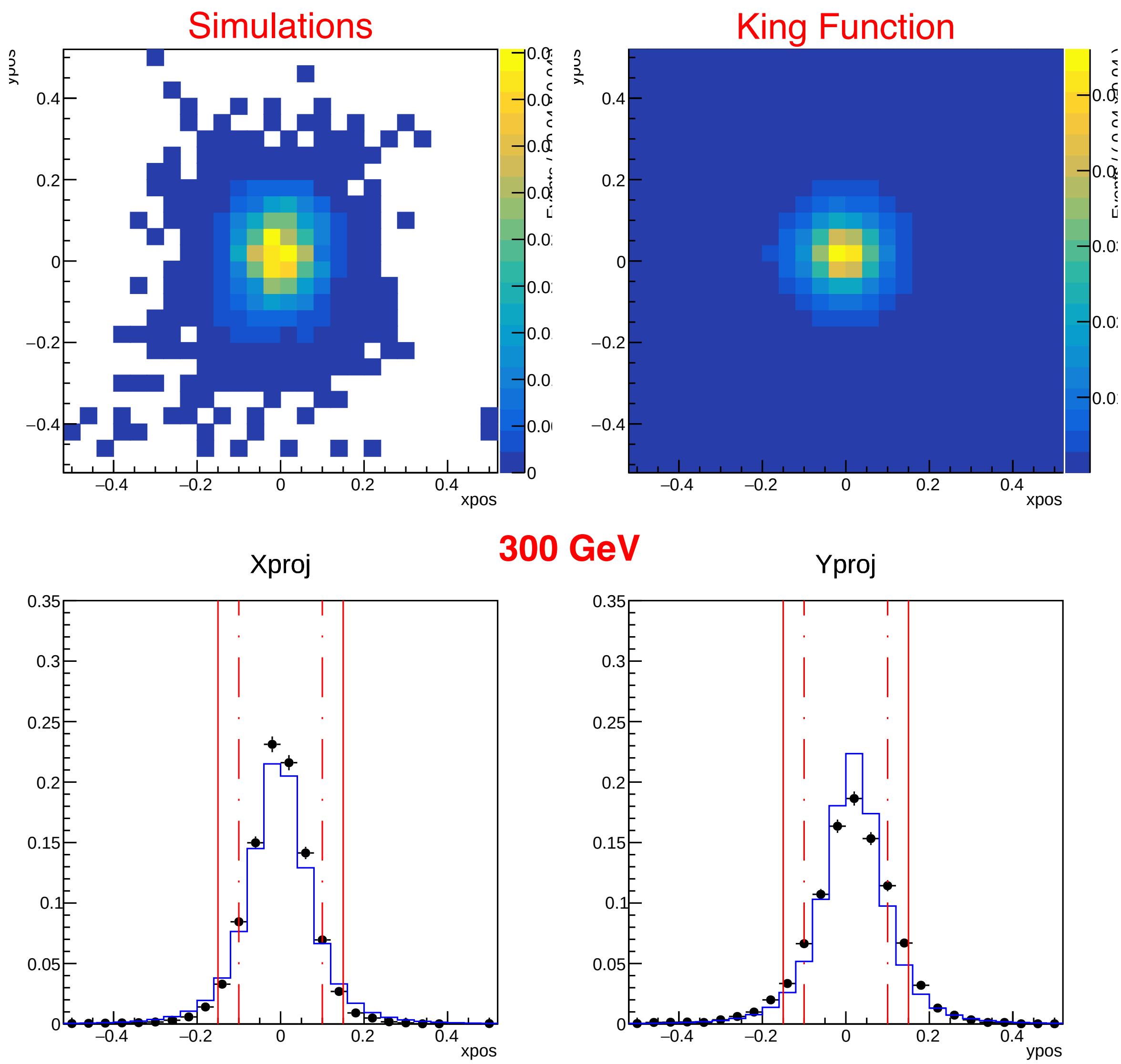


Figure B.5: A 2-D distribution of events simulated at 1.50° offset and 300 GeV, the resulting 2-D plotted King function post-fitting, and the overlaid data and fitted King function, projected in x and y. These plots are all fit with the symmetric King function, for events $0.8 < MSW < 1.1$.

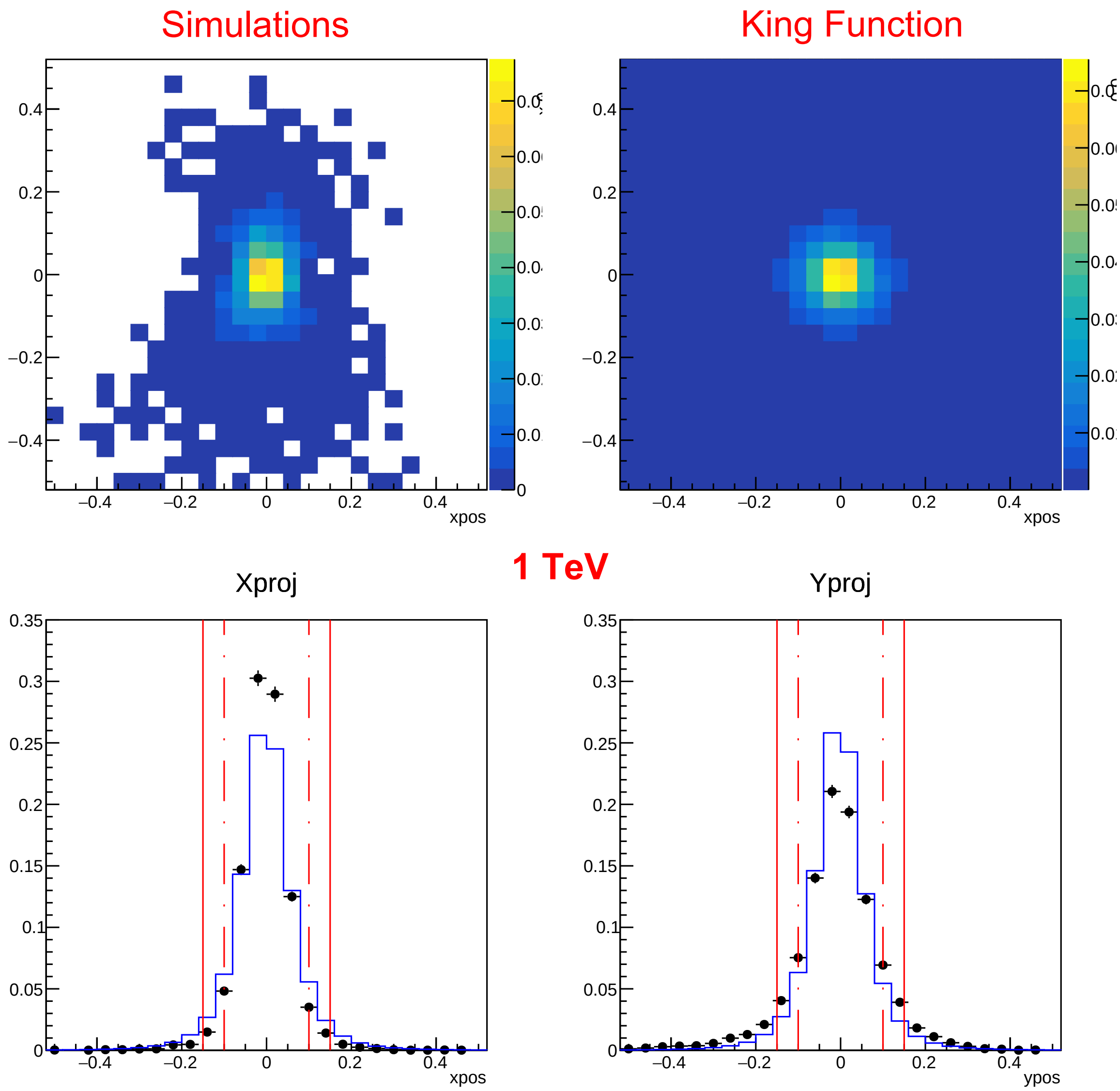


Figure B.6: A 2-D distribution of events simulated at 1.50° offset and 1 TeV, the resulting 2-D plotted King function post-fitting, and the overlaid data and fitted King function, projected in x and y. These plots are all fit with the symmetric King function, for events $0.8 < MSW < 1.1$.

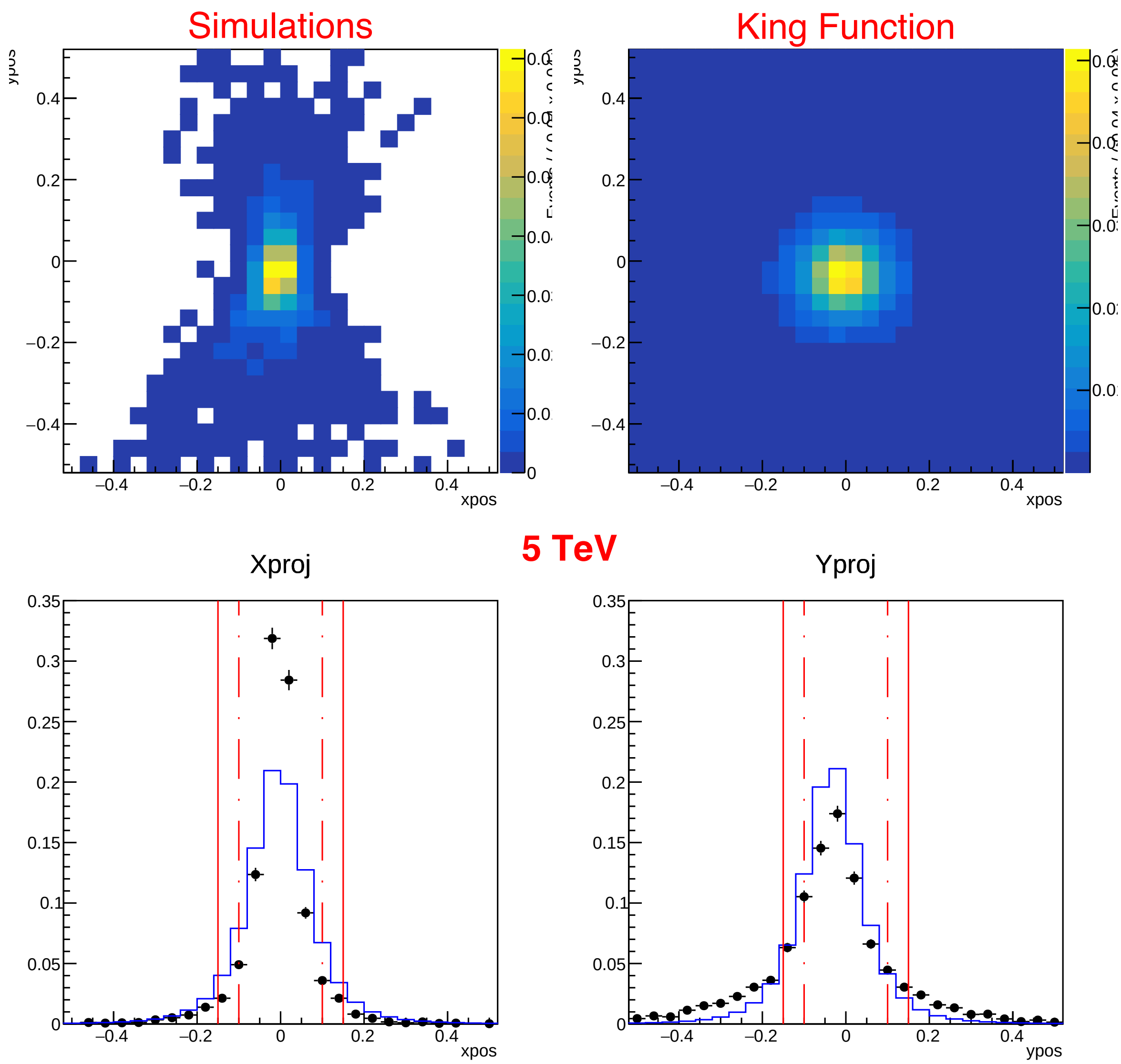


Figure B.7: A 2-D distribution of events simulated at 1.50° offset and 5 TeV, the resulting 2-D plotted King function post-fitting, and the overlaid data and fitted King function, projected in x and y. These plots are all fit with the symmetric King function, for events $0.8 < MSW < 1.1$.

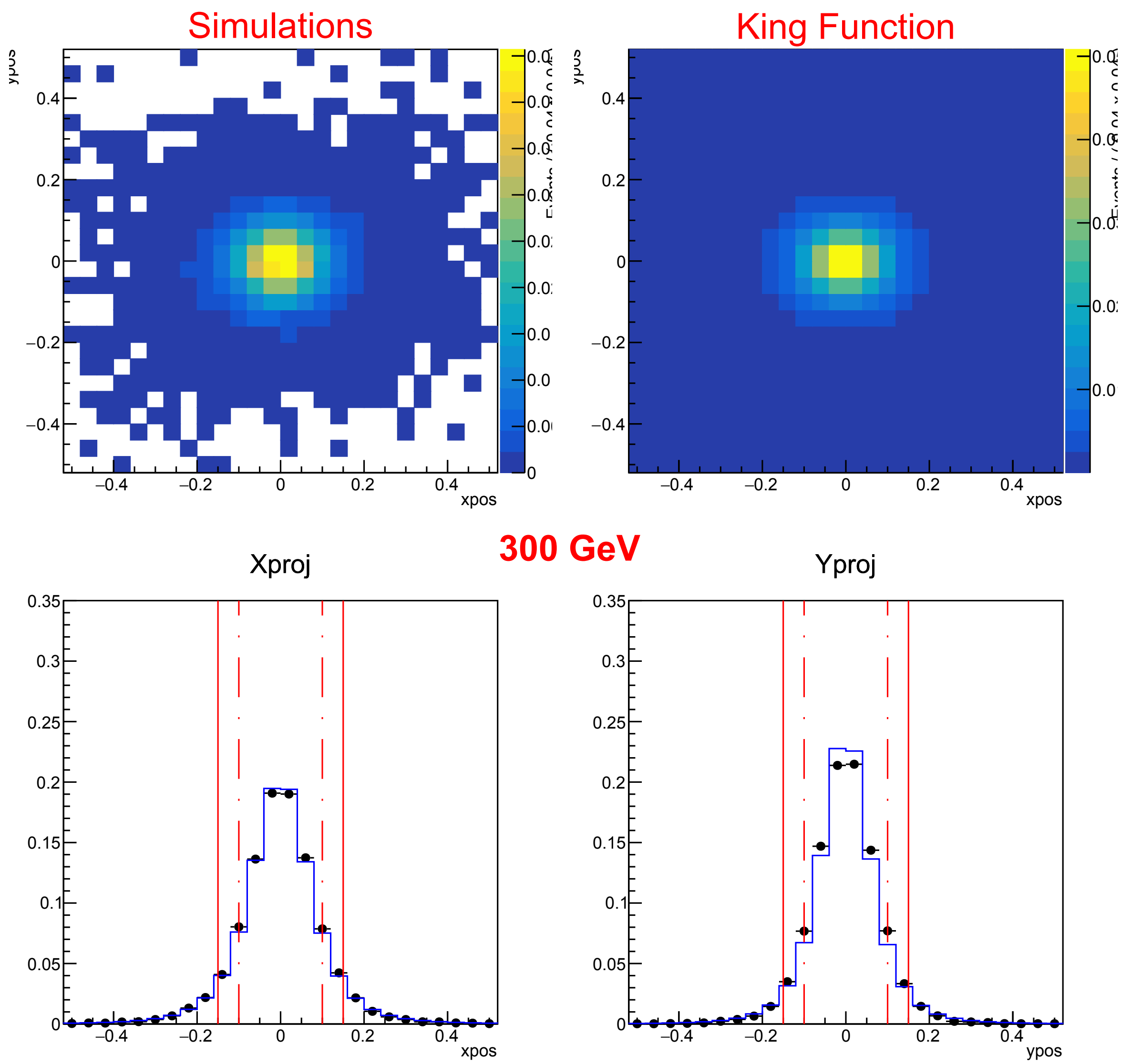


Figure B.8: A 2-D distribution of events simulated at 0.50° offset and 300 GeV, the resulting 2-D plotted King function post-fitting, and the overlaid data and fitted King function, projected in x and y. These plots are all fit with the asymmetric King function, for events $0.8 < MSW < 1.1$.

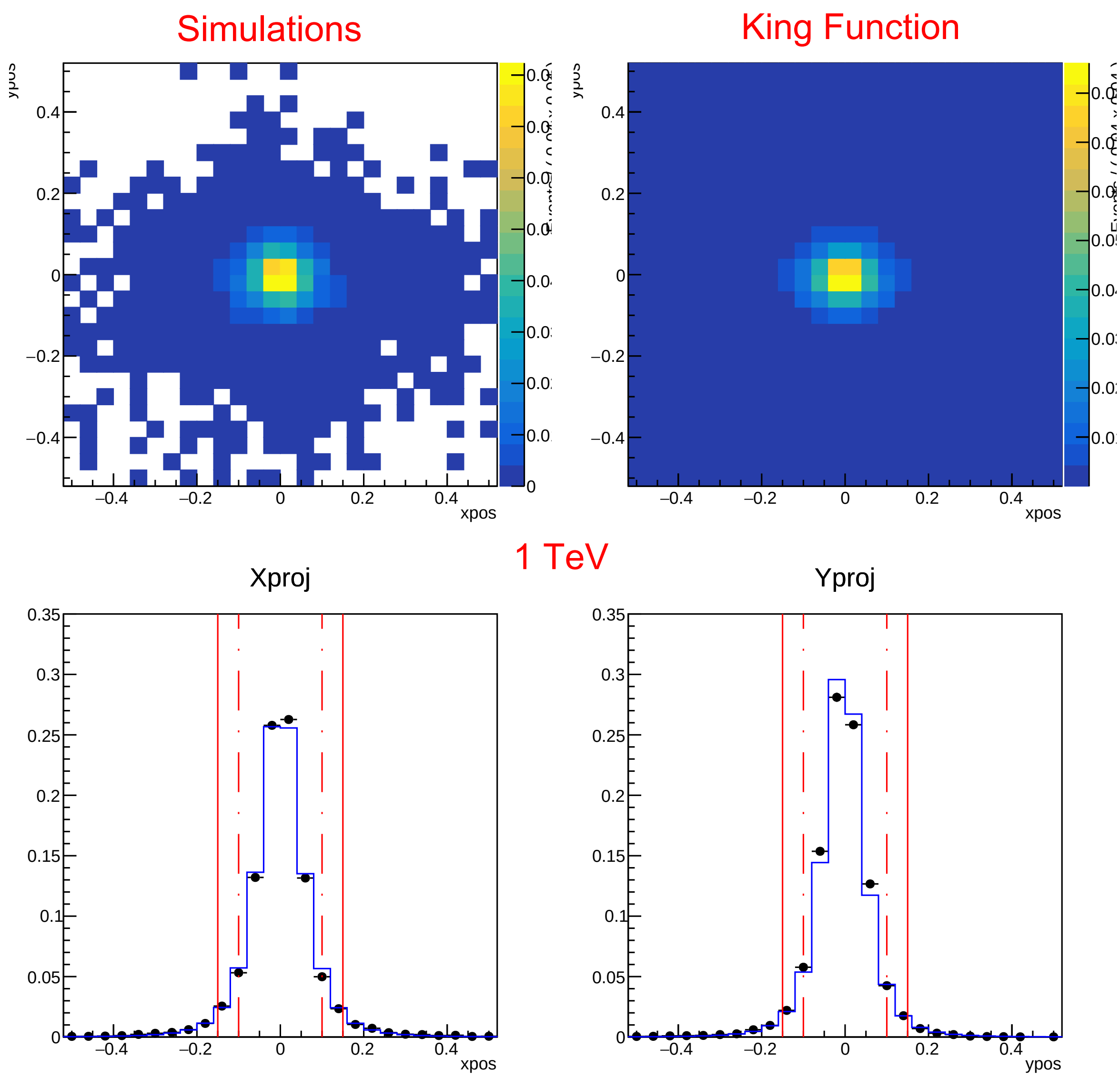


Figure B.9: A 2-D distribution of events simulated at 0.50° offset and 1 TeV, the resulting 2-D plotted King function post-fitting, and the overlaid data and fitted King function, projected in x and y. These plots are all fit with the asymmetric King function, for events $0.8 < MSW < 1.1$.

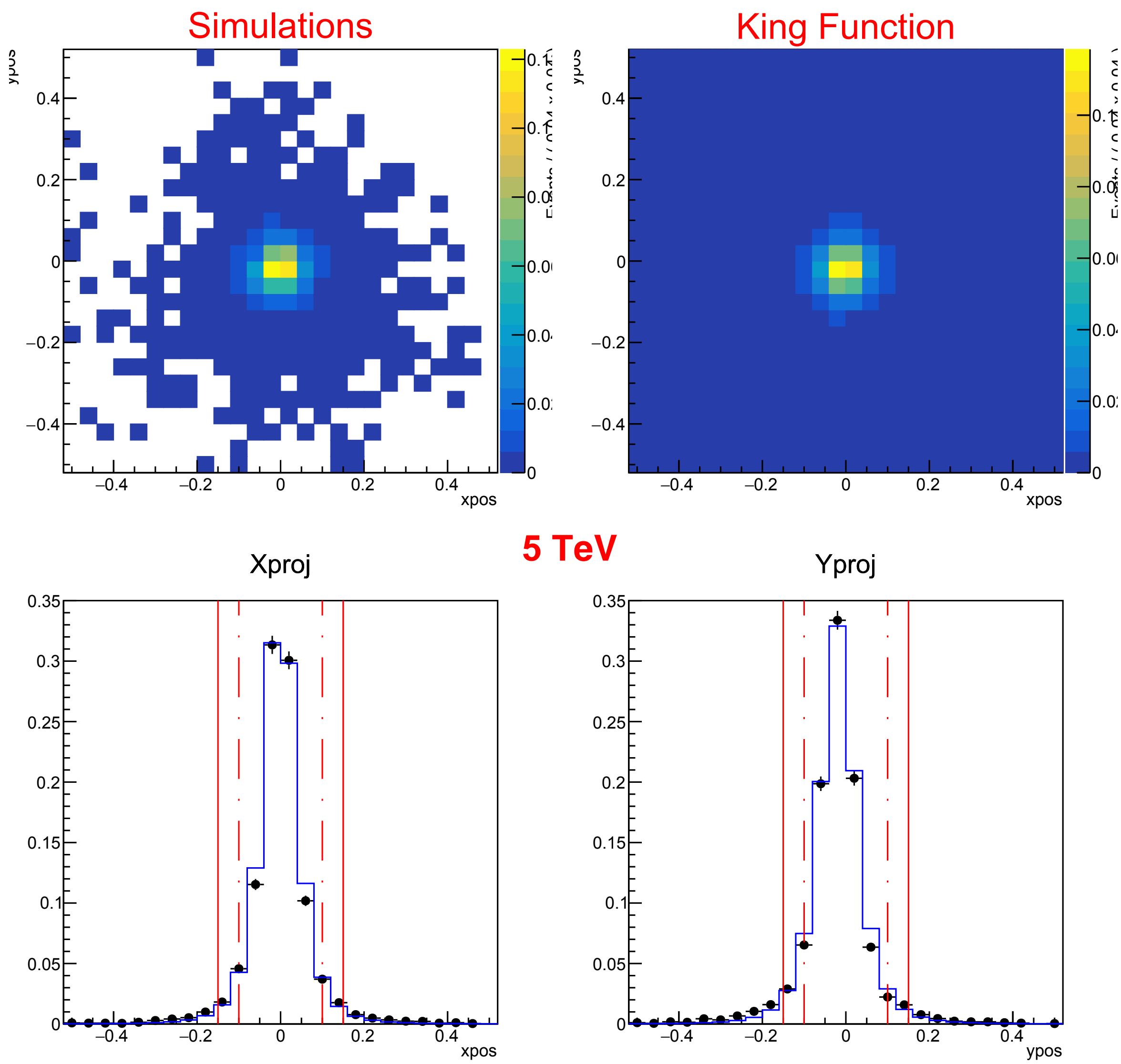


Figure B.10: A 2-D distribution of events simulated at 0.50° offset and 5 TeV, the resulting 2-D plotted King function post-fitting, and the overlaid data and fitted King function, projected in x and y. These plots are all fit with the asymmetric King function, for events $0.8 < MSW < 1.1$.

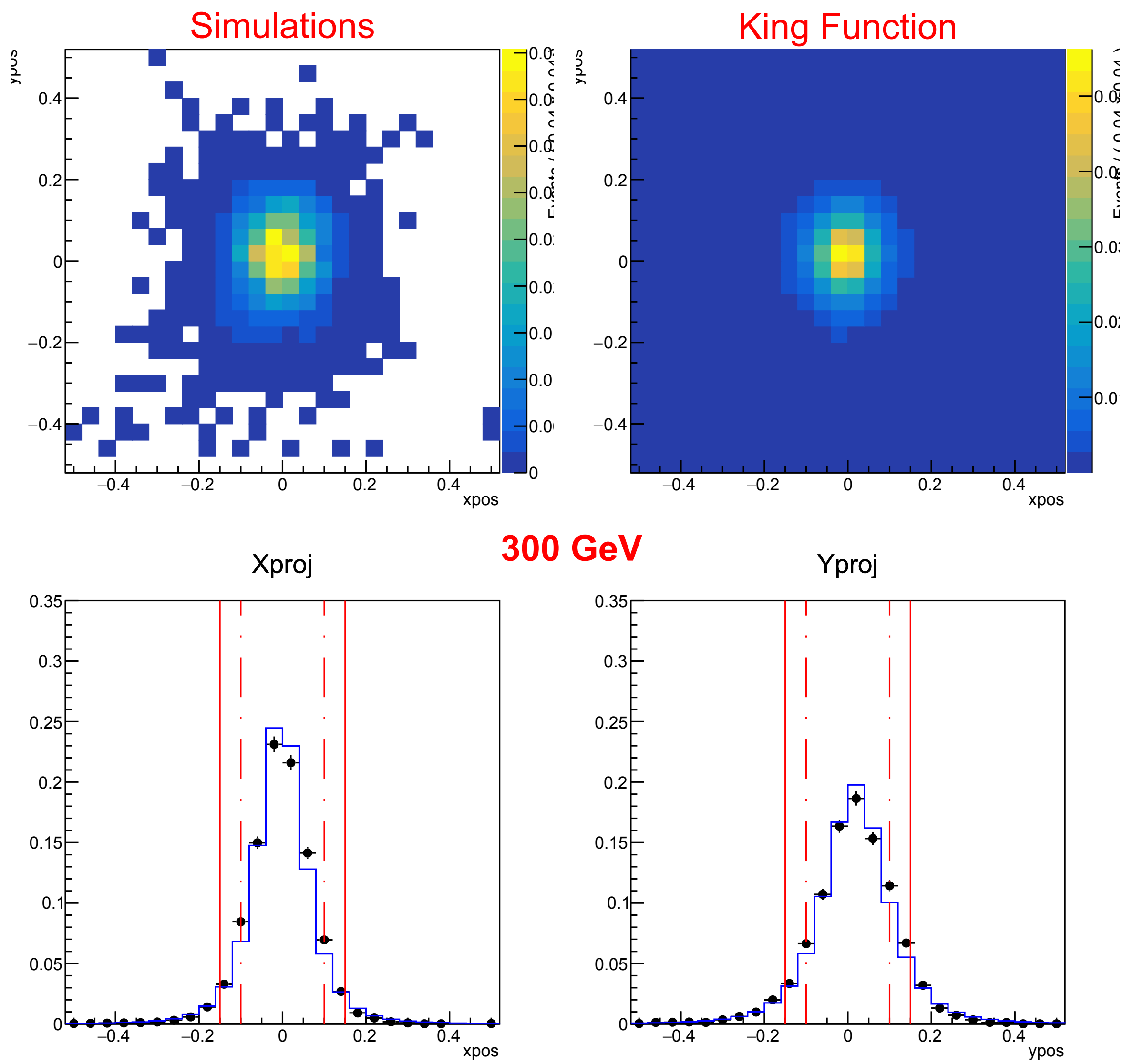


Figure B.11: A 2-D distribution of events simulated at 1.50° offset and 300 GeV, the resulting 2-D plotted King function post-fitting, and the overlaid data and fitted King function, projected in x and y. These plots are all fit with the asymmetric King function, for events $0.8 < MSW < 1.1$.

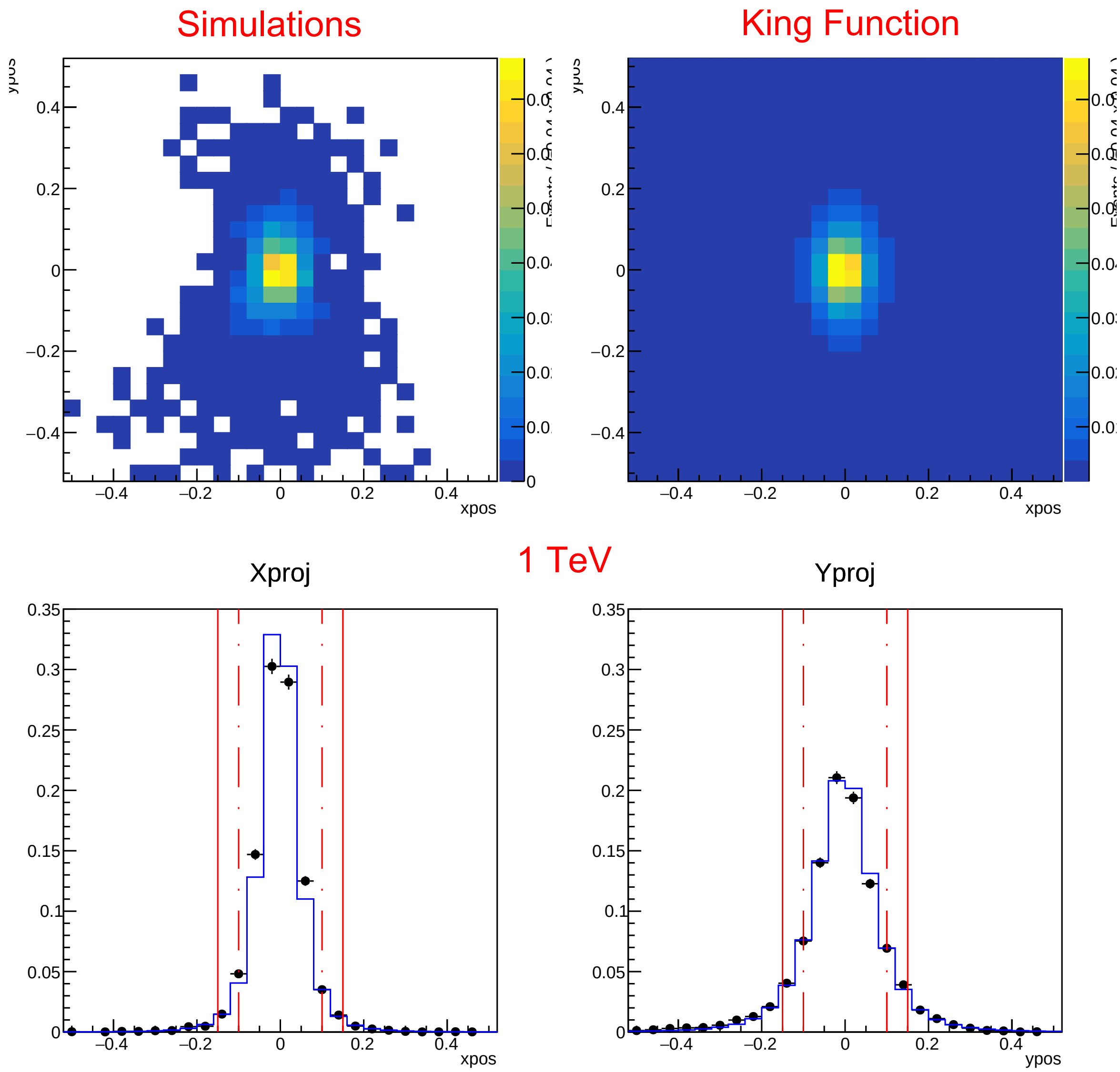


Figure B.12: A 2-D distribution of events simulated at 1.50° offset and 1 TeV, the resulting 2-D plotted King function post-fitting, and the overlaid data and fitted King function, projected in x and y. These plots are all fit with the asymmetric King function, for events $0.8 < MSW < 1.1$.

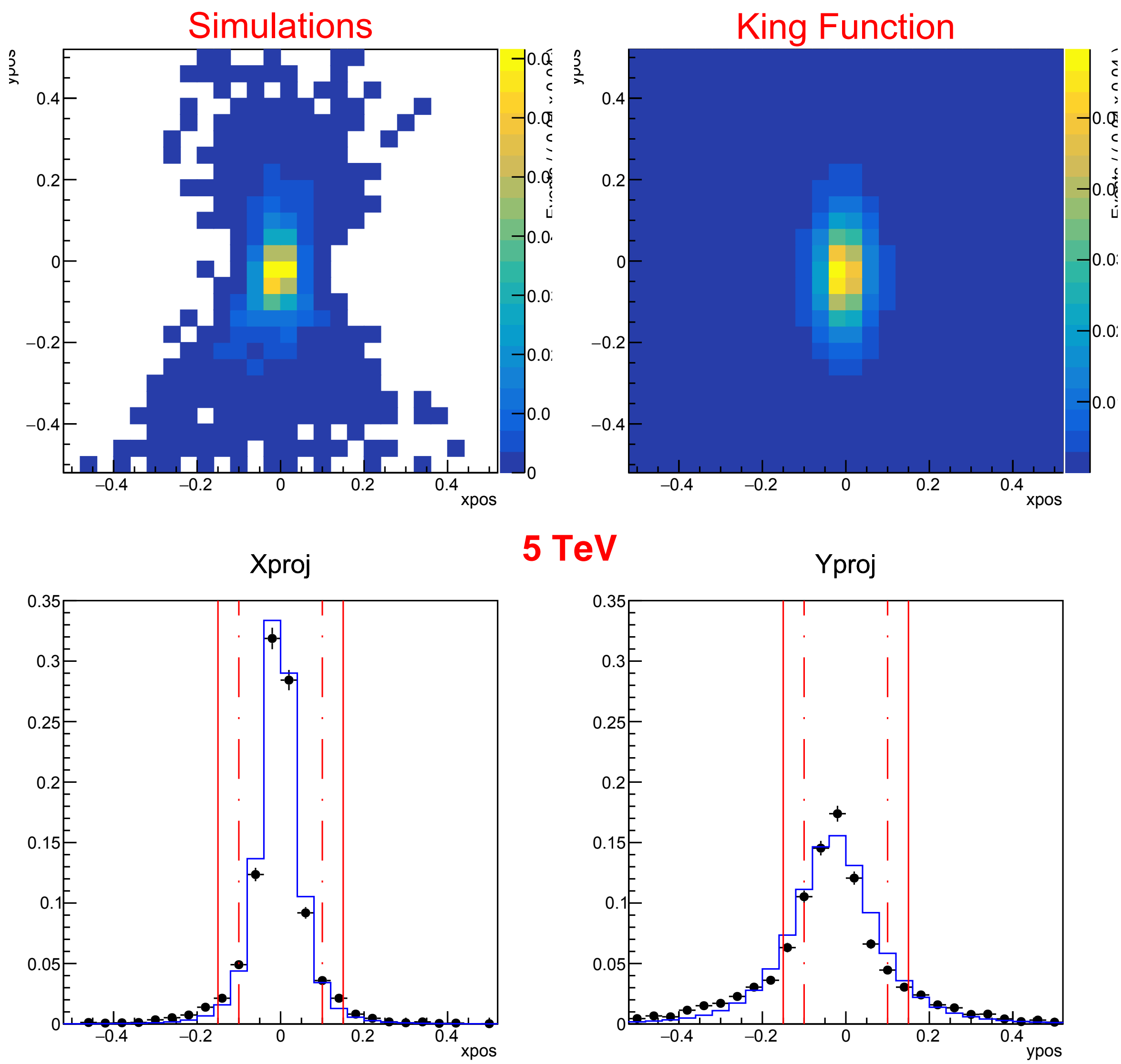


Figure B.13: A 2-D distribution of events simulated at 1.50° offset and 5 TeV, the resulting 2-D plotted King function post-fitting, and the overlaid data and fitted King function, projected in x and y. These plots are all fit with the asymmetric King function, for events $0.8 < MSW < 1.1$.

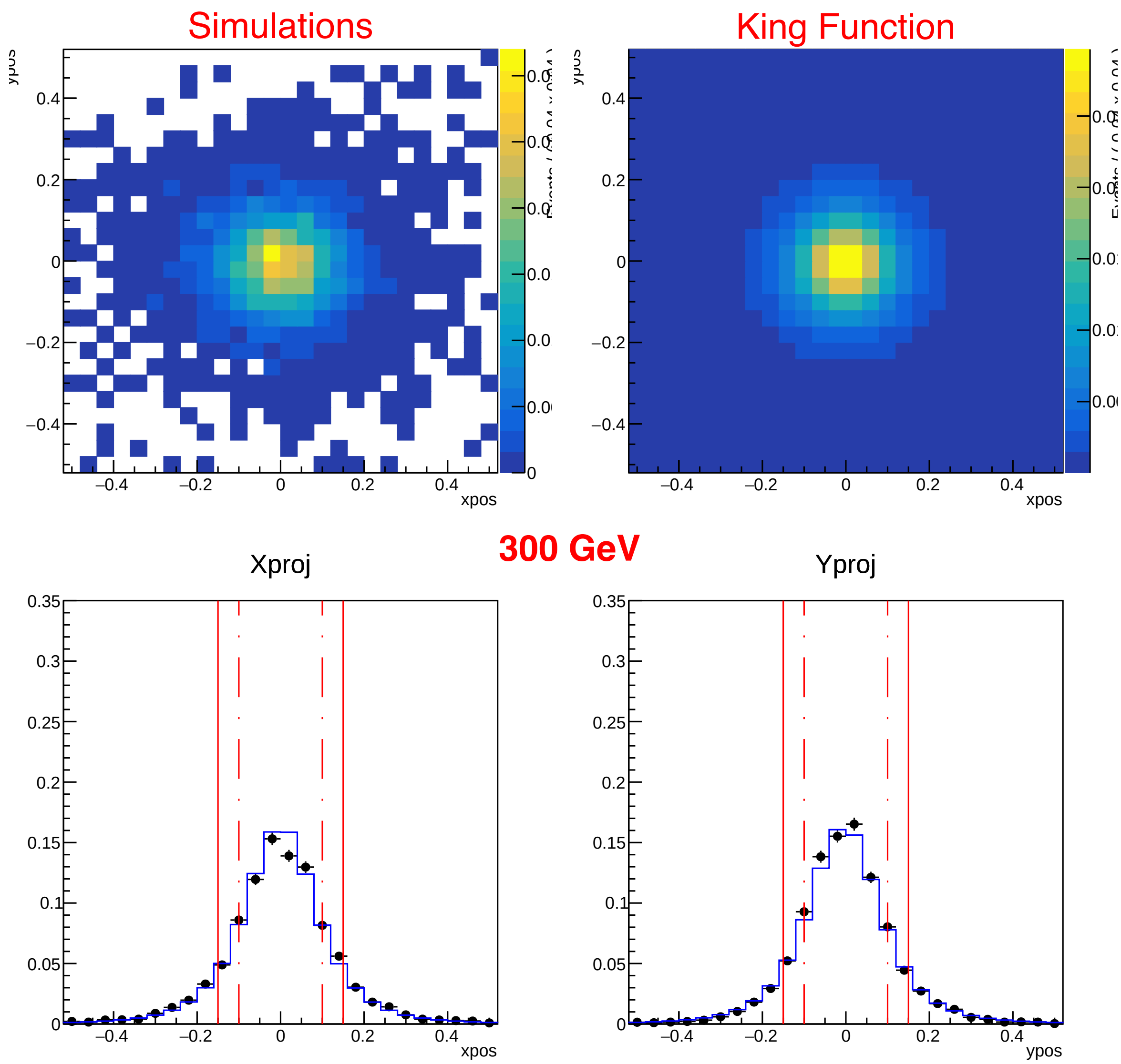


Figure B.14: A 2-D distribution of events simulated at 0.50° offset and 300 GeV, the resulting 2-D plotted King function post-fitting, and the overlaid data and fitted King function, projected in x and y. These plots are all fit with the symmetric King function, for events $1.1 < MSW < 1.3$.

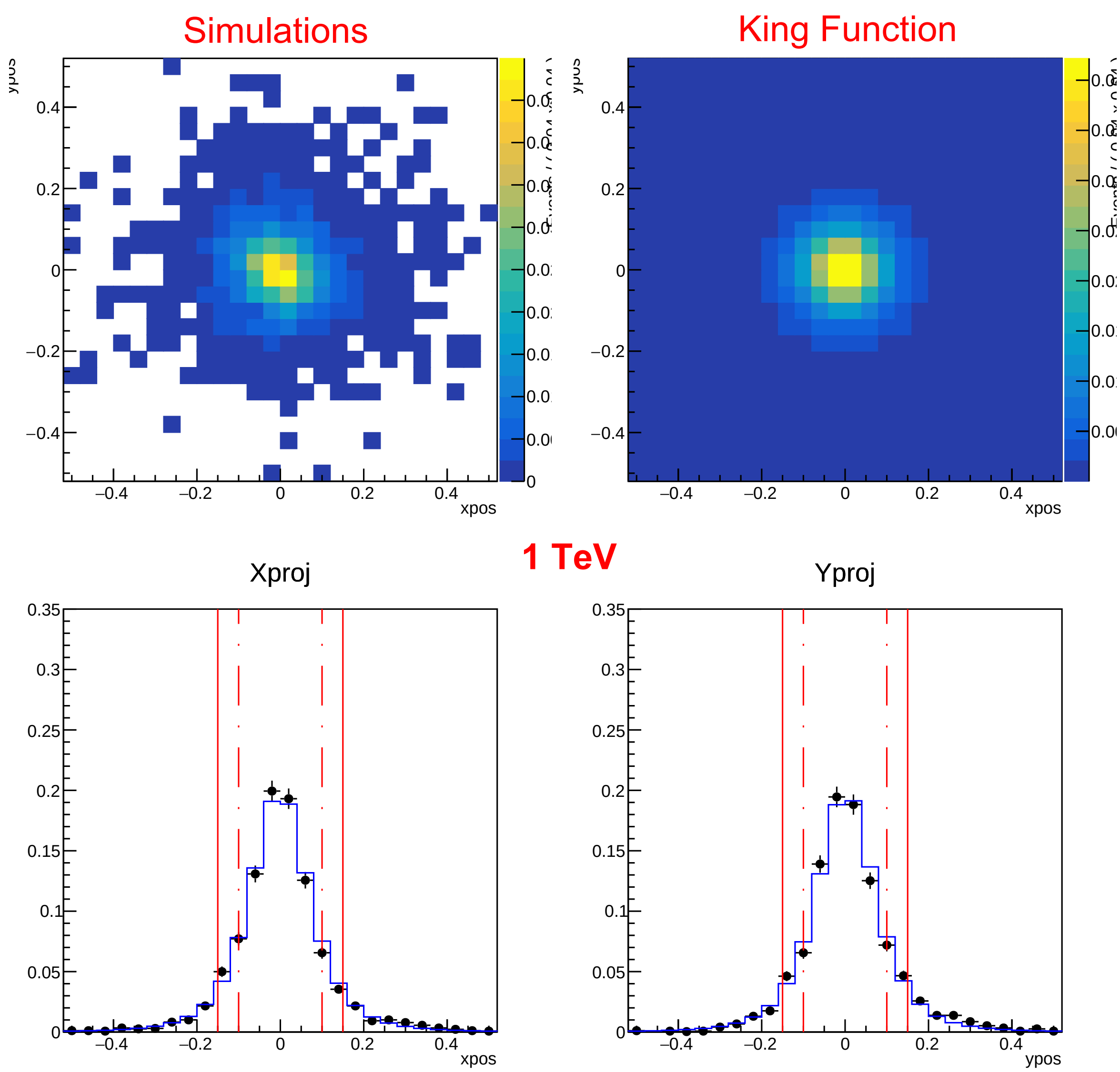


Figure B.15: A 2-D distribution of events simulated at 0.50° offset and 1 TeV, the resulting 2-D plotted King function post-fitting, and the overlaid data and fitted King function, projected in x and y. These plots are all fit with the symmetric King function, for events $1.1 < MSW < 1.3$.

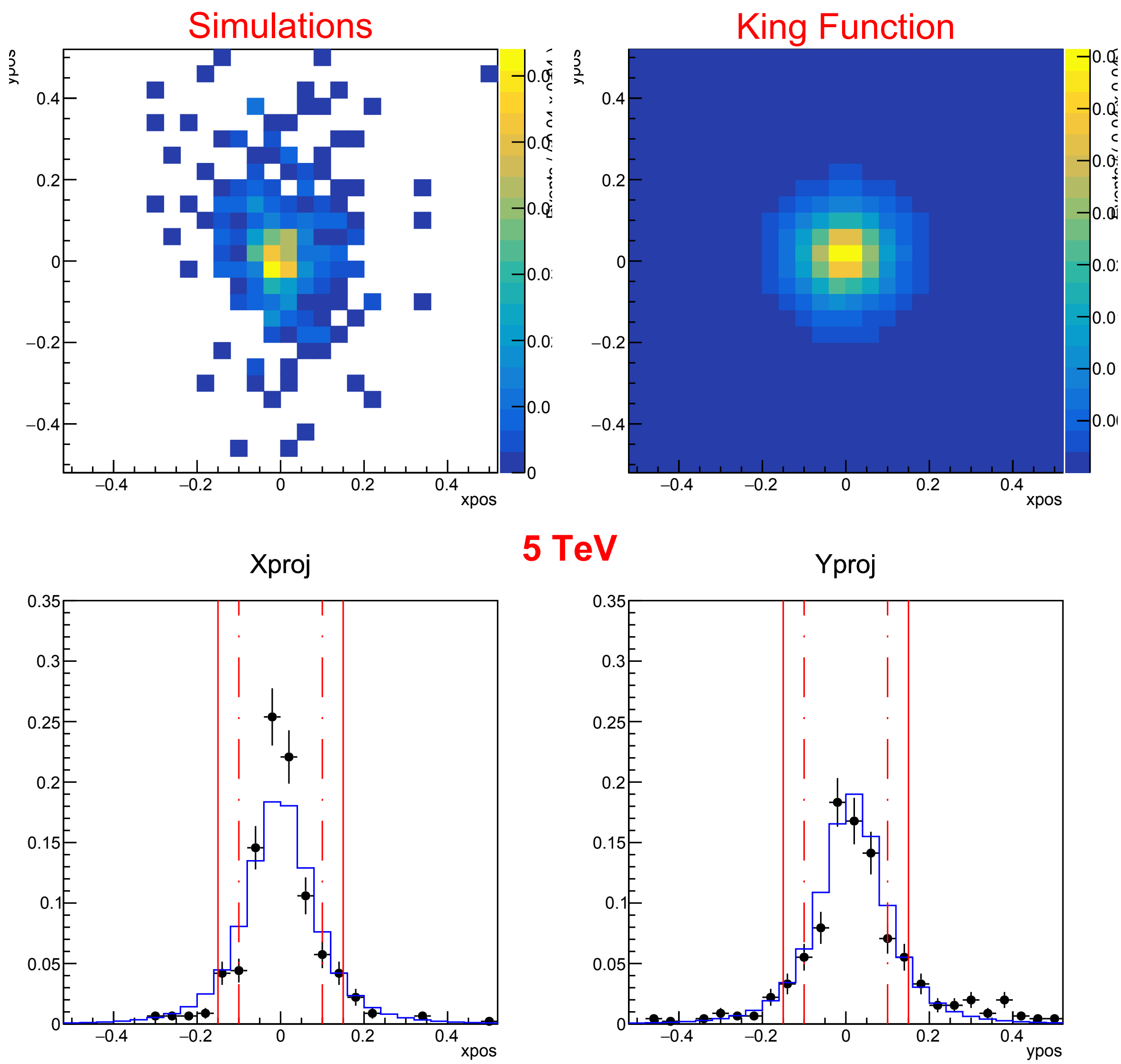


Figure B.16: A 2-D distribution of events simulated at 0.50° offset and 5 TeV, the resulting 2-D plotted King function post-fitting, and the overlaid data and fitted King function, projected in x and y. These plots are all fit with the symmetric King function, for events $1.1 < MSW < 1.3$.

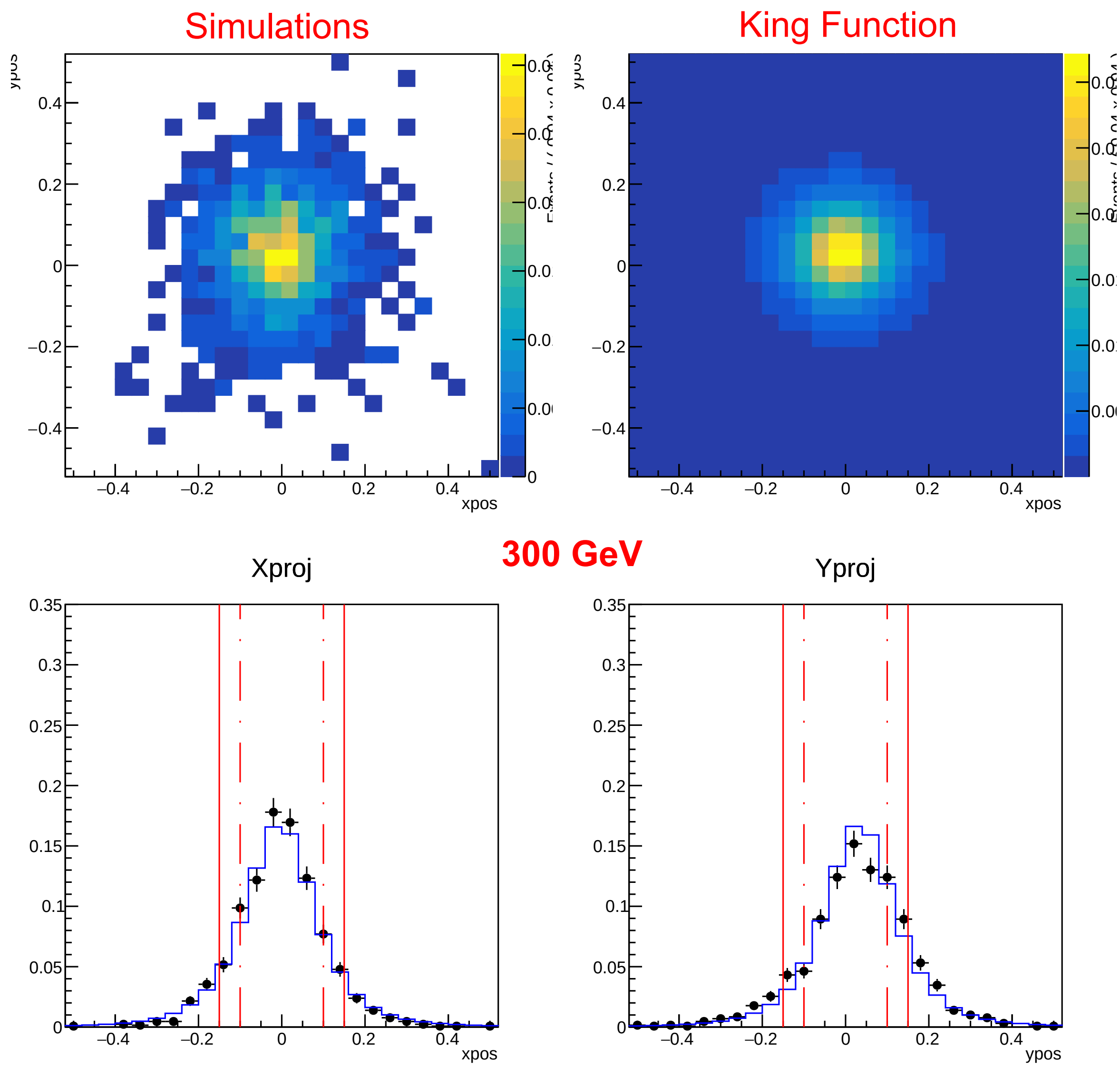


Figure B.17: A 2-D distribution of events simulated at 1.50° offset and 300 GeV, the resulting 2-D plotted King function post-fitting, and the overlaid data and fitted King function, projected in x and y. These plots are all fit with the symmetric King function, for events $1.1 < MSW < 1.3$.

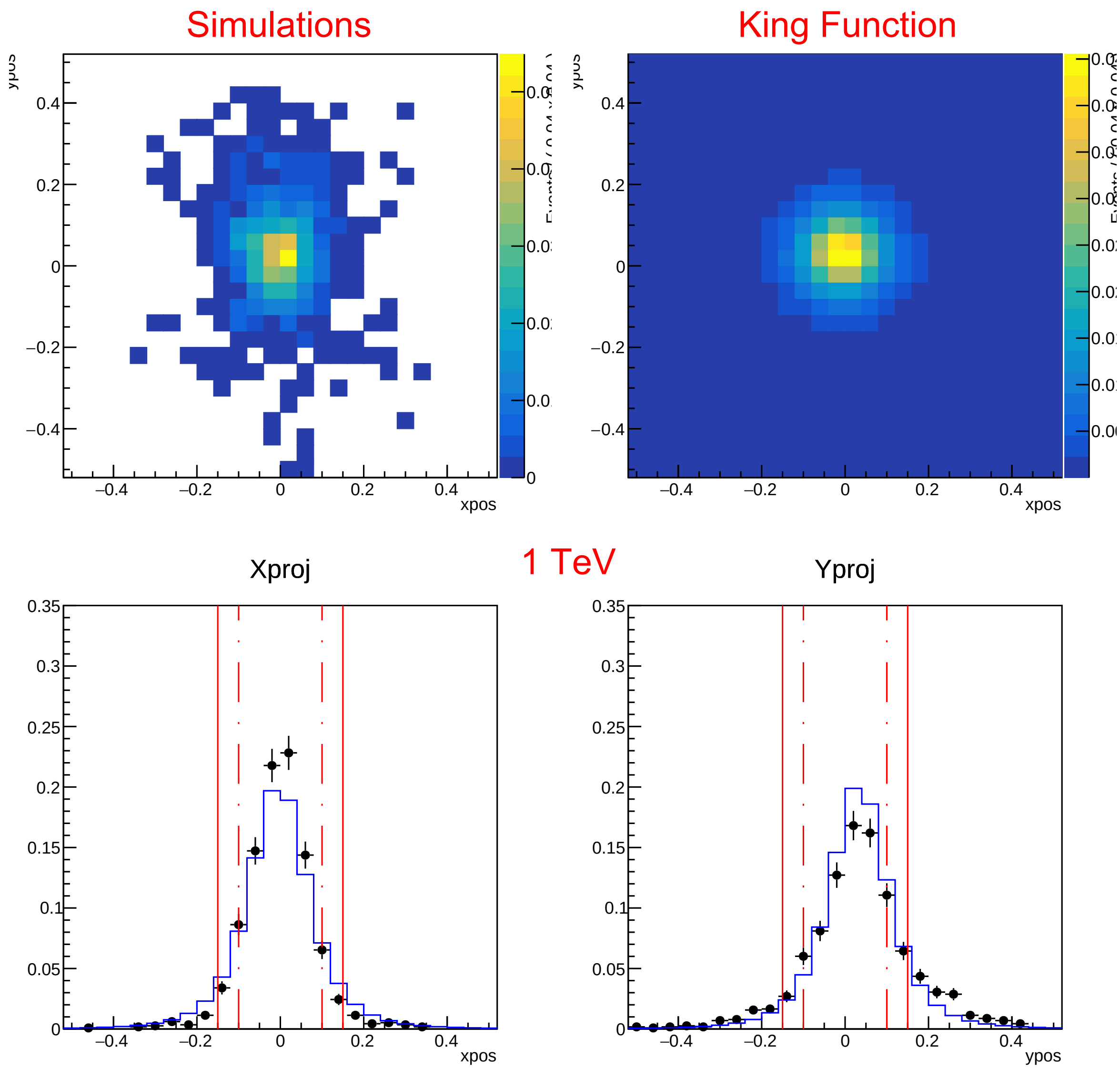


Figure B.18: A 2-D distribution of events simulated at 1.50° offset and 1 TeV, the resulting 2-D plotted King function post-fitting, and the overlaid data and fitted King function, projected in x and y. These plots are all fit with the symmetric King function, for events $1.1 < MSW < 1.3$.

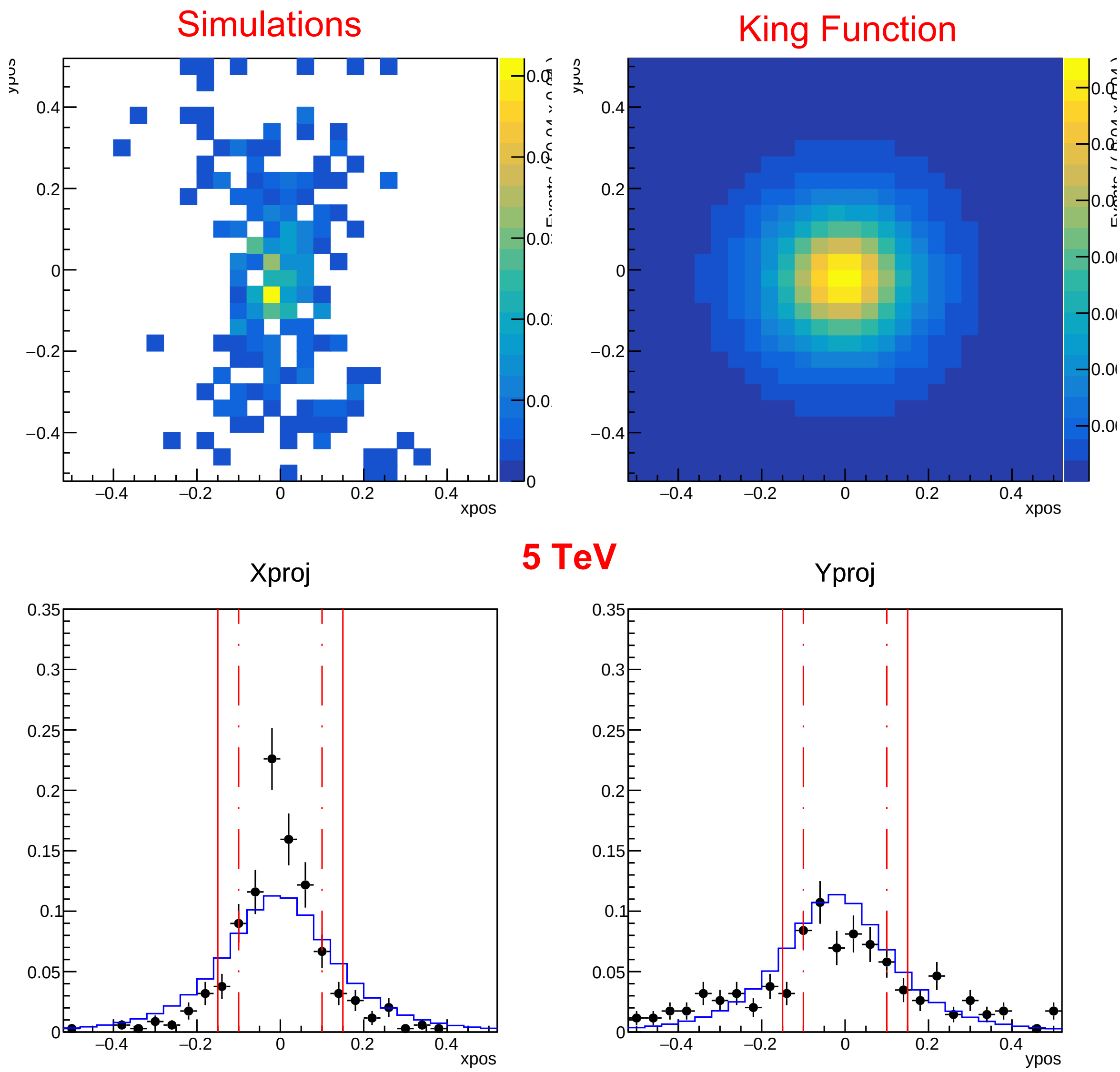


Figure B.19: A 2-D distribution of events simulated at 1.50° offset and 5 TeV, the resulting 2-D plotted King function post-fitting, and the overlaid data and fitted King function, projected in x and y. These plots are all fit with the symmetric King function, for events $1.1 < MSW < 1.3$.

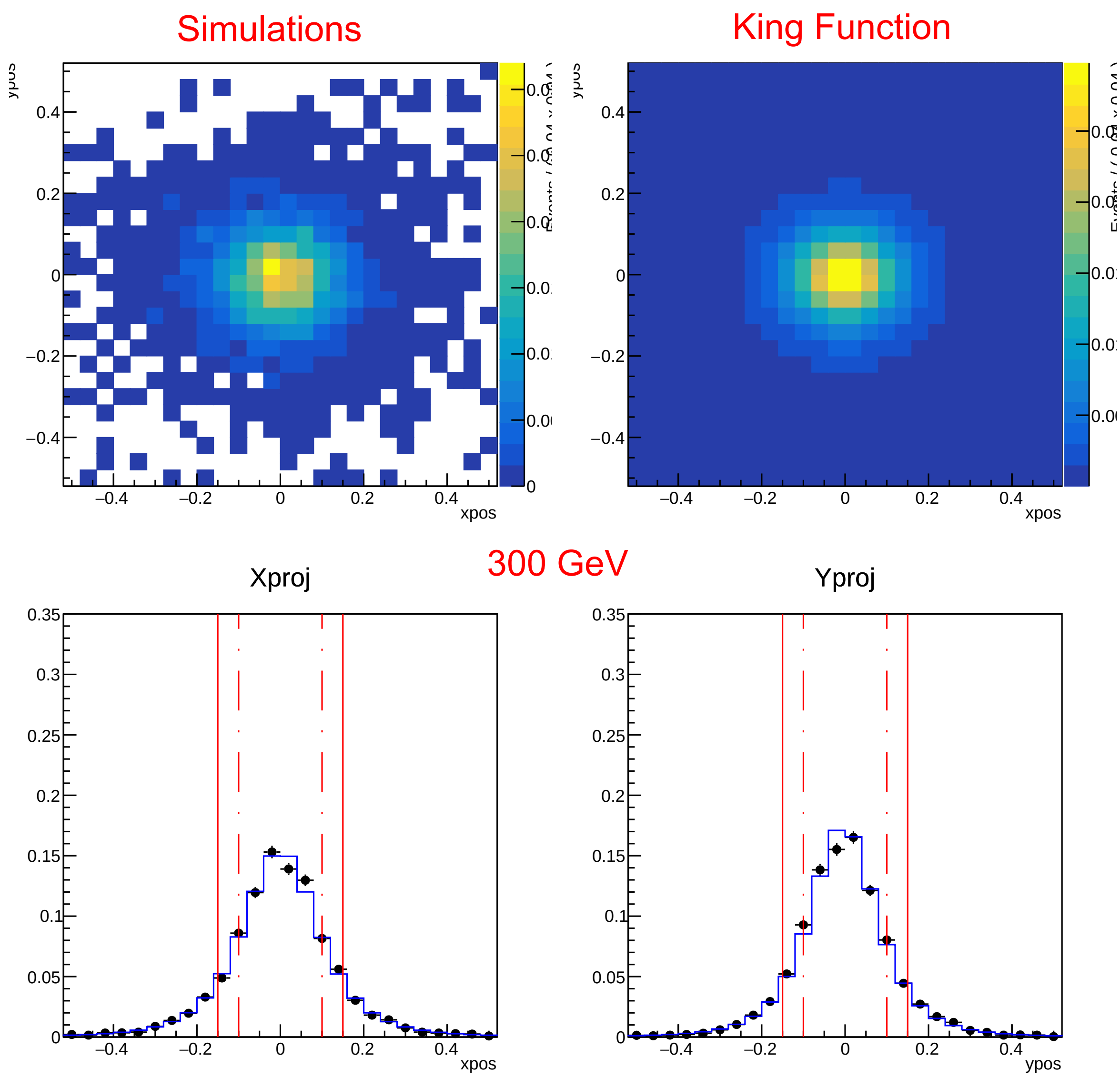


Figure B.20: A 2-D distribution of events simulated at 0.50° offset and 300 GeV, the resulting 2-D plotted King function post-fitting, and the overlaid data and fitted King function, projected in x and y. These plots are all fit with the asymmetric King function, for events $1.1 < MSW < 1.3$.

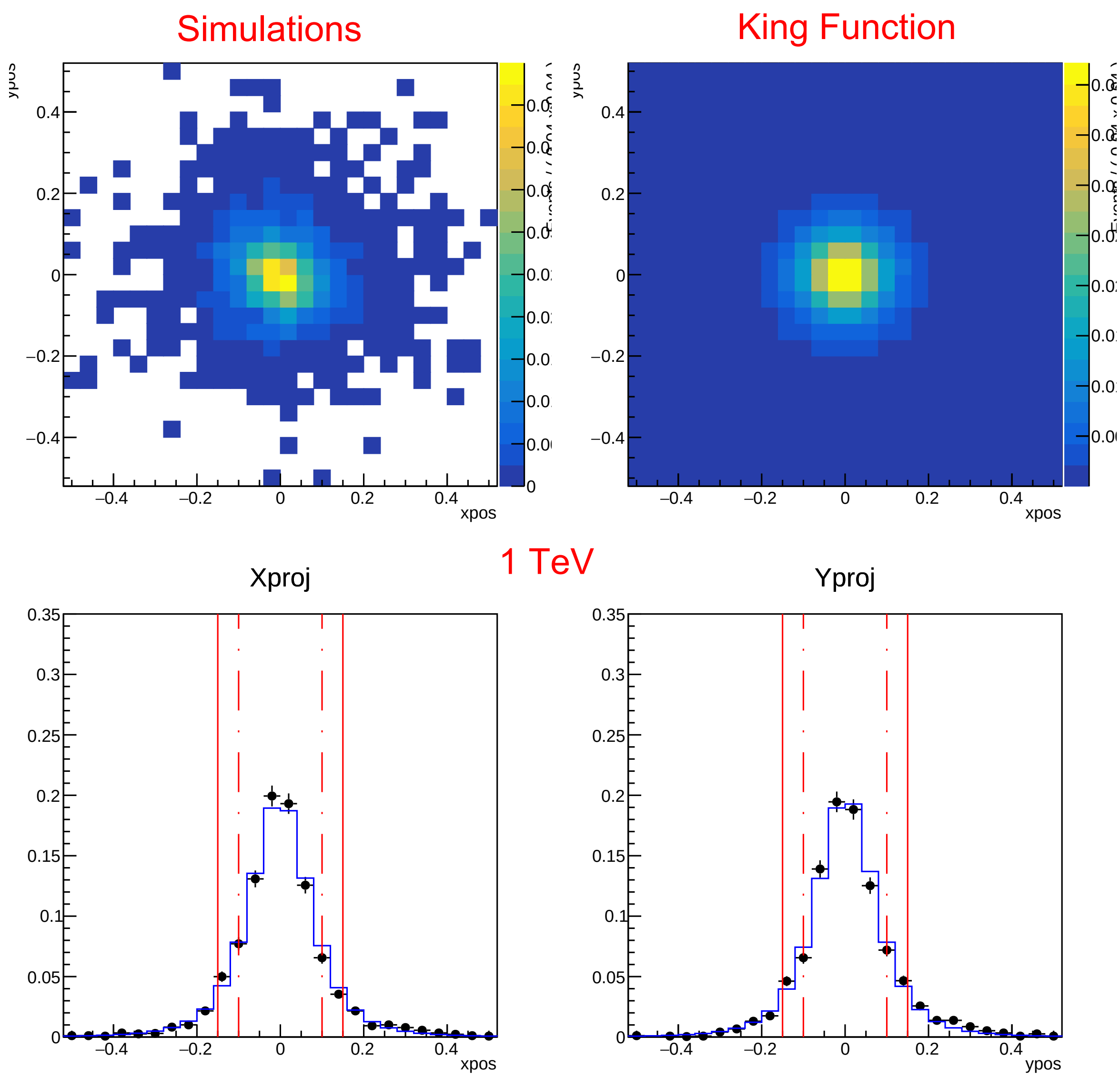


Figure B.21: A 2-D distribution of events simulated at 0.50° offset and 1 TeV, the resulting 2-D plotted King function post-fitting, and the overlaid data and fitted King function, projected in x and y. These plots are all fit with the asymmetric King function, for events $1.1 < MSW < 1.3$.

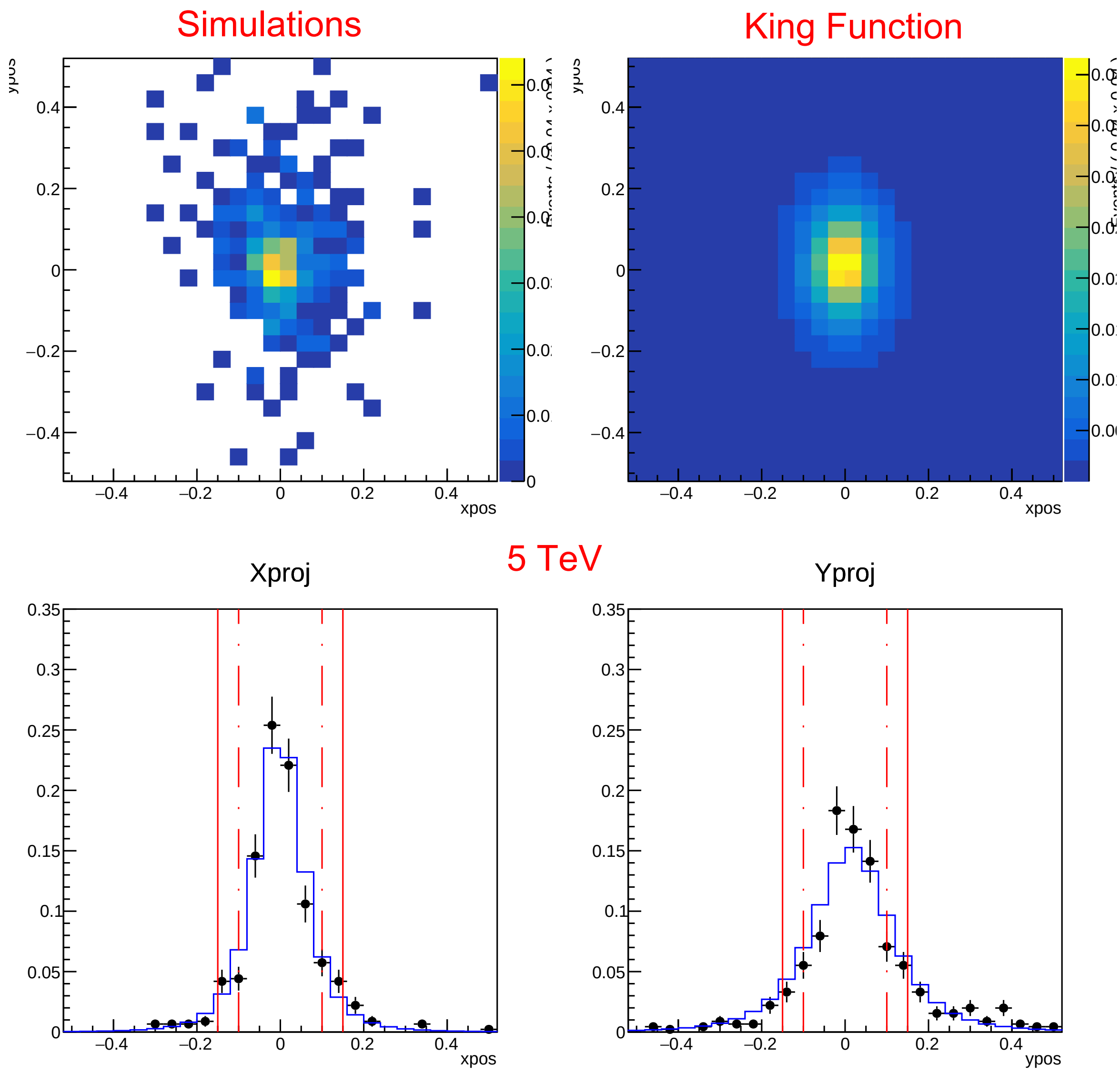


Figure B.22: A 2-D distribution of events simulated at 0.50° offset and 5 TeV, the resulting 2-D plotted King function post-fitting, and the overlaid data and fitted King function, projected in x and y. These plots are all fit with the asymmetric King function, for events $1.1 < MSW < 1.3$.

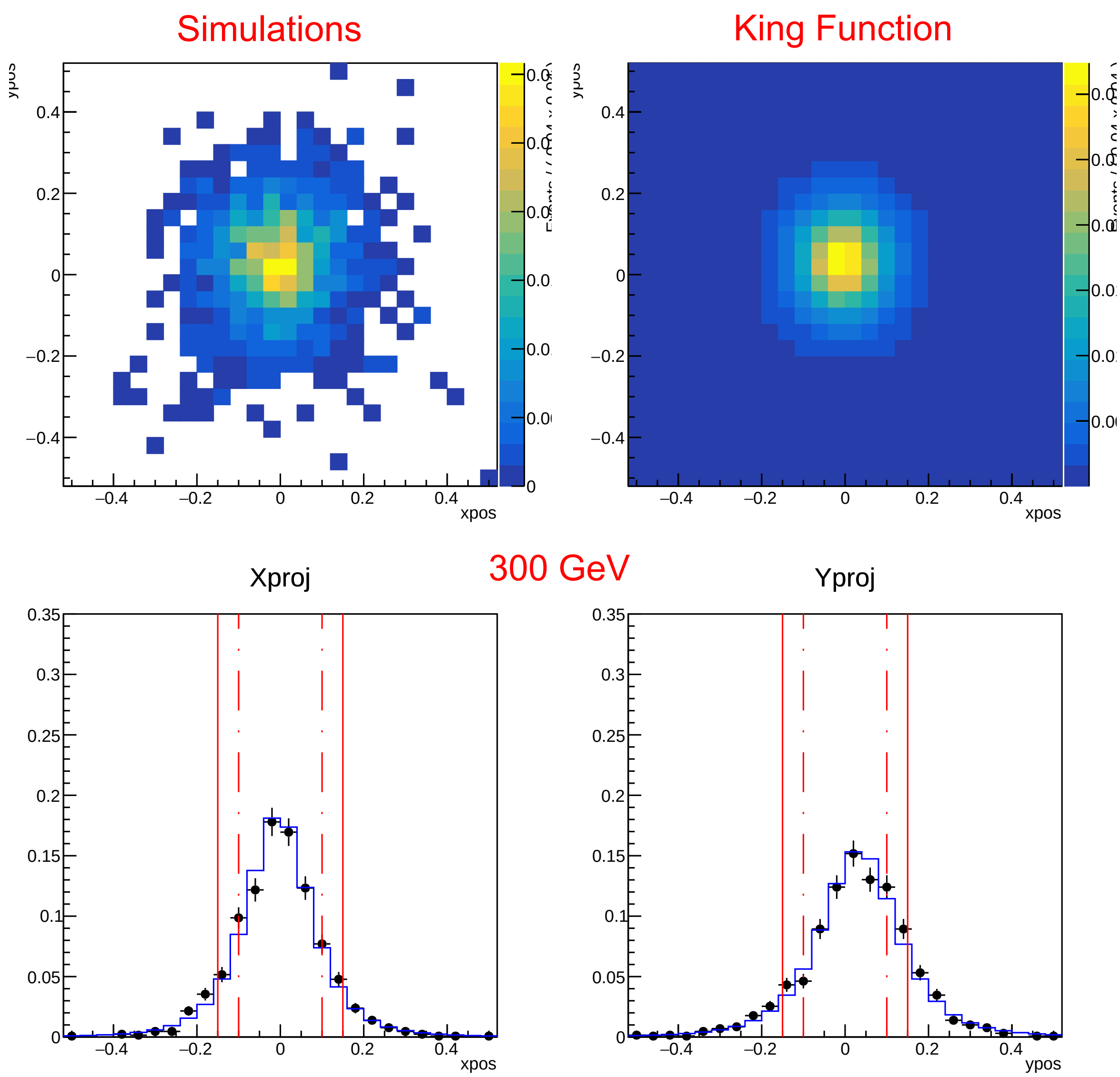


Figure B.23: A 2-D distribution of events simulated at 1.50° offset and 300 GeV, the resulting 2-D plotted King function post-fitting, and the overlaid data and fitted King function, projected in x and y. These plots are all fit with the asymmetric King function, for events $1.1 < MSW < 1.3$.

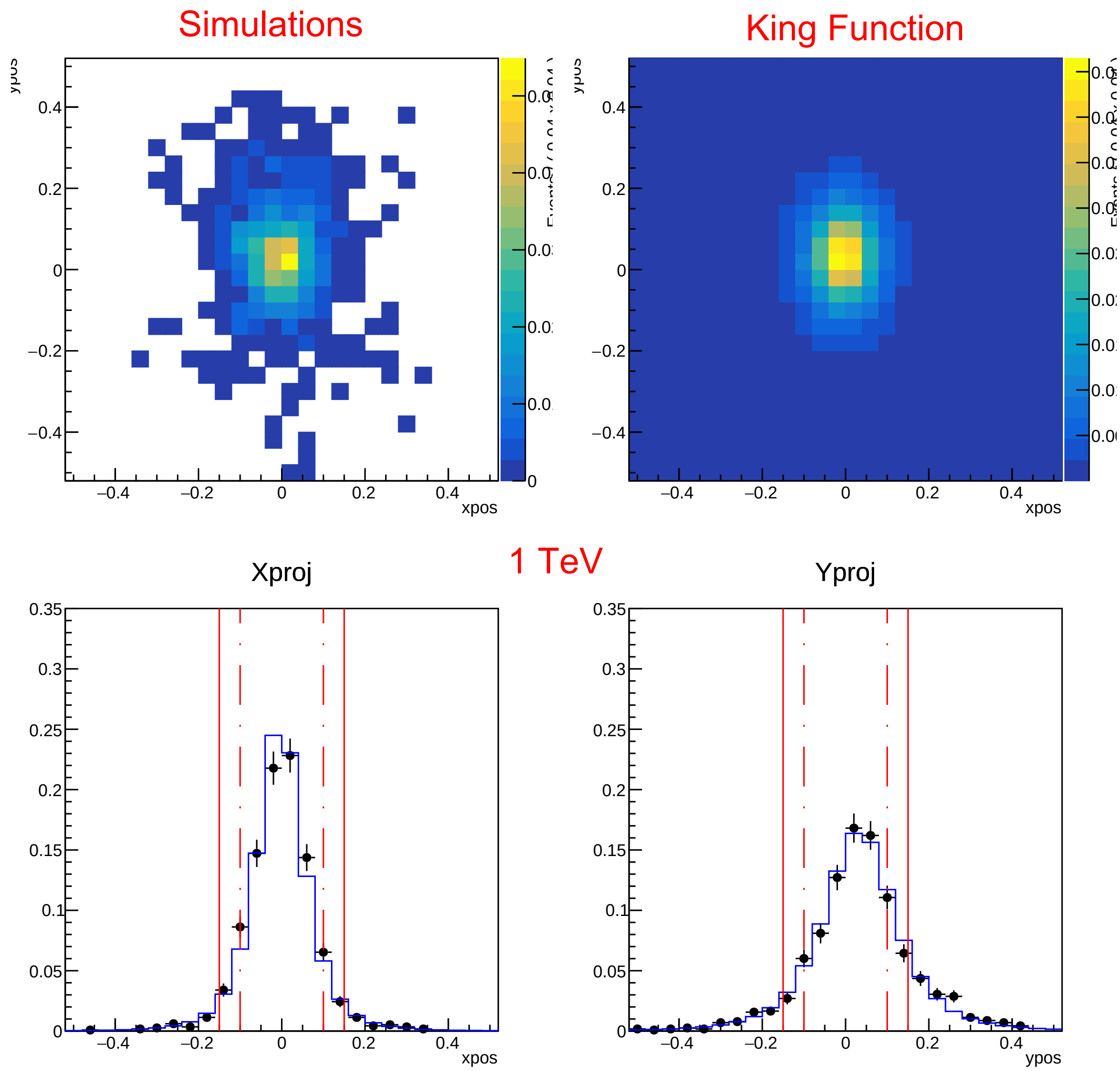


Figure B.24: A 2-D distribution of events simulated at 1.50° offset and 1 TeV, the resulting 2-D plotted King function post-fitting, and the overlaid data and fitted King function, projected in x and y. These plots are all fit with the asymmetric King function, for events $1.1 < MSW < 1.3$.

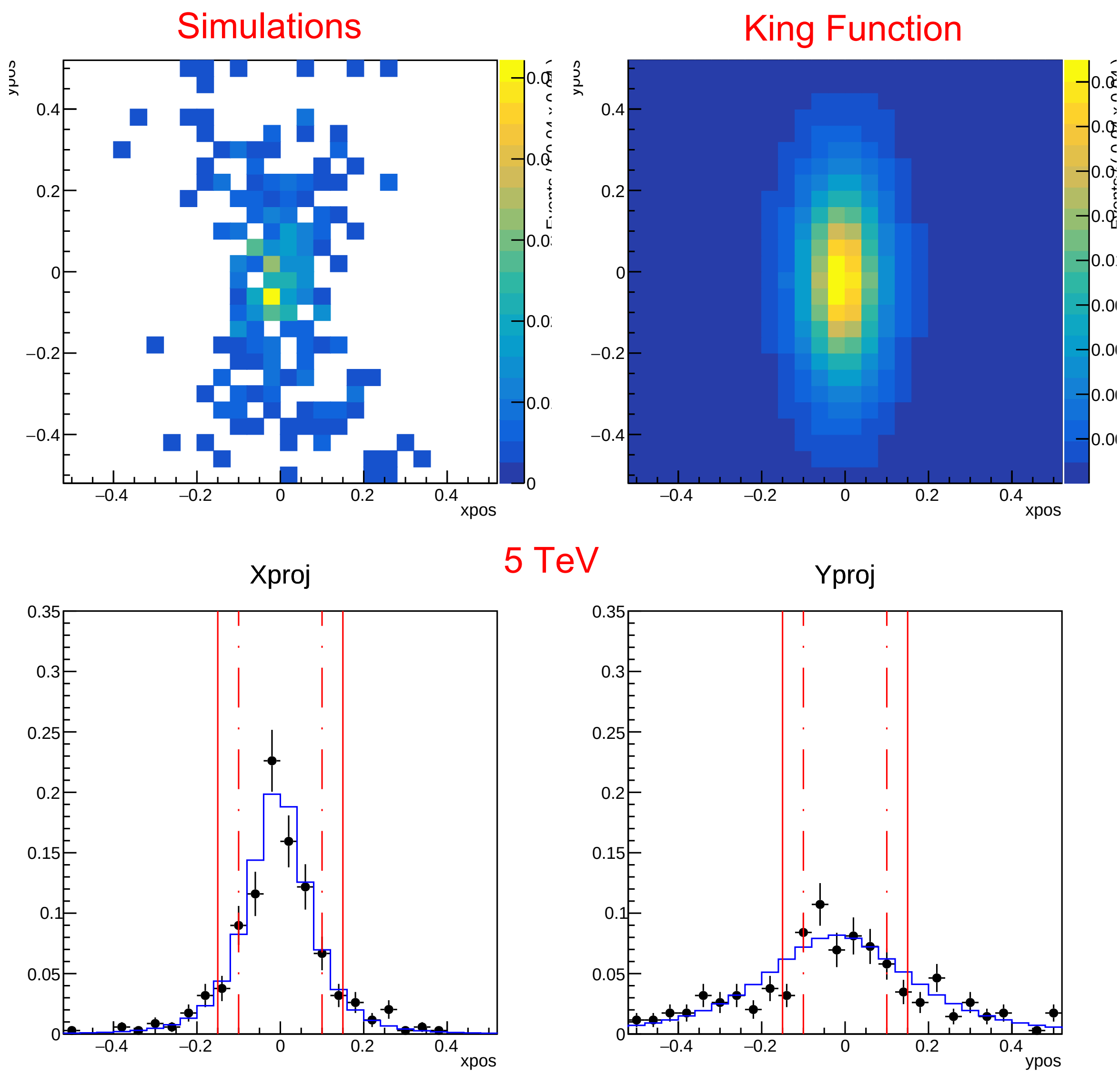


Figure B.25: A 2-D distribution of events simulated at 1.50° offset and 5 TeV, the resulting 2-D plotted King function post-fitting, and the overlaid data and fitted King function, projected in x and y. These plots are all fit with the asymmetric King function, for events $1.1 < MSW < 1.3$.